

Ministry of Education and Science of the Russian Federation
Saint Petersburg National Research University of Information
Technologies, Mechanics, and Optics

NANOSYSTEMS:
PHYSICS, CHEMISTRY, MATHEMATICS

2020, volume 11(3)

Наносистемы: физика, химия, математика

2020, том 11, № 3



NANOSYSTEMS:

PHYSICS, CHEMISTRY, MATHEMATICS

ADVISORY BOARD MEMBERS

Chairman: V.N. Vasiliev (*St. Petersburg, Russia*),
V.M. Buznik (*Moscow, Russia*); V.M. Ievlev (*Voronezh, Russia*), P.S. Kop'ev (*St. Petersburg, Russia*), N.F. Morozov (*St. Petersburg, Russia*), V.N. Parmon (*Novosibirsk, Russia*),
A.I. Rusanov (*St. Petersburg, Russia*),

EDITORIAL BOARD

Editor-in-Chief: I.Yu. Popov (*St. Petersburg, Russia*)

Section Co-Editors:

Physics – V.M. Uzdin (*St. Petersburg, Russia*),
Chemistry, material science – V.V. Gusarov (*St. Petersburg, Russia*),
Mathematics – I.Yu. Popov (*St. Petersburg, Russia*).

Editorial Board Members:

V.M. Adamyan (*Odessa, Ukraine*); O.V. Al'myasheva (*St. Petersburg, Russia*);
A.P. Alodjants (*Vladimir, Russia*); S. Bechta (*Stockholm, Sweden*); J. Behrndt (*Graz, Austria*);
M.B. Belonenko (*Volgograd, Russia*); A. Chatterjee (*Hyderabad, India*); S.A. Chivilikhin
(*St. Petersburg, Russia*); A.V. Chizhov (*Dubna, Russia*); A.N. Enyashin (*Ekaterinburg, Russia*),
P.P. Fedorov (*Moscow, Russia*); E.A. Gudilin (*Moscow, Russia*); V.K. Ivanov
(*Moscow, Russia*), H. Jónsson (*Reykjavik, Iceland*); A.A. Kiselev (*Durham, USA*);
Yu.S. Kivshar (*Canberra, Australia*); S.A. Kozlov (*St. Petersburg, Russia*); P.A. Kurasov
(*Stockholm, Sweden*); A.V. Lukashin (*Moscow, Russia*); I.V. Melikhov (*Moscow, Russia*);
G.P. Miroshnichenko (*St. Petersburg, Russia*); I.Ya. Mittova (*Voronezh, Russia*); Nguyen
Anh Tien (*Ho Chi Minh, Vietnam*); V.V. Pankov (*Minsk, Belarus*); K. Pankrashkin (*Orsay, France*);
A.V. Ragulya (*Kiev, Ukraine*); V. Rajendran (*Tamil Nadu, India*); A.A. Rempel
(*Ekaterinburg, Russia*); V.Ya. Rudyak (*Novosibirsk, Russia*); D Shoikhet (*Karmiel, Israel*);
P Stovicek (*Prague, Czech Republic*); V.M. Talanov (*Novocherkassk, Russia*); A.Ya. Vul'
(*St. Petersburg, Russia*); A.V. Yakimansky (*St. Petersburg, Russia*), V.A. Zagrebnev
(*Marseille, France*).

Editors:

I.V. Blinova; A.I. Popov; A.I. Trifanov; E.S. Trifanova (*St. Petersburg, Russia*),
R. Simoneaux (*Philadelphia, Pennsylvania, USA*).

Address: University ITMO, Kronverkskiy pr., 49, St. Petersburg 197101, Russia.

Phone: +7(812)312-61-31, **Journal site:** <http://nanojournal.ifmo.ru/>,

E-mail: popov1955@gmail.com

AIM AND SCOPE

The scope of the journal includes all areas of nano-sciences. Papers devoted to basic problems of physics, chemistry, material science and mathematics inspired by nanosystems investigations are welcomed. Both theoretical and experimental works concerning the properties and behavior of nanosystems, problems of its creation and application, mathematical methods of nanosystem studies are considered.

The journal publishes scientific reviews (up to 30 journal pages), research papers (up to 15 pages) and letters (up to 5 pages). All manuscripts are peer-reviewed. Authors are informed about the referee opinion and the Editorial decision.

CONTENT

MATHEMATICS

Shibsankar Das, Shikha Rai

M-polynomial and related degree-based topological indices of the third type of hex-derived network 267

V.D. Lukyanov, D.A. Bulekbaev, A.V. Morozov, L.V. Nosova

Approximate analytical method for finding eigenvalues of Sturm-Liouville problem with generalized boundary condition of the third kind 275

PHYSICS

V.Ya. Rudyak, E.V. Lezhnev

Stochastic molecular modeling the transport coefficients of rarefied gas and gas nanosuspensions 285

M.H.A. Badarneh, G.J. Kwiatkowski, P.F. Bessarab

Mechanisms of energy-efficient magnetization switching in a bistable nanowire 294

G.F.A. Malik, M.A. Kharadi, F.A. Khanday, K.A. Shah

Negative differential resistance in gate all-around spin field effect transistors 301

S.Z. Rakhmanov, O.V. Karpova, F.S. Khashimova, B.Kh. Eshchanov

High harmonic generation by an atom confined in nanoscale cavity 307

CHEMISTRY AND MATERIAL SCIENCE

The papers in the section "Chemistry and Material Science" are dedicated to the 70th anniversary of prominent Russian scientist-chemist - Pavel P. Fedorov

P.P. Fedorov

Nanotechnology and material science 314

S.V. Kuznetsov, A.S. Nizamutdinov, E.I. Madirov, V.V. Voronov,

K.S. Tsoy, A.R. Khadiev, A.D. Yapryntsev, V.K. Ivanov,

S.S. Kharintsev, V.V. Semashko

Near infrared down-conversion luminescence of $\text{Ba}_4\text{Y}_3\text{F}_{17}:\text{Yb}^{3+}:\text{Eu}^{3+}$ nanoparticles under ultraviolet excitation 316

M.M. Sozarukova, E.V. Proskurnina, A.E. Baranchikov, V.K. Ivanov CeO₂ nanoparticles as free radical regulators in biological systems	324
L.N. Ignatieva, N.N. Savchenko, Y.V. Marchenko, V.A. Mashchenko, V.M. Bouzник Raman study of glasses in the NbO₂F-BaF₂-InF₃-ErF₃ and CdNbOF₅-BaF₂-InF₃ systems	333
A.S. Svinolupova, M.S. Lomakin, S.A. Kirillova, O.V. Almjasheva Formation of Bi₂WO₆ nanocrystals under conditions of hydrothermal treatment	338
V.P. Vorob'eva, A.E. Zelenaya, V.I. Lutsyk, M.V. Lamueva 3D computer models of the T-x-y diagrams, forming the LiF-NaF-CaF₂-LaF₃ T-x-y-z diagram	345
A.N. Bugrov, V.K. Vorobiov, M.P. Sokolova, G.P. Kopitsa, S.A. Bolshakov, M.A. Smirnov Hydrothermal synthesis of CeO₂ nanostructures and their electrochemical properties	355
Information for authors	365

M-polynomial and related degree-based topological indices of the third type of hex-derived network

Shibsankar Das, Shikha Rai

Department of Mathematics, Institute of Science, Banaras Hindu University, Varanasi-221005, Uttar Pradesh, India
shib.iitm@gmail.com, shikharai48@gmail.com

PACS 02.10.Ox, 61.48.-c

DOI 10.17586/2220-8054-2020-11-3-267-274

In the field of chemical graph theory, a topological index is a real number which is correlated with the various physical properties, biological activities and chemical reactivities of molecular graphs. In recent trends, M-polynomials are used to compute numerous degree-based topological indices. Hex-derived networks have a wide range of applications in pharmaceutical sciences, electronics and communication networks. In this paper, we would like to determine a general form of M-polynomial for the third type of hex-derived network of dimension n and hence generate the related degree-based topological indices. Additionally, we plot the M-polynomial and all the related degree-based topological indices for several n .

Keywords: Third type of hex-derived network, Degree-based topological indices, M-polynomial, Graph polynomial.

Received: 13 April 2020

Revised: 26 April 2020

1. Introduction

Let $G = (V, E)$ be a simple connected graph, where $V = V(G)$ and $E = E(G)$ respectively denote the vertex set and the edge set which contains unordered pairs of vertices. The *degree* of a vertex $u \in V(G)$ in G is the number of vertices that are adjacent to u and is denoted by $d(u)$ [1].

1.1. A brief review on topological indices and M-polynomials

Mathematical aspects of chemical compounds and their behaviors are being investigated in the area of Chemical Graph Theory (CGT). For a given chemical compound, each atom is represented by a vertex and each chemical bond between the atoms is represented by an edge to form a graph. Several chemical applications of graphs and the connection between graph theory and chemistry have been reported in [2–5]. In the graph-theoretical representation of a molecule, we can study various biological activities, physical properties, chemical reactivities and other properties of chemical compounds. In the area of CGT, a *topological index* (also known as a *graph-theoretic index* or *connectivity index*) specifies the properties of a molecular structure. Generally, it is a numerical representation of a molecule, which is used in the development of Quantitative Structure Activity Relationships (QSARs) and Quantitative Structure Property Relationships (QSPRs). For more details please refer to [6, 7].

The topological indices are usually partitioned into degree-based topological indices [8], distance-based topological indices [9], degree and distance-based topological indices [10] and counting related topological indices [11]. These indices describe the physical, biological, chemical and other properties of various structures. Generally, by the definitions of the respective topological indices, we can calculate their numeric values. Instead, a general method can be found to directly produce the different topological indices of a particular class. Keeping this idea in mind, the concept of polynomials [12] is introduced in graph theory. By constructing a general polynomial corresponding to a given structure, one can derive several topological indices by differentiating or integrating (or a different combination of both) the corresponding polynomial.

In literature, several such polynomials are proposed. Some of which are the matching polynomial [13], the Clar covering polynomial (also known as the Zhang-Zhang polynomial) [14], the Schultz polynomial [15], the Tutte polynomial [16], the Hosoya polynomial [17], etc. Among all of these polynomials, the Hosoya polynomial is used for finding the distance-based topological indices such as the Wiener index [18].

The degree-based topological indices play a major role to understand various properties of a molecular structure. In the recent studies, the idea of M-polynomial is proposed by Deutsch and Klavžar [19] and determined how to evaluate several degree-based topological indices. Please refer to the papers [20–24], in each of which the M-polynomial corresponding to a chemical network is derived and henceforth their related degree-based topological indices are evaluated.

Definition 1 ([19]). For a simple connected graph G , the expression

$$M(G; x, y) = \sum_{\delta \leq i \leq j \leq \Delta} m_{i,j}(G) x^i y^j$$

is known as the M -polynomial of a graph G , where $\delta = \min\{d(u)|u \in V(G)\}$, $\Delta = \max\{d(u)|u \in V(G)\}$ and $m_{i,j}(G)$ is the number of edges $uv \in E(G)$ such that $d(u) = i, d(v) = j$ ($i, j \geq 1$).

A degree-based topological index of a graph G is one of a kind of graph invariants, which is denoted as $I(G)$ and as discussed in [25], it can be written as:

$$I(G) = \sum_{i \leq j} m_{i,j}(G) f(i, j).$$

Theorem 2 ([19], Theorems 2.1, 2.2). Let G be a simple connected graph.

(1) If $I(G) = \sum_{e=uv \in E(G)} f(d(u), d(v))$, where $f(x, y)$ is a polynomial in x and y , then

$$I(G) = f(D_x, D_y)(M(G; x, y))|_{x=y=1}.$$

(2) If $I(G) = \sum_{e=uv \in E(G)} f(d(u), d(v))$, where $f(x, y) = \sum_{i,j \in \mathbb{Z}} \alpha_{i,j} x^i y^j$, then $I(G)$ can be obtained from $M(G; x, y)$ using the operators D_x, D_y, S_x , and S_y .

(3) If $I(G) = \sum_{e=uv \in E(G)} f(d(u), d(v))$, where $f(x, y) = \frac{x^r y^s}{(x + y + \alpha)^t}$, where $r, s \geq 0, t \geq 1$ and $\alpha \in \mathbb{Z}$, then

$$I(G) = S_x^t Q_\alpha J D_x^r D_y^s (M(G; x, y))|_{x=1}.$$

1.2. Associated degree-based topological indices

In this section, we discuss a brief about certain degree-based topological indices that can be derived from the M -polynomial of our considered network. Gutman and Trinajstić [26] proposed the *Zagreb indices* in 1972. These indices help in determining the total π -electron energy which is related to the thermodynamic stability of a molecule. The Zagreb indices give higher weightage to the inner edges and vertices rather than the outer edges and vertices. With the opposite intuition, the definitions of *modified Zagreb indices* are proposed in [27].

TABLE 1. Formula for degree-based topological indices of a graph G

Sl. No.	Topological Index	Notation	Formula of Topological Indices
1.	First Zagreb Index [26]	$M_1(G)$	$M_1(G) = \sum_{uv \in E(G)} (d(u) + d(v))$
2.	Second Zagreb Index [26]	$M_2(G)$	$M_2(G) = \sum_{uv \in E(G)} (d(u)d(v))$
3.	Modified Second Zagreb Index [27]	${}^m M_2(G)$	${}^m M_2(G) = \sum_{uv \in E(G)} \frac{1}{d(u)d(v)}$
4.	General Randić Index [28]	$R_\alpha(G)$	$R_\alpha(G) = \sum_{uv \in E(G)} (d(u)d(v))^\alpha$
5.	Inverse Randić Index [29]	$RR_\alpha(G)$	$RR_\alpha(G) = \sum_{uv \in E(G)} \frac{1}{(d(u)d(v))^\alpha}$
6.	Symmetric Division (Deg) Index [30]	$SDD(G)$	$SDD(G) = \sum_{uv \in E(G)} \left\{ \frac{\min(d(u),d(v))}{\max(d(u),d(v))} + \frac{\max(d(u),d(v))}{\min(d(u),d(v))} \right\}$
7.	Harmonic Index [31]	$H(G)$	$H(G) = \sum_{uv \in E(G)} \frac{2}{d(u)+d(v)}$
8.	Inverse Sum (Indeg) Index [30]	$ISI(G)$	$ISI(G) = \sum_{uv \in E(G)} \frac{d(u)d(v)}{d(u)+d(v)}$
9.	Augmented Zagreb Index [32]	$AZ(G)$	$AZ(G) = \sum_{uv \in E(G)} \left\{ \frac{d(u)d(v)}{d(u)+d(v)-2} \right\}^3$

Another very well-known degree-based topological index is the *Randić index*. It is introduced by Milan Randić [33] in 1975. It is also known as a *connectivity index* or *branching index*. This index has wide applications in the field of drug design. Two decades later, observing the advancement of Randić index, the mathematicians Bollobás and Erdős [28], and Amić et al. [29] introduced the generalized version of the Randić index (for an arbitrary real number α) in 1998, which is known as *general Randić index*. For $\alpha = -\frac{1}{2}$, R_α becomes a Randić index [33]; for $\alpha = 1$, R_α becomes a second Zagreb index; and for $\alpha = -1$, R_α turns out to be a modified second Zagreb index. Around 2010, the *symmetric division (deg) index* is proposed in [30] to determine the total surface area of polychlorobiphenyls. Whereas, the *inverse sum (indeg) index* [30, 34] predicts the total surface area of octane isomers. For the study of the heat of formation of alkanes, the *augmented Zagreb index* [32] is beneficial. Table 1 lists the formulas of the different degree-based topological indices (of a graph G) which are associated with M-polynomial.

1.3. The hex-derived network of type 3 of dimension n

The Hexagonal network of dimension n is introduced in [35] and is denoted by $HX[n]$. It has several applications in the image processing to model the benzenoid hydrocarbons in the field of chemistry, wireless sensor networks and computer graphics. Later in 2008, the hex-derived network of type 1 ($HDN1$) and hex-derived network of type 2 ($HDN2$) of dimension n (where n denotes the number of vertices in a side of the HDN structure) are constructed from the $HX[n]$ [36]. Again in 2017, based on the structure of the $HX[n]$, Raj and George [37] have derived a new network called hex-derived network of type 3 of dimension n (denoted as $HDN3[n]$). Fig. 1 depicts the pictorial representation of the third type of hex-derived network of dimension 4 (that is, $HDN3[4]$). The metric dimension of $HDN3[n]$ has a wide range of applications in robotics, networking etc.

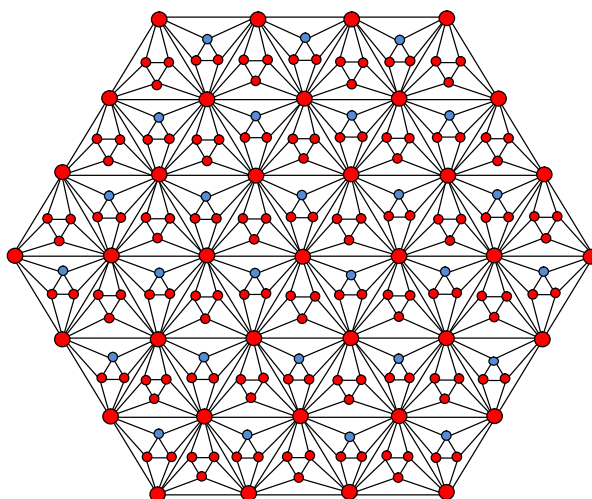


FIG. 1. Type 3 hex-derived network of dimension 4 ($HDN3[4]$)

1.4. Our contribution and roadmap

Recently, Wei et. al. [38] computed several degree-based topological indices of $HDN3[n]$. The indices are calculated separately as well as directly by using their degree-based formulas mentioned in Table 1. As an alternative of the above, we derive a closed-form of M-polynomial for the $HDN3[n]$ in Section 2. Henceforward, we calculate the related degree-based topological indices of the network (for different values of n) via using the M-polynomial. Moreover, the graphical representation of the M-polynomial and related topological indices for different dimensions of the network are plotted in Section 3.

2. Deriving a M-polynomial for $HDN3[n]$ network

Theorem 3. Let $HDN3[n]$ be the third type of hex-derived network of dimension $n (\geq 4)$. Then a M-polynomial of $HDN3[n]$ is

$$M(HDN3[n]; x, y) = (18n^2 - 36n + 18)x^4y^4 + 24x^4y^7 + (36n - 72)x^4y^{10} + (36n^2 - 108n + 84)x^4y^{18} + 12x^7y^{10} + 6x^7y^{18} + (6n - 18)x^{10}y^{10} + (12n - 24)x^{10}y^{18} + (9n^2 - 33n + 30)x^{18}y^{18}.$$

Proof. Let us first enumerate the cardinality of the vertex set and the edge set of the $HDN3[n]$ by observing the Fig. 1 of $HDN3[4]$.

$$|V(HDN3[n])| = 21n^2 - 39n + 19, \text{ and}$$

$$|E(HDN3[n])| = 63n^2 - 123n + 60.$$

Observe that, based on the degree of vertices of $HDN3[n]$, the network consists of 4, 7, 10 and 18 degrees vertices only, and each of whose cardinality is $18(n - 1)^2$, 6, $6(n - 2)$ and $3n^2 - 9n + 7$, respectively. Also, we partition the edge set $E(HDN3[n])$ of $HDN3[n]$ into nine disjoint sub-classes depending on the degrees of the end vertices of each edge, as: $E_{\{i,j\}} = \{e = uv \in E(HDN3[n]) : d(u) = i, d(v) = j\}$ where $\{i, j\} = \{4, 4\}, \{4, 7\}, \{4, 10\}, \{4, 18\}, \{7, 10\}, \{7, 18\}, \{10, 10\}, \{10, 18\}, \{18, 18\}$. And the cardinality of each of the above edge sets is given by $|E_{\{4,4\}}| = 18n^2 - 36n + 18$, $|E_{\{4,7\}}| = 24$, $|E_{\{4,10\}}| = 36n - 72$, $|E_{\{4,18\}}| = 36n^2 - 108n + 84$, $|E_{\{7,10\}}| = 12$, $|E_{\{7,18\}}| = 6$, $|E_{\{10,10\}}| = 6n - 18$, $|E_{\{10,18\}}| = 12n - 24$, $|E_{\{18,18\}}| = 9n^2 - 33n + 30$. Observe that the hex-derive network structure does not have any edge uv such that $d(u) = 7 = d(v)$ and as a consequence $|E_{\{7,7\}}| = 0$. Therefore, by the basic definition of M-polynomial, the M-polynomial of $HDN3[n]$ is

$$M(HDN3[n]; x, y)$$

$$= \sum_{i \leq j} m_{i,j} x^i y^j, \text{ where } i, j \in \{4, 7, 10, 18\}$$

$$= |E_{\{4,4\}}| x^4 y^4 + |E_{\{4,7\}}| x^4 y^7 + |E_{\{4,10\}}| x^4 y^{10} + |E_{\{4,18\}}| x^4 y^{18} + |E_{\{7,10\}}| x^7 y^{10}$$

$$+ |E_{\{7,18\}}| x^7 y^{18} + |E_{\{10,10\}}| x^{10} y^{10} + |E_{\{10,18\}}| x^{10} y^{18} + |E_{\{18,18\}}| x^{18} y^{18}$$

$$= (18n^2 - 36n + 18) x^4 y^4 + 24 x^4 y^7 + (36n - 72) x^4 y^{10} + (36n^2 - 108n + 84) x^4 y^{18}$$

$$+ 12 x^7 y^{10} + 6 x^7 y^{18} + (6n - 18) x^{10} y^{10} + (12n - 24) x^{10} y^{18} + (9n^2 - 33n + 30) x^{18} y^{18}.$$

□

TABLE 2. Formulas for degree-based topological indices derived from the M-polynomial of a graph G

Sl. No.	Topological Index	Notation	f(x,y)	Derivation from $(M(G; x, y))$
1.	First Zagreb Index	$M_1(G)$	$x + y$	$(D_x + D_y)(M(G; x, y)) _{x=y=1}$
2.	Second Zagreb Index	$M_2(G)$	xy	$(D_x D_y)(M(G; x, y)) _{x=y=1}$
3.	Modified Second Zagreb Index	${}^m M_2(G)$	$\frac{1}{xy}$	$(S_x S_y)(M(G; x, y)) _{x=y=1}$
4.	General Randić Index	$R_\alpha(G)$	$(xy)^\alpha$	$(D_x^\alpha D_y^\alpha)(M(G; x, y)) _{x=y=1}$
5.	Inverse Randić Index	$RR_\alpha(G)$	$\frac{1}{(xy)^\alpha}$	$(S_x^\alpha S_y^\alpha)(M(G; x, y)) _{x=y=1}$
6.	Symmetric Division (Deg) Index	$SDD(G)$	$\frac{x^2 + y^2}{xy}$	$(D_x S_y + D_y S_x)(M(G; x, y)) _{x=y=1}$
7.	Harmonic Index	$H(G)$	$\frac{2}{x+y}$	$2S_x J(M(G; x, y)) _{x=1}$
8.	Inverse Sum (Indeg) Index	$ISI(G)$	$\frac{xy}{x+y}$	$S_x J D_x D_y (M(G; x, y)) _{x=1}$
9.	Augmented Zagreb Index	$AZ(G)$	$\left(\frac{xy}{x+y-2}\right)^3$	$S_x^3 Q_{-2} J D_x^3 D_y^3 (M(G; x, y)) _{x=1}$

To calculate the concerned topological indices (as mentioned in Table 1) of a given graph G from the $M(G; x, y)$, the formulas of derivations in terms of integral or derivative (or both integral and derivative) are listed in Table 2 [19], where $D_x = x \frac{\partial(f(x, y))}{\partial x}$, $D_y = y \frac{\partial(f(x, y))}{\partial y}$, $S_x = \int_0^x \frac{f(t, y)}{t} dt$, $S_y = \int_0^y \frac{f(x, t)}{t} dt$, $J(f(x, y)) = f(x, x)$, and $Q_\alpha(f(x, y)) = x^\alpha f(x, y)$, $\alpha \neq 0$.

The following theorem determines the values of the related degree-based topological indices of the $HDN3[n]$ from the above proposed M-polynomial $M(HDN3[n]; x, y)$.

Theorem 4. Let $HDN3[n]$ be the third type of hex-derived network of dimension $n (\geq 4)$. Then

(1) $M_1(HDN3[n]) = 6(210n^2 - 482n + 275)$.

- (2) $M_2(HDN3[n]) = 12(483n^2 - 1237n + 777)$.
- (3) ${}^m M_2(HDN3[n]) = \frac{1}{16}(18n^2 - 36n + 18) + \frac{24}{28} + \frac{1}{40}(36n - 72) + \frac{1}{72}(36n^2 - 108n + 84) + \frac{12}{70} + \frac{6}{126} + \frac{1}{100}(6n - 18) + \frac{1}{180}(12n - 24) + \frac{1}{324}(9n^2 - 33n + 30) = \frac{119}{72}n^2 - \frac{1907}{675}n + \frac{50921}{37800}$.
- (4) $R_\alpha(HDN3[n]) = 4^{2\alpha}(18n^2 - 36n + 18) + 24 \times 28^\alpha + 40^\alpha(36n - 72) + 72^\alpha(36n^2 - 108n + 84) + 12 \times 70^\alpha + 6 \times 126^\alpha + 10^{2\alpha}(6n - 18) + 180^\alpha(12n - 24) + 18^{2\alpha}(9n^2 - 33n + 30)$.
- (5) $RR_\alpha(HDN3[n]) = \frac{(18n^2 - 36n + 18)}{4^{2\alpha}} + \frac{24}{28^\alpha} + \frac{(36n - 72)}{40^\alpha} + \frac{(36n^2 - 108n + 84)}{72^\alpha} + \frac{12}{70^\alpha} + \frac{6}{126^\alpha} + \frac{(6n - 18)}{10^{2\alpha}} + \frac{(12n - 24)}{180^\alpha} + \frac{(9n^2 - 33n + 30)}{18^{2\alpha}}$.
- (6) $SDD(HDN3[n]) = 224n^2 - \frac{1510}{3}n + \frac{30487}{105}$.
- (7) $H(HDN3[n]) = 2 \times \left[\frac{1}{8}(18n^2 - 36n + 18) + \frac{24}{11} + \frac{1}{14}(36n - 72) + \frac{1}{22}(36n^2 - 108n + 84) + \frac{12}{17} + \frac{6}{25} + \frac{1}{20}(6n - 18) + \frac{1}{28}(12n - 24) + \frac{1}{36}(9n^2 - 33n + 30) \right] = \frac{91}{11}n^2 - \frac{4637}{330}n + \frac{15959}{2550}$.
- (8) $ISI(HDN3[n]) = 2(18n^2 - 36n + 18) + \frac{672}{11} + \frac{40}{14}(36n - 72) + \frac{72}{22}(36n^2 - 108n + 84) + \frac{840}{17} + \frac{756}{25} + 5(6n - 18) + \frac{180}{28}(12n - 24) + \frac{324}{36}(9n^2 - 33n + 30) = \frac{2583}{11}n^2 - \frac{5637}{11}n + \frac{115452}{425}$.
- (9) $AZ(HDN3[n]) = \frac{4^6}{6^3}(18n^2 - 36n + 18) + \frac{24 \times 28^3}{9^3} + \frac{40^3}{12^3}(36n - 72) + \frac{72^3}{20^3}(36n^2 - 108n + 84) + \frac{12 \times 70^3}{15^3} + \frac{6 \times 126^3}{23^3} + \frac{10^6}{18^3}(6n - 18) + \frac{180^3}{26^3}(12n - 24) + \frac{18^6}{34^3}(9n^2 - 33n + 30)$.

Proof. One can directly derive the above topological indices by applying the respective derivation formulas over the proposed M-polynomial $M(HDN3[n]; x, y)$ as directed in the fifth column of Table 2. These calculations are trivial and hence they are left to the ambitious reader. □

Remark 5. In the paper [38], the general Randić index is calculated for the HDN3[n] for different values of α . Instead of calculating this index individually, we can simply put these values of α in the above formula of $R_\alpha(HDN3[n])$ to generate the respective values of the general Randić index.

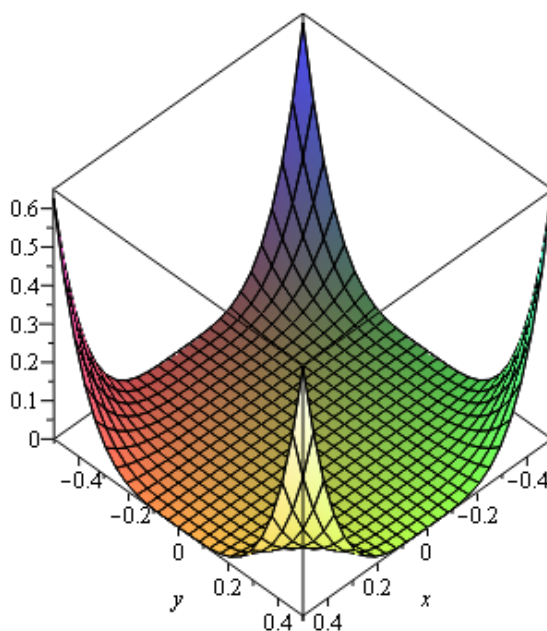


FIG. 2. The plot of the M-polynomial of HDN3[4] in region $-0.5 \leq x, y \leq 0.5$

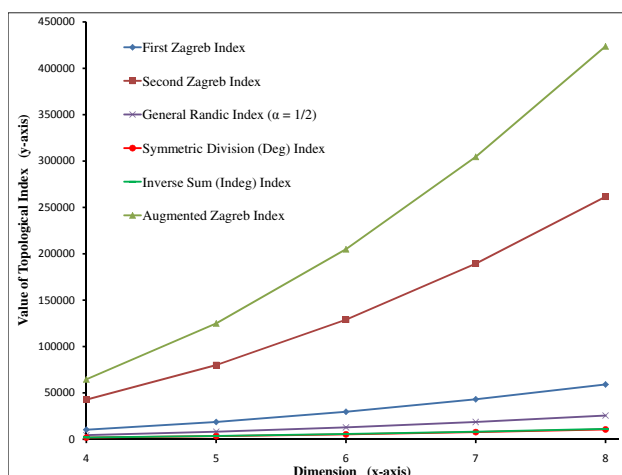


FIG. 3. A plot of first Zagreb, second Zagreb, general Randić ($\alpha = 1/2$), symmetric division (deg), inverse sum (indeg) and augmented Zagreb indices of $HDN3[n]$ for different values of n ($4 \leq n \leq 8$)

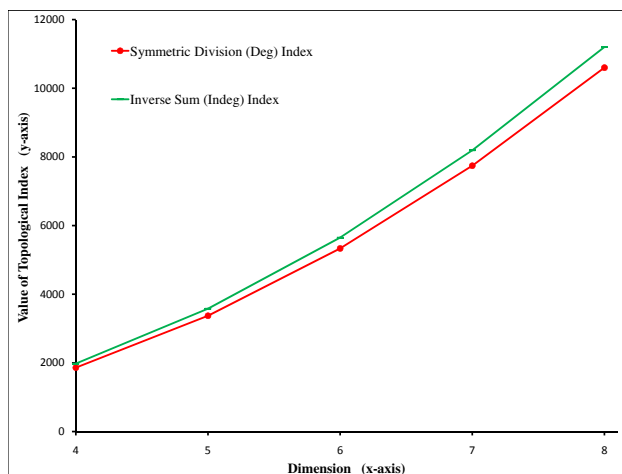


FIG. 4. A plot of only symmetric division (deg) and inverse sum (indeg) indices of $HDN3[n]$ for different values of n ($4 \leq n \leq 8$)

3. Experimental results related to the M-polynomial

Fig. 2 pictorially models the M-polynomial $M(HDN3[4]; x, y)$ of the hex-derived network of type 3 of dimension 4 ($HDN3[4]$) in the domain $-0.5 \leq x, y \leq 0.5$, by using MapleTM 13 software.

Additionally, by observing the broad range of values of the degree-based topological indices of $HDN3[n]$ for different dimensional values of n ($4 \leq n \leq 8$), we plot the values of the first Zagreb, second Zagreb, general Randić ($\alpha = 1/2$), symmetric division (deg), inverse sum (indeg) and augmented Zagreb indices in Fig. 3, and the values of the modified second Zagreb, inverse Randić ($\alpha = 1/2$) and Harmonic indices in Fig. 5. The curves plotted in the Fig. 3 for the symmetric division (deg) and inverse sum (indeg) indices are almost overlapping and hence separately redrawn in Fig. 4. It is evident from the figures that the values of each of the topological indices are increasing when the dimensions are in increasing order.

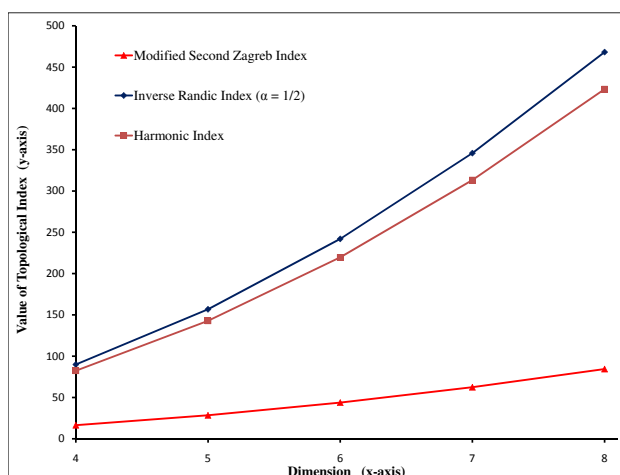


FIG. 5. A plot of modified second Zagreb, inverse Randić ($\alpha = 1/2$) and Harmonic indices of $HDN3[n]$ for different values of n ($4 \leq n \leq 8$)

4. Conclusion

In this paper, we have considered the third type of hex-derived network of dimension n ($HDN3[n]$) which has several applications in pharmaceutical sciences, electronics and communication networks. Instead of calculating the various degree-based topological indices separately, we have determined a general and closed-form of M-polynomial and thus directly derived the related degree-based topological indices of $HDN3[n]$. Also, we have graphically represented the M-polynomial, and all the associated topological indices for different dimensions.

References

- [1] West D. B. *Introduction to Graph Theory*. 2nd Edition, Prentice Hall., 2000.
- [2] Hammack R., Imrich W., Klavžar S. *Handbook of Product Graphs*. 2nd Edition, CRC Press, Inc., Boca Raton, FL, USA, 2011.
- [3] Estrada E. Randić index, irregularity and complex biomolecular networks. *Acta Chimica Slovenica*, 2010, **57**, P. 597–603.
- [4] García-Domenech R., Gálvez J., de Julián-Ortiz J. V., Pogliani L. Some new trends in chemical graph theory. *Chemical Reviews*, 2008, **108**(3), P. 1127–1169.
- [5] Balaban A. T. *Chemical applications of graph theory*. Mathematical Chemistry. Academic Press., 1976.
- [6] Trinajstić N. *Chemical Graph Theory*. Mathematical Chemistry Series. 2nd edition, CRC Press., 1992.
- [7] Gross J. L., Yellen J., Zhang P. *Handbook of Graph Theory*. Discrete Mathematics and Its Applications. 2nd edition, Chapman and Hall/CRC., 2013.
- [8] Gutman I. Degree-based topological indices. *Croatica Chemica Acta*, 2013, **86**(4), P. 351–361.
- [9] Balaban A. T. Highly discriminating distance-based topological index. *Chemical Physics Letters*, 1982, **89**(5), P. 399–404.
- [10] Pattabiraman K. Degree and distance based topological indices of graphs. *Electronic Notes in Discrete Mathematics*, 2017, **63**, P. 145–159.
- [11] Khadikar P. V., Deshpande N. V., Kale P. P., Dobrynin A., Gutman I., Domotor G. The szeged index and an analogy with the wiener index. *Journal of Chemical Information and Computer Sciences*, 1995, **35**(3), P. 547–550.
- [12] Gutman I. The acyclic polynomial of a graph. *Publications de l'Institut Mathématique*, 1977, **22**(36) (42), P. 63–69.
- [13] Farrell E. J. An introduction to matching polynomials. *Journal of Combinatorial Theory, Series B*, 1979, **27**(1), P. 75–86.
- [14] Zhang H., Zhang F. The clar covering polynomial of hexagonal systems I. *Discrete Applied Mathematics*, 1996, **69**(1-2), P. 147–167.
- [15] Gutman I. Some relations between distance-based polynomials of trees. *Bulletin (Académie serbe des sciences et des arts. Classe des sciences mathématiques et naturelles. Sciences mathématiques)*, 2005, **30**, P. 1–7.
- [16] Kauffman L. H. A tutte polynomial for signed graphs. *Discrete Applied Mathematics*, 1989, **25**(1-2), P. 105–127.
- [17] Hosoya H. On some counting polynomials in chemistry. *Discrete Applied Mathematics*, 1988, **19**(1-3), P. 239–257.
- [18] Wiener H. Structural determination of paraffin boiling points. *Journal of the American Chemical Society*, 1947, **69**(1), P. 17–20.
- [19] Deutsch E., Klavžar S. M-polynomial and degree-based topological indices. *Iranian Journal of Mathematical Chemistry*, 2015, **6**(2), P. 93–102.
- [20] Munir M., Nazeer W., Rafique S., Kang S. M. M-polynomial and degree-based topological indices of polyhex nanotubes. *Symmetry*, 2016, **8**(12), P. 149.
- [21] Munir M., Nazeer W., Rafique S., Kang S. M. M-polynomial and related topological indices of nanostar dendrimers. *Symmetry*, 2016, **8**(9), P. 97.
- [22] Munir M., Nazeer W., Nizami A. R., Rafique S., Kang S. M. M-polynomial and topological indices of titania nanotubes. *Symmetry*, 2016, **8**(1-9), P. 117.
- [23] Kwun Y. C., Munir M., Nazeer W., Rafique S., Kang S. M. M-polynomials and topological indices of V-phenylenic nanotubes and nanotori. *Scientific Reports*, P. 2017, **7**(1), P. 1–9.

- [24] Kang S. M., Nazeer W., Zahid M. A., Nizami A. R., Aslam A., Munir M. M-polynomials and topological indices of hex-derived networks. *Open Physics*, 2018, **16**(1), P. 394–403.
- [25] Deng H., Yang J., Xia F. A general modeling of some vertex-degree based topological indices in benzenoid systems and phenylenes. *Computers & Mathematics with Applications*, 2011, **61**(10), P. 3017–3023.
- [26] Gutman I., Trinajstić N. Graph theory and molecular orbitals. Total π -electron energy of alternant hydrocarbons. *Chemical Physics Letters*, 1972, **17**(4), P. 535–538.
- [27] Miličević A., Nikolić S., Trinajstić N. On reformulated zagreb indices. *Molecular Diversity*, 2004, **8**, P. 393–399.
- [28] Bollobás B., Erdős P. Graphs of extremal weights. *Ars Combinatoria*, 1998, **50**, P. 225–233.
- [29] Amić D., Bešlo D., Lučić B., Nikolić S., Trinajstić N. The vertex-connectivity index revisited. *Journal of Chemical Information and Computer Sciences*, 1998, **38**(5), P. 819–822.
- [30] Vukičević D., Gašperov M. Bond additive modeling 1. adriatic indices. *Croatica Chemica Acta*, 2010, **83**(3), P. 243–260.
- [31] Favaron O., Mahéo M., Saclé J. -F. Some eigenvalue properties in graphs (conjectures of graffiti-II). *Discrete Mathematics*, 1993, **111**(1-3), P. 197–220.
- [32] Furtula B., Graovac A., Vukičević D. Augmented zagreb index. *Journal of Mathematical Chemistry*, 2010, **48**(2), P. 370–380.
- [33] Randić M. Characterization of molecular branching. *Journal of the American Chemical Society*, 1975, **97**(23), P. 6609–6615.
- [34] Sedlar J., Stevanović D., Vasilyev A. On the inverse sum indeg index. *Discrete Applied Mathematics*, 2015, **184**, P. 202–212.
- [35] Nocetti F. G., Stojmenovic I., Zhang J. Addressing and routing in hexagonal networks with applications for tracking mobile users and connection rerouting in cellular networks. *IEEE Transactions on Parallel and Distributed Systems*, 2002, **13**(9), P. 963–971.
- [36] Manuel P., Bharati R., Rajasingh I., Monica M. C. On minimum metric dimension of honeycomb networks. *Journal of Discrete Algorithms*, 2008, **6**(1), P. 20–27.
- [37] Raj F. S., George A. On the metric dimension of HDN 3 and PHDN 3. *2017 IEEE International Conference on Power, Control, Signals and Instrumentation Engineering (ICPCSI)*, 2017, P. 1333–1336.
- [38] Wei C. -C., Ali H., Binyamin M. A., Naeem M. N., Liu J. -B. Computing degree based topological properties of third type of hex-derived networks. *Mathematics*, 2019, **7**(4), P. 368.

Approximate analytical method for finding eigenvalues of Sturm-Liouville problem with generalized boundary condition of the third kind

V. D. Lukyanov¹, D. A. Bulekbaev², A. V. Morozov², L. V. Nosova²

¹Joint-Stock Company “Avangard”, Kondrat’evsky, 72, St. Petersburg, 195271, Russia

²Mozhaisky Military Space Academy, Zhdanovskaya, 13, St. Petersburg, 197198, Russia

lukyanovvd@rambler.ru, atiman@mail.ru, alex.morozof@gmail.com, lvn1201@gmail.com

PACS 02.60.Lj, 47.61.Fg, 62.25.-g

DOI 10.17586/2220-8054-2020-11-3-275-284

The Sturm-Liouville problem is solved for a linear differential second-order equation with generalized boundary conditions of the third kind. Generalized boundary conditions consist of a linear combination of the boundary values of a function and its derivative. The coefficients of the linear combination are polynomials of the boundary problem eigenvalue. A method of approximate analytical calculation of boundary problem eigenvalues is proposed. The calculation error of an eigenvalue is estimated.

Keywords: Sturm-Liouville problem, boundary conditions of the third kind, eigenfunctions, eigenvalues, approximation.

Received: 21 June 2020

1. Introduction

Advances of nanotechnologies make it possible to design and create microelectromechanical systems (MEMS) and nanoelectromechanical systems (NEMS). These systems find use as primary converters in miniature sensors of physical quantities [1].

Characteristic dimensions of used systems elements: hundreds of nanometers for MEMS with operating frequencies of sensors up to 10 GHz and tens of nanometers for NEMS with operating frequencies of sensors up to tens of GHz [2, 3].

High-quality electromechanical resonators are used as primary converters to provide sensor sensitivities and measurement accuracy of physical quantities. Various aspects of these devices research, technological developments and their various applications are presented in the reviews [4–12].

The simplest resonators in MEMS and NEMS are one-dimensional distributed elastic structures (strings, rods, beams loaded with sensitive elements - masses). Technologies for making such resonators are presented, for example, in [13, 14].

The mathematical model of time harmonic elastic oscillations of resonators is the Sturm-Liouville boundary problem. The Sturm-Liouville problem is a boundary problem on a segment for an ordinary linear homogeneous differential equation with homogeneous boundary conditions at the ends of the segment [15].

To describe the motion of an MEMS or NEMS element, a generalized boundary condition of the third kind is used, containing eigenvalues [15–17]. A generalized boundary condition is a linear combination of the sought function and its first-order derivative, wherein the coefficients of the linear combination are polynomials with respect to the sought eigenvalue of the problem. The mathematical theory such of problems is built in the works [18, 19], where a generalization of the classical Sturm-Liouville problem theory is given [20, 21].

2. Statement of the Sturm-Liouville problem with generalized boundary conditions of the third kind

We consider the Sturm-Liouville boundary problem for a linear homogeneous ordinary second-order differential equation

$$y'' = -\mu y, \quad (1)$$

where $y = y(x)$ at $-1 \leq x \leq 1$, μ is an eigenvalue of the problem, $\mu > 0$. Taking into account the positivity μ we will accept $\mu = \lambda^2$, where $\lambda > 0$.

As boundary conditions for the differential equation, we have generalized homogeneous conditions of the third kind [15–17]:

$$\alpha_1(\mu)y(1) + \beta_1(\mu)y'(1) = 0, \quad (2)$$

$$\alpha_2(\mu)y(-1) + \beta_2(\mu)y'(-1) = 0. \quad (3)$$

Multipliers $\alpha_k = \alpha_k(\mu)$ and $\beta_k = \beta_k(\mu)$ ($k=1,2$) are polynomials with respect to μ . Polynomials coefficients are parameters of the problem. Parameters depend on characteristics of physical models in application problems. If the

total number of such parameters under conditions (2) and (3) is equal to the number S , then we will call the boundary problem S -parametric. We will denote problem parameters by $\gamma_1, \gamma_2, \dots, \gamma_S$.

If the homogeneous boundary problem (1)–(3) has a non-zero solution $y_0(x)$ at a value $\mu = \mu_0$, then the value μ_0 is called an eigenvalue, and the corresponding solution $y_0(x)$ is called an eigenfunction of the boundary problem.

3. Sturm-Liouville problem eigenvalues calculation algorithm

To solve the Sturm-Liouville problem means to find all the problem eigenvalues and eigenfunctions.

Eigenvalues are analytically calculated for the simplest boundary conditions of the first and second kind. In cases of boundary conditions of the third kind, eigenvalues are calculated as the roots of a transcendental equation lacking an exact analytical solution. Therefore, various approximate methods are used to find eigenvalues. These methods produce only an asymptotic estimate of an eigenvalue without discussing the accuracy of the result obtained, which is important in applied research.

The proposed new method makes it possible to calculate a set of boundary problem eigenvalues and to evaluate effectively the accuracy of their calculation.

Consider the problem of finding all eigenvalues and eigenfunctions of the Sturm-Liouville problem (1)–(3).

To solve the problem, we find the general solution of the differential equation (1)

$$y = C_1 \cos \lambda x + C_2 \sin \lambda x, \quad (4)$$

where C_1 and C_2 depend on the value of λ .

Satisfying the boundary conditions (2) and (3), we obtain a homogeneous system of linear algebraic equations for finding quantities C_1 and C_2 in the general solution (4):

$$\begin{cases} C_1 p_1^-(\lambda) + C_2 q_1^+(\lambda) = 0, \\ C_1 p_2^+(\lambda) + C_2 q_2^-(\lambda) = 0, \end{cases} \quad (5)$$

where

$$\begin{aligned} p_k^\pm(\lambda) &= \alpha_k(\lambda^2) \cos \lambda \pm \lambda \beta_k(\lambda^2) \sin \lambda, \\ q_k^\pm(\lambda) &= \pm \alpha_k(\lambda^2) \sin \lambda + \lambda \beta_k(\lambda^2) \cos \lambda \end{aligned}$$

at $k=1,2$. We take upper or lower symbol in formulas for $p_k^\pm(\lambda)$ and $q_k^\pm(\lambda)$ simultaneously.

The principal determinant of the homogeneous system of algebraic equations (5) is in the form of

$$\Delta(\lambda, \gamma_1, \gamma_2, \dots, \gamma_S) = p_1^-(\lambda) q_2^-(\lambda) - p_2^+(\lambda) q_1^+(\lambda). \quad (6)$$

The arguments of the determinant are a sought value λ and parameters $\gamma_1, \gamma_2, \dots, \gamma_S$ included in the conditions (2) and (3).

In order to find a non-zero solution to the homogeneous system of linear algebraic equations (5), we will require that the principal determinant of this system to be zero:

$$\Delta(\lambda, \gamma_1, \gamma_2, \dots, \gamma_S) = 0. \quad (7)$$

Equation (7) is called a characteristic equation. To find an eigenvalues μ of the Sturm-Liouville problem, we look for the positive roots λ of characteristic equation (7), and then look for the eigenvalue $\mu = \lambda^2 > 0$.

As can be seen from equality (6), the principal determinant is the sum of the components consisting of the works of the polynomial and trigonometric functions that depend on a sought λ value. Thus, equation (7) is transcendental and does not allow an analytic solution of the form of

$$\lambda = \varphi(\gamma_1, \gamma_2, \dots, \gamma_S), \quad (8)$$

which would allow to calculate an eigenvalue from known problem parameter values.

The proposed approximate method provides an approximate representation of the view (8) and estimates the accuracy of this representation.

Let us give an algorithm of the proposed method of obtaining an approximate solution of the characteristic equation.

In the first step we will make a table of function values $\lambda = \varphi(\gamma_1, \gamma_2, \dots, \gamma_S)$ on some set of variable $\gamma_1, \gamma_2, \dots, \gamma_S$ values. To do this, we record the determinant $\Delta(\lambda, \gamma_1, \gamma_2, \dots, \gamma_S)$ as a linear combination of trigonometric functions with multipliers representing some polynomials with respect to λ value. Coefficients of these polynomials are calculated through parameter $\gamma_1, \gamma_2, \dots, \gamma_S$ values.

The dependence of the determinant on each parameter is not more than quadratic, since the problem parameters are coefficients of the polynomials and enter in the polynomials linearly, and the polynomials themselves are only multiplied according to formula (6).

Using this circumstance, we solve equation (7) with respect to some arbitrarily chosen parameter γ_i with the i number. We get a functional dependence of the form of

$$\gamma_i = \varphi_i(\lambda, \gamma_1, \gamma_2, \dots, \gamma_{i-1}, \gamma_{i+1}, \dots, \gamma_S). \tag{9}$$

We now arbitrarily set argument values of the function φ_i and calculate the value γ_i . For example, we can select arguments values of the function φ_i on a uniform grid of the $\lambda, \gamma_1, \gamma_2, \dots, \gamma_{i-1}, \gamma_{i+1}, \dots, \gamma_S$ arguments. Values of the parameter γ_i are then calculated. If necessary, if the values obtained for the parameter γ_i are not sufficient, the relation (9) can be recorded with another selection of the parameter on the left hand side of the equality (9). We can now choose additional values for the γ_i parameter. As a result, we create a table of function φ_i values.

In the second step of solving characteristic equation we have a sufficient number of function φ_i values. We find an approximating function $\Gamma_i = \Phi_i(\lambda, \gamma_1, \gamma_2, \dots, \gamma_{i-1}, \gamma_{i+1}, \dots, \gamma_S)$ using the obtained set of the function values φ_i given by formula (9). We will select the approximation function Φ_i so that it has an inverse function Φ_i^{-1} with respect to the variable λ at fixed values of the $\gamma_2, \dots, \gamma_{i-1}, \gamma_{i+1}, \dots, \gamma_S$ arguments:

$$\lambda = \Phi_i^{-1}(\gamma_1, \gamma_2, \dots, \gamma_{i-1}, \Gamma_i, \gamma_{i+1}, \dots, \gamma_S).$$

In order to calculate the approximate value of the sought λ_* value, we set in this formula $\Gamma_i = \gamma_i$:

$$\lambda_* = \Phi_i^{-1}(\gamma_1, \gamma_2, \dots, \gamma_{i-1}, \gamma_i, \gamma_{i+1}, \dots, \gamma_S). \tag{10}$$

Then we calculate our eigenvalue $\mu_* = \lambda_*^2$.

As an example of the implementation of the method, we consider the problem of finding eigen frequencies of a longitudinally oscillating rod loaded with masses at the ends.

4. Statement of eigen frequencies problem for a longitudinally oscillating rod loaded at the ends with masses

We have an elastic uniform rod: the rod length is $2l$, the constant cross-sectional area is F , the rod material has Young's modulus E , linear density is ρ . Body 1 with mass M_1 and body 2 with mass M_2 are fixed at the rod ends. The placement of rod (R) and bodies 1 and 2 in the coordinate system is shown in Fig. 1.

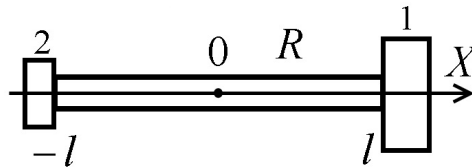


FIG. 1. Longitudinally oscillating rod (R) loaded at the ends with bodies 1 and 2. Choice of the coordinate system is shown

Small longitudinal displacements $U = U(X, t)$ of rod cross section with coordinate X from equilibrium position at moment of time t satisfy to the equation

$$\rho F \frac{\partial^2 U(X, t)}{\partial t^2} = EF \frac{\partial^2 U(X, t)}{\partial X^2} \tag{11}$$

at $-l < X < l$.

Boundary conditions describe masses oscillations under the action of the elastic rod: we have on the right end of the rod if $X = l$

$$M_1 \frac{\partial^2 U(l, t)}{\partial t^2} = -EF \frac{\partial U(l, t)}{\partial X}, \tag{12}$$

we have on the left end of the rod if $X = -l$

$$M_2 \frac{\partial^2 U(-l, t)}{\partial t^2} = EF \frac{\partial U(-l, t)}{\partial X}. \tag{13}$$

In order to find eigen frequencies of rod oscillations it is considered that dependence of longitudinal displacement of rod cross-section on time is harmonic with circular frequency ω : $U(X, t) = Y(X) e^{-i\omega t}$, $Y = Y(X)$ is the amplitude of longitudinal displacement of rod cross-section at the point with coordinate X .

Let us pass in equations (11)–(13) to dimensionless values. We introduce the dimensionless coordinate $x = X/l$, then $-1 \leq x \leq 1$, and introduce the dimensionless amplitude of the longitudinal displacement of rod cross-section $y(x) = Y(X)/l$.

We introduce also dimensionless quantities: dimensionless eigenvalue $\mu = \rho\omega^2 l^2/E$, dimensionless eigen frequency $\lambda = \sqrt{\mu}$, and two dimensionless parameters of the problem: $\gamma_1 = M_1/M_0$ and $\gamma_2 = M_2/M_1$, where the mass M_0 is equal to half the mass of the rod: $M_0 = \rho Fl$. Note that problem parameters have the properties: $\gamma_1 > 0$, $\gamma_2 \geq 0$.

Taking into account the introduced dimensionless quantities problem (11)–(13) takes the form of boundary problem (1)–(3)

$$y'' = -\lambda^2 y, \tag{14}$$

at $-1 \leq x \leq 1$, with edge conditions of type (2) and (3) where $\alpha_1(\lambda^2) = \gamma_1 \lambda^2$, $\alpha_2(\lambda^2) = \gamma_1 \gamma_2 \lambda^2$, here $\beta_k = \beta_k(\lambda^2) = (-1)^k$ at $k=1,2$:

$$\gamma_1 \lambda^2 y(1) - y'(1) = 0, \tag{15}$$

$$\gamma_1 \gamma_2 \lambda^2 y(-1) + y'(-1) = 0. \tag{16}$$

We have a two-parametric boundary problem with parameters γ_1 and γ_2 .

A simpler single-parameter problem is discussed in [22], when the masses attached to the rod ends are the same: $M_1 = M_2$ or $\gamma_2 = 1$.

The general solution of equation (14) has the form (4). We obtain from the boundary conditions (15) and (16) a system of linear algebraic equations of the form of (5), where

$$p_k^\pm(\lambda) = \alpha_k(\lambda^2) \cos \lambda \pm \lambda \sin \lambda, \quad q_k^\pm(\lambda) = \pm \alpha_k(\lambda^2) \sin \lambda \mp \lambda \cos \lambda$$

at $k = 1, 2$.

The characteristic equation (7) for finding non-zero eigen frequencies is converted to the form of

$$\gamma_1^2 \gamma_2 \lambda^2 \sin 2\lambda - \gamma_1(1 + \gamma_2) \lambda \cos 2\lambda - \sin 2\lambda = 0. \tag{17}$$

The obtained equation defines the implicit dependence of the dimensionless frequency λ on the problem parameters γ_1 and γ_2 . As shown in item 3 and seen from equation (17), it is not possible to obtain an analytical solution of the characteristic equation with respect to a sought value λ .

The proposed method of solving the characteristic equation makes it possible to obtain an approximate analytical $\lambda = \lambda(\gamma_1, \gamma_2)$ dependence.

Note that the characteristic equation (17) was obtained in 6.2 [23] in solving the problem of a substance diffusion through a permeable wall. The equation was solved graphically for the particular $\gamma_2 = 1$ case, when this equation is converted to the form of $\cot 2\lambda = (\gamma_1^2 \lambda^2 - 1)/2\gamma_1 \lambda$. The graphs of functions from the right and left hand sides of the equation were drawn at a fixed value of the γ_1 parameter. The sought frequency values λ were obtained as abscissas of the intersections points of these graphs.

As a result, in [23] there is a table of values of five first sought eigen frequency values λ_s for three parameter γ_1 values. It is difficult to use the obtained results in practice: first, the number of frequencies found is insufficient for the qualitative numerical simulation of a physical problem, second, modeling may require a different parameter value γ_1 than the table value, third, the case $\gamma_2 \neq 1$ will be interesting.

5. Approximate solution of characteristic equation for the problem of longitudinal oscillations of elastic rod loaded with masses

In computer simulation of practical problems it is convenient to have an approximate analytical solution of the characteristic equation for all roots of this equation and at any values of problem parameters.

Approximate methods used to solve equations of type (17) give analytical estimates for eigenvalues sufficient for large eigenvalues [24]. Obtaining approximate formulas for the first eigenvalues near zero causes difficulties. Estimates of the accuracy of approximate formulas for eigenvalues near zero are not usually considered. The proposed method of solving the characteristic equation allows for solve these problems.

5.1. Finding dependencies of eigen frequency λ on Sturm-Liouville problem parameters γ_1 and γ_2 in tabular and graphical view

Let's take advantage of the fact that the characteristic equation (17) cannot be solved in elementary functions relative to the eigen frequency λ , but can be resolved relative to the parameters γ_1 or γ_2 .

Consider the values λ and γ_2 in the characteristic equation as independent variables ($0 < \lambda < +\infty$, $\gamma_2 \geq 0$), and consider the parameter $\gamma_1 > 0$ as dependent variable. The left hand side of equation (17) is a quadratic function relative to the γ_1 variable. We find the dependence of the value γ_1 on the variables λ and γ_2 , if we calculate the roots of quadratic equation (17):

$$\gamma_1^\pm = \gamma_1^\pm(\lambda, \gamma_2) = \frac{1}{2\gamma_2 \lambda^2} \left(W(\lambda, \gamma_2) \pm \sqrt{W^2(\lambda, \gamma_2) + 4\gamma_2 \lambda^2} \right), \tag{18}$$

where the function $W(\lambda, \gamma_2) = (1 + \gamma_2)\lambda \cot 2\lambda$ is used. In formula (18), either the upper or lower signs are taken at the same time.

Denote the functions $\gamma_1^\pm = \gamma_1^\pm(\lambda, \gamma_2)$ by $\gamma_{1n}^\pm = \gamma_{1n}^\pm(\lambda, \gamma_2)$ if argument λ belongs to the interval $(\nu_{n-1}, \nu_n]$ with the number n :

$$\gamma_1^\pm(\lambda, \gamma_2) = \gamma_{1n}^\pm(\lambda, \gamma_2) \text{ at } \lambda \in (\nu_{n-1}, \nu_n].$$

5.2. Properties of $\gamma_{1n}^\pm(\lambda, \gamma_2)$ functions

1. Functions $\gamma_{1n}^\pm(\lambda, \gamma_2)$ are defined for all $\lambda > 0$ but values $\nu_n = \pm\pi n/2$ at $n = 1, 2, \dots$. Direct substitution of values $\lambda \neq \nu_n$ into equation (17) proves that relations (17) and (18) are equivalent.

2. Functions $\gamma_{1n}^\pm(\lambda, \gamma_2)$ are even relative to the λ variable, since the function $W(\lambda, \gamma_2)$ in equality (18) is even, and the degrees of λ are even.

3. Functions $\gamma_{1n}^\pm(\lambda, \gamma_2)$ are continuous on each $(\nu_{n-1}, \nu_n]$ interval.

4. Functions $\gamma_{1n}^\pm(\lambda, \gamma_2)$ are of constant signs: $\gamma_{1n}^+(\lambda, \gamma_2) \geq 0, \gamma_{1n}^-(\lambda, \gamma_2) \leq 0$. Taking into account the positivity of possible parameter γ_1 values we will study further only the functions $\gamma_{1n}^+(\lambda, \gamma_2)$.

5. We have the equality $\gamma_{1n}^+(\nu_{n+1}, \gamma_2) = 0$ and the limit value $\gamma_{1n}^+(\lambda, \gamma_2) \rightarrow +\infty$ as $\lambda \rightarrow \nu_n + 0$.

6. The graphs of functions $\gamma_1^+(\lambda) = \gamma_{1n}^+(\lambda, \gamma_2)$ at $n = 1, 2, 3$ are shown in Fig. 2(a) for three fixed values of the γ_2 parameter. One can see that functions $\gamma_{1n}^+(\lambda, \gamma_2)$ decrease monotonically. Function graphs with different values of the parameter γ_2 do not intersect. A function graph with a larger parameter γ_2 value is below a function graph with a smaller parameter γ_2 value. This follows from the comparison of function values $\gamma_{1n}^+ = \gamma_{1n}^+(\lambda, \gamma_2)$ in the middle of the n interval at $\lambda_n^* = \nu_{n-1} + \pi/4$. We have according to formula (18) $W(\lambda_n^*, \gamma_2) = 0$, and we get the value of the function $\gamma_{1n}^+(\lambda_n^*, \gamma_2) = 1/(\lambda_n^* \sqrt{\gamma_2})$. Comparing two such values for two curves with different parameter values $\gamma_2^{(1)} > \gamma_2^{(2)}$ gives

$$\frac{\gamma_{1n}^+(\lambda_n^*, \gamma_2^{(1)})}{\gamma_{1n}^+(\lambda_n^*, \gamma_2^{(2)})} = \sqrt{\frac{\gamma_2^{(2)}}{\gamma_2^{(1)}}} < 1. \tag{19}$$

7. Functions $\gamma_{1n}^+ = \gamma_{1n}^+(\lambda, \gamma_2)$ are monotonic and continuous in the domain of their definition $\lambda \in (\nu_{n-1}, \nu_n]$ at $n = 1, 2, \dots$, and have inverse functions for a fixed parameter value $\gamma_2 = \gamma_2^{(0)}$. We denote these inverse functions by $\lambda_n = \lambda_n^+(\gamma_1, \gamma_2)$. Functions $\lambda_n = \lambda_n^+(\gamma_1, \gamma_2)$ are monotonic, continuous in the domain of their $\gamma_1 > 0$ definition. The inverse function graphs $\lambda_n = \lambda_n^+(\gamma_1, \gamma_2)$ are shown in Fig. 2(b) for the same values of the γ_2 parameter. The graphs of these functions are symmetrical to the graphs of the functions $\gamma_{1n}^+ = \gamma_{1n}^+(\lambda, \gamma_2)$ with respect to the bisector of the first quadrant.

Function graphs $\lambda_n = \lambda_n^+(\gamma_1, \gamma_2)$ for $n = 1, 2, 3$ are graphs of the exact solution of the problem at fixed values of the γ_2 parameter. We find the sought values λ_n of the Sturm-Liouville problem at the value of the parameter $\gamma_1 = \gamma_1^{(0)}$ as ordinates of intersection points of the straight line (vertical straight line in Fig. 2(b)) with function graphs $\lambda = \lambda_n^+(\gamma_1, \gamma_2)$ at $n = 1, 2, \dots$

5.3. Approximation functional dependencies between eigenvalues and parameters of the Sturm-Liouville problem

The result of the first step of the proposed method was obtaining functional dependencies $\gamma_1^+ = \gamma_{1n}^+(\lambda, \gamma_2)$ and graphs of the exact $\lambda_n = \lambda_n^+(\gamma_1, \gamma_2)$ solution. The disadvantage of the graphical solution of the characteristic equation is the difficulty of using its results in computer modeling of a physical problem.

In the second step, we approximate the functions $\gamma_1^+ = \gamma_{1n}^+(\lambda, \gamma_2)$ with elementary functions $\Gamma_{1n} = \Gamma_{1n}(\lambda, \gamma_2)$, where the first index 1 coincides with the index of the parameter γ_1 , and the second index n is the number of interval $(\nu_{n-1}, \nu_n]$ at which the functions are defined.

Let's choose functions $\Gamma_{1n}(\lambda, \gamma_2)$ so that they have the properties **1–7** of the $\gamma_{1n}^+(\lambda, \gamma_2)$ functions. Let interpolation-approximation functions $\Gamma_{1n}(\lambda, \gamma_2)$ interpolate the values of the functions $\gamma_{1n}^+ = \gamma_{1n}^+(\lambda, \gamma_2)$ at $\lambda = \nu_n$ and provide their limit values as $\lambda \rightarrow \nu_{n-1} + 0$; let $\Gamma_{1n}(\lambda, \gamma_2)$ approximate the values of the functions $\gamma_{1n}^+ = \gamma_{1n}^+(\lambda, \gamma_2)$ at internal points of interval (ν_{n-1}, ν_n) [25].

Taking into account properties **5** and **7** of the $\gamma_{1n}^+ = \gamma_{1n}^+(\lambda, \gamma_2)$ functions, select functions $\Gamma_{1n} = \Gamma_{1n}(\lambda, \gamma_2)$ in the form of

$$\gamma_{1n}^+ \approx \Gamma_{1n} = \Gamma_{1n}(\lambda, \gamma_2) = A_n \gamma_2^{s_n} \left(\frac{v_{n+1}^2 - \lambda^2}{\lambda^2 - v_n^2} \right)^{r_n}, \tag{20}$$

where parameters A_n, s_n and r_n are introduced. The additional condition $r_n > 0$ provides the required function values at the ends of the $(\nu_{n-1}, \nu_n]$ interval. By verifying directly, one can find out that the functions selected in the form (20) satisfy the **1–4** properties. The additional condition $s_n < 0$ ensures that property **6** is met.

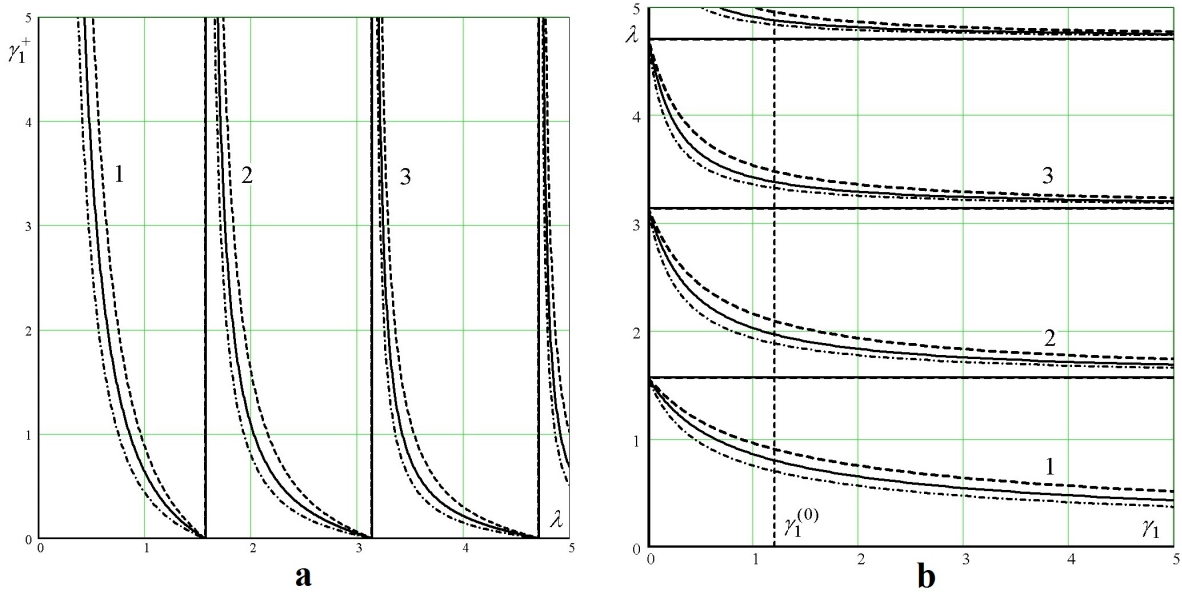


FIG. 2. Mutually inverse functions: $\gamma_1^+ = \gamma_{1n}^+(\lambda, \gamma_2)$ – (a); $\lambda = \lambda_n^+(\gamma_1, \gamma_2)$ – (b). Curves 1, 2, 3 are constructed for functions with indices $n = 1, 2, 3$ at three values of the γ_2 parameter: $\gamma_2 = 0.5$ – dashed lines; $\gamma_2 = 1.0$ – solid lines; $\gamma_2 = 2.0$ – chain-dotted lines

The parameters A_n , s_n and r_n introduced in the right side of formula (20) allow one to approximate the functions $\gamma_{1n}^+ = \gamma_{1n}^+(\lambda, \gamma_2)$ at the internal points of the $(\nu_{n-1}, \nu_n]$ interval using the least squares method.

After calculating parameters, we get elementary functions $\Gamma_{1n} = \Gamma_{1n}(\lambda, \gamma_2)$.

Further consideration is carried out for an arbitrary fixed number n of the $(\nu_{n-1}, \nu_n]$ interval.

The function $\Gamma_{1n} = \Gamma_{1n}(\lambda, \gamma_2)$ has the inverse function at interval $(\nu_{n-1}, \nu_n]$, and the inverse function is also elementary:

$$\lambda_n \approx \hat{\lambda}_n = \sqrt{\frac{v_{n+1}(A_n \gamma_2^{s_n})^{q_n} + v_{n+1}(\Gamma_{1n})^{q_{n+1}}}{(A_n \gamma_2^{s_n})^{q_n} + (\Gamma_{1n})^{q_n}}}, \quad (21)$$

where $q_n = 1/r_n$.

Note that when solving the *single-parameter* problem in [22], when choosing the form of approximation $\Gamma = \Gamma_n(\lambda)$ function, evenness of the function $\gamma_n^+(\lambda)$ relative to variable λ was not taken into account. Accounting for the evenness of the function $\gamma_{1n}^+(\lambda, \gamma_2)$ relative to variable λ in formula (20) increases the approximation's accuracy.

We find the approximation parameters r_n , s_n and A_n by the least squares method, which provides the best approximation of the $\gamma_{1n}^+ = \gamma_{1n}^+(\lambda, \gamma_2)$ function.

After calculating approximation parameters, the values for λ_n are obtained using formula (21) at the given values of the problem parameters γ_1 and γ_2 . Then, we find the eigenvalue $\mu_n = \lambda_n^2$ of the Sturm-Liouville problem.

5.4. Finding of approximation parameters

To find approximation parameters A_n , s_n and r_n we set J of values for the problem parameter γ_2 : $\gamma_2^{(j)}$, where $j = 1, 2, \dots, J$. We will also select M_n of values for the argument λ_{nm} , where $m = 1, 2, \dots, M_n$ on each interval (ν_{n-1}, ν_n) . The values of the arguments $\gamma_2^{(j)} \in (0, T)$ and $\lambda_{nm} \in (\nu_{n-1}, \nu_n]$ must cover uniformly the domain of the function $\gamma_{1n}^+ = \gamma_{1n}^+(\lambda, \gamma_2)$ definition, the quantity T being determined by the largest value the parameter γ_2 can take.

Let's calculate MJ of values of the $\gamma_{1n}^+ = \gamma_{1n}^+(\lambda, \gamma_2)$ function: $\gamma_{1nmj} = \gamma_{1n}^+(\lambda_{nm}, \gamma_2^{(j)})$.

To apply the least squares method, take the logarithm of both sides of equation (20)

$$\ln(\Gamma_{1n}(\lambda, \gamma_2)) = q_n + s_n \ln \gamma_2 + r_n R_n(\lambda), \quad (22)$$

where

$$q_n = \ln(A_n), \quad (23)$$

$$R_n(\lambda) = \ln\left(\frac{v_{n+1}^2 - \lambda^2}{\lambda^2 - v_n^2}\right). \quad (24)$$

We will look for the q_n , s_n and r_n values from the condition of ensuring the minimum value of the function $F_n(q_n, s_n, r_n)$. The function $F_n(q_n, s_n, r_n)$ is the average value of the sum of the difference squares for values $\ln(\gamma_{1nmj}^+)$ and $\ln(\Gamma_{1n}(\lambda_{nm}, \gamma_2^{(j)}))$:

$$F_n(q_n, s_n, r_n) = \overline{\left(\ln \gamma_{1nmj}^+ - \ln(\Gamma_{1n}(\lambda_{nm}, \gamma_2^{(j)})) \right)^2} = \frac{1}{M_n J} \sum_{j=1}^J \sum_{m=1}^{M_n} \left(\ln \gamma_{1nmj}^+ - q_n - s_n \ln \gamma_2^{(j)} - r_n R_n(\lambda_{nm}) \right)^2. \quad (25)$$

Here and elsewhere, we use the symbol of averaging to calculate the average value of some variable value Z if Z takes the $z_{11}, z_{12}, \dots, z_{MJ}$ values:

$$\bar{Z} = \frac{1}{MJ} \sum_{m=1}^M \sum_{j=1}^J z_{mj}.$$

The condition of the minimum for function $F_n(q_n, s_n, r_n)$ is the equality to zero of its partial derivatives regarding the arguments q_n, s_n and r_n . This condition results in a system of linear algebraic equations regarding the quantities q_n, r_n , and s_n

$$\mathbf{A}_n \mathbf{X}_n = \mathbf{B}_n, \quad (26)$$

where the elements of the third order matrix are: $A_{11} = 1, A_{12} = A_{21} = \overline{\ln \gamma_2}, A_{13} = A_{31} = \overline{R_n}, A_{22} = \overline{(\ln \gamma_2)^2}, A_{23} = A_{32} = \overline{R_n \ln \gamma_2}, A_{33} = \overline{(R_n)^2}$; $\mathbf{X}_n = (q_n, s_n, r_n)^T$ is matrix column of the required values, sign T means transposition of matrix;

$$\mathbf{B}_n = (\overline{\ln \gamma_{1nmj}^+}, \overline{\ln \gamma_{1nmj}^+ \ln \gamma_2}, \overline{\ln \gamma_{1nmj}^+ R_n})^T$$

is the free member column.

The solution of system (26) gives values

$$\mathbf{X}_n = \mathbf{A}_n^{-1} \mathbf{B}_n. \quad (27)$$

We find the approximation parameter A_n from the relation (23)

$$A_n = e^{q_n}. \quad (28)$$

5.5. Results of numerical calculations of eigen frequencies

To calculate the values of the function $\Gamma_{1n} = \Gamma_{1n}(\lambda, \gamma_2)$ at each n interval $(\nu_{n-1}, \nu_n]$, $n = 1, 2, \dots, N$, we select the values of the first argument as $\lambda_{nm} = \lambda_{n0} + \Delta\lambda(m-1)$, $m = 1, 2, \dots, M$, where λ_{n0} is the initial value, and $\Delta\lambda$ is the step of changing the argument λ . We select the values of the second argument $\gamma_{2j} = \gamma_0 + \Delta\gamma(j-1)$, $j = 1, 2, \dots, J$, where γ_0 is the initial value, and $\Delta\gamma$ is the step of changing the argument γ_2 . It was accepted for calculations: $M = 8, J = 5, \lambda_{n0} = \nu_n + 0.001, \Delta\lambda = \nu_1/(M+1) - 0.01, \gamma_0 = 0.5, \Delta\gamma = 0.5$.

The results for calculation of the approximation constants A_n and r_n by formulas (27) and (28) for the first ten intervals $(\nu_{n-1}, \nu_n]$, $n = 1, 2, \dots, 10$ are shown by points in Figs. 3,4.

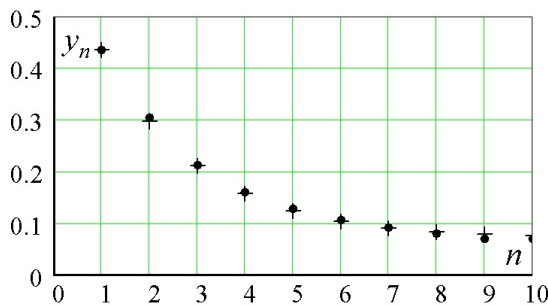


FIG. 3. Dependencies $y_n = A_n$ and $y_n = \hat{A}_n$ on interval number n are shown by points and crosses respectively

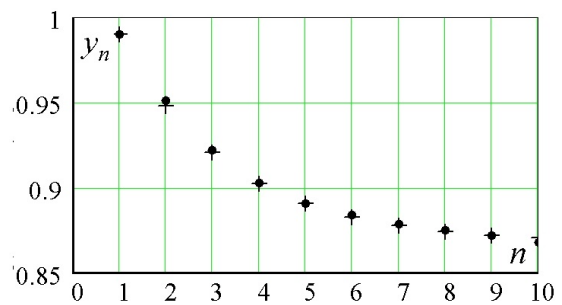


FIG. 4. Dependencies $y_n = r_n$ and $y_n = \hat{r}_n$ on interval number n are shown by points and crosses respectively

Calculations showed also that the third approximation constant s_n does not depend on the problem parameters γ_1 and γ_2 . The value s_n is equal to -0.5 for any n with relative error not more than 0.1%, which is in full compliance with the property 6 and the relation (19), of item 5.2.

For numerical calculations of eigen frequency with *any* number n according to formula (21), we use the found numerical values for parameters A_n and r_n at $n = 1, 2, \dots, N$ to obtain their interpolation-approximation values \hat{A}_n and \hat{r}_n [25].

We find dependencies of the parameters \hat{A}_n and \hat{r}_n on interval number n in the form:

$$\hat{A}_n = \varphi_n(p_A) = A_N + (A_1 - A_N) e^{-p_A (n-1)}; \quad (29)$$

$$\hat{r}_n = \psi_n(p_r) = r_N + (r_1 - r_N) e^{-p_r (n-1)}, \quad (30)$$

where we distinguish interpolation nodes $n = 1, n = N$ and approximation nodes $2 \leq n \leq N - 1$. You have introduced parameters p_A and p_r to approximate dependencies.

We find the parameter p_A so that approximate equalities $\hat{A}_n \approx A_n$ at $n = 1, 2, \dots, N$ are performed in the best way.

According to equation (29) we have the exact equality $\hat{A}_1 = A_1$ at $n = 1$, and we have the approximate equality $\hat{A}_N \approx A_N$, where N is large enough.

We find values p_n providing the equalities $A_n = \varphi_n(p_n)$ for other values $n = 2, \dots, N - 1$:

$$p_n = \varphi_n^{-1}(A_n) = \frac{1}{n-1} \ln \left(\frac{A_1 - A_N}{A_n - A_N} \right).$$

Using the least squares method, we calculate the optimal value of the parameter p_A , which provides the minimum of the value d . This value is average squared displacement of the value p_A from all calculated values p_n at $n = 2, \dots, N - 1$

$$d = d(p_A) = \frac{1}{N-2} \sum_{n=2}^{N-1} (p_n - p_A)^2.$$

From the minimum condition of the function $d = d(p_A)$ we get the optimal value of the approximation parameter as the average value of all calculated p_n

$$p_A = \frac{1}{N-2} \sum_{n=2}^{N-1} p_n, \quad (31)$$

where averaging is performed without taking into account edge values A_1 and A_N .

Similar reasoning for parameter p_r leads to the formula

$$p_r = \frac{1}{N-2} \sum_{n=2}^{N-1} \frac{1}{n-1} \ln \left(\frac{r_1 - r_{10}}{r_n - r_{10}} \right). \quad (32)$$

The calculation of parameters p_A and p_r by formulas (31) and (32) using the data given in Figs. 3,4 gave values $p_A = 0.48$ and $p_r = 0.42$. Having obtained the optimal value of approximation parameters p_A and p_r we calculate values \hat{A}_n and \hat{r}_n for $n = 1, 2, \dots, N$ by formulas (29) and (30).

The calculation results \hat{A}_n and \hat{r}_n at $N = 10$ are shown by crosses in Figs. 3,4.

Fig. 5 shows the graphs of the exact dependencies of the first two eigen frequencies $\lambda_1 = \lambda_1(\gamma_1, \gamma_2)$ and $\lambda_2 = \lambda_2(\gamma_1, \gamma_2)$ on the parameter γ_1 for three fixed values of the parameter γ_2 . These dependencies are represented by solid lines. The exact frequencies values were plotted using the technique shown in Fig. 2(b). The dependencies of approximate values of eigen frequencies $\hat{\lambda}_1 = \hat{\lambda}_1(\gamma_1, \gamma_2)$ and $\hat{\lambda}_2 = \hat{\lambda}_2(\gamma_1, \gamma_2)$ on the parameter γ_1 are shown in Fig. 5 by dashed lines. Approximate frequencies values were calculated using formulas (21), (31) and (32).

5.6. About error of eigen frequencies calculation

We calculate relative error of found eigen frequency value on n interval for estimation of accuracy of approximate formula (21)

$$\delta_n = \left| \frac{\lambda_n - \hat{\lambda}_n}{\lambda_n} \right| = \left| 1 - \frac{\hat{\lambda}_n}{\lambda_n} \right|. \quad (33)$$

We have the previously obtained analytical dependence $\gamma_{1n}^+ = \gamma_{1n}^+(\lambda, \gamma_2)$ given by formula (18). Approximation of this dependence $\Gamma_{1n} = \Gamma_{1n}(\lambda, \gamma_2)$ is introduced by formula (20). The function $\Gamma_{1n} = \Gamma_{1n}(\lambda, \gamma_2)$ has the inverse function $\hat{\lambda}_n = \Gamma_{1n}^{-1}(\gamma_1, \gamma_2)$.

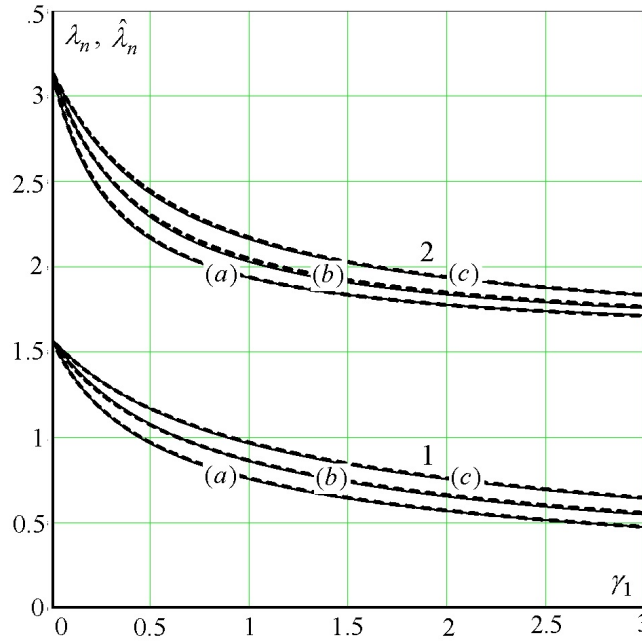


FIG. 5. Dependencies of exact eigen frequencies λ_1 and λ_2 (solid curves 1,2) and approximate eigen frequencies $\hat{\lambda}_1$ and $\hat{\lambda}_2$ (dashed lines 1,2) on parameter γ_1 at three fixed values of parameter γ_2 : curves (a) – for $\gamma_2 = 2, 0$; curves (b) – for $\gamma_2 = 1, 0$; curves (c) – for $\gamma_2 = 0, 5$

We get a parametric functional dependence $\delta_n = \delta_n(\gamma_1, \gamma_2)$ if we consider the quantity λ as a parameter. Indeed, if the value λ_n is set, we have the following values: $\gamma_{1n}^+(\lambda_n) = \gamma_{1n}^+(\lambda_n, \gamma_2)$ and $\hat{\lambda}_n = \Gamma_{1n}^{-1}(\gamma_{1n}^+, \gamma_2) = \Gamma_{1n}^{-1}(\gamma_{1n}^+(\lambda_n, \gamma_2), \gamma_2)$. Then, taking into account equality (33), we give the function $\delta_n = \delta_n(\gamma_1, \gamma_2)$ parametrically:

$$\begin{cases} \delta_n(\lambda_n) = \left| 1 - \frac{1}{\lambda_n} \Gamma_{1n}^{-1}(\gamma_{1n}^+(\lambda_n, \gamma_2), \gamma_2) \right|, \\ \gamma_{1n}^+(\lambda_n) = \gamma_{1n}^+(\lambda_n, \gamma_2). \end{cases} \quad (34)$$

Relative errors of eigen frequency calculations at the first ten intervals were obtained by formulas (34) for case $\gamma_2 = 1$.

The table shows estimates Δ_n of the largest values of relative errors at the first ten intervals: $\delta_n \leq \Delta_n$ at $\lambda \in (\nu_{n-1}, \nu_n]$.

TABLE 1. Estimates Δ_n of relative error of eigen frequency calculations on intervals with number n

n	1	2	3	4	5	6	7	8	9	10
Δ_n	0.01%	1.0%	0.9%	0.5%	0.3%	0.2%	0.1%	0.1%	0.05%	0.01%

It can be seen from the table that relative errors of eigen frequency calculations, starting from the third, monotonically decrease.

6. Conclusion

The presence of approximate analytical dependencies for the eigenvalues of the Sturm-Liouville problem on the problem parameters makes it possible to carry out a comprehensive mathematical study of the physical phenomenon from which the Sturm-Liouville problem is derived.

For example, it may be recommended to use the proposed method of solving characteristic equations to solve inverse problems, such as identification of boundary conditions of spectral problems by eigenvalues [26], identification of local defects in mechanical objects (rods, beams, pipelines) [27].

Use of the proposed method in solving inverse problems of oscillations of micro- and nano-objects, in particular MEMS and NEMS, will allow expanding the possibilities of nanometrology.

References

- [1] Margolin V.I. Zhabrev V.A., Lukyanov G.N., Tupik V.A. *Introduction to Nanotechnologies*. Lan', Saint Petersburg, 2012, 464 p.
- [2] Voitovich I.D., Korsunsky V.M. *Intellectual sensors*. BINOMIAL. Knowledge Laboratory, M., 2012, 624 p.
- [3] Nguyen C.T.-C. MEMS technology for timing and frequency control. *IEEE Trans. Ultrason. Ferroelectr. Freq. Control*, 2007, **54**, P. 251–270.
- [4] Basu J., Bhattacharyya T.K. Microelectromechanical resonators for radio frequency communication applications. *Microsyst. Technol.*, 2011, **17**, P. 1557–1580.
- [5] NEMS/MEMS Technology and Devices. Edited by Lynn Khine and Julius M. Tsai. International Conference on Materials for Advanced Technologies (ICMAT 2011), Symposium G: NEMS/MEMS and microTAS, June 26–July 1, Suntec, Singapore, 2011, 242 p.
- [6] Greenberg Y.S., Paskin Yu.A., Ilichev K.V. Nanomechanical resonators. *Successes of Physical Sciences*, 2012, **4**(182), P. 408–436.
- [7] Mukhurov N.I., Efremov G.I. *Electromechanical micro-devices*. Belarusian. Navuka, Minsk, 2012, 257 p.
- [8] Van Beek, J.T.M., Puers, R. A review of MEMS oscillators for frequency reference and timing applications. *J. Micromech. Microeng.*, 2012, **22**, P. 13001.
- [9] Nguyen, C.T.-C. MEMS-based RF channel selection for true software-defined cognitive radio and low-power sensor communications. *IEEE Commun. Mag.*, 2013, **51**, P. 110–119.
- [10] Uranga A., Verd J., Barniol N. CMOS–MEMS resonators: From devices to applications. *Microelectron. Eng.*, 2015, **132**, P. 58–73.
- [11] Abdolvand R., Bahreyni B., Lee J., & Nabki F. Micromachined Resonators: A Review. *Micromachines*, 2016, **7**(9), 2016, P. 160–213.
- [12] Ali W.R., Prasad M. Piezoelectric MEMS based acoustic sensors: A review. *Sensors and Actuators A: Physical. Sensors and Actuators A.*, 2020, **301**, P. 2–31.
- [13] Lyshevski S.E. *MEMS and NEMS Systems, Devices, and Structures*. CRC Press, New York, 2002, 461 p.
- [14] Kolmakov A.G., Barinov S.M., Alymov M.I. *Basis of technologies and application of nanomaterials*. Fizmatlit, M., 2012, 208 p.
- [15] Zaytsev V.F., Polyanin A.D. *Handbook on Ordinary Differential Equations*. Fizmatlit, M., 2001, 576 p.
- [16] Collatz L. *Tasks for own values (with technical annexes)*. Science, M., 1968, 504 pp.
- [17] *Vibrations in engineering: Reference. T. 1. Fluctuations of linear systems*. Under Ed. V.V. Bolotina. Mashinostroenie, M., 1978, 352 p.
- [18] Charles T. Fulton Two-point boundary value problems with eigenvalue parameter contained in the boundary conditions. *Proceedings of the Royal Society of Edinburgh*, 1977, **77 A**, P. 293–308.
- [19] Shkalikov A.A. Boundary problems for ordinary differential equations with parameter under boundary conditions. *Works of I.G. Petrovsky Seminar*, 1983, **9**, P. 190–229.
- [20] Titchmarsh E.C. *Eigenfunction expansions associated with second order differential equations. V. 1*. Oxford Univ. Press, London, 1962, 203 p.
- [21] Naimark M.A. *Linear differential operators*. Science, M., 1969, 528 p.
- [22] Lukyanov V.D., Nosova L.V., Bogorodsky A.V. et al. Approximate solution to the Sturm-Liouville problem with complicated boundary conditions. *Sea intellectual technologies*, 2019, **1**(43), P. 142–146.
- [23] Beckman I.N. *Mathematics of Diffusion*. OntoPrint, M., 2016, 400 p.
- [24] Koshlyakov N.S., Gliner E.B., Smyrnov M. M. *Differential equations of mathematical physics*. Fizmatgiz, M., 1962, 768 p.
- [25] Lukyanov V.D. On the construction of an interpolation-approximation polynomial. *Nanosystems: physics, chemistry, mathematics*. 2012, **3**(6), P. 5–15.
- [26] Akhtyamov A.M. *Theory of identification of edge conditions and its application*. Fizmatlit, M., 2009, 272 p.
- [27] Akhtyamov A. M., Ilgamov M. A. Review of research on identification of local defects of rods. *Problems of machine building and reliability*, 2020, **2**, P. 3–15.

Stochastic molecular modeling the transport coefficients of rarefied gas and gas nanosuspensions

V. Ya. Rudyak^{1,2}, E. V. Lezhnev¹

¹Novosibirsk State University of Architecture and Civil Engineering, Leningradskaya, 113, Novosibirsk, Russia

²Novosibirsk State University, Pirogova, 1, Novosibirsk, Russia

valery.rudyak@mail.ru, lionlev@yandex.ru

PACS 02.70.Ns, 02.70.Tt, 47.55.-n, 51.20.+d, 47.57.J

DOI 10.17586/2220-8054-2020-11-3-285-293

The subject of this paper is the stochastic molecular modelling of the transport coefficients for rarefied gases and gas nanosuspensions. The proposed method is an alternative one to the molecular dynamics method. However, unlike the latter, the phase trajectories of the molecular system are simulated stochastically. Adequate integral characteristics of the studied system are obtained by averaging the calculated data over independent phase trajectories. The efficiency of the proposed algorithm is demonstrated by calculation of the diffusion and viscosity coefficients of several noble and polyatomic gases and rarefied gas nanosuspensions. The modeling accuracy increases when a greater number of molecules and phase trajectories are employed.

Keywords: diffusion, gas nanosuspension, rarefied gas, stochastic molecular simulation; transport processes, transport coefficients, viscosity.

Received: 18 April 2020

Revised: 22 April 2020

1. Introduction

Transport processes determine characteristics of all natural and industrial flows of liquids and gases. The description of these processes requires knowledge of the corresponding transport coefficients: diffusivity, viscosity, thermal conductivity, etc. Of course, there are fairly reliable experimental methods for measuring them, however, the necessity of their theoretical calculations or simulations is also understandable. In rarefied gases, this problem is solved using kinetic theory of gases (see, for example, [1]). However, calculation of these coefficients is generally a non-trivial task. It is necessary to solve complex integral equations. The solution of these equations is a rather cumbersome and complicated procedure [2, 3]. In addition, so-called Ω -integrals have to be calculated. There are the sufficiently detailed tables of the values of these integrals for the Lennard-Jones potential only.

Molecular modeling is single alternative of the experimental determination of the transport coefficients of liquid and gases. Practically, the molecular dynamics (MD) method is the only consistent method for such modeling. However this method is not applicable to simulation of the rarefied gases because the corresponding simulation cell should have a characteristic linear dimension much larger than the mean free path of molecules and it is therefore necessary to use a huge number of molecules. On the other hand, systematic studies of the MD method have shown that it does not provide true phase trajectories of molecular systems (see [4–6]). Adequate results of MD simulations can be obtained only by averaging the corresponding dynamical variables over an ensemble of independent phase trajectories.

In our papers [7, 8], a stochastic algorithm to model the transport coefficients of the rarefied gases has been developed. In this algorithm the phase trajectories of the molecular system are simulated stochastically. In the present paper, the given algorithm is generalized for modeling the transport coefficients of rarefied polyatomic gases and rarefied gas nanosuspensions.

2. Simulation of the molecules phase trajectories

In rarefied gases, only binary collisions of molecules take place and the molecules themselves are material points. The spatiotemporal scales of the order of the time of the molecules interaction and their size are indistinguishable. This implies that the intermolecular interactions do not contribute to the transport coefficients and the equation of state. Such contributions appear only in the next approximation for density (for moderately dense gas) [9, 10]. For this reason, the transport coefficients of a rarefied gas are only functions of the velocities of molecules [1–3, 10]. Therefore, to model the transport coefficients of the rarefied gas, it is sufficient to study its evolution in the space of velocities.

Let us consider the system of gas molecules with numerical density n . At the initial time, the velocities of the molecules are distributed according to the Maxwell distribution function at a given temperature T . Simulation of the gas dynamics starts with generating a list of velocities of the molecules at the initial time t . Thus, at time t , the

molecules have velocities $(\mathbf{v}_1, \mathbf{v}_2, \dots, \mathbf{v}_N)$. It is necessary to obtain the values of the molecules velocities at successive times in the simulation interval (t, t_s) .

The dynamics of the molecules are determined by their interactions. Below these interactions are described by the Lennard-Jones potential:

$$U(r) = 4\varepsilon \left[\left(\frac{\sigma}{r} \right)^{12} - \left(\frac{\sigma}{r} \right)^6 \right]. \quad (1)$$

Here, σ is the effective radius of the molecule and ε is the maximum value of the attraction energy. In this paper, the gas mixtures are considered; therefore, in addition to the interaction of their molecules, which are described by the potential parameters (1), σ_{ii} , ε_{ii} ($i=1,2$), it is necessary to determine the parameters of the cross-interactions of molecules of type i with molecules of type j : σ_{ij} , ε_{ij} . These parameters were determined using the simplest combination relations: $\varepsilon_{ij} = \sqrt{\varepsilon_{ii}\varepsilon_{jj}}$, $\sigma_{ij} = (\sigma_{ii} + \sigma_{jj})/2$. Since the potentials have an infinite radius of action, they should be truncated in the course of simulation. The truncation radii are equal to 2.5σ for potential (1).

As the first step of the algorithm constructing the time interval $\tau_1 = \sigma/v_{\max}$ is determined. Here, v_{\max} is the maximum magnitude of the velocity of the molecules in the system at the given time. The generation of a list of the molecules velocities at the time $(t + \tau_1)$ starts with a consideration of molecule 1. For a one-component system, to determine whether a molecule 1 collides with any other molecule during time τ_1 , a random number P uniformly distributed in the interval $(0, 1)$ is generated. If, in time τ_1 , it is less than the average probability of molecule collision $P_{\tau_1} = 4\tau_1 n r_c^2 \sqrt{\pi kT/m}$ (see [1]), then molecule with which molecule 1 collides is randomly selected from the remaining $(N - 1)$ molecules (here r_c is the potential cut-off radius of the potential (1), m is the mass of molecule and k is the Boltzmann constant). As a result, the velocities of the colliding molecules change according to the laws of elastic collision:

$$\mathbf{v}'_1 = \mathbf{v}_1 + (\mathbf{v}_{1j} \cdot \mathbf{e}_{1j}) \mathbf{e}_{1j}, \quad \mathbf{v}'_j = \mathbf{v}_j - (\mathbf{v}_{1j} \cdot \mathbf{e}_{1j}) \mathbf{e}_{1j}, \quad (2)$$

where $\mathbf{v}_{1j} = (\mathbf{v}_1 - \mathbf{v}_j)$ is the vector of relative velocity and \mathbf{e}_{1j} is the unit vector from center of molecule j to molecule 1. The actual mechanisms of the molecules interaction is described in detailed in paper [8].

If the generated number P is greater than the average probability of collision, molecule 1 does not collide in this time interval and its velocity does not change. If it collides, the velocities of molecules 1 and j in the initial list change. The remaining molecules are treated similarly. As a result, a new list of the velocities of the molecules $(\mathbf{v}'_1, \mathbf{v}'_2, \dots, \mathbf{v}'_N)$ is generated.

After the generation of the list for the time $(t + \tau_1)$, the next time interval is selected as $\tau_2 = \sigma/v_{\max}$, where v_{\max} is the maximum magnitude of the velocity of the molecules of the system at the time $(t + \tau_1)$ and the procedure is repeated. This procedure is repeated until the given simulation time t_s equal to $t_s = \tau_1 + \tau_2 + \dots + \tau_k$ is reached. The calculation result is the full set of the velocities of all the molecules of the simulated system at successive times.

For mixer of the gases this algorithm is slightly modified. Consider, for example, the binary mixer. In this case, the time step τ_1 is determined by the following relation $\tau_1 = \sigma_{\min}/v_{\max}$, where $\sigma_{\min} = \min(\sigma_{11}, \sigma_{22})$. Now the molecule of sort 1 can collide with molecule of the same type or molecule of sort 2. Let us consider for definiteness, a particle of the first sort (for the second the formulas are similar). In this case, the collision probability is equal to:

$$P_{\tau_1} = 4\tau_1 n_1 r_{c11}^2 \sqrt{\frac{\pi kT}{m_1}} + 2\tau_1 n_2 r_{c22}^2 \sqrt{\frac{2\pi kT}{x_1 m_2}} = P_{11} + P_{12}.$$

Here, r_{cii} is the cut-off intermolecular radius of the potential (1) for molecules of sort i and x_1 is the molar fraction of the molecules of the first sort.

So, if the generated number P is smaller than P_{τ_1} , the collision will occur and for molecule 1 of sort 1, randomly from the $N - 1$ remaining molecules, the particle j is selected with which this collision will be realized. Moreover, if $P < P_{11}$, a molecule of the first sort is selected, and if $P_{11} < P$ then it is of the second sort molecule. In addition, the velocities of the molecules after collision are determined by the following relation (compare with equation (2)):

$$\mathbf{v}'_1 = \mathbf{v}_1 + 2M_j (\mathbf{v}_{1j} \cdot \mathbf{e}_{1j}) \mathbf{e}_{1j}, \quad \mathbf{v}'_j = \mathbf{v}_j - 2M_1 (\mathbf{v}_{1j} \cdot \mathbf{e}_{1j}) \mathbf{e}_{1j},$$

where $M_i = m_i/(m_1 + m_j)$.

3. Diffusion and viscosity coefficients of rarefied gases

The described algorithm permits one to model transport processes in rarefied gases. In particular, using this algorithm it may be used to calculate the transport coefficients. The transport coefficients of the molecular system considered are calculated using fluctuation-dissipation theorems, which relate transport coefficients to the evolution of the corresponding correlation functions. In the literature, these relations are called the Green-Kubo formulas [4, 10–12]. The identity of these formulas and relations of the kinetic theories [1–3] was studied and established in paper [13, 14].

According to the fluctuation-dissipation theorem the binary diffusion coefficient is described by the following formulas [15]:

$$D = \frac{1-x_1}{x_1} L_{11} + \frac{x_1}{1-x_1} L_{22} - L_{12} - L_{21}, \quad (3)$$

where

$$L_{\alpha\beta} = \frac{1}{3N} \int_0^{\tau_p} dt \chi_{\alpha\beta}(0, \tau),$$

$$\chi_{\alpha\beta}(0, t) = \sum_k^{N_\alpha} [v_{k\alpha}(0) - v(0)] \cdot \sum_l^{N_\beta} [v_{l\beta}(0) - v(0)],$$

$$v(t) = \frac{x_1}{N_1} \sum_k^{N_\alpha} v_{k\alpha}(t) + \frac{1-x_1}{N_2} \sum_l^{N_\beta} v_{l\beta}(t).$$

Here, t_p is so named plateau time of the calculation of the integral (3) [16].

In the formulas (3), the integrand defines the correlation functions of the molecular velocities, the time integrals of which give the value of the diffusion coefficient. The autocorrelation velocity function (ACVF) of the rarefied gas should decay exponentially [4]. As an example in Fig. 1 (left), the evolution of the ACVF χ_{11} for the Kr-Ar mixture is given. Here, $t' = t/\tau$, where τ is the mean free path time of Kr molecules. In actuality, ACVF decays exponentially. Therefore, the plateau value of the diffusion coefficient is reached within 10–15 mean free path times (see Fig. 1 right).

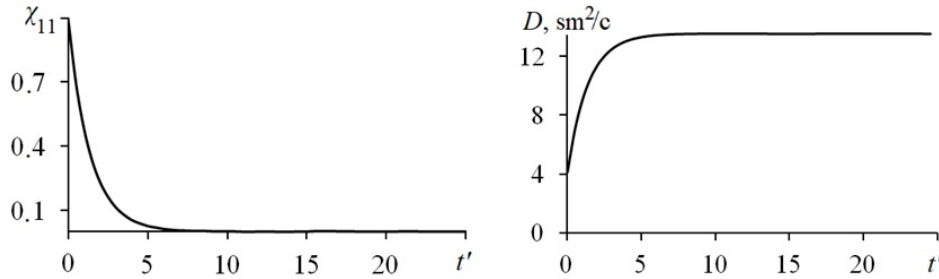


FIG. 1. The evolution of ACVF (left) and diffusion coefficient of Kr-Ar mixer (right)

The accuracy of the simulation was evaluated by comparison with experimental data. Firstly, the diffusion coefficients for mixtures of rarefied noble gases Kr-Ar, Xe-Ar, Xe-Kr at atmospheric pressure and temperature of 295 K were analyzed. The following intermolecular potential parameters (see (1)) were used: $\sigma = 0.311$ nm, $\varepsilon/k = 116$ K for argon, $\sigma = 0.351$ nm, $\varepsilon/k = 190$ K for krypton and $\sigma = 0.386$ nm, $\varepsilon/k = 190$ K for Xenon [2]. Calculation of each phase trajectory was performed for 50 mean free paths time. The diffusion coefficient D was calculated by averaging over 1000 independent phase trajectories. 3500 molecules were used in the calculations. Comparison of simulated and experimental data for the three mixtures is presented in Table 1. Here the second line corresponds to the experimental data D_e [17] and the relative error of the simulation is given in the last line.

TABLE 1. Comparison of simulated and experimental data of the diffusion coefficients

T	Kr-Ar	Xe-Ar	Xe-Kr
$D_e, \text{sm}^2/\text{s}$	13.58	11.1	7.43
$D, \text{sm}^2/\text{s}$	13.22	11.42	7.19
$\Delta, \%$	2.63	2.88	3.28

The simulation error of the diffusion coefficients was about 3% (see Table 1). It should be noted that the accuracy of measuring the diffusion coefficient also usually lies in the range of 1–3%. So the accuracy of modeling, even with the use of this relatively small number of molecules, is quite acceptable. However, the accuracy of the simulation using the presented algorithm increases with the number of molecules used and/or the number of phase trajectories used for averaging. It will be discussed later.

One of the main problems of the kinetic theory of gases is the modeling transport processes of polyatomic gases. Different approaches are used here, including the use of various semi-classical or quantum methods (see, for example, [2, 3, 18, 19]). Nevertheless, even in the simplest case of a single-component gas, the calculation of the transport coefficients of a rarefied polyatomic gas has not completely solved. Therefore, it would be of utility to understand

the applicability of the algorithm described above for modeling transport coefficients of polyatomic gases. Below this problem is analyzed on example of modeling the viscosity coefficient both monatomic (Ar, Kr, Ne, Xe) and polyatomic gases (CH₄, CO, CO₂, O₂).

The calculation of the viscosity coefficient, as using MD method, is based on the fluctuation-dissipation theorem, which has the form for the viscosity coefficient [4, 10–12]:

$$\eta = \frac{1}{3VKT} \int_0^{t_p} dt \chi_\eta(0, t) = \frac{1}{3VKT} \int_0^{t_p} dt \langle \sigma_{xy}(0) \sigma_{xy}(t) \rangle, \quad (4)$$

where V is the volume of the system. The components of the stress tensor for a rarefied gas are calculated as:

$$\sigma_{xy}(0, t) = \frac{1}{Nl} \sum_j^l \sum_k^N m [v_{xk}(j\Delta t) v_{yk}(t + j\Delta t)].$$

Here Δt is the time interval of the calculation of the velocities.

To simulate the viscosity of the gases the following intermolecular potential parameters were used: $\sigma = 0.382$ nm, $\varepsilon/k = 137$ K for CH₄, $\sigma = 0.359$ nm, $\varepsilon/k = 110$ K for CO, $\sigma = 0.448$ nm, $\varepsilon/k = 189$ K for CO₂, $\sigma = 0.343$ nm, $\varepsilon/k = 113$ K for O₂, $\sigma = 0.178$ nm, $\varepsilon/k = 35.7$ K for Ne. The viscosity coefficients were calculated at a temperature of 273 K and atmospheric pressure. In all cases 3200 molecules were used in the calculations, and the obtained data were averaged over 1000 independent phase trajectories.

The correlation of the stress tensor $\chi_n(t)$ decays exponentially also. The obtained values of the viscosity coefficient are presented in Table 2 (second line). The corresponding experimental values of η_e taken from the reference book [20] are also shown here. The relative error of the simulation is given in the last line again.

TABLE 2. Comparison of simulated and experimental data of the viscosity coefficients of the rarefied gases

	CH ₄	CO	CO ₂	O ₂	Ar	Kr	Ne	Xe
$\eta \cdot 10^6$ (Pa·s)	10.48	15.95	13.0	18.91	22.25	25.87	32.28	23.78
$\eta_e \cdot 10^6$ (Pa·s)	10.37	16.6	13.8	19.3	22.7	25.5	31.7	23.3
Δ , %	1.06	3.94	5.84	2.02	1.97	1.46	1.84	2.05

Comparison of simulation and experimental data shows that the simulation accuracy is within the accuracy of obtaining experimental data for monoatomic gases and oxygen (about 2%). At the same time, the situation for polyatomic gases is more complicated. Good data are obtained for methane, whose molecules are spherically symmetric and for oxygen. On the other hand, for non-spherical molecules, of course, more adequate potentials should be applied. Although here, the accuracy of modeling the viscosity coefficient is not bad. In addition, it can also be increased by using a larger number of molecules (see the next section).

4. Accuracy of the modeling

The calculations presented in previous section showed that the proposed algorithm for modeling gas transport coefficients allows one, using a relatively small number of molecules, to obtain data comparable in accuracy with experimental results. However, the dependence of the simulation results on the molecules number used is a very important feature of the algorithm. The dependence of the accuracy of the number of particles was studied in modeling different transport coefficients. Below, the obtained results will be shown for calculating the diffusion and viscosity coefficients of a few rarefied gases. In all cases, the simulation results were compared with the corresponding experimental ones.

Let us consider the diffusion of Ar-Kr mixture. The number of the used molecules N was varied from 850 to 6800. The obtained relative error ranges from 4.9% to 1.9%. These data indicate that the accuracy of the simulation increases with an increasing number of molecules. One can show that the resulting relative errors Δ are well described by the dependence $\Delta \sim 1/\sqrt{N}$.

A similar result is obtained when modelling the viscosity coefficient. As an example, the dependence of the accuracy of the number of particles was studied in modeling the viscosity coefficient of argon. The data obtained in simulations of 10, 100, 500, 1600, and 3200 molecules are analyzed. The obtained relative error is changed from 9.7% to 0.8% and again, $\Delta \sim 1/\sqrt{N}$.

Another important factor determining the simulation's accuracy is the number of ensemble members over which the averaging is performed. The ensemble of the phase trajectories for averaging is a typical Gibbs ensemble characterized by different initial phase states of molecules with given mean values of macroscopic observables (temperature,

pressure, density). To study the dependence of the simulation accuracy on the number of ensemble members L (the number of independent phase trajectories) over which the averaging is performed, the diffusion of an Ar-Kr mixture is again considered. The parameter L was changed from 125 to 1000, the number of the molecules was the same and equal to 3200. The relative accuracy of the diffusion coefficient changed from 5.8% to 2.6%. These (and many other) test calculations have shown that the simulation's accuracy $\Delta_s \sim 1/\sqrt{L}$. This estimate is expected, of course. However, it is clear that the value $\Delta_s \sim 10^{-2}$ does not mean that accuracy of the order of one percent is achieved. The accuracy also depends on the number of molecules in the computational cell.

Averaging the simulated observables over a sufficiently large number of the independent phase trajectories is connected in particular with the nonmonotonic damping of the two-time correlation functions of the molecular systems (see, for example, papers [21, 22], in which the quasi-periodic behavior of ACVF was predicted). In finite number molecule system the amplitude of these fluctuations may be rather large. Therefore, a comparatively large number of the used phase trajectories is required to achieve the high accuracy of the modelling.

On the other hand, one needs to repeat that the simulation accuracy, of course, depends on the number of molecules used. For a very small number of particles, sufficiently accurate results were not obtained. The reason in the rarefied gas is clear: in a rarefied gas, the collided molecules do not collide in future. The probability of such collisions is negligible, and they are a characteristic feature of the dynamics of dense gases [9, 10]. On the other hand, in a system of a small number of molecules, modeling the rarefied gas during the time τ_i there are a significant number of repeated collisions involving the same molecules [23, 24]. The simulation's accuracy can be substantially increased by eliminating such collisions. In the Bird method [25] of direct statistical Monte-Carlo method, this was done in paper [26]. Elimination of repeated collisions made it possible to achieve the same accuracy for ten particles as when using the standard method for one thousand particles. A similar procedure was realized in the algorithm we describe here. The procedure of eliminating repeated collisions is extremely simple. If, in the selection of the collision of the i -th molecule, it is to collide with molecule k , and this collision has already occurred in the given time interval, then a different pair for collision is selected. The example of the calculations of the viscosity coefficients of CH_4 gas with (second line) and without (third line) repeated collisions are presented in Table 3. In all presented calculations the averaging of the data were fulfilled over thousand independent phase trajectories. The result is excellent, the acceptable accuracy is obtained when using only ten molecules.

TABLE 3. Comparison of simulated data of the viscosity coefficients for methane

N	10	100	500	2500
$\Delta_0, \%$	11.06	5.89	4.83	4.24
$\Delta_1, \%$	2.18	1.76	1.43	1.27

Using the described algorithm for eliminating repeated collisions it is possible to reduce by one or even several orders of magnitude the number of molecules used for modeling. Naturally, eliminating repeated collisions the simulation time may be considerably reduced. On the other hand, it is clear that the effectiveness of the procedure for excluding repeated collisions decreases with an increasing the number of molecules used in the simulation.

5. Modeling the transport processes in rarefied gas nanosuspensions

A gas nanosuspension is a two-phase medium in which the carrier medium is a rarefied gas and dispersed particles are nanoparticles having the size from 1 to 100 nm. For considering gas nanosuspensions, the mean free path of the molecules is more than size of dispersed particles, as a rule. The key point for modeling the dynamics of gas nanosuspensions is the interaction potentials of the nanoparticles with molecules of the carrier gas and nanoparticles with each other. In MD modeling of transport processes of nanofluids, the nanoparticles are often simulated by the clusters of different size (see review [27] and references therein). But molecular cluster is not nanoparticle because in gas and liquid it may change (and change!) its size and shape. In addition, the atoms of such cluster can be replaced by the base fluid molecules. On the other hand, in real physical experiment we have stable nanoparticles, these particles have constant shape and size. In order to simulate the transport processes in such nanofluids, it is necessary to determine correctly the interaction potentials of nanoparticles with base fluid molecules and between each other. Such potentials were constructed early in papers [28, 29]. Later the use of this potential was experimentally checked [30].

The interaction of molecules of the carrier medium with a nanoparticle was determined by the Rudyak-Krasnolutskii (RK) potential as follows [28, 29]:

$$\Psi(r) = \Psi_9(r) - \Psi_3(r). \quad (5)$$

$$\Psi_i(r) = C_i \{ [(r - R)^{-i} - (r + R)^{-i}] \} - a_i r^{-1} [(r - R)^{-i+1} - (r + R)^{-i+1}],$$

where $i=9,3$, $a_9=9/8$, $a_3=3/2$, $C_9 = (4\pi\varepsilon_{12}\sigma_{12}^{12})/45V_p$, $C_3 = (2\eta\varepsilon_{12}\sigma_{12}^6)/3V_p$, and $V_p^{-1} = \rho_p/m_p$.

Here, ρ_p is the density of the nanoparticle material, m_p is the molecular mass of the substance of the nanoparticle, R is the nanoparticle radius, σ_{ij} and ε_{ij} are the parameters of potential (1) of the interactions of a carried medium molecule with a nanoparticle atom (or molecule).

As the interaction potential for nanoparticles, we are using the potential [31], which has the following form for monodisperse particles:

$$U(r, R) = U_7(r, R) - U_1(r, R) \quad (6)$$

$$U_7(r) = \frac{\pi^2 \tilde{\varepsilon} \tilde{\sigma}^{12}}{315V_p^2} \left\{ \frac{R^2}{r} \left[\frac{1}{(r-2R)^7} + \frac{2}{R^7} + \frac{1}{(r+2R)^7} \right] - \frac{R}{3r} \left[\frac{1}{(r-2R)^6} - \frac{1}{(r+2R)^6} \right] - \frac{1}{30r} \left[\frac{1}{(r-2R)^5} - \frac{2}{R^5} + \frac{1}{(r+2R)^5} \right] \right\},$$

$$U_1(r) = \frac{2\pi^2 \tilde{\varepsilon} \tilde{\sigma}^6}{3V_p^2} \left[\ln \left(\frac{r^2 - 4R^2}{r^2} \right) + 2R^2 \left(\frac{1}{r^2 - 4R^2} + \frac{1}{r^2} \right) \right],$$

here $\tilde{\varepsilon}$ and $\tilde{\sigma}$ are the parameters of the Lennard-Jones interaction potential (1) of the nanoparticle atoms (molecules). Potentials (5) and (6) were constructed on the assumption that the interaction of carrier fluid molecules with nanoparticle atoms and nanoparticle atoms with each other is described by a potential of the form (1) with the parameters σ_{12} , ε_{12} and $\tilde{\sigma}$, $\tilde{\varepsilon}$, respectively. Since these potentials have an infinite radius of action, they should be truncated in the course of simulation. The truncation radii are equal to $R + b\sigma_{12}$ for potentials (5) and (6). Factor b was selected such that the force with which a nanoparticle acts on a molecule is equal to the force of interaction between two molecules over the truncation radius for potential (5). This factor depends on the nanoparticle material and the properties of carrier molecules.

In this paper, rarefied gas nanosuspensions are considered. It is a binary system. The algorithm to simulate such system is described in section 2. The result of the calculations is a complete set of velocities of all molecules and nanoparticles of the simulated system at successive times. Using this information, it is possible to calculate all the observable characteristics of the system studied. The transport coefficients studied here were calculated again using the fluctuation-dissipation theorems (3) and (4).

One of the goals of this paper was to study the possibilities of the proposed simulation algorithm for modeling the diffusion of nanoparticles in gas. Previously, the diffusion of Cu_2O nanoparticles in nitrogen at atmospheric pressure and temperature 294.15 K was studied experimentally [30]. Therefore for testing the proposed algorithm, namely this diffusion was modeled. The following parameters of the intermolecular interaction potential were used: $\sigma=0.3798$ nm, $\varepsilon/k=71.4$ K for N_2 , $\sigma=0.4124$ nm, $\varepsilon/k=2909$ K for Cu_2O [30]. The diameter of Cu_2O particle was varied from 2.55 to 8.94 nm. The number of molecules in the calculations varied from 450 to 20,000, depending on the size of the nanoparticle.

The comparison of simulation D and experimental D_e data of the diffusion coefficient of Cu_2O particles is shown in Table 4. Here, the first column is the diameter of the nanoparticle and the fourth is the relative error of the simulation. In all cases, the simulation accuracy is quite high and practically does not depend on the size of the nanoparticles.

TABLE 4. Calculations of the diffusion coefficient of the nanoparticles

R , nm	D , $\text{m}^2/\text{s}\cdot 10^{-7}$	D_e , $\text{m}^2/\text{s}\cdot 10^{-7}$	Δ , %
2.55	5.156	5.063	1.84
2.94	4.046	4.102	1.37
3.33	3.386	3.418	0.95
4.51	2.158	2.118	1.87
4.79	1.968	1.932	1.88
5.35	1.632	1.601	1.95
6.33	1.236	1.215	1.71
7.54	9.196	9.044	1.68
8.94	6.625	6.694	1.03

The rarefied gas nanosuspension is a special case of a nanofluid. Nanofluids with spherical nanoparticles and carbon nanotubes have already been successfully used or are proposed for use in various applications (see for example

[32–35]). The model of the viscosity of coarse dispersed fluid was developed by Einstein [36] and then generalized by many authors (see [37–40] and references therein). It was established that viscosity of coarse dispersed fluid is always larger than the viscosity of based fluid and this increase depends on volume concentration of the dispersed particles. In nanofluids this tendency is conserved but their viscosity depends not only on the particles concentration but also on size and material of nanoparticles [41,42]. However, in papers [43,44], it is shown using the kinetic theory that the viscosity of the rarefied gas nanosuspensions can be either greater or less than the viscosity of the carrier gas. One of the tasks of this paper is to test the possibility of describing this effect using the proposed stochastic molecular modeling algorithm. The viscosity of the two different gas nanosuspensions (Zn-Ne U-H₂) are studied. The following parameters of the intermolecular interaction potential were used: $\sigma = 0.2968$ nm, $\varepsilon/k = 33.3$ K for H₂, $\sigma = 0.3343$ nm, $\varepsilon/k = 2703.6$ K for U, $\sigma = 0.246$ nm, $\varepsilon/k = 1040$ K for Zn [43, 44]. The transport coefficients are calculated using fluctuation-dissipation theorems (4) generalized for binary mixer.

First consider the viscosity of the gas nanosuspension U-H₂. The size of the particles is equal to 1 nm. The dependence of the viscosity coefficients of this gas nanosuspension on the nanoparticle volume concentration ϕ , % at different temperatures is presented in Fig. 2. Here, the different lines correspond to the kinetic theory data obtained in [43] at 200, 300 and 500 K bottom-up respectively. In all cases, the volume concentration of the particle is very small (from 0.02 to 0.08%), however the mass concentration is sufficiently large. In Fig. 2 different markers correspond to the simulation data. These data are in good agreement with the kinetic theory ones. The viscosity of gas nanosuspension increases with increasing particle concentration and it is more than the viscosity of carrier gas. The viscosity of gas nanosuspension exceeds the viscosity of the carrier gas by about 90% at concentrations of the order of 0.02% and at room temperature. This effect increases with increasing temperature. For example, at 1000 K, the relative viscosity coefficient $\eta_r = \eta/\eta_g \approx 2.3$ (here, η and η_g are the viscosity coefficients of the gas nanosuspension and carrier gas respectively).

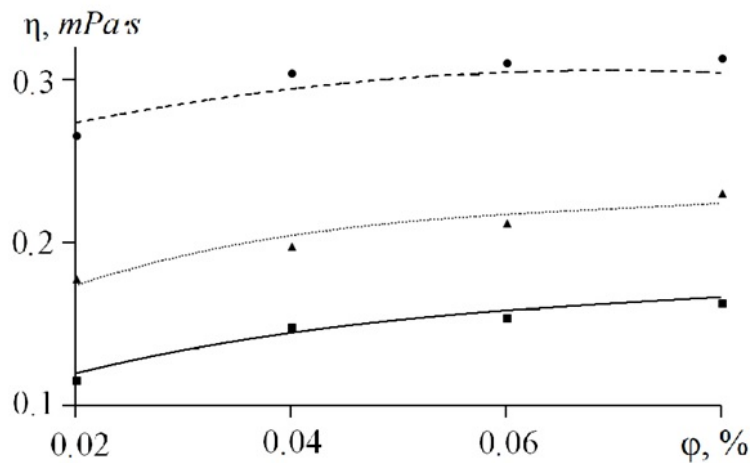


FIG. 2. The viscosity coefficients of U-H₂ gas nanosuspension versus nanoparticles volume concentration ϕ , % at different temperature. The different markers correspond to the simulation data at the temperature 200, 300 and 500 K bottom-up respectively. Different lines correspond to data of the kinetic theory [43]

On the other hand, in [44], it is shown that in certain situations, gas nanosuspensions may have viscosity less than in carrier gas. To check this conclusion, the viscosity of the Zn-Ne gas nanosuspension was calculated. The size of the particles is equal to 1 nm again. The obtained data are presented in Fig. 3. The lines correspond to the kinetic theory data [44] at the temperature 200, 300, 500 and 1000 K, bottom-up respectively. The different labels correspond to our calculated data for appropriate temperature and particle volume concentrations.

The viscosity of the gas nanosuspensions considered at all temperatures is lower than the viscosity of the carrier gas. At room temperature and particle volume concentration of 0.02%, the effective viscosity of this gas nanosuspension is about 15% lower than that of pure neon, and this effect increases with increasing temperature. The simulation and kinetic theory data coincide with each other. Thus the proposed algorithm permits one to model the viscosity of the gas nanosuspensions.

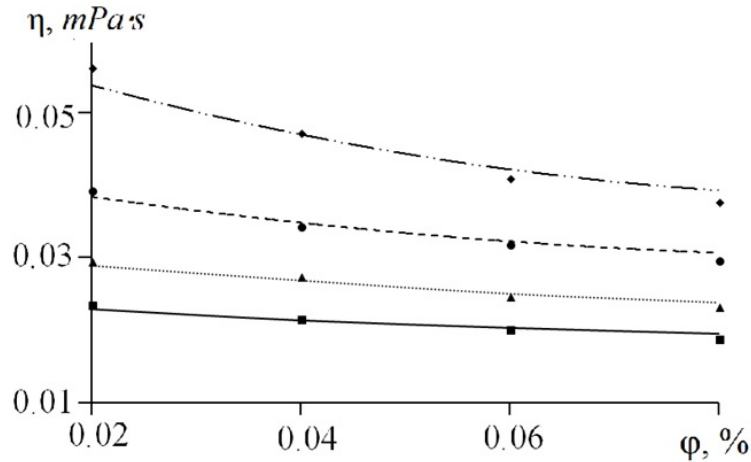


FIG. 3. The viscosity coefficients of Ne-Zn gas nanosuspension versus nanoparticles volume concentration ϕ , % at different temperatures. The different labels on the lines corresponds to the simulation data at the temperature 200, 300, 500 and 1000 K, bottom-up respectively. The lines correspond to the data of the kinetic theory [44] for appropriate temperature and the particles volume concentrations

6. Conclusion

The proposed algorithms for calculating gas transport coefficients allow one, using a relatively small number of molecules, to obtain data comparable in accuracy with experimental results. It is the stochastic algorithm because all phase trajectories of the modelled system are built stochastically. However it is not the Monte-Carlo type algorithm, because we do not build the stochastic process to solve any equation. The dynamics of the molecular gas in corresponding phase space are modeled.

In this paper, the simulation of the transport coefficients of the rarefied gases are considered. All transport coefficients of such gases are dependent on the velocity of the particles of the system (see, for example (3) and (4)). Therefore the dynamics of the molecules in the velocity space were studied. However, strictly speaking the determination of the velocities of the particles after collision (see (2) requires knowledge of the vector $\mathbf{e}_{ij} = (\mathbf{r}_j - \mathbf{r}_i) / |\mathbf{r}_j - \mathbf{r}_i|$. There are two different ways to determine this vector during each time step. In the first case, at time t , all positions of the molecules are defined $(\mathbf{r}_1, \mathbf{r}_2, \dots, \mathbf{r}_N)$. Then, at selected time interval τ_1 , the coordinate of the molecule i is changed as follows $\mathbf{r}_i(t + \tau_1) = \mathbf{r}_i(t) + \mathbf{v}_i(t)\tau_1$. In this case, the calculation result is the full set of the coordinates and velocities of all the molecules of the simulated system at successive times. In the second way to determine the vectors \mathbf{e}_{ij} the initial data of the molecules were used. It is clear that the second way is much more efficient. Both described procedures were used in the developed algorithm. It was shown that the accuracy of the simulation is practically identical.

In all cases, the accuracy of the simulation increases with both the number of particles used and the number of phase trajectories for averaging the results. The relative error of the viscosity coefficient calculation is well described by the following formula: $\Delta \sim 1/\sqrt{NL}$. This means, in particular, that in order to achieve a given accuracy, the number of molecules can be “exchanged” for the number of phase trajectories. It is very important for example to model the gas nanosuspensions with large particles.

It is very interesting that the viscosity of gas nanosuspensions may be either larger or less than viscosity of the carrier gas. The decrease in the viscosity can be quite significant, at normal temperatures it can reach 10–15%. This effect increases with increasing the temperature. It should be emphasized that the volume concentrations of nanoparticles are very low and do not exceed 0.02%. A decrease in the effective viscosity coefficient compared to the corresponding value for the carrier gas should be expected if the sizes of the carrier gas molecules and nanoparticles differ significantly. If the sizes of the nanoparticles are sufficiently small, then a decrease in the effective viscosity coefficient can be expected if the ratio of the density of the nanoparticle material to the density of the carrier gas molecules is small enough also, e.g., when light particles are added to a heavy gas. Physically, the decreasing the effective viscosity of gas nanosuspension is due to a decrease in the frequency of molecule-molecule collisions due to collisions of molecules with nanoparticles, as well as due to a decrease in the molar fraction of gas molecules.

This work is partially supported by the Russian Foundation for Basic Research (grant No. 20-01-00041).

References

- [1] Chapman S., Cowling T.G. *The Mathematical Theory of Non-Uniform Gases*, Cambridge University Press, Cambridge, 1990, 423 p.
- [2] Hirschfelder J.O., Curtiss Ch.F., Bird R. B. *Molecular Theory of Gases and Liquids*, John Wiley and Sons, Inc. Chapman and Hall, Lim., 1954, 1219 p.
- [3] Ferziger J., Kaper H. *Mathematical Theory of Transport Processes in Gases*, North-Holland Publishing Company, Amsterdam–London, 1972, 546 p.
- [4] Rudyak V.Ya. *Statistical AeroHydromechanics of Homogeneous and Heterogeneous Media. Vol. 2. Hydromechanics*, NSUACE, Novosibirsk, 2005, 468 p.
- [5] Norman G.E., Stegailov V.V. The stochastic properties of a molecular dynamical Lennard-Jones system in equilibrium and nonequilibrium states. *J. Exp. Theor. Phys.*, 2001, **92**, P. 879–886.
- [6] Norman G.E., Stegailov V.V. Stochastic and dynamic properties of molecular dynamics systems: simple liquids, plasma and electrolytes, polymers. *Comput. Phys. Commun.*, 2002, **147**, P. 678–683.
- [7] Rudyak V.Ya., Lezhnev E.V. Stochastic method of the simulation of the rarefied gas transport coefficients. *Math. Mod.*, 2017, **29**, P. 113–122.
- [8] Rudyak V.Ya., Lezhnev E.V. Stochastic algorithm for simulating gas transport coefficients. *J. Computational Physics*, 2018, **355**, P. 95–103.
- [9] Klimontovich Y. *Kinetic Theory of Non-Ideal Gases and Non-Ideal Plasmas*, Pergamon Press, Oxford, 1982, 314 p.
- [10] Rudyak V.Ya. *Statistical Theory of Dissipative Processes in Gases and Liquids*, Science, Novosibirsk, 1987, 287 p.
- [11] Zubarev D.N. *Nonequilibrium Statistical Thermodynamics*, Consultants Bureau, New York, 1974, 371 p.
- [12] Hoover W.G. *Computational Statistical Mechanics*, Elsevier, Amsterdam, 1991, 324 p.
- [13] Ernst M.H. Formal theory of transport coefficients to general order in the density. *Physica*, 1966, **32**, P. 209–243.
- [14] Khon'kin A.D. Equations for space-time and time correlation functions and proof of the equivalence of results of the Chapman-Enskog and time correlation methods. *Theoretical and Mathematical Phys.*, 1970, **5**, P. 1029–1037.
- [15] Krishna R., Wesselingh J.A. The Maxwell-Stefan approach to mass transfer. *Chemical Engineering Science*, 1997, **52**, 1997, P. 861–911.
- [16] Rudyak V.Ya., Belkin A.A., Ivanov D.A., Egorov V.V. The simulation of transport processes using the method of molecular dynamics. Self-diffusion coefficient. *High Temperature*, 2008, **46**(1), P. 30–39.
- [17] Van Heijningen R.J.J., Harpe J.P., Beenakker J.M. Determination of the diffusion coefficients of binary mixtures of the noble gases as a function of temperature and concentration. *Physica*, 1968, **38**, P. 1–34.
- [18] Valander S.V., Nagnibeda E.A., Ridalevskaya M.A. *Some Questions of the Kinetic Theory of Chemical Reacting Gas Mixture*, LSU, Leningrad, 1977, 289 p.
- [19] Zhdanov V.M., Alievskii M.Ya. *Transport Processes and Relaxation in Molecular Gases*, Science, Moscow, 1989, 335 p.
- [20] Grigoriev I.S., Meilihova E.Z. *Physical values. Handbook*, Energoatomizdat, Moscow, 1991, 978 p.
- [21] Helfand E. Theory of molecular friction. *Phys. Fluids*, 1961, **4**, P. 681–691.
- [22] Suddaby A., Gray P. Relation between the friction constant and the force correlation integral in Brownian movement theory. *Proc. Phys. Soc.*, 1960, **75**, P. 109–118.
- [23] Rudyak V. Basic kinetic equation of a rarefied gas. *Fluid Dynamics*, 1989, **24**, 954–959.
- [24] Rudyak V. Correlations in a finite number of particles system simulating a rarefied gas. *Fluid Dynamics*, 1991, **26**, P. 909–914.
- [25] Bird G., *Molecular Gas Dynamics*, Clarendon Press, 1976, Oxford. 302 p.
- [26] Gimelshtein S.F., Rudyak V.Ya. Simulation of rarefied gas by the small number particles system. *Sov. Tech.-Phys. Letters*, 1991, **17**, P. 74–77.
- [27] Jabbari F., Rajabpour A., Saedodin S. Thermal conductivity and viscosity of nanofluids: a review of recent molecular dynamics studies. *Chemical Engineering Science*, 2017, **17**, P. 67–81.
- [28] Rudyak V.Ya., Krasnolutski S.L. Diffusion of nanoparticles in a rarefied gas. *Technical Physics*, 2002, **47**, P. 807–813.
- [29] Rudyak V.Ya., Krasnolutski S.L. Kinetic description of nanoparticle diffusion in rarefied gas. *Doklady Physics*, 2001, **46**, P. 897–899.
- [30] Rudyak V.Ya., Krasnolutski S.L., Nasibulin A.G., Kauppinen E.I. Methods of measuring the diffusion coefficient and sizes of nanoparticles in rarefied gas. *Doklady Physics* 2002, **47**, P. 758–761.
- [31] Rudyak V.Ya., Krasnolutski S.L., Ivanov D.A. The interaction potential of nanoparticles *Doklady Physics*, 2012, **57**, P. 3335.
- [32] Wang X-Q., Mujumdar A.S. A review on nanofluids – Part II: experiments and applications. *Brazilian J. Chem. Eng.*, 2008, **25**(4), P. 631–648.
- [33] Wong K.V., De Leon O. Applications of nanofluids: Current and future. *Advances in Mech. Eng.*, 2010, **2**, Article ID 519659.
- [34] Usoltseva L.O., Volkov D.S., Avramenko N.V., Korobov M.V., Proskurnin M.A. Nanodiamond aqueous dispersions as potential nanofluids: the determination of properties by thermal lensing and other techniques. *Nanosystems: Physics, Chemistry, Mathematics*, 2018, **9**(1), P. 17–20.
- [35] Lari H., Morsali A., Heravi M.M. The prediction of COOH functionalized carbon nanotube application in melphalan drug delivery. *Nanosystems: Physics, Chemistry, Mathematics*, 2019, **10**(4), P. 438–446.
- [36] Einstein A. Eine neue Bestimmung der Molekiildimensionen. *Annalen der Physik*, 1906, **19**, P. 289–306.
- [37] Batchelor G.K. The effect of Brownian motion on the bulk stress in a suspension of spherical particles. *J. Fluid Mech.* 1977, **83**, P. 97–117.
- [38] Acrivos A. Chang E.Y. A model for estimating transport quantities in two-phase materials *Phys. Fluids*, **29** P. 459–464.
- [39] Mooney M. The viscosity of a concentrated suspension of spherical particles *J. Colloid Sci*, 1951, **6-8**, P. 162170.
- [40] Frankel N.A., Acrivos A. On the viscosity of a concentrated suspension of solid spheres *Chem. Eng. Sci*, 1967, **22**, P. 847853.
- [41] Rudyak V.Ya., Minakov A.V. Thermophysical properties of nanofluids *Eur. Phys. J. E*, 2018, **41**, P. 15.
- [42] Rudyak V.Ya. Thermophysical characteristics of nanofluids and transport process mechanisms. *J. of Nanofluids*, 2019, **8**(1), P. 1–16.
- [43] Rudyak V.Ya., Krasnolutski S.L. About viscosity of rarefied gas suspensions with nanoparticles. *Doklady Physics*, 2003, **48**, P. 583–586.
- [44] Rudyak V.Ya., Krasnolutski S.L. Effective viscosity coefficient for rarefied nano gas suspensions. *Atmosphere and Ocean Optics*, 2004, **17**, P. 468–475.

Mechanisms of energy-efficient magnetization switching in a bistable nanowire

M. H. A. Badarneh¹, G. J. Kwiatkowski¹, P. F. Bessarab^{1,2,3}

¹Science Institute, University of Iceland, 107 Reykjavík, Iceland

²ITMO University, 197101 St. Petersburg, Russia

³Peter Grünberg Institute and Institute for Advanced Simulation,
Forschungszentrum Jülich, 52425 Jülich, Germany

bessarab@hi.is

PACS 62.23.Hj, 75.10.Dg, 75.30.Ds

DOI 10.17586/2220-8054-2020-11-3-294-300

Theoretical calculations of optimal control paths minimizing the energy cost of the magnetization reversal in 1D magnetic nanowires are presented. The energy-efficient reversal mechanism is studied as a function of the nanowire length and Gilbert damping parameter. For short nanowires, the optimal reversal mechanism corresponds to a uniform rotation of magnetization. If the length of the wire exceeds a certain critical length defined by the material parameters, switching time and damping, a standing spin wave emerges during magnetization switching. Comparison between the calculated optimal control paths and minimum energy paths reveals that realization of high energy efficiency of switching does not necessarily translate to the minimization of the energy barrier between the target magnetic states.

Keywords: magnetic nanowire, magnetization switching, optimal control.

Received: 8 May 2020

1. Introduction

Magnetic nanowires are characterized by an extended length and a nanoscale lateral size [1]. The high length-to-width aspect ratio gives rise to large magnetic anisotropy, which usually results in two stable orientations of magnetization along the wire's axis. Bistability makes magnetic nanowires particularly promising as a basis of novel devices for data transmission, storage and processing where information can be encoded by domains with opposite magnetization [2]. Development of this technology depends critically on the knowledge about mechanisms of the magnetization reversal – a physical implementation of a bit operation. How reversal modes depend on the switching stimulus, magnetic parameters and geometry of the wire is also interesting from a fundamental point of view. Previous theoretical [3–9] and experimental [10–14] studies revealed three main mechanisms of magnetization switching in nanowires, including homogeneous rotation of magnetization and propagation of transverse and vortex domain walls. The possibility to achieve magnetization switching by following different transition mechanisms leads to a notion about the existence of a special mechanism that is optimal in terms of the termination time and energy cost. Definite identification of such optimal reversal mechanisms is particularly important for the development of energy-efficient information technologies based on magnetic nanowires.

In this article, we describe the application of the optimal control theory [15, 16] to the problem of energy-efficient magnetization reversal in a 1D magnetic nanowire. The theory makes it possible to identify optimal control paths (OCPs), i.e. reversal trajectories minimizing the energy cost of magnetization switching. We present numerical calculations of OCPs for various values of the nanowire length and Gilbert damping parameter. We report a crossover between the coherent rotation of magnetization and spin wave assisted switching. Finally, we compare calculated OCPs with the other distinguished paths in the configuration space – the minimum energy paths (MEPs).

The article is organized as follows. In Section 2, theoretical background and details of numerical calculations are described. Results of applications of the optimal control method are given in Section 3. A single macrospin test system is considered first. Then, the application to the magnetization reversal in a nanowire is described. Comparison between calculated OCPs and MEPs is also given. Summary and outlook are presented in Section 4.

2. Methods

Magnetic nanowire is modeled as a 1D chain of N magnetic moments extending along the x axis, where each moment has the same magnitude μ . The energy of the wire is given by a classical Heisenberg-type Hamiltonian:

$$E = -J \sum_{i=1}^{N-1} \vec{s}_i \cdot \vec{s}_{i+1} - K \sum_{i=1}^N (\vec{s}_i \cdot \vec{e}^x)^2, \quad (1)$$

where \vec{s}_i is the unit vector defining the orientation of the magnetic moment at site i . The first term in Eq. (1) describes the exchange interaction between nearest neighbours with ferromagnetic coupling constant $J > 0$. The second term is due to magnetic uniaxial anisotropy characterized by the easy axis \vec{e}^x along the wire and effective parameter $K > 0$. Due to the anisotropy, there are two stable states in the system with moments aligned parallel or antiparallel to the x axis, as illustrated in Fig. 1. The following values of the material parameters are used:

$$J = 562 \text{ meV}, \quad (2)$$

$$K = 37 \text{ meV}, \quad (3)$$

$$\mu = 4076 \mu_B, \quad (4)$$

where μ_B is Bohr magneton.

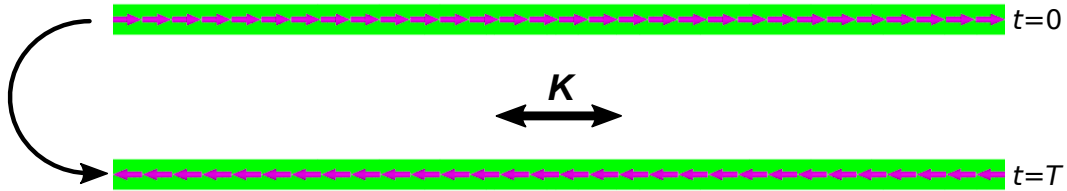


FIG. 1. Stable orientations of the magnetization in a nanowire. The nanowire is represented by a chain of $N = 30$ magnetic moments. Arrows indicate orientation of the moments. Direction of the anisotropy axis is shown with the double-headed arrow. Transition between the states is schematically shown with the black arrow. In the OCP, the initial state is realized at $t = 0$, while the final state is realized at $t = T$

We consider energy-efficient switching of magnetization in the wire from one stable orientation to the other. The switching process is induced by application of external magnetic field. The aim is to find the optimal field that realizes switching in a given time T while minimizing the energy cost. Following Refs. [15, 16], we define the energy cost to be proportional to the amplitude of the applied magnetic field squared:

$$\Phi = \int_0^T \sum_{j=1}^N |\vec{B}_j(t)|^2 dt, \quad (5)$$

where $\vec{B}_j(t)$ is the applied magnetic field at site j and time t . Summation over the sites where magnetic moments are localized is equivalent to spatial integration for a continuous system. The functional Φ needs to be minimized subject to the boundary conditions

$$s_j^x(t=0) = 1, \quad j = 1, \dots, N, \quad (6)$$

$$s_j^x(t=T) = -1, \quad j = 1, \dots, N, \quad (7)$$

and an equation of motion which is taken to be the Landau-Lifshitz-Gilbert equation:

$$(1 + \alpha^2) \dot{\vec{s}}_j = -\gamma \vec{s}_j \times (\vec{B}_{\text{int},j} + \vec{B}_j) - \alpha \gamma \vec{s}_j \times [\vec{s}_j \times (\vec{B}_{\text{int},j} + \vec{B}_j)], \quad (8)$$

where α is the Gilbert damping factor, γ is the gyromagnetic ratio, dot means time derivative and $\vec{B}_{\text{int},j}$ is the internal magnetic field defined through the following equation:

$$\vec{B}_{\text{int},j} = -\frac{1}{\mu} \frac{\partial E}{\partial \vec{s}_j}, \quad (9)$$

with internal energy E given by Eq. (1). Equation (8) can be used to express $\vec{B}_j(t)$ in terms of the dynamical trajectory of the system as well as the magnetic field [16]:

$$\vec{B}_j(t) = \frac{\alpha}{\gamma} \dot{\vec{s}}_j(t) + \frac{1}{\gamma} [\vec{s}_j(t) \times \dot{\vec{s}}_j(t)] - \vec{B}_{\text{int},j}^\perp(t). \quad (10)$$

Here, $\vec{B}_{\text{int},j}^\perp(t)$ is a transverse component of $\vec{B}_{\text{int},j}$:

$$\vec{B}_{\text{int},j}^\perp = \vec{B}_{\text{int},j} - (\vec{B}_{\text{int},j} \cdot \vec{s}_j) \vec{s}_j. \quad (11)$$

Upon substituting Eqs.(10)-(11) into Eq. (5), the energy cost Φ becomes a functional of $\vec{s}_1(t), \vec{s}_2(t), \dots, \vec{s}_N(t)$. Before applying the variational principle to the functional Φ , we discretize the time integral in Eq. (5) using the midpoint rule:

$$\Phi[\vec{s}_1(t), \dots, \vec{s}_N(t)] \approx \Phi(\mathbf{s}) = \sum_{p=0}^Q \sum_{j=1}^N B_{p+\frac{1}{2},j}^2 (t_{p+1} - t_p), \quad (12)$$

where $\{t_p\}$ is a partition of the time interval $[0, T]$ such that $0 = t_0 < t_1 < \dots < t_Q < t_{Q+1} = T$. In the current implementation, all time subintervals are the same, $t_{p+1} - t_p = \Delta t = T/(Q+1)$, $p = 0, \dots, Q$. Trajectory of each magnetic moment, $\vec{s}_j(t)$, is then represented by a polygeodesic line connecting $Q+2$ images, $\vec{s}_j(t): \{\vec{s}_{0,j}, \dots, \vec{s}_{Q+1,j}\}$, with $\vec{s}_{p,j} = \vec{s}_j(t_p)$, where the end points are fixed according to the boundary conditions [see Eqs. (6)-(7)], but Q intermediate images need to be adjusted to an optimal configuration representing the minimum of Φ . The functional Φ is turned into a $3QN$ -dimensional function of image positions, $\Phi = \Phi(\mathbf{s})$, with $\mathbf{s} = \{\vec{s}_{1,1}, \vec{s}_{1,2}, \dots, \vec{s}_{1,N}, \vec{s}_{2,1}, \dots, \vec{s}_{Q,N}\}$. The sought-for optimal control path (OCP) minimizing the energy cost of switching is found by choosing some initial guess for the position of the images and then bringing that to a local minimum of $\Phi(\mathbf{s})$ by means of the (limited-memory) Broyden-Fletcher-Goldfarb-Shanno algorithm [17] adapted to magnetic degrees of freedom [18, 19]. The final, relaxed configuration of the images gives a discrete representation of the OCP. The optimal external field pulse is then obtained from the OCP using Eq. (10).

3. Results and discussion

3.1. Test problem

The numerical method described earlier is first illustrated with calculations of the OCP for the reversal of a single magnetic moment whose internal energy is defined by the anisotropy along z axis,

$$E_1 = -K (\vec{s} \cdot \vec{e}^z)^2. \quad (13)$$

The value of the anisotropy constant K is defined in Eq. (3). The OCP between the energy minima at $s^z = \pm 1$ for this system can be obtained analytically in terms of elliptic functions [16], providing a benchmark for numerical calculations. Discrete representations of the OCP were obtained numerically by relaxing Q movable images to a local minimum of the energy cost Φ . The calculations were considered converged when the magnitude of the gradient of Φ had dropped by twelve orders of magnitude.

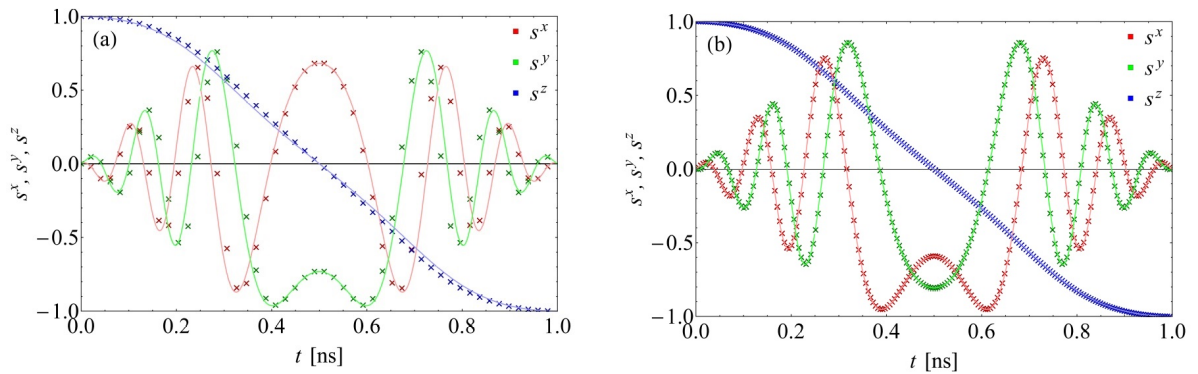


FIG. 2. Evolution of the magnetic moment along the OCP for switching time $T = 1$ ns and damping parameter $\alpha = 0.1$. Analytical solution is given by solid lines, position of images included in the numerical calculations is shown with crosses. $Q = 50$ (a) and $Q = 200$ (b) movable images were used in the numerical OCP calculations

Figure 2 shows comparison between the analytical solution and numerical results obtained for $Q = 50$ and $Q = 200$ images. Both analytical and numerical calculations were performed for $\alpha = 0.1$ and $T = 1$ ns. Agreement between the analytical and numerical results is better for larger number of images, as expected. We have found that using $Q \approx 200$ movable images in the OCP calculations was sufficient to ensure relative error to be below 1%.

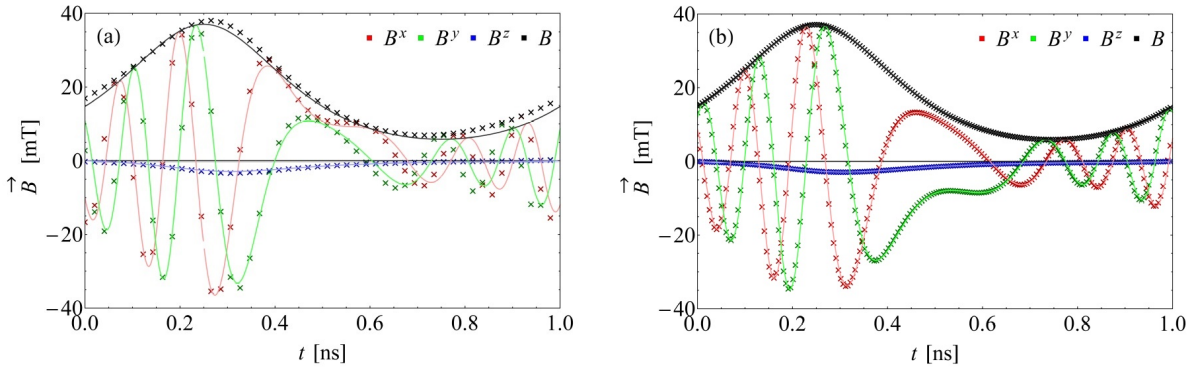


FIG. 3. Optimal switching field derived from the OCP shown in Fig. 2. Switching time $T = 1$ ns and damping parameter $\alpha = 0.1$. Analytical solution is given by solid lines, crosses correspond to position of images included in the numerical OCP calculations. $Q = 50$ (a) and $Q = 200$ (b) movable images were used in the OCP calculations

The calculated OCP describes a steady motion of the magnetic moment from the initial state at $s^z = 1$ to the final state at $s^z = -1$. The monotonic decrease in s^z is accompanied by a precessional motion around the anisotropy axis. Note that the precession reverses its direction upon reaching the top of the energy barrier at $t = T/2$. Fig. 3 shows how the optimal switching field derived from the OCP depends on time. Direction of the calculated optimal field is synchronized with the motion of the magnetic moment so that it is orthogonal to \vec{s} at any time. Moreover, $\vec{B}(t)$ is modulated in amplitude. The internal torque arising due to damping counteracts the switching motion before crossing the energy barrier. Therefore, overall larger field needs to be applied in the first half of the reversal process compared to that in the second half, where the damping torque aids switching. A careful analysis demonstrates that $B(t)$ reaches a maximum at $t = T/4$ and a minimum at $t = 3T/4$, which coincides with the position of the extrema of the polar component of the internal torque.

3.2. Magnetization switching in a nanowire

Fig. 4 illustrates mechanisms of energy efficient magnetization reversal in the nanowire revealed by the OCP calculations. Possible mechanisms include uniform rotation of magnetization [see Fig. 4(a)] and emergence of a standing spin wave with variable wavelength [see Fig. 4(b,c)]. In the case of the coherent rotation mechanism, each magnetic moment in the wire follows the same trajectory presented in the previous subsection.

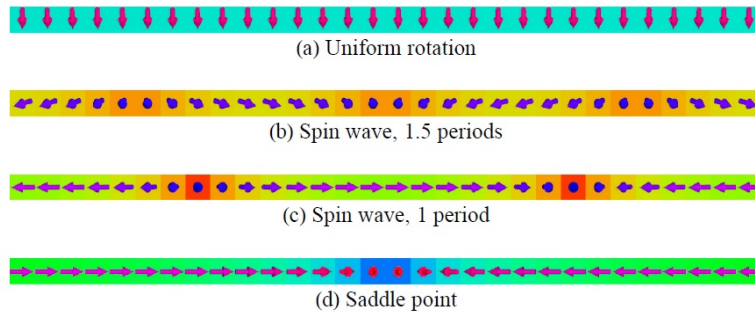


FIG. 4. Magnetic configurations realized along OCPs (a)-(c) and MEP (d) for magnetization switching in the nanowire of length $N = 30$. For the OCPs, configurations at $t = T/2$ are shown where $T = 1$ ns. For the MEP, the saddle point configuration is presented. OCP corresponds to a coherent rotation of magnetic moments for $\alpha = 0.1$ (a) and to spin wave assisted switching with 1.5 wave periods for $\alpha = 0.5$ (b) and with 1 wave period for $\alpha = 0.6$ (c). MEP corresponds to a transient domain wall nucleation and propagation (d)

How the result of the OCP calculations depend on the parameters of the nanowire is illustrated in Fig. 5. Specifically, Fig. 5(a) shows the calculated energy cost Φ of optimal switching as a function of the length N of the wire for the fixed values of the switching time and damping factor with $T = 1$ ns and $\alpha = 0.4$. For relatively short nanowires, Φ

scales linearly with the wire length which is a consequence of the uniform rotation of the magnetization. At $N \approx 60$, a salient point is evident in the $\Phi(N)$ dependence as a result of the crossover to spin-wave assisted switching. As the number of magnetic moments in the wire increases, progressively more periods of the spin wave is observed. Note that the number of the spin-wave periods can assume both half-integer and integer values [see Fig. 4(b,c)].

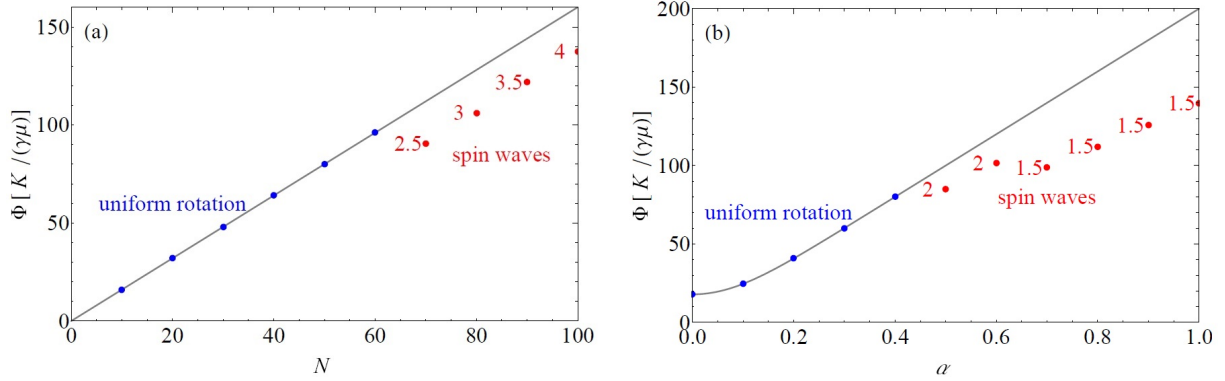


FIG. 5. Minimum energy cost of magnetization switching as a function of the nanowire length N for $\alpha = 0.4$ and $T = 1$ ns (a) and damping parameter α for $N = 50$ and $T = 1$ ns (b). Uniform rotation and spin wave solutions are shown with blue and red circles, respectively. Red labels indicate the number of wavelengths in the spin-wave solutions. Solution for the macrospin approximation is shown with a gray line

Interestingly, the mechanism of the energy-efficient magnetization switching depends on the damping parameter, as illustrated in Fig. 5(b) showing Φ as a function of α for $N = 50$ and $T = 1$ ns. When $\alpha \leq 0.4$, the optimal switching mechanism corresponds to the uniform rotation of magnetization and $\Phi(\alpha)$ follows the dependence predicted in Ref. [16]. As the damping factor increases, the switching mechanism changes to the spin-wave, first with 2 periods and then with 1.5 periods. Each crossover event is accompanied by a sharp change in the slope of the $\Phi(\alpha)$ function.

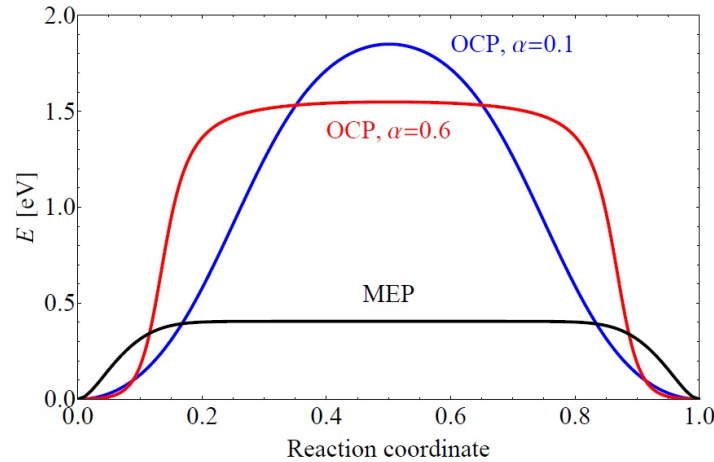


FIG. 6. Variation of the energy of the nanowire with $N = 50$ along the MEP (black line) and the OCP for $T = 1$ ns, $\alpha = 0.1$ (blue line) and $\alpha = 0.6$ (red line). Reaction coordinate is defined as a normalized displacement along the path

It is informative to compare the calculated OCPs with the other distinguished paths in the configuration space – minimum energy paths (MEPs). An MEP connecting two stable states is a path lying lowermost on the energy surface, and the point of the highest energy along the MEP – a saddle point on the energy surface – defines the energy barrier between the states, the primary quantity determining their thermal stability within harmonic rate theories [20–22]. The MEPs for the magnetization reversal in the nanowires considered here were calculated using the geodesic nudged elastic band method [23]. The MEP changes from the uniform rotation to the nucleation and propagation of a transient

domain wall when the length of the wire exceeds the domain wall width. The saddle-point configuration for the nanowire with $N = 30$ is shown in Fig. 4(d) as an example. These paths are very different from the calculated OCPs. In fact, the OCP calculations have never converged on the path corresponding to the single domain wall propagation, even if the initial guess was set to be the MEP. Note that an MEP is completely defined by the energy surface of the system, and, therefore, is independent of dynamical properties such as the switching time or damping parameter. In contrast, an OCP is a valid dynamical trajectory, which in particular results in that the mechanism of energy-efficient magnetization reversal depends on α , as demonstrated above.

Finally, the energy variations along the calculated MEP and OCPs are compared in Fig. 6 for the nanowire with $N = 50$. The energy profile along the MEP is flat, which is a typical feature for the domain wall propagation costing almost no energy. The energy barrier derived from the MEP is much smaller than the highest energy point along the OCPs. This result suggests a conclusion that optimal control of magnetization switching which minimizes the energy cost does not necessarily translates into the minimization of the energy barrier between the target states. Following an OCP involves rotation of magnetic moments in such a way that the influence of the external stimulus is minimized, but the system's internal dynamics is effectively used to aid magnetization switching.

4. Conclusion

In conclusion, we have studied energy-efficient magnetization reversal in bistable magnetic nanowires by means of OCP calculations. The calculations demonstrate that short nanowires reverse their magnetization via coherent rotation that combines a steady advancement toward the target state and precession around the anisotropy axis. If the length of the wire exceeds a certain critical length, a standing spin wave emerges during magnetization switching. In contrast to MEPs, OCPs demonstrate dependence on dynamical parameters such as switching time and damping. Our results deepen the understanding of the optimal control of magnetization switching in nanowires.

Acknowledgements

The authors would like to thank T. Sigurjónsdóttir for helpful discussions. This work was funded by the Russian Science Foundation (Grant No. 19-72-10138), the Icelandic Research Fund (Grant No. 184949-052), and the Alexander von Humboldt Foundation.

References

- [1] Staño M., Fruchart O. Magnetic nanowires and nanotubes. In *Handbook of Magnetic Materials*, vol. 27, ed. Brück E. Elsevier, Amsterdam., 2018, P. 155–267.
- [2] Parkin S. S. P., Hayashi M. Thomas L. Magnetic domain-wall racetrack memory. *Science*, 2008, **320**(5873), P. 190–194.
- [3] Hinzke D., Nowak U. Magnetization switching in nanowires: Monte Carlo study with fast Fourier transformation for dipolar fields. *Journal of Magnetism and Magnetic Materials*, 2000, **221**, P. 365–372.
- [4] Hertel R., Kirschner J. Magnetization reversal dynamics in nickel nanowires. *Physica B*, 2004, **343**, P. 206–210.
- [5] Allende S., Altbir D., Salcedo E., Bahiana M., Sinnecker J. P. Propagation of transverse domain walls in homogeneous magnetic nanowires. *Journal of Applied Physics*, 2008, **104**, P. 013907.
- [6] Ivanov Yu. P., Vázquez M., Chubykalo-Fesenko O. Magnetic reversal modes in cylindrical nanowires. *Journal of Physics D: Applied Physics*, 2013, **46**, P. 485001.
- [7] Goussev A., Lund R. G., Robbins J. M., Slastikov V., Sonnenberg C. Domain wall motion in magnetic nanowires: an asymptotic approach. *Proceedings of the Royal Society A*, 2013, **469**, P. 20130308.
- [8] Sultan M. S., Atkinson D. Aspect-ratio dependence of magnetization reversal in cylindrical ferromagnetic nanowires. *Materials Research Express*, 2016, **3**, P. 056104.
- [9] Kuncser A., Antohe S., Kuncser, V. A general perspective on the magnetization reversal in cylindrical soft magnetic nanowires with dominant shape anisotropy. *Journal of Magnetism and Magnetic Materials*, 2017, **423**, P. 34–38.
- [10] Endo Y., Fujimoto H., Kumano S., Matsumura Y., Sasaki I., Kawamura Y., Yamamoto M., Nakatani R. Study on the magnetization reversal process in a magnetic nanowire and a magnetic dot observed by magnetic field sweeping magnetic force microscopy measurements. *Journal of Applied Physics*, 2008, **103**, P. 07D918.
- [11] Lavín R., Denardin J. C., Escrib J., Altbir D., Cortés A., Gómez H. Angular dependence of magnetic properties in Ni nanowire arrays. *Journal of Applied Physics*, 2009, **106**, P. 103903.
- [12] Vivas L. G., Vazquez M., Escrib J., Allende S., Altbir D., Leitao D. C., Araujo J. P. Magnetic anisotropy in CoNi nanowire arrays: Analytical calculations and experiments. *Physical Review B*, 2012, **85**, P. 035439.
- [13] García J., Prida V. M., Vivas L. G., Hernando B., Barriga-Castro E. D., Mendoza-Reséndez R., Luna C., Escrib J., Vázquez M. Magnetization reversal dependence on effective magnetic anisotropy in electroplated Co-Cu nanowire arrays. *Journal of Materials Chemistry C*, 2015, **3**, P. 4688.
- [14] Sultan M. S. Angular dependence of switching behaviour in template released isolated NiFe nanowires. *Physics Letters A*, 2017, **381**, P. 3896–3903.
- [15] Barros N., Rassam M., Jirari H., Kachkachi H. Optimal switching of a nanomagnet assisted by microwaves. *Physical Review B*, 2011, **83**, P. 144418.

- [16] Kwiatkowski G. J., Badarneh M. H. A., Berkov D. V., Bessarab P. F. Optimal control of magnetization reversal in a monodomain particle by means of applied magnetic field, 2020. arXiv: <https://arxiv.org/abs/2004.02146>.
- [17] Nocedal J., Wright S. J. *Numerical Optimization* (2nd ed.). Springer, New York, 2006.
- [18] Ivanov A. V., Uzdin V. M., Jónsson H. Fast and robust algorithm for the energy minimization of spin systems applied in an analysis of high temperature spin configurations in terms of skyrmion density, 2019. arXiv: <https://arxiv.org/abs/1904.02669>.
- [19] Ivanov A. V., Dagbjartsson D., Tranchida J., Uzdin V. M., Jónsson H. Efficient optimization method for finding minimum energy paths of magnetic transitions. *Journal of Physics: Condensed Matter*, 2020. *Accepted manuscript*. URL: <https://doi.org/10.1088/1361-648X/ab8b9c>.
- [20] Kramers H. Brownian motion in a field of force and the diffusion model of chemical reactions. *Physica*. 1940. **7**. P. 284–304.
- [21] Vineyard G. H. Frequency factors and isotope effects in solid state rate processes. *Journal of Physics and Chemistry of Solids*, 1957, **3**, P. 121–127.
- [22] W. F. Brown W. F. Thermal fluctuation of fine ferromagnetic particles. *IEEE Transactions on Magnetics*, 1979, **MAG-15**, P. 1196–1208.
- [23] Bessarab P. F., Uzdin V. M., Jónsson H. Method for finding mechanism and activation energy of magnetic transitions, applied to skyrmion and antivortex annihilation. *Computer Physics Communications*, 2015, **196**, P. 335–347.

Negative differential resistance in gate all-around spin field effect transistors

G. F. A. Malik¹, M. A. Kharadi¹, F. A. Khanday^{1,*}, K. A. Shah², N. Parveen³

¹Department of Electronics and Instrumentation Technology, University of Kashmir, Srinagar-190006, India

²Department of Physics, S. P. College, Cluster University Srinagar, M. A. Road Srinagar-190001, India

³Islamia College of Science and Commerce, Srinagar, J&K, India

Gfarozam@gmail.com, kharadimubashir@gmail.com,

*farooqkhanday@kashmiruniversity.ac.in, drkhursheda@gmail.com

PACS 73.50.Dn, 75.80.+q, 85

DOI 10.17586/2220-8054-2020-11-3-301-306

In this paper, novel gate all-around spin field effect transistors (GAA Spin-FETs) with three different channel materials are proposed and their transport properties are presented. The three channel materials used are Indium Arsenide (InAs), Indium Phosphide (InP) and Aluminum Antimonide (AlSb). Based on the type of semiconducting channel, the results are obtained and a comparison of transport properties among these three FETs is made. The proposed device offers both advantages of reduced power dissipation and compact size. The results reveal that the negative differential resistance (NDR) is observed in all modeled devices and the peak to valley current ratio (PVCR) is different in all structures and is maximum in AlSb based field effect transistor. It is expected that these results will find enormous applications in analog electronics and in the design of oscillators. Additionally, the observed results in this study have great potential for the design of various logic gates and digital circuits.

Keywords: Spin-FET, gate all-around spin field effect transistors, multi-gate FETs, NDR, datta-das transistor.

Received: 12 April 2020

Revised: 19 April 2020

1. Introduction

Spin-based devices promise to be a technology of beyond-CMOS computing [1]. Various spin devices have also been proposed and studied for various applications, such as two-terminal giant magnetoresistance (GMR) and tunneling magneto-resistance devices (TMR), which find applications in designing non-volatile spin based RAMs called STT-RAM (spin transfer torque random access memory) [2]. Spin field effect transistor (Spin-FET) is believed to be a better device than conventional semiconductor field effect transistor devices due to its exceptional properties, such as control of conductivity using spin degree of freedom [3]. Owing to less energy required for control of spin, Spin-FET is well suited for low-power applications, and hence, can resolve the power issues of conventional transistors [4]. Spin-FET was proposed by S. Datta and B. Das in the year 1990 and has appeared as one among the mostly researched device for various applications [5]. Spin-FET differs from the conventional MOSFET in structure, as the conventional MOSFET has semiconductor material-based source and drain terminals, while spin-FET has ferromagnetic material based source and drain electrodes [5]. Since there are various ferromagnetic materials like iron, cobalt and nickel, thus there is a choice of using the material of desired magnetic properties for a particular device [6].

The spin-FET works on the principle similar to that of conventional MOSFET, with the difference being that spin-FET only allows the electrons with one desired polarization and rejecting all other electrons with other polarizations [7]. The main function of using ferromagnetic source is to spin polarize the source current, the gate voltage rotates the orientation of the injected spins in the current by an angle that depends on the gate voltage (because of the Rashba effect induced by the gate voltage in the channel) [8]. The drain acts as a filter that preferentially transmits spin of one polarization and blocks spins of the opposite polarization [9], [10]. The added advantage in the proposed device is that gate all-around structure is used, and has the better control over the flow of electrons through the channel [11].

Various types of gate all-around field effect transistors (GAA-FETs) have been studied in the open literature over the past several years [12–16]. For example, in 2016, the negative differential resistance (NDR) was obtained in a boron nitrogen co-doped axial carbon nanotube field effect transistor [12], whereas NDR is observed in a molecular junction of carbon nanotube and benzene [13]. In 2012, R. Grassi et al [14], exploited NDR in monolayer graphene FETs for high voltage gains and in 2013 A. Sengupta et al [15], reported negative differential resistance behavior in MoS₂ armchair nanoribbon MOSFETs. Moreover, Y. Wu et al [16], have experimentally demonstrated prototypes of novel three-terminal graphene NDR device and provided an analytic model to elucidate such NDR behavior.

Compared to the devices presented in [12–16], where the different materials and methods are used which may not be compatible with existing technology, the most important advantage of our proposed device is that it has no compatibility issue with the existing silicon technology. In addition, its fabrication process is also feasible. The

proposed device is simply an addition of a gate stack to the magnetic tunnel junction (MTJ). In recent years MTJs have been commercially fabricated, thus this advantage can be exploited which makes the proposed device more feasible to be fabricated. Later the channel materials have been changed from InAs to InP to AlSb.

A total of 14 molecules were used for semiconducting channel materials. The value of the lattice constants for the Indium Arsenide (InAs), Indium Phosphide (InP) and Aluminium Antimonide (AlSb) are 0.60 nm, 0.58 nm and 0.61 nm respectively. Hence the channel length is determined to be approximately 20 nm. The channel material length affects the performance of GAA Spin-FET. In order to accommodate a greater number of devices on a single chip, the channel length is scaled down, which reduces the device dimensions. However, the decrease in channel length leads to deterioration of the performance and causes second order short channel effects. Thus, in order to have sufficiently large number of devices on a single chip as well as satisfactory performance, the channel length is chosen in mid-range i.e., 20 nm.

In this paper, the gate all-around spin-FET is proposed and analyzed for the first time as per the authors' best knowledge. The source and drain terminals are made of cobalt, which is a ferromagnetic material. The three employed channel materials are InAs, GaAs and AlSb, as they have the potential to be used in spin-FETs. A layer of dielectric material of dielectric constant 4 is employed on the channel over which a metallic layer is made. The effects in IV-curves and conductance curves with channel materials are presented. One of the important characteristics of the modeled devices is that, they show negative differential resistance, which finds immense applications in analog electronics like high-frequency oscillators etc. Although various spin-FET devices have been reported varying in channel material as well as drain/source material, but as per authors' best knowledge, this type of spin-FET i.e., gate all around with InAs/InP/AlSb channel based spin-FETs has been studied for the first time in this paper.

The paper has been organized as: Section 2 introduces the model and methods applied for the proposed device. Section 3 introduces the simulation results and discussion. The paper is concluded in Section 4.

2. Models and methods

In this paper, a gate all-around spin field effect transistor (GAA-SF) is introduced. Since the drain and source regions of a Spin-FET are of ferromagnetic material, here we have used cobalt (which is a ferromagnetic material) for drain and source. The channel materials used in the proposed device are the compound semiconductors, viz., InAs, InP and AlSb. The dielectric material of dielectric constant $K=4$ (SiO_2) is used to insulate channel from the gate terminal. The gate terminal surrounds the channel from all the sides and forms a cylindrical gate-all around or co-axial structure as shown in Fig. 1(a) (front view without gate and dielectric material), Fig. 1(b) (cross-sectional view) and Fig. 1(c) (3D-view). The main advantage of using the gate all-around structure is symmetry along an axis is achieved, which in turn simplifies the calculations of electronic transport, and in turn, permits the self-consistent electrostatics. The proposed device has been simulated using Quantum Atomistic Tool Kit Software (version 13.8.1) [17, 18]. After building the device, it has been simulated using Extended Huckel Theory (EHT) combined with non-equilibrium Green's function (NEGF) for the calculations of transport. The temperature of electrodes has been set to 300 K. The set of k -points were selected as $1 \times 1 \times 100$ in addition of having density mesh cut-off of 100 Hartree.

3. Simulation results

Since the device formed is due to the combination of materials having different bandgaps, consequently, a quantum well is formed. Due to this, the motion of electrons is restricted in one direction, and in such devices, within the well, a parallel transport is observed. When electrons cross the barrier (potential barrier formed due to the formation of quantum well), other transport known as perpendicular transport is observed. The perpendicular transport is a quantum mechanical phenomena due to which the negative differential resistance is observed. The proposed device has been simulated using Quantum Atomistic Tool Kit Software (version 13.8.1). The behavior of the devices is analyzed by plotting IV-curve and conductance curves for InAs, InP and AlSb based transistors. For InAs based Spin-FET, the IV and conductance curves are shown in Fig. 2(a) and Fig. 2(b) respectively, whereas for InP based Spin-FET, the IV and conductance curves are shown in Fig. 3(a) and Fig. 3(b) respectively. Fig. 4(a) and Fig. 4(b) shows the IV and conductance curves for AlSb based Spin-FET respectively.

From the simulation results, it is clear that all the devices show negative differential resistance (NDR), but it can also be seen that the behavior is different while the channel material is varied from InAs to AlSb while keeping the electrodes (drain and source), oxide, gate and structure the same. It happens because of the fact the materials used for channel differ in structure and have different forbidden energy gaps. For InAs, the bandgap is approximately 0.420 eV while if we take the case of InP, the bandgap is approximately 1.421 eV and for AlSb, it is approximately 1.6 eV at 300 K temperature. Since the NDR is caused due to the band to band tunneling (BTBT) [12] and hence, it is clear that the resistance will vary as the bandgap varies.

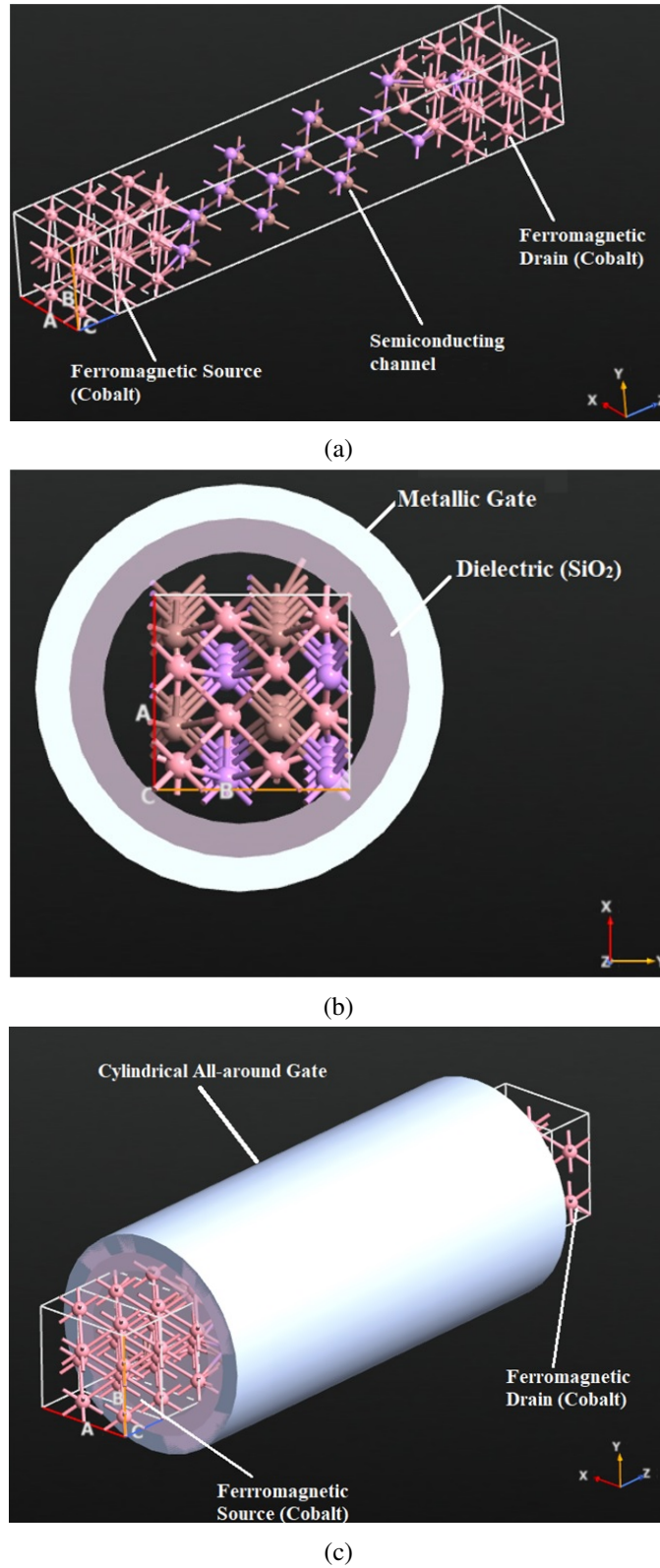


FIG. 1. (a) View of proposed device without dielectric and gate material in order to show the channel region, (b) Cross-sectional view of gate all-around spin field effect transistor (GAA Spin-FET), (c) Three dimensional (3D) view of gate all-around spin field effect transistor (GAA Spin-FET)

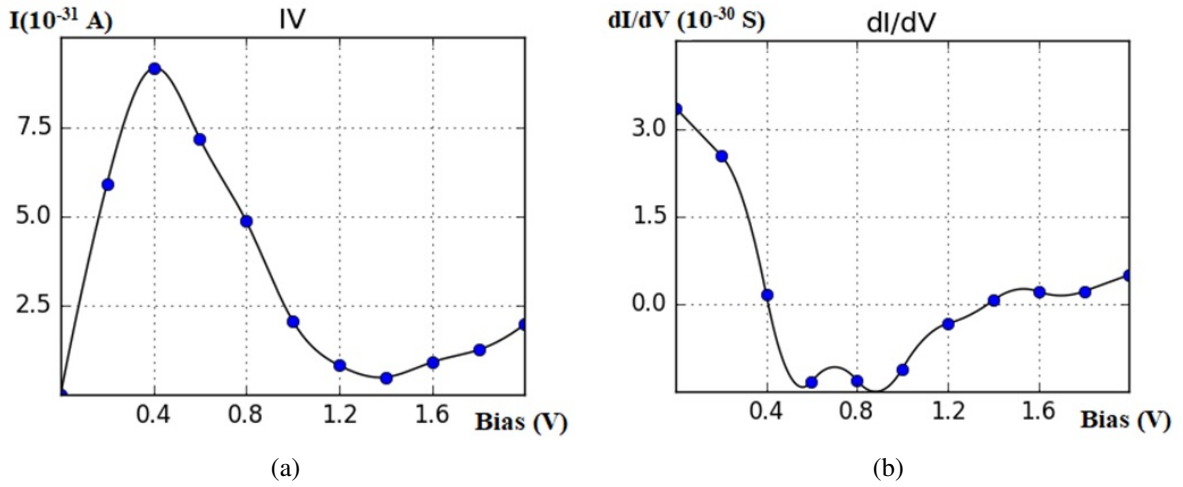


FIG. 2. (a) IV-curve for GAA Spin-FET with InAs as channel material. (b) Conductance curve for GAA Spin-FET with InAs as channel material

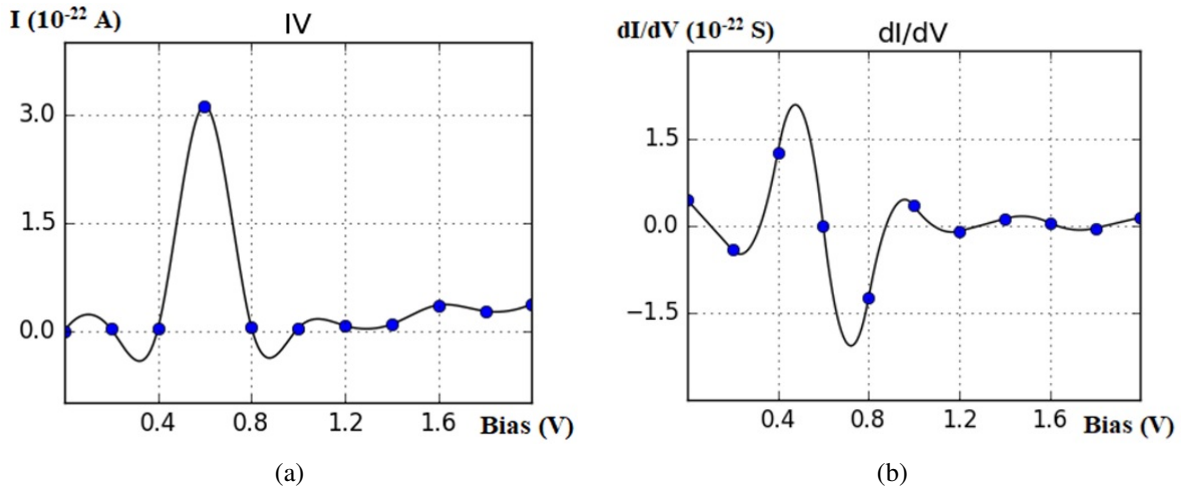


FIG. 3. (a) IV-curve for GAA Spin-FET with InP as channel material. (b) Conductance curve for GAA Spin-FET with InP as channel material

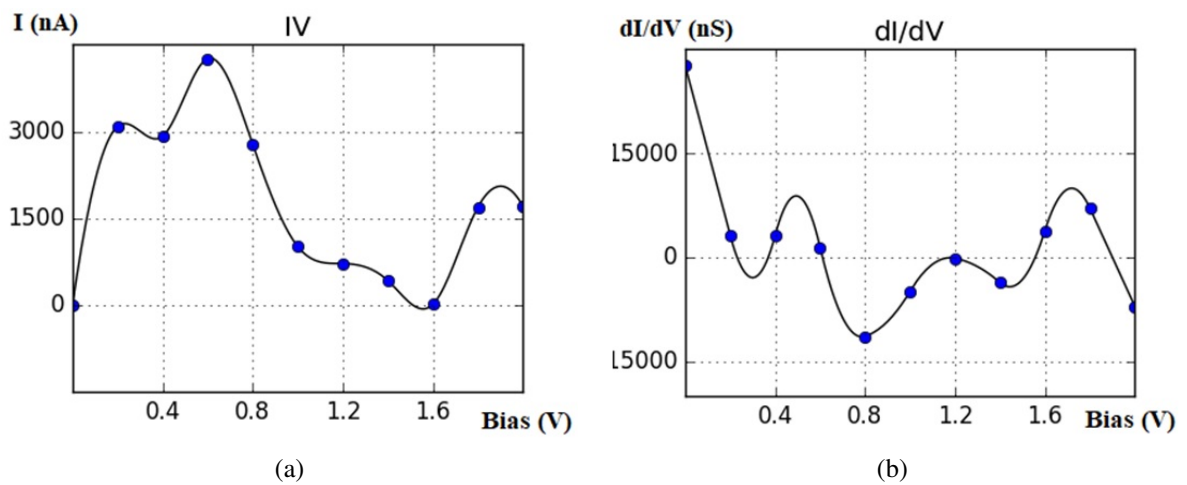


FIG. 4. (a) IV-curve for GAA Spin-FET with AISb as channel material. (b) Conductance curve for GAA Spin-FET with AISb as channel material

In the proposed device, spin-current is evaluated in all the three different channel materials and current comes out to be in the order of $10e-31$ A for InAs, $10e-22$ for InP and in nA for AlSb. The changes occurred have been explained based on different bandgaps of different channel materials. However, there are several other reasons responsible for the change in current. These include spin polarization, spin detection, spin-precession and spin-relaxation. Since the source and drain material is same in all the three cases viz., cobalt (a ferromagnetic material) thus, spin polarization and spin detection will be same. However, the spin precession takes place in channel region. As the electrons of specified spin polarization move through the channel region, the spin changes without applying any voltage at the gate terminal, there exists some magnetic field like Dresselhaus field inside the channel, due to which, spin precession occurs and spin-current reduces. Furthermore, there occur various spin relaxations inside the channel of spin-FET like DP (D'yakonov Perel) relaxation, BAP (Bir-Aronov-Pikus) relaxation or EY (Elliott-Yafet) relaxation and superfine interaction which contributes to the drastic changes in spin currents in case of different channel materials [19–24].

In the case of InAs based Spin-FET, the region of NDR is wide and hence have potential applications in analog electronics, but at the same time, the magnitude of the current is very low (refer Fig. 3(a)). However, if we take the case of InP based Spin-FET, the region of NDR is not as wide as in the case of InAs, but the magnitude of current improves to a larger extent (Refer Fig. 4(a)). Similarly, in AlSb based Spin-FET, the region of NDR is narrower as compared to the InAs based Spin-FET and InP based Spin-FET, but the magnitude of current is high, and hence, the problems of current drive cannot be faced in the Spin-FET with AlSb as channel material. Since InAs and InP are direct bandgap semiconductors, while AlSb is an indirect bandgap semiconductor, the effect of which can be observed from the ripples produced in IV curves, viz., less in InAs and InP while more in AlSb based Spin-FETs. The table for peak to valley current ratio (PVCR) is given in Table 1. From Table 1, it is clear that PVCR is maximum for GAA Spin-FET having AlSb channel material and minimum for InAs based GAA Spin-FET.

TABLE 1. Calculated PVCR of different channel material based GAA-SFETs

	I (for InAs Spin-FET)	I (for InP Spin-FET)	I (for AlSb Spin-FET)
PVCR	9	30	40

4. Conclusions

In this study, the transport properties of proposed gate all-around spin field effect transistors were studied with comparative studies. The I-V and conduction curves show that the proposed device with different channel materials can exhibit negative differential resistance (NDR). The NDR is attained in the proposed device due to the tunneling mechanism caused by the perpendicular transport in heterostructure formed by combination of materials with different bandgap. In addition, the nature of the channel material changes the I-V and conductance curves. The employed channel materials are indium arsenide (InAs), indium phosphide (InP) and aluminum antimonide (AlSb) which differs in forbidden energy gap at 300 K and also vary in structure. The simulated models therefore can find massive uses in analog electronics and specifically in the design of oscillators. Additionally, it has the remarkable potential in designing various logic gates and digital circuits as the size is in the nanoscale regime. Furthermore, the proposed spin-device will address the power issues, which is the main concern in the contemporary world, and at the same time can work in nanoscale-regime, thereby offering increase in chip density, functionality and decreased power consumption.

Acknowledgements

The authors would like to thank Science and Engineering Research Board (SERB), Department of Science and Technology (DST), Government of India for supporting this work, under the Extra Mural Research (EMR) scheme (EMR/2016/007125 and EMR/002866/2017).

References

- [1] Friedman J.S., Rangaraju N., Ismail Y.I. and Wessels B.W. A Spin-Diode Logic Family. *IEEE Trans. on Nanotechnology*, 2012, **11**(5), P. 1026–1032.
- [2] Sun Z., Bi X., Li H., Wong W.F., and Zhu X. STT-RAM Cache Hierarchy with Multiretention MTJ Designs, *IEEE Trans. On VLSI systems*, 2014, **22**(6), P. 1281–1293.
- [3] Malik G.F.A., Kharadi M.A. and Khanday F.A. Electrically Reconfigurable Logic Design Using Multi-Gate Spin Field Effect Transistors. *Microelectronics Journal*, 2019, **90**, P. 278–284.
- [4] Malik G.F.A., Kharadi M.A., Parveen N. and Khanday F.A. Modelling for Triple Gate Spin-FET and Design of Triple Gate Spin-FET-Based Binary Adder. *IET Circuits, Devices and Systems*, 2020, DOI: 10.1049/iet-cds.2019.0329.
- [5] Datta S. and Das B. Electronic analog of the electro-optic modulator. *Appl. Phys. Lett*, 1990, **56**(7), P. 665467.

- [6] Sugahara S. Spin MOSFETs as a basis for integrated spin-electronics, Proceedings of 2005 5th IEEE Conference on Nanotechnology, Nagoya, Japan, 2005, P. 1243–1279.
- [7] Sato Y., Gozu S., Kita T. and Yamada S. Study for realization of spin-polarized field effect transistor in $\text{In}_{0.75}\text{Ga}_{0.25}\text{As}/\text{In}_{0.75}\text{Al}_{0.25}\text{As}$ heterostructure. *PHYSICA E*, 2002, **12**(4), P. 399–402.
- [8] Pramanik S., Bandyopadhyay S. and Cahay M. Spin transport in nanowires. *Third IEEE Conference on Nanotechnology*, IEEE-NANO, Virginia, 2003, **2**, P. 87–90.
- [9] Nitta J. and Bergsten T. Electrical Manipulation of Spin Precession in an InGaAs-Based 2DEG Due to the Rashba Spin-Orbit Interaction. *IEEE Trans. on Electron devices*, 2007, **54**(5), P. 955–960.
- [10] Takahashi S. and Maekawa S. Spin injection and detection in magnetic nanostructures. *Phys Rev B*, 2003, **67**(5), P. 52409.
- [11] Chen X. and Tan C.M. Modeling and analysis of gate-all-around silicon nanowire FET. *Microelectronics Reliability*, 2014, **54**(7), P. 1103–1108.
- [12] Shah K.A. and Parvaiz M.S. Negative differential resistance in BN co-doped coaxial carbon nanotube field effect transistor. *Superlattices and Microstructures*, 2012, **19**(2), P. 299–303.
- [13] Sai M.A., Mei L.L., Xin Z.Y. and Peng Z. Negative differential resistance in a molecular junction of carbon nanotube and benzene. *SCIENCE CHINA Physics, Mechanics and Astronomy*, 2011, **54**(8), P. 1433–1437.
- [14] Grassi R., Gnudi A., Lecce V.D., Gnani E., Reggiani S. and Baccarani G. Exploiting negative differential resistance in monolayer graphene FETs for high voltage gains. *IEEE Trans. on Electron Devices*, 2014, **61**(2), P. 617–624.
- [15] Sengupta A. and Mahapatra S. Negative differential resistance and effect of defects and deformations in MoS₂ armchair nanoribbon MOSFET. *Journal of Applied Physics*, 2013, **114**(19), P. 194513(1-5).
- [16] Wu Y., Farmer D.B., Zhu W., Han S.J., Dimitrakopoulos C.D., Bol A.A., Avouris P. and Lin Y.M. Three-Terminal Graphene Negative Differential Resistance Devices. *American Chemical Society*, 2012, **6**(3), P. 2610–2616.
- [17] Kharadi M.A., Malik G.F.A., Shah K.A. and Khanday F.A. Sub-10-nm Silicene Nanoribbon Field Effect Transistor. *IEEE T Electron Dev.*, 2019, **66**(11), P. 4976–4981.
- [18] Atomistic Tool Kit version 13.8.1 currently available online at www.quantumwise.com.
- [19] Santos T., Lee J., Migdal P., Lekshmi I., Satpati B. and Moodera J. Room temperature tunnel magnetoresistance and spin polarized tunneling through an organic semiconductor barrier. *Phys. Rev. Lett.*, 2007, **98**, P. 016601.
- [20] Yue G., Chen L., Barreda J., Bevara V., Hu L., Wu L., Wang Z., Andrei P., Bertaina S. and Chiorescu I. Sensitive spin detection using an on-chip SQUID-waveguide resonator. *Appl. Phys. Lett.*, 2017, **111**(20), P. 202601.
- [21] Jedema F.J., Nijboer M.S., Philip A.T. and Wees B.J.V. Spin injection and spin 26 accumulation in all metal spin valves. *Phys. Rev. B*, 2003, **67**, P. 085319.
- [22] Pramanik S., Bandyopadhyay S. and Cahay M. Spin relaxation of “upstream” electrons in quantum wires: Failure of the drift diffusion model. *Phys. Rev. B*, 2006, **73**, P. 125309.
- [23] Merkulov I.A., Efros A.L. and Rosen M. Electron spin relaxation by nuclei in semiconductor quantum dots. *Phys. Rev. B*, 2002, **65**, P. 205309.
- [24] Amasha S., MacLean K., Radu I., Zumbuhl D.M., Kastner M.A., Hanson M.P. and Gossard A.C. Electrical control of spin relaxation in a quantum dot. *Phys Rev Lett.*, 2008, **100**(4), P. 046803.

High harmonic generation by an atom confined in nanoscale cavityS. Z. Rakhmanov¹, O. V. Karpova², F. S. Khashimova³, B. Kh. Eshchanov^{1,4}¹Physics Department, National University of Uzbekistan, Vuzgorodok, 100174, Tashkent, Uzbekistan²Turin Polytechnic University in Tashkent, 17 Niyazov Str., 100095, Tashkent, Uzbekistan³Navoi State Mining Institute, Galaba street, Navoi, Uzbekistan⁴Chirchik State Pedagogical Institute, 104 Amir Temur Str., Chirchik, Uzbekistan

saparboy92@gmail.com

PACS 03.65.-w, 05.45.Ac**DOI 10.17586/2220-8054-2020-11-3-307-313**

We consider optical high harmonic generation in a hydrogen-like atom confined in a spherical cavity caused by interaction with a monochromatic field. The whole system is considered as to be centrally symmetric, i.e., atomic nucleus as fixed at the center of sphere. In such a spherically symmetric atom, the high harmonic generation spectrum is calculated at different values of the oscillation amplitude, frequency of the external field and size of the confining domain.

Keywords: high harmonic generation, spectrum of high harmonic generation, atom in cavity, atom in monochromatic field, confined atom.

Received: 19 May 2020

Revised: 12 June 2020

1. Introduction

Study of the nonlinear optical phenomena in the interaction of atoms and molecules with external optical fields is of practical and fundamental importance for the problems, e.g., attosecond physics, high-power laser generation, optical materials design and optoelectronic device fabrication. An interesting aspect of this topic is optical harmonic generation in the quantum regime, which attracted much attention recently [1–10]. One of the main tasks in this field is achieving slowly-decaying (as a function of harmonic order) harmonic generation intensity. Solving of such problem is complicated due to the typical features of the harmonic emission spectra of an atom in a strong optical field, which are known as the plateau and the cutoff. These latter are a wide frequency region with harmonics of comparable intensities, and an abrupt intensity decrease at the end of the plateau. Physical mechanisms of such effects have been explained within the so-called “three-step” model [11, 12]. Existence of such an effect makes difficult the generation of very high order harmonics and ultrashort pulses, as their intensity becomes very small at high harmonic orders. Therefore, revealing the high harmonic generation regime, where the intensity would slowly decay as a function of harmonic order, is of importance for different practical tasks. One such way could be the confining of atoms and molecules in finite spatial domain, where by changing confinement size and geometry, one can control the harmonic generation.

Atoms and molecules confined in nanoscale domains have the modeling behavior of spatially confined atoms and molecules attracted much attention since early stage of the development of quantum mechanics. Such interest is caused by different practically important reasons, such as modification of atomic properties under high pressure, confinement size effects, the role of confinement geometry in the macroscopic properties of atomic systems, etc. The first studies of atom-in-box system date back to the Refs. [15, 16], where effect of the pressure on an atom was explored in a quantum approach. Later, the problem was studied within the perturbation theory. Different aspects of atom-in-box problem have been studied in the literature during past few decades (see, e.g., [17–36] and review paper [37] for more references). A comprehensive study of the electronic properties of the atom-in-box system can be found in the Refs. [20, 23, 35, 36]. Refs. [26, 28, 29] present the analysis of the quantum dynamics of hydrogen atom confined in a spherical box in the presence of an external electric field.

Atom-in-box system can be realized in experiments with atom optic billiards, which have been extensively studied earlier in the Refs. [38–40]. These systems represent a rapidly scanning and tightly focused laser beam creating a time-averaged quasi-static potential for atoms. In such system, one can create various box (billiard) shapes by controlling the deflection angles of the laser beam. Confining atoms inside the fullerene [13, 14] can be considered as an version of atom-in-box system. A review of different versions of the atom-inside-cage system can be found in [37]. As for the atom-in-box system interacting with external electromagnetic field and optical harmonic generation in such system, several models have been proposed earlier in the Ref. [29], where the box is considered as to be formed by high density environment (e.g., electron gas, plasma, etc). According to the assumptions of the model considered in [29],

at sufficiently high intensities of the laser and high densities of the medium (which consists of an ensemble of atoms) the quantum path of the electron wave packet in the continuum can be perturbed by the fields of the other atoms (or ions) in the vicinity. In such a model, the neighboring atoms will cause reflections on the boundary of the spherical box. Detailed justification of such a model can be found in [29].

In this paper, we address the problem of optical high harmonic generation in atom confined in a nanoscale cavity of spherical shape and interacting with external monochromatic field. In particular, we compute the spectrum of harmonic generation at different values of the field parameters. Our results obtained in this study are considerably different from those for unconfined counterpart by the values, as well as by the shape of the spectrum curve.

This paper is organized as follows. In the next section we give brief description of a hydrogen-like atom in a static spherical box. In section 3, quantum system, consisting of one-electron atom confined in a spherical box with external field is given. Section 4 presents detailed treatment of high harmonic generation in such system. Finally, section 5 provides some concluding remarks.

2. The hydrogen-like atom in a static spherical box

The hydrogen-like (one-electron) atom confined in a spherical box with impenetrable walls with the radius r_0 is considered in many paper. Assuming that the nucleus of the atom is fixed at the center of box, the dynamics of atomic electron in such system can be described by stationary radial Schrödinger equation which is given as (atomic units, $m_e = e = \hbar = 1$ are used throughout this paper):

$$\left[-\frac{1}{2} \frac{\partial^2}{\partial r^2} - \frac{1}{r} \frac{\partial}{\partial r} + \frac{l(l+1)}{2r^2} - \frac{Z}{r} \right] R_{nl}(r) = E_{nl} R_{nl}(r), \quad (1)$$

where R_{nl} is the radial part of the wave function, Z is the charge of the nucleus, n and l are the principal and orbital quantum numbers, respectively. The energy eigenvalues, E_{nl} can be found from the boundary conditions for $R_{nl}(r)$

$$R_{nl}(r)|_{r=r_0} = 0. \quad (2)$$

Unlike the unconfined atom, the energy spectrum of atom-in-box system is completely discrete. It should be noted that equation (2) is not convenient for computing of the energy spectrum of this system, as it does not allow to compute high number of eigenvalues, especially, at small radii of the box. Here, we compute the energy levels of the atom-in-box system by diagonalization of the Hamiltonian (left part of Eq. (1)) of the system over the spherical box eigenfunctions basis. This method allows one to compute an arbitrarily high number of eigenvalues for any value of the box radius.

3. Quantum dynamics of hydrogen-like atom confined in driven static spherical box

Consider first the hydrogen-like (one-electron) atom confined in a spherical box with impenetrable walls with the radius r_0 and driven by external linearly polarized monochromatic field with the strength F and frequency ω_0 which is propagating along Z axis. Assuming that the nucleus of the atom is fixed at the center of box, for the dynamics of atomic electron in such system we have the nonstationary radial Schrödinger equation which is given as :

$$i \frac{\partial \Psi(\mathbf{r}, t)}{\partial t} = (\hat{H}_0 + V) \Psi(\mathbf{r}, t), \quad (3)$$

where

$$\hat{H}_0 = -\frac{1}{2} \frac{\partial^2}{\partial r^2} - \frac{1}{r} \frac{\partial}{\partial r} + \frac{l(l+1)}{2r^2} - \frac{Z}{r},$$

and

$$V = -Fz \cos(\omega_0 t).$$

For such a regime, the boundary conditions for Eq.(3) are imposed as

$$\Psi(r_0, t) = 0. \quad (4)$$

and initial condition is ground state of hydrogen-like atomic electron in a spherical box.

To solve Eq.(3), one should expand the solutions in terms of the set of the unperturbed spherical box eigenfunctions as

$$\Psi(\mathbf{r}, t) = \sum_{nlm} C_{nlm}(t) u_{nlm}(\mathbf{r}, t). \quad (5)$$

where $u_{nlm}(\mathbf{r})$ are the eigenfunction of the quantum particle confined in spherical box to be found from stationary Schrödinger equation

$$\left[-\frac{1}{2} \frac{\partial^2}{\partial r^2} - \frac{1}{r} \frac{\partial}{\partial r} + \frac{l(l+1)}{2r^2} \right] u_{nlm}(\mathbf{r}) = \epsilon_{nl} u_{nlm}(\mathbf{r}). \quad (6)$$

Here is a spherical symmetric, therefore solutions of Eq.(6) can be separated into radial and angular parts, $u_{nlm}(\mathbf{r}) = R_{nl}(r)Y_{lm}(\theta, \varphi)$, where $Y_{lm}(\theta, \varphi)$ are spherical harmonics. Radial eigenfunctions of box can be written as

$$R_{nl}(r) = N_{nl} j_l(\lambda_{nl} r), \quad (7)$$

where j_l are the spherical Bessel functions and $\lambda_{nl} = \sqrt{2\epsilon_{nl}}$. Eigenvalues, ϵ_{nl} , are found from the boundary condition given on surface of the sphere. These are zeros of wave functions of spherical box at sphere surface, $R_{nl}(r)|_{r=r_0} = 0$.

The function u_{nlm} fulfill the orthonormality condition given by

$$\int u_{n'l'm'}^* u_{nlm} d\mathbf{r} = \delta_{n'n} \delta_{l'l} \delta_{m'm} \quad (8)$$

For expansion coefficients, $C_{nlm}(t)$ using Eq.(3) we have a system of first order differential equations given by

$$i\dot{C}_{nlm}(t) = \epsilon_{nl} C_{nlm} + \sum_{n'l'm'} C_{n'l'm'}(t) V_{n'l'm'nlm}, \quad (9)$$

where

$$V_{n'l'm'nlm} = \int u_{n'l'm'}^* \left(-\frac{Z}{r} - Fr \cos \theta \cos(\omega_0 t) \right) u_{nlm} d\mathbf{r}. \quad (10)$$

4. High harmonic generation by hydrogen-like atom confined in a static spherical box

The main characteristics of the high harmonic generation is the average dipole moment, which can be used for calculating the intensity of the generated harmonics [1]- [8]. This is applicable also for harmonic generation in atom-in-box system. The dipole moment is given by (in atomic units, $m_e = e = \hbar = 1$) [29]

$$\bar{d}(t) = -\langle \Psi(\mathbf{r}, t) | z | \Psi(\mathbf{r}, t) \rangle,$$

where the wave function $\Psi(\mathbf{r}, t)$ is solution of Eq.(3).

We are interested in the study of optical harmonic generation in the system described by Eqs.(3) . The spectrum of harmonic generation is characterized by the power spectrum, which is given as [1]

$$|\bar{d}(\omega)|^2 = \left| \frac{1}{T} \int_0^T e^{-i\omega t} \bar{d}(t) dt \right|^2, \quad (11)$$

where T is the interaction time.

In Fig. 1 $|d(\omega)|^2$ which determines the intensity of harmonic generation, is plotted at different values of the box radius, r_0 for the values of external field amplitude and frequency, $F = 50$ GV/m and $\omega_0 = 26 \cdot 10^{16} \text{ sec}^{-1}$, $Z = 1$, $T = 2.44$ fs. As it can be seen from this plot, the intensity of the harmonic generation is inverse proportional to the box size, i.e. as the box radius is larger, as higher the intensity. Such difference can be explained by the confinement effect, which causes scattering of the light waves at the cavity's wall and its re-interaction with the atom.

Fig. 2 presents $|d(\omega)|^2$ as a function of harmonic order at different values of the external monochromatic field frequencies for the values of parameters $r_0 = 12.5$ nm, $F = 50$ GV/m, $Z = 1$ and $T = 2.44$ fs. Unlike the unconfined (bulk) counterpart (see, e.g., [1]), the behavior of the spectrum is characterized by much higher values at large frequencies and by the absence of fluctuations.

In Fig. 3, $|d(\omega)|^2$ is plotted for the different values of external field strength, F for the values of other parameters, $r_0 = 12.5$ nm and $\omega_0 = 26 \cdot 10^{16} \text{ sec}^{-1}$, $Z = 1$, $T = 2.44$ fs. Again, one can observe the absence of fluctuations and plateau, which are the characteristic features of the high harmonic generation in an unconfined atom. Also, a stronger external field, produced higher intensity harmonic generation. In addition, numerical values of $|d(\omega)|^2$, which characterize the intensity of harmonic generation, are much higher than those for the unconfined counterpart.

To see the role of the Coulomb potential in harmonic generation by atom-in-box system, we computed harmonic generation spectrum at different values of the nucleus charge. In Fig. 4, $|d(\omega)|^2$ is plotted for the values of nuclear charge of hydrogen-like atom, $Z = 1; 2; 3$, for $r_0 = 12.5$ nm, $F = 50$ GV/m and $\omega_0 = 26 \cdot 10^{16} \text{ sec}^{-1}$, $T = 2.44$ fs. As the nucleus charge is higher, as lower the intensity of harmonic generation. We should note that unlike the free (unconfined) atom, according to the Ref. [41], the spectrum of the atom-in-box system is always discrete, i.e. electron

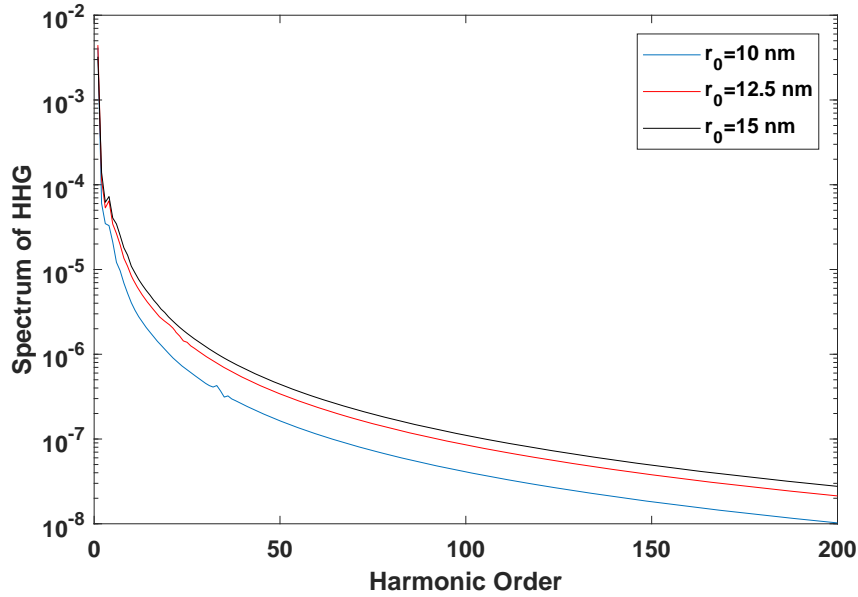


FIG. 1. (Color online) Harmonic generation spectrum for hydrogen-like atom confined in a spherical box driven by external, linearly polarized monochromatic potential at different values of the radius of sphere, r_0 (blue for 10 nm, red for 12.5 nm, black for 15 nm) and fixed amplitude, $F = 50$ GV/m for $\omega_0 = 26 \cdot 10^{16} \text{ sec}^{-1}$, $Z = 1$ and $T = 2.44$ fs

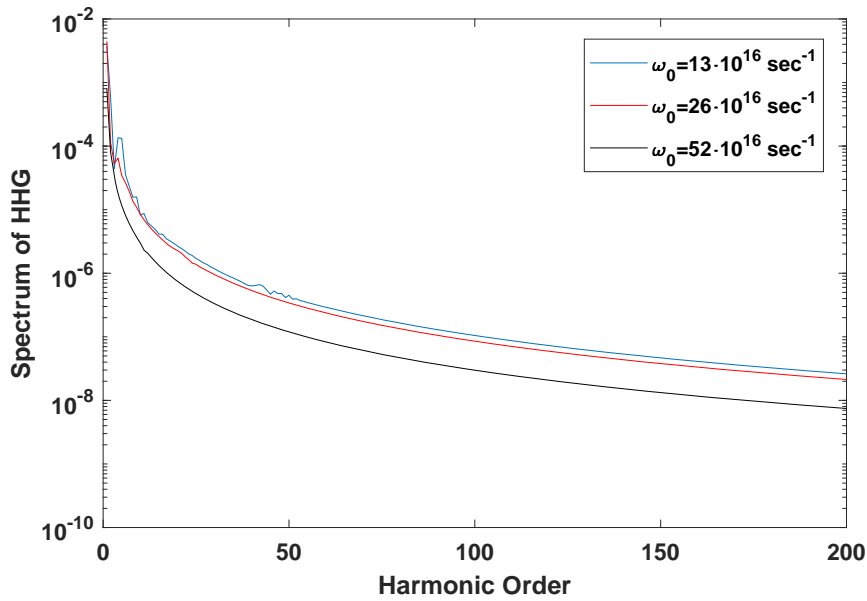


FIG. 2. (Color online) Harmonic generation spectrum for hydrogen-like atom in a spherical box driven by external, linearly polarized monochromatic potential at different ω_0 (blue for $13 \cdot 10^{16} \text{ sec}^{-1}$, red for $26 \cdot 10^{16} \text{ sec}^{-1}$, black for $52 \cdot 10^{16} \text{ sec}^{-1}$) and fixed amplitude, $F = 50$ GV/m for $r_0 = 12.5$ nm, $Z = 1$ and $T = 2.44$ fs

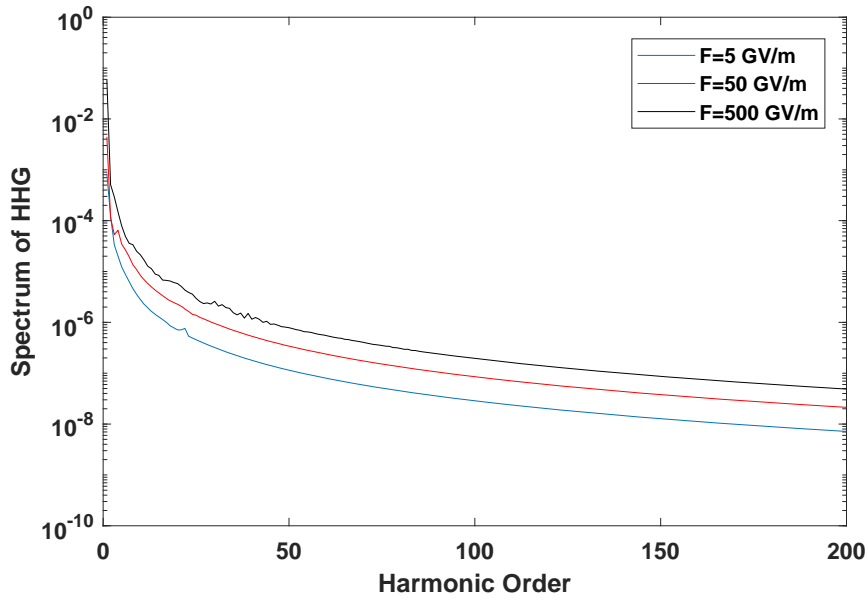


FIG. 3. (Color online) Harmonic generation spectrum for hydrogen-like atom in a spherical box driven by external, linearly polarized monochromatic potential at different amplitudes of the external field (blue for 5 GV/m, red for 50 GV/m, black for 500 GV/m) for $\omega_0 = 26 \cdot 10^{16} \text{ sec}^{-1}$, $r_0 = 12.5 \text{ nm}$, $Z = 1$ and $T = 2.44 \text{ fs}$

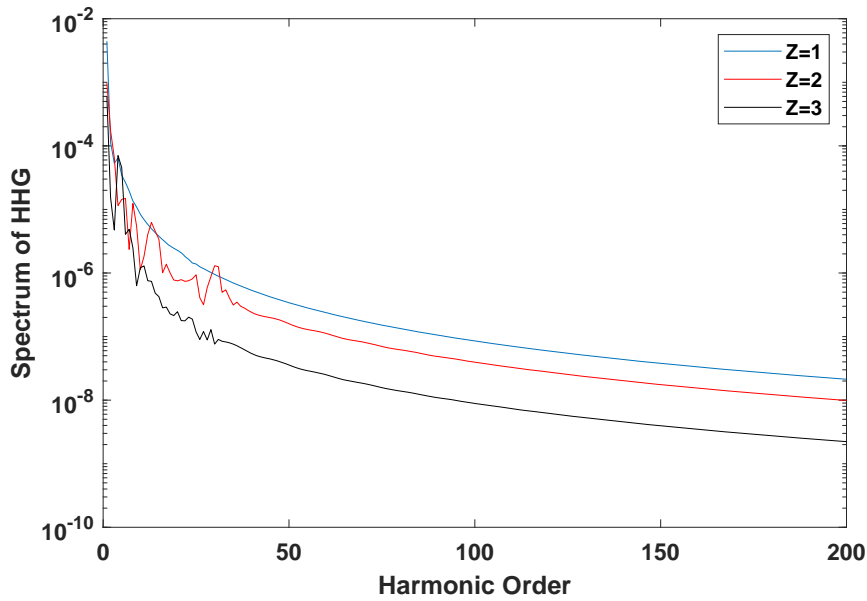


FIG. 4. (Color online) Harmonic generation spectrum for hydrogen-like atom in a spherical box driven by external, linearly polarized monochromatic potential at different nuclear charge of atom for $\omega_0 = 26 \cdot 10^{16} \text{ sec}^{-1}$, $r_0 = 12.5 \text{ nm}$, $F = 50 \text{ GV/m}$ and $T = 2.44 \text{ fs}$

is always in the bound state, due to the pressure by the box's wall. Such difference in the harmonic generation intensity at different charges can be caused by pressure.

5. Conclusions

We studied high harmonic generation by hydrogen-like atom confined in a nanoscale cavity confined and interacting with a linearly polarized monochromatic field. The main focus of the study is given to the dependence of high harmonic generation intensity on the box size, oscillation amplitude and frequency of external monochromatic field. The main characteristic of the high harmonic generation spectra, the Fourier transform of the average dipole moment is computed using the direct numerical solutions of time-dependent Schrödinger equation for Coulomb potential, for which the finite (box) boundary conditions are imposed. It is found that harmonic generation spectrum and its intensity for confined atom is considerably different than those for unconfined counterpart. In particular, the intensity in the confined case is much higher than that for unconfined counterpart and the fluctuations are negligibly small for this case. All these implies that confined atom can be more attractive from the viewpoint of high harmonic generation and attosecond physics.

References

- [1] Tong X., Chu Sh. Theoretical study of multiple high-order harmonic generation by intense ultrashort pulsed laser fields: A new generalized pseudospectral time-dependent method. *Chem. Phys. B*, 1997, **217**(2-3), P. 119–130.
- [2] Brabec T. and Krausz F. Intense few-cycle laser fields: Frontiers of nonlinear optics. *Rev. Mod. Phys.*, 2000, **72**(2), P. 545–591.
- [3] Yousef I., *et.al.* Relativistic high-power laser matter interactions. *Phys. Rep.*, 2006, **427**(2-3), P. 41–155.
- [4] Winterfeldt C., Spielmann C., and Gerber G. Colloquium: Optimal control of high-harmonic generation. *Rev. Mod. Phys.* 2008, **80**(1), P. 117–140.
- [5] Krausz F., Ivanov M. Attosecond physics. *Rev. Mod. Phys.*, 2009, **81**, P. 163–234.
- [6] Nisoli M., Sansone G. New frontiers in attosecond science Author links open overlay panel. *Prog. Quant. Electr.*, 2009, **33**, P. 17–59.
- [7] Kohler M.C., Pfeifer T., Hatsagortsyan K.Z., Keitel C.H. Frontiers of Atomic High-Harmonic Generation. *Advances In Atomic, Molecular, and Optical Physics*, 2012, **61**, P. 159–208.
- [8] Strelkov V.V., Platonenko V.T., Sterzhantov A.F. and Ryabikin M.Yu. Attosecond electromagnetic pulses: generation, measurement, and application. Generation of high-order harmonics of an intense laser field for attosecond pulse production. *Phys. Uspekhi*, 2016, **59**(5), P. 425–445.
- [9] de Morisson Faria C. F. and Rost J-M. High-order harmonic generation from a confined atom. *Phys. Rev. A*, 2000, **62**(5), P. 051402(R)/1-4.
- [10] Boyd R.W. *Nonlinear Optics*. 3rd ed., Academic Press, 2007, 613 p.
- [11] Lewenstein M., Balcou Ph., Ivanov M. Yu., LHuillier A., and Corkum P.B. Theory of high-harmonic generation by low-frequency laser fields. *Phys. Rev. A*, 1994, **49**(3), P. 2117–2132.
- [12] Becker W., Long S. and McIver J.K. Higher-harmonic production in a model atom with short-range potential. *Phys. Rev. A*, 1990, **41**(7), P. 4112–4115.
- [13] Connerade J.-P., Dolmatov V.K., Lakshmi P.A. and Manson S.T. Electron structure of endohedrally confined atoms: atomic hydrogen in an attractive shell. *J. Phys. B*, 1999, **32**(10), P. L239–L246.
- [14] Connerade J.-P. and Semaoune R. Atomic compressibility and reversible insertion of atoms into solids. *J. Phys. B*, 2000, **33**(17), P. 3467–3484.
- [15] Michels A., de Boer J. and Bijl A. Remarks concerning molecular interaction and their influence on the polarisability. *Physica (The Hague)*, 1937, **4**(10), P. 981–994.
- [16] Sommerfeld A. and Welker H. Känstliche grenzbedingungen beim Keplerproblem. *Ann. Phys.*, 1938, **32**, P. 56–65.
- [17] Suryanarayana D. and Weil J. A. On the hyperfine splitting of the hydrogen atom in a spherical box *J. Chem. Phys.*, 1975, **64**(2), P. 510–513.
- [18] Ley-Koo E., Rubinstein S. The hydrogen atom within spherical boxes with penetrable walls. *J. Chem. Phys.*, 1979, **71**(1), P. 351–357.
- [19] Last I. and George Th. F. Light absorption by an atom moving inside a spherical box. *Chem. Phys. Lett.*, 1987, **142**(1-2), P. 19–24.
- [20] Laughlin C., Burrows B. L., Cohen M. A hydrogen-like atom confined within an impenetrable spherical box. *J. Phys. B*, 2002, **35**(3), P. 701–716.
- [21] Kang Sh., Yang Y-Ch., He J., Xiong F-Q., Xu N. The hydrogen atom confined in both Debye screening potential and impenetrable spherical box. *Cent. Eur. J. Phys.*, 2013, **11**, P. 584–593.
- [22] Zhou Sh-G., Zhao J. and E-G. A spherical-box approach for resonances in the presence of the Coulomb interaction. *J. Phys. B*, 2009, **42**(24), P. 245001/1-4.
- [23] Burrows B. L., Cohen M. Exact solutions for perturbed confined hydrogen atoms: Polarizabilities and nuclear shielding factors. *Phys. Rev. A*, 2005, **72**(3), P. 032508/1-6.
- [24] Kang S., Liu Q., Meng H-Y., Shi T-Y. Hydrogen atom in ellipsoidal cavity. *Phys. Lett. A*, 2007, **360**(4-5), P. 608–614.
- [25] Capitelli M. Energy levels of atomic hydrogen in a closed box: A natural cutoff criterion of the electronic partition function. *Phys. Rev. A*, 2009, **80**(3), P. 032113/1-5.
- [26] Masovic D. R. Unusually kicked dynamics: Hydrogen atom in a spherical box. *Cent. Eur. J. Phys.*, 2012, **10**, P. 768–778.
- [27] Cabrera-Trujillo R., Cruz S. A. Confinement approach to pressure effects on the dipole and the generalized oscillator strength of atomic hydrogen. *Phys. Rev. A*, 2013, **87**(1), P. 012502/1-10.
- [28] Lumb S., Lumb S., Prasad V. Laser-induced excitation and ionization of a confined hydrogen atom in an exponential-cosine-screened Coulomb potential. *Phys. Rev. A*, 2014, **90**(3), P. 032505/1-9.
- [29] Masovic D. R. High-harmonic generation and spherically confined hydrogen atom. *Can. J. Phys.*, 2015, **93**(4), P. 434–444.
- [30] Strelkov V. V., Platonenko V. T. and Becker A. High-harmonic generation in a dense medium. *Phys. Rev. A*, 2005, **71**(5), P. 053808/1-8.

- [31] McDonald C. R., Amin K. S., Aalmalki S. and Brabec T. Enhancing High Harmonic Output in Solids through Quantum Confinement. *PRL*, 2017, **119**(18), P. 183902/1-6.
- [32] Heyl C. M., Gdde J. L'Huillier A. and Hfer U. High-order harmonic generation with μJ laser pulses at high repetition rates. *J. Phys. B: At. Mol. Opt. Phys.*, 2012, **45**(7), P. 074020/1-9.
- [33] Topcu T., Bleda E. A. and Altun Z. Drastically enhanced high-order harmonic generation from endofullerenes. *Phys. Rev. A*, 2019, **100**(6), P. 063421/1-12.
- [34] Friedman N., Khaykovich L., Ozeri R. and Davidson N. Compression of cold atoms to very high densities in a rotating-beam blue-detuned optical trap. *Phys. Rev. A*, 2000, **61**(3), P. 031403(R)/1-4.
- [35] Burrows B. L., Cohen M. Confined systems within arbitrary enclosed surfaces. *J. Phys. B*, 2016, **49**(12), P. 125001/1-6.
- [36] Burrows B. L. and Cohen M. Confined one- and two-center systems. *Phys. Rev. A*. 2013. **88**(5). P. 052511.6p.
- [37] Jaskolski W. Confined many-electron systems. *Phys. Rep.*, 1996, **271**(1), P. 1-66.
- [38] Milner V., Hanssen J. L., Campbell W. C. and Raizen M. G. Optical Billiards for Atoms. *Phys.Rev.Lett.*, 2001, **86**(8), P. 15141517.
- [39] Rohwedder B. Quantum billiard atom optics. *EPL*, 2002, **60**(4), P. 505–511.
- [40] Friedman N., Kaplan A. Dark optical traps for cold atoms. *Adv. At. Mol. Phys.*, 2002, **48**, P. 99–151.
- [41] Rakhmonov S., Matrasulov D. and Matveev V. Quantum dynamics of a hydrogen-like atom in a time-dependent box: non-adiabatic regime. *Eur. Phys. J. D.*, 2018, **72**, P. 177/1-8.

Nanotechnology and material science

P. P. Fedorov

Prokhorov General Physics Institute of the Russian Academy of Sciences 119991, Moscow, Russia

ppfedorov@yandex.ru

DOI 10.17586/2220-8054-2020-11-3-314-315

The general features of nanotechnology processes are summarized. There are three key problems that require theoretical understanding: crystal faceting, crystal shaping and hierarchical organization of matter

Keywords: nanotechnology, nanomaterials, nanofluorides, Ostwalds step rule, labile states, oriented attachment, third law of thermodynamics.

Received: 14 May 2020

Nanomaterials in general, in particular nanofluorides, exist in the realm of non-equilibrium states. They are products of special technologies and are obtained by non-equilibrium physical and chemical transformations. Very often, the latter leads to the formation of previously unknown phases of variable composition and enhanced reactivity [1]. For example, nanofluorides are prone to light pyrohydrolysis [2].

High reactivity can create significant problems for the reproducibility of results and in their interpretation, thus challenging the experimenter's skill. Conversely, these circumstances also make possible unsurpassed opportunities for manipulation in the design of materials, functional features and architecture of the resulting products. It is often possible to produce completely different materials using the same starting reagents. The realm of nanotechnology demonstrates unusual connections between composition, structure, and properties that differ from those found in previously known bulk materials.

Control over nanotechnology-based processes requires – in addition to a cybernetics component (i.e., targeted process control [3]) – mandatory accounting for the spontaneously occurring synergetic transformations [4]. The latter includes, in particular, agglomeration of nanoparticles, which usually demonstrates a clear stepwise hierarchy [5–7].

The available data refute the well-known postulate of thermodynamics, namely, it is generally accepted that labile states are unrealizable, because its transition to the equilibrium state is not associated with overcoming the potential barrier, there is no force that returns the system to its original state, and after the fluctuation out of equilibrium, the system moves away from it with acceleration [8,9]. For example, the crystalline solid solution $Ba_{1-x}Ca_xF_2$ samples, prepared by mechanochemical treatment, can exist in a non-equilibrium state indefinitely. After heating, the system goes to the equilibrium state, namely, the decomposition of the solid solution takes place, and it is accompanied by heat release (exothermic effect) [10]. Apparently, the relative stability of the crystalline samples of the $Ba_{1-x}Ca_xF_2$ solid solution is due to the extremely low values for the diffusion coefficients of the cations. The system is “falling”, but very slowly.

Ostwald's step rule [11] works unequivocally for the nano-objects, and phase transformation sequences always start with the most non-equilibrium amorphous products that turn into more stable phases in a stepwise manner.

A separate problem is to establish the true picture of phase equilibria at low temperatures. Very long equilibrium times, in many cases, make experimental studies impossible [12]. The use of molten salt synthetic techniques allows ones to significantly expand the temperature range available to the study [13, 14]. It is worth noting that, according to the third law of thermodynamics, all solid solutions are non-stable phases at low temperatures [12].

The nanotechnology realm systematically displays non-classical crystallization by oriented attachment crystal growth [15, 16]. These processes are implemented as in the primary formation of nanoparticles (see Fig. 1), and the behavior of nanoparticle ensembles during their thermal treatment [17]. The formation of associated crystals with an increased content of defects can trigger the classical Barton–Prim–Slichter mechanism of crystals growth [15].

The lack of a theoretical description of non-classical crystallization processes is acutely felt. At least three problems remain to be solved.

- (1) The problem of crystal faceting. Nanoparticles conceived do not obey the Curie–Wulf principle [18]. It is possible that there is another dimensional effect [19], which consists in lowering the temperature of the phase transition of the faceting while reducing the particle size.
- (2) The problem of shaping. A number of experiments show that agglomerating nanocrystals tend to assume the correct microcrystal shape (habit) in advance, followed by filling the volume with a crystalline material [14].

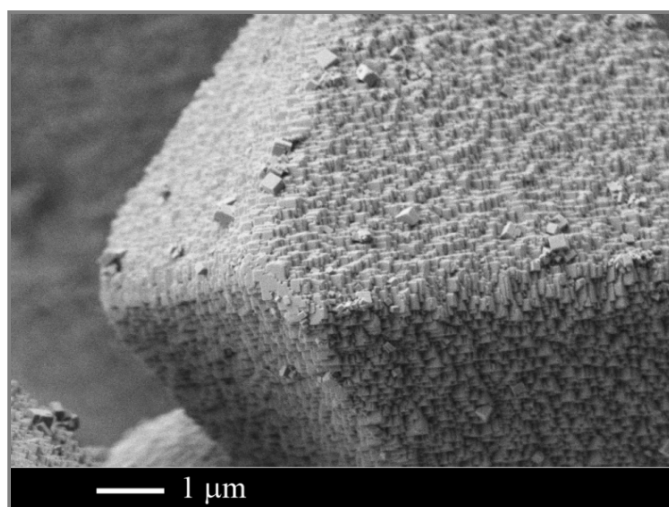


FIG. 1. SrF₂ microcrystal, consisting of nanocubic particles, which were synthesized by the reaction of SrCl₂ + KF = SrF₂ ↓ + KCl at 1000 °C. Synthesis was performed by V. A. Maslov and SEM was performed by A. E. Baranchikov

- (3) The problem of understanding the hierarchical organization of matter and quantization of particle size: in the processes of agglomeration and dispersion in the range of 10⁻⁹ – 10⁸ m, a spectrum of the most probable particle sizes corresponding to the geometric progression is regularly observed [20].

Acknowledgements

The work was carried out under the RFBR grant 18-29-12050mk.

References

- [1] Fedorov P.P., Kuznetsov S.V., Osiko V.V. Elaboration of nanofluorides and ceramics for optical and laser applications. In *Photonic & Electronic Properties of Fluoride Materials*, Ed. A. Tressaud, K. Poeppelemeier, Elsevier, 2016, P. 7–31.
- [2] Fedorov P.P., et al. Coprecipitation of Barium–Bismuth Fluorides from Aqueous Solutions: Nanochemical Effects. *Nanotechnologies in Russia*, 2011, **6**, P. 203–210.
- [3] Wiener N. *Cybernetics*, New York, J. Wiley, 1961.
- [4] Nicolis G., Prigogine I. *Self-Organization in Nonequilibrium Systems: From Dissipative Structures to Order through Fluctuations*, Wiley, New York, 1977.
- [5] Fedorov P.P., Osiko V.V. Formation of nanoparticles aggregates by soft chemistry. *Rare Metals (China)*, 2009, **28**, P. 671–673.
- [6] Mayakova M.N., et al. Synthesis and Characterization of Fluoride Xerogels. *Inorganic Materials*, 2013, **49**, P. 1152–1156.
- [7] Fedorov P.P., et al. Flintstone as nanocomposite material. *Nanosystems: Physics, Chemistry, Mathematics*, 2018, **9**, P. 603–608.
- [8] Storonkin A.V. *Thermodynamics of heterogeneous systems*, Leningrad State University, Leningrad, USSR, 1967, 448 pp. (in Russian)
- [9] Münster A. *Chemische Thermodynamik*. Berlin, Akademie Verlag, 1969.
- [10] Düvel A., et al. Thermal Stability of Ca_{1-x}Ba_xF₂ Solid Solution. *Solid State Science*, 2018, **83**, P. 188–191.
- [11] Ostwald W. Studienüber die Bildung und Umwandlung fester Körper. *Zeitschrift für Physikalische Chemie*, 1897, **22**, P. 289–330.
- [12] Fedorov P.P. Third law of thermodynamics as applied to phase diagrams. *Rus. J. Inorg. Chem.*, 2010, **55** (11), P. 1722–1739.
- [13] Yashima M., Kakihana M., Yoshimura M. Metastable-stable phase diagrams in the zirconia-containing systems utilized in solid-oxide fuel cell application. *Solid State Ionics*, 1996, **86–88**, P. 1131–1149.
- [14] Fedorov P.P., et al. The melt of sodium nitrate as a new medium for synthesis of fluorides. *Inorganics*, 2018, **6**, P. 38–55.
- [15] Ivanov V.K., Fedorov P.P., Baranchikov A.Y., Osiko V.V. Oriented aggregation of particles: 100 years of investigations of non-classical crystal growth. *Russ. Chem. Rev.*, 2014, **83** (12), P. 1204–1222.
- [16] Fedorov P.P., Ivanov V.K., Osiko V.V. Basic Features and Crystal Growth Scenarios Based on the Mechanism of Oriented Attachment Growth of Nanoparticles. *Doklady Physics*, 2015, **60**, P. 483–485.
- [17] Fedorov P.P., et al. Evolution of Yttria nanoparticle ensembles. *Nanotechnologies in Russia*, 2010, **5**, P. 624–634.
- [18] Fedorov P.P., Osiko V.V. Relationship between the Faceting of Crystals and Their Formation Mechanism. *Doklady Physics*, 2019, **64**, P. 353–355.
- [19] Andrievski R.A. Size-dependent effects in properties of nanostructured materials. *Rev. Adv. Mater.*, 2009, **21**, P. 107–133.
- [20] Fedorov P.P. Quantization of nano-, micro-, and macro objects. Materials of nano-, micro-optoelectronics and fiber optics: physical properties and application. *Proceedings of the 12th International scientific conference-school*, Saransk, October 1–4, 2013. Saransk: MSU Publishing House, 2013, P. 76–77. (in Russian)

Near infrared down-conversion luminescence of $\text{Ba}_4\text{Y}_3\text{F}_{17}:\text{Yb}^{3+}:\text{Eu}^{3+}$ nanoparticles under ultraviolet excitation

S. V. Kuznetsov^{1*}, A. S. Nizamutdinov², E. I. Madirov², V. V. Voronov¹, K. S. Tsoy², A. R. Khadiev²,
A. D. Yaprntsev³, V. K. Ivanov³, S. S. Kharintsev², V. V. Semashko²

¹Prokhorov General Physics Institute of the Russian Academy of Sciences, Russia

²Kazan Federal University, Russia

³Kurnakov Institute of General and Inorganic Chemistry of the Russian Academy of Sciences, Russia

*kouznetzovsv@gmail.com

PACS 42.70.-a, 81.20.Fw

DOI 10.17586/2220-8054-2020-11-3-316-323

The single-phase solid solutions $\text{Ba}_4\text{Y}_3\text{F}_{17}:\text{Yb}:\text{Eu}$ with fluorite-type structure were synthesized by co-precipitation from aqueous solution technique. The average particle size was approximately 100 nm without agglomeration. The sensitized down-conversion luminescence of Yb^{3+} ions was observed under 296 nm excitation. The quantum yield of Yb^{3+} luminescence was found to reach a value of 0.4 % for samples with Eu/Yb ratios of 0.1/1.0 and 0.1/10.0.

Keywords: nanofluoride, down-conversion, luminescence.

Received: 16 April 2020

1. Introduction

According to the International Energy Agency (IEA) and the European Environment Agency (EEA), the energy consumption increases from year to year. It stimulates the search for new sources of energy and improving the efficiency of existing ones. According to the forecast, the terawatt energy will be generated by means of photovoltaic devices until 2030 years with a simultaneous reduction of kW/h cost [1]. One of the most affordable source of energy is solar energy. Silicon-based solar cells are mostly used for solar energy utilization. Most of this energy will be generated by silicon solar panels. In addition to silicon, various multilayer compositions such as GaAs, CdTe, Cu(In,Ga)Se₂, and recently proposed perovskite structures [2, 3]. The latter are expensive and difficult to produce on an industrial scale. Additionally, there is the problem to dispose them after the expiration due to toxic components and use of such compositions is contrary to the principles of green chemistry. The advantages of silicon are chemical availability and the maturity of the technological chains, the disposal of electronic components, including those containing rare-earth elements.

At the same time, one serious drawback of silicon-based solar cells is relatively low light-to-electrical energy conversion efficiency (LECE), namely, no higher than 25 % for the best samples [4, 5]. The region of the highest photosensitivity of silicon is located about 1 μm and his LECE spectrum poorly corresponds the solar emission spectrum.

The enhancement of silicon solar panels efficiency by down-conversion of solar irradiation from ultraviolet and blue spectral range to the 1 μm spectral range is an urgent task and it is extremely actual for space applications [6–9]. Prospective emitter is trivalent ytterbium ion due to near-infrared (NIR) luminescence band around 1000 nm ($^2\text{F}_{5/2}-^2\text{F}_{7/2}$ transition) [9–13], which well coincides with the top of LECE spectrum of silicon batteries. One of the new thoroughly investigated luminescence matrices is $\text{Ba}_4\text{Y}_3\text{F}_{17}$ [14–17], because it demonstrated the high quantum yield of down-conversion luminescence [14].

Energy transfer from the UV and blue spectral regions to ytterbium is possible for various sensitizing cations absorbing in these spectral regions. One especially efficient mechanism of energy transfer is through stepwise relaxation of a sensitizer ion, resulting in the excitation of two acceptor ions by quantum cutting mechanism [12, 13, 18, 19]. The quantum cutting demonstrated high quantum efficiency coefficient up to 195 % but the quantum yield of NIR luminescence is low. A more efficient pathway is simple downshifting in a systems with higher quantum yield of luminescence. A promising composition is Yb/Eu doping pair, because absorption spectrum of europium comprises several lines in the UV and blue spectral regions. The highest directly measured quantum yield of ytterbium luminescence (2.5 %) upon 266 nm pumping was reached for the $\text{SrF}_2:\text{Yb}$ (1.0 mol %):Eu (0.05 mol %) powder [20].

The purpose of this paper is to synthesize $\text{Ba}_4\text{Y}_3\text{F}_{17}:\text{Yb}:\text{Eu}$ solid solution and to study its luminescent properties. This specimen of interest is intended to be utilized for enhancing of LECE of silicon solar cells.

2. Experimental

$Ba_4Y_3F_{17}:Yb:Eu$ powders were synthesized by co-precipitation from aqueous nitrate solutions technique as reported earlier [14]. 99.99 wt. % dihydrate potassium fluoride (REACHEM, Russia), 99.99 wt. % yttrium, ytterbium, and europium nitrate hexahydrates, barium nitrate (all reagents from LANHIT, Russia), and double distilled water were used as starting materials without additional purification. Potassium fluoride was preliminarily dried at 350 °C for 3 hours and it was taken with a 50 % excess from stoichiometry. 0.08 M aqueous solutions of barium nitrate and rare earth nitrate were added dropwise to potassium fluoride (0.16 M) with vigorous stirring. Precipitates were washed several times by double distilled water and collected by centrifugation. The resulting precipitates were dried at 45 °C and annealed in a platinum crucible in air at 600 °C for 1 hour. X-ray powder diffraction analysis was performed on a Bruker D8 Advance diffractometer with $CuK\alpha$ radiation. The TOPAS software ($R_{wp} < 10$) was used for calculation of X-ray coherent scattering domain and unit cell parameters. The morphology, particle size, and composition of the samples were analyzed by a Carl Zeiss NVision 40 scanning electron microscope equipped with an EDX detector.

Raman spectra were captured with a multi-purpose analytical instrument NTEGRA SPECTRA™ (NT-MDT) in epi-configuration. The spectrometer was wavelength calibrated with a silicon wafer by registering a first-order Raman band centered at 520 cm^{-1} . A sensitivity of the spectrometer was as high as ca. 3500 photon counts per 0.1 s provided that we used a 100× objective (N.A. = 0.7), an exit slit of 100 μm and a linearly polarized light with the wavelength of 532 nm and the intensity of 5.4 MW/cm^2 . The Raman spectra were collected with the EMCCD camera cooled down to -100 °C and registered with spectral resolution of 3 cm^{-1} using a 600 grooves/mm grating.

Photoluminescence was excited by pulsed UV and visible laser radiation from the H_2 Raman shifter cell converting the 266 nm UV radiation from LS2147 laser and/or OPO laser system produced by JV Lotis TII. The pulse duration was 10 ns, repetition rate 10 Hz. The luminescence spectra were registered by a StellarNet EPP2000 portable spectrometer with a spectral resolution of about 0.5 nm. The luminescence kinetics were registered with a MDR-23 monochromator and FEU-100 photomultiplier tube for the UV-visible spectral range and FEU-62 photomultiplier tube for the NIR spectral range and recorded with the 1 GHz 8 bit Rhode-Schwartz oscilloscope. The direct measurements of luminescence quantum yield were performed using the luminescence spectra recorded in a Thorlabs IS200 integrating sphere coupled to a StellarNet EPP2000 spectrometer via an optical fiber. The spectral sensitivity of this system was calibrated using an approach described previously [21].

3. Sample characterization

The samples were single-phase according to X-ray powder diffraction after annealing at 600 °C (Fig. 1). The unit cell parameters are in convenience with preliminary data published elsewhere (Table 1) [14, 22].

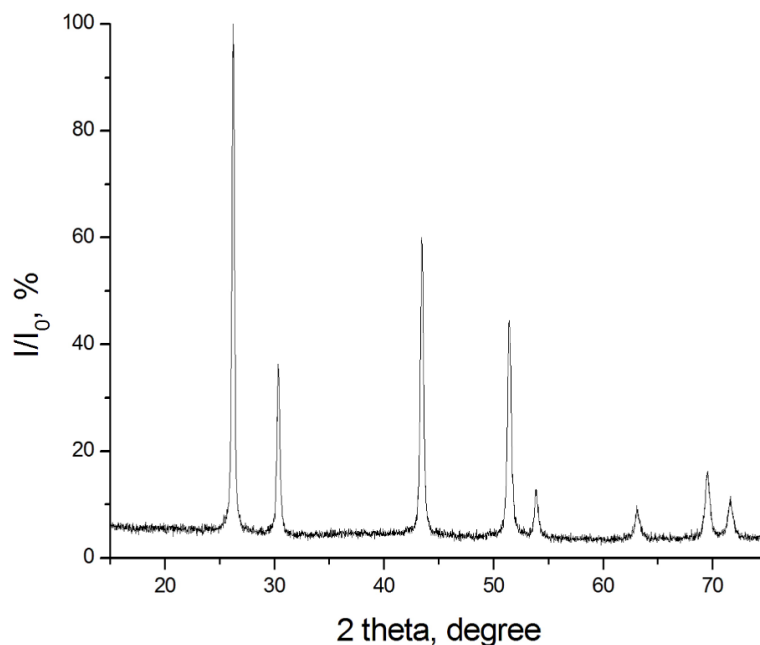


FIG. 1. X-ray powder diffraction for $Ba_4Y_3F_{17}:Yb(5.0 \text{ mol.}\%): Eu(0.1 \text{ mol.}\%)$ powder after annealing at 600 °C

TABLE 1. Unit cell parameters and X-ray coherent scattering domain for $\text{Ba}_4\text{Y}_3\text{F}_{17}$: Yb:Eu samples

Nominal composition	a , Å	X-ray coherent scattering domain, nm
$\text{Ba}_4\text{Y}_3\text{F}_{17}$:Yb(1.0 mol. %):Eu(0.1 mol. %)	5.9252(2)	73 ± 5
$\text{Ba}_4\text{Y}_3\text{F}_{17}$:Yb(5.0 mol. %):Eu(0.1 mol. %)	5.8960(2)	49 ± 3
$\text{Ba}_4\text{Y}_3\text{F}_{17}$:Yb(10.0 mol. %):Eu(0.1 mol. %)	5.8793(3)	75 ± 11
$\text{Ba}_4\text{Y}_3\text{F}_{17}$:Yb(1.0 mol. %):Eu(0.05 mol. %)	5.8890(3)	96 ± 15
$\text{Ba}_4\text{Y}_3\text{F}_{17}$:Yb(5.0 mol. %):Eu(0.05 mol. %)	5.8801(3)	> 100
$\text{Ba}_4\text{Y}_3\text{F}_{17}$:Yb(10.0 mol. %):Eu(0.05 mol. %)	5.8843(3)	> 100

Scanning electron microscopy revealed that the particles were about 100 nm without agglomeration (Fig. 2). The particle sizes well correlated with X-ray coherent scattering domains (Table 1), which means that all particles are single crystalline.

The real compositions were revealed by energy-dispersion analysis (Table 2). The content of the yttrium and barium are close to nominal content. In contrast, the contents of ytterbium and europium are higher than nominal ones, but it is lower than the error of analysis.

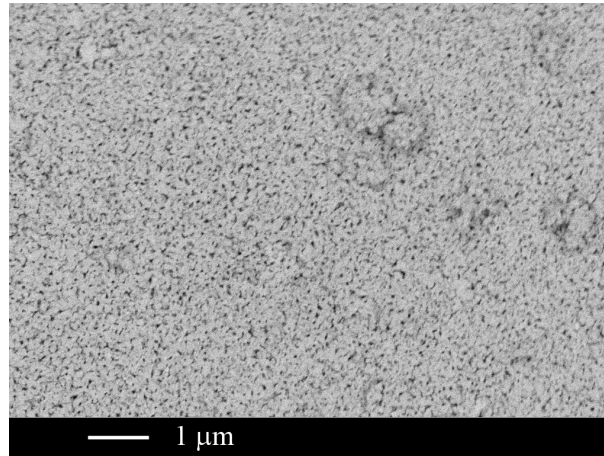


FIG. 2. The typical scanning electron microscopy image for $\text{Ba}_4\text{Y}_3\text{F}_{17}$:Yb (5.0 mol.%): Eu (0.1 mol.%) powder after annealing at 600 °C

TABLE 2. Compositions based on EDX analysis of $\text{Ba}_4\text{Y}_3\text{F}_{17}$: Yb:Eu samples

Initial nominal compositions	Real chemical compositions from EDX analysis
$\text{Ba}_4\text{Y}_3\text{F}_{17}$:Yb(1.0 mol. %):Eu(0.1 mol. %)	$\text{Ba}_{0.638}\text{Y}_{0.344}\text{Yb}_{0.014}\text{Eu}_{0.004}\text{F}_{2.362}$
$\text{Ba}_4\text{Y}_3\text{F}_{17}$:Yb(5.0 mol. %):Eu(0.1 mol. %)	$\text{Ba}_{0.568}\text{Y}_{0.364}\text{Yb}_{0.065}\text{Eu}_{0.004}\text{F}_{2.435}$
$\text{Ba}_4\text{Y}_3\text{F}_{17}$:Yb(10.0 mol. %):Eu(0.1 mol. %)	$\text{Ba}_{0.585}\text{K}_{0.021}\text{Y}_{0.363}\text{Yb}_{0.138}\text{Eu}_{0.004}\text{F}_{2.706}$
$\text{Ba}_4\text{Y}_3\text{F}_{17}$:Yb(1.0 mol. %):Eu(0.1 mol. %)	$\text{Ba}_{0.530}\text{K}_{0.014}\text{Y}_{0.387}\text{Yb}_{0.065}\text{Eu}_{0.003}\text{F}_{2.439}$
$\text{Ba}_4\text{Y}_3\text{F}_{17}$:Yb(10.0 mol. %):Eu(0.05 mol. %)	$\text{Ba}_{0.543}\text{Y}_{0.323}\text{Yb}_{0.131}\text{Eu}_{0.003}\text{F}_{2.457}$

The Raman spectrum contains several bands around 300 cm^{-1} and 600 cm^{-1} , which is characteristic for fluorides with narrow phonon spectra, see Fig. 3. On the other hand, the Raman spectra tail spreads above 800 cm^{-1} , which is non-typical for fluorides and may influence on the energy transfer processes.

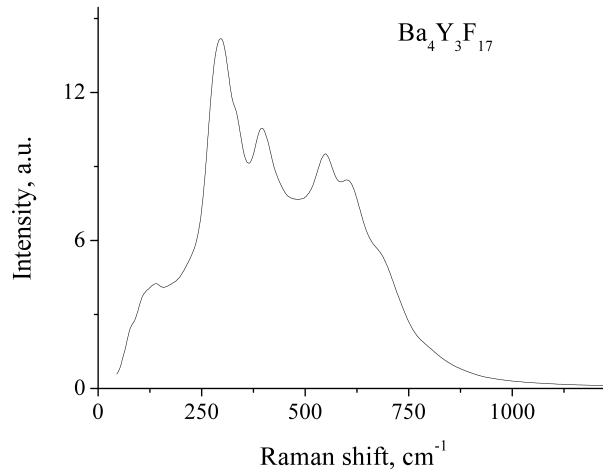


FIG. 3. Raman spectrum of $Ba_4Y_3F_{17}$ sample

Luminescence of Eu^{3+} ions can be excited by transitions from the 7F_0 ground state to the 5D_J manifolds, in particular, due to ${}^7F_0 \rightarrow {}^5D_2$ transition located around 465 nm with relatively large cross-section. The excitation of luminescence is also possible in UV spectral range as the result of transitions to 5I_J and 5K_J manifolds or the charge transfer states (Fig. 4). In order to avoid photodynamic processes initiated under intense UV pumping and following color center formation [23], which can distort the spectral-luminescent properties, excitation was performed at 296 , 399 and 463 nm (transitions ${}^7F_0 \rightarrow {}^5H_{5,6}$, 5L_6 and 5D_2 , correspondingly) only.

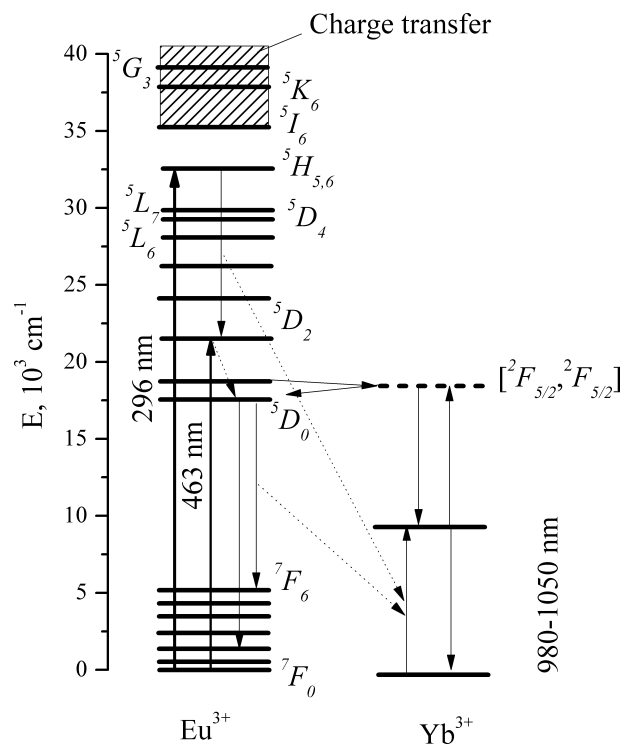


FIG. 4. Energy diagram of Eu^{3+} and Yb^{3+} ions and the energy transfer processes from Eu^{3+} to Yb^{3+} ions [24]

In the case of double doped samples by Eu^{3+} and Yb^{3+} ions, the energy gap between ${}^5\text{H}_{5,6}$ and ${}^5\text{D}_2$ states of Eu^{3+} ions is close to the ${}^2\text{F}_{7/2}$ - ${}^2\text{F}_{5/2}$ transition energy of Yb^{3+} ions. Following the results of [24] the energy transfer from Eu^{3+} to Yb^{3+} ions may occur through various mechanisms, for example: ${}^5\text{H}_{5,6}(\text{Eu}^{3+}) + {}^2\text{F}_{7/2}(\text{Yb}^{3+}) \rightarrow {}^5\text{D}_2(\text{Eu}^{3+}) + {}^2\text{F}_{5/2}(\text{Yb}^{3+})$, or ${}^5\text{D}_0(\text{Eu}^{3+}) + {}^2\text{F}_{7/2}(\text{Yb}^{3+}) \rightarrow {}^7\text{F}_6(\text{Eu}^{3+}) + {}^2\text{F}_{5/2}(\text{Yb}^{3+})$ as it is illustrated in Fig. 4.

The luminescence spectrum under pulsed excitation at 296 nm consists of Eu^{3+} transitions from ${}^5\text{D}_3$, ${}^5\text{D}_2$, ${}^5\text{D}_1$ and ${}^5\text{D}_0$ states localized in 400 – 750 nm range, as well as luminescence of Yb^{3+} ions ${}^2\text{F}_{5/2} \rightarrow {}^2\text{F}_{7/2}$, which is situated around 980 – 1000 nm (Fig. 5). The most intense luminescence bands at 465 nm, 488 nm and 511 nm correspond to ${}^5\text{D}_2 \rightarrow {}^7\text{F}_{0,2,3}$ transitions, at 526 nm, 538 nm and 557 nm bands – to ${}^5\text{D}_1 \rightarrow {}^7\text{F}_{0,1,2}$ and at 576 nm, 592 nm, 617 nm and 699 nm – to ${}^5\text{D}_0 \rightarrow {}^7\text{F}_{0,1,2,4}$ transitions, respectively. The NIR luminescence of Yb^{3+} ions is evidence of the energy transfer processes from Eu^{3+} to Yb^{3+} ions. At the same time, the luminescence of ${}^2\text{F}_{5/2}$ - ${}^2\text{F}_{7/2}$ of Yb^{3+} ions was not detected for the case of excitation at 399 nm or 463 nm.

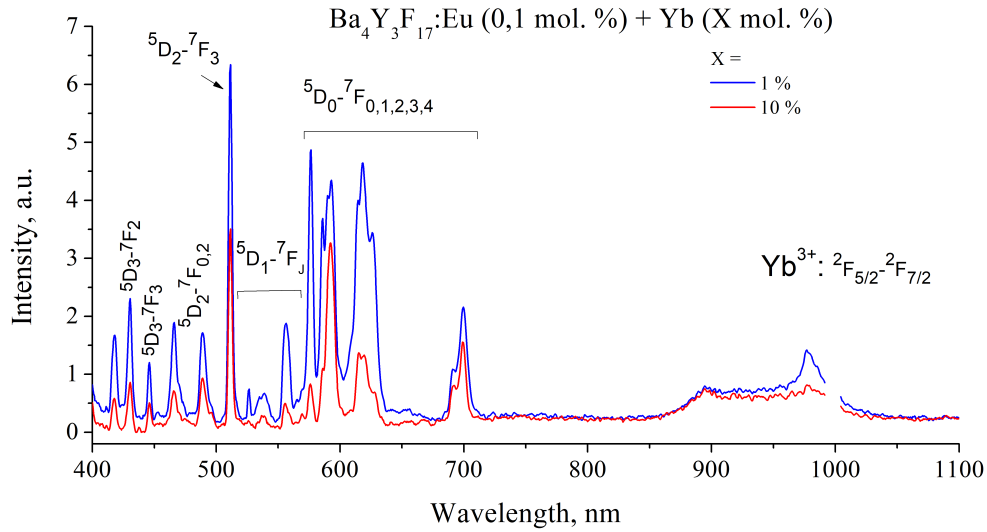


FIG. 5. Typical luminescence spectra of $\text{Ba}_4\text{Y}_3\text{F}_{17}:\text{Yb}:\text{Eu}$ samples under pulsed excitation at 296 nm

The energy transfer coefficients from Eu^{3+} to Yb^{3+} were estimated from the luminescence spectra using expression (1):

$$q^E = \frac{\int I^{Yb}(\lambda) d\lambda}{\int (I^{Yb}(\lambda) + I^{Eu}(\lambda)) d\lambda} \times 100 \%, \quad (1)$$

where $I^{Yb}(\lambda)$ is the luminescence intensity of Yb^{3+} and $I^{Eu}(\lambda)$ is the luminescence intensity of Eu^{3+} (Table 3). The increase of doping level leads to some saturation of energy transfer coefficient most probably due to luminescence concentration quenching effect. Thus there should be some optimal content ratio for Yb/Eu ions contents.

TABLE 3. Energy transfer coefficients (%) from Eu^{3+} to Yb^{3+} in $\text{Ba}_4\text{Y}_3\text{F}_{17}:\text{Yb}:\text{Eu}$ samples

Eu content, mol. %	Yb content, mol. %		
	1.0	5.0	10.0
0.05	8 ± 1	5 ± 1	9 ± 1
0.10	11 ± 1	15 ± 1	9 ± 1

It is exhibited in fluorescence kinetics. The luminescence decays of $\text{Ba}_4\text{Y}_3\text{F}_{17}:\text{Yb}^{3+}:\text{Eu}^{3+}$ samples from ${}^5\text{D}_1$ and ${}^5\text{D}_0$ states of Eu^{3+} at 556 nm and 617 nm, correspondingly, and from ${}^2\text{F}_{5/2}$ of Yb^{3+} ion (at 1020 nm) were investigated under the excitation at 296 nm (Figs. 6 and 7, respectively). The kinetics from ${}^5\text{D}_1$ state (Fig. 6a) exhibit the long lasting raise (few ms for $\text{Ba}_4\text{Y}_3\text{F}_{17}:\text{Eu}^{3+}$ (0.1 mol. %)), which is evidence for cross-relaxation effects between

manifolds of Eu^{3+} ions [22]. However, the lifetime of 5D_1 state is weakly dependent on Yb^{3+} ions' doping level. The luminescence decay from 5D_0 state of Eu^{3+} ions is more complicated and consists of fast and slow components. The contribution of the last one grows with a simultaneous increase of Yb^{3+} content, which can be attributed to reverse energy transfer from Yb^{3+} to Eu^{3+} via cooperative processes [25].

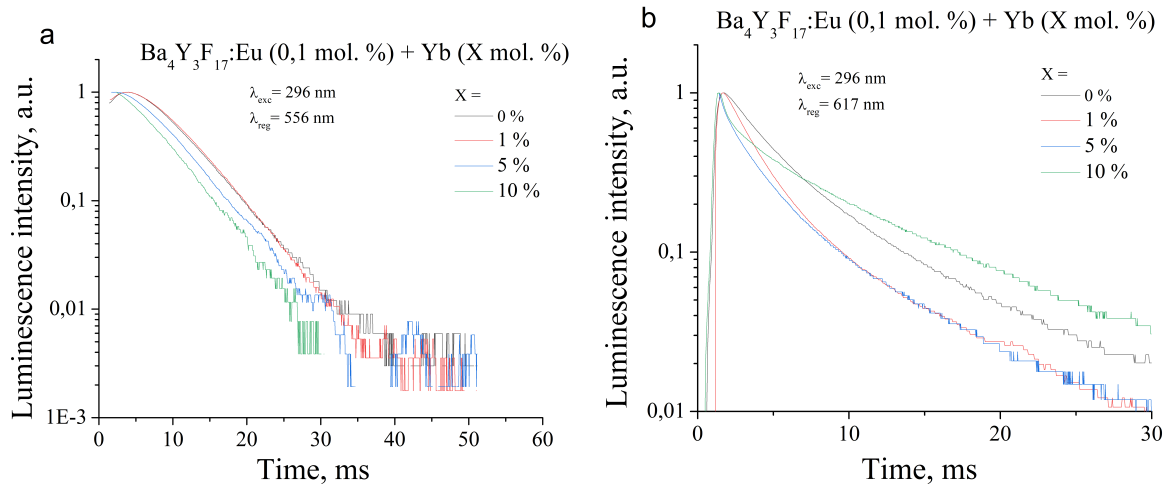


FIG. 6. Luminescence decays of $Ba_4Y_3F_{17}:Eu(0.1 \text{ mol.}\%):Yb(x \text{ mol.}\%)$, $x = 0, 1.0, 5.0, 10.0$ samples at 556 nm (from 5D_1 state) (a) and 617 nm (from 5D_0) (b) under 296 nm excitation

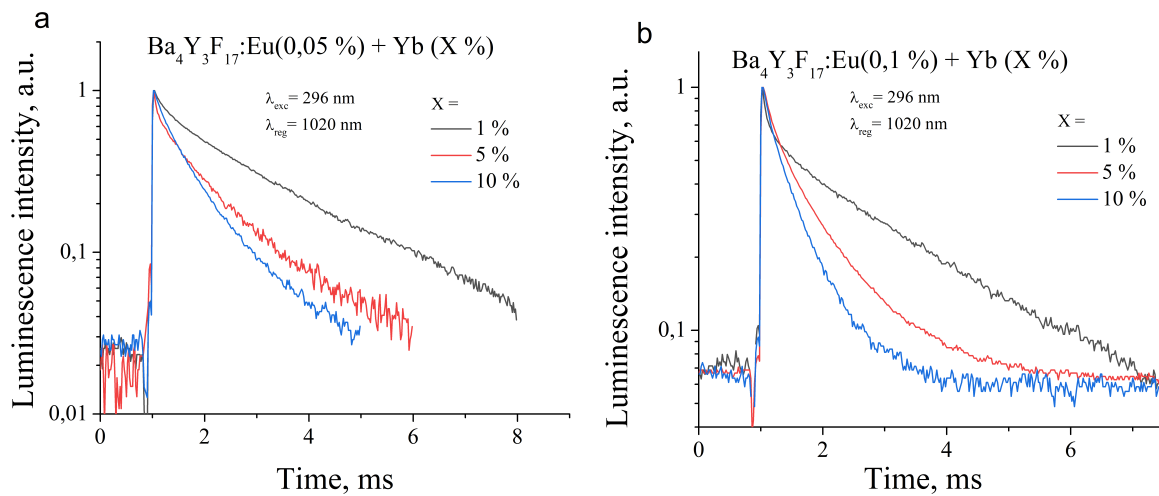


FIG. 7. Luminescence decay kinetics of $Ba_4Y_3F_{17}:Yb:Eu$ samples at 1020 nm upon 296 nm excitation

The luminescence decays of Yb^{3+} ions registered at 1020 nm under excitation at 296 nm are not exponential too, and look faster with the increase of Yb^{3+} ions content. It also proves the reverse energy transfer processes from two excited Yb^{3+} ($^2F_{5/2}$) to 5D_1 manifold of Eu^{3+} ions.

Since the dependence of the luminescence decay of Eu^{3+} ions at 617 nm differs from the exponential law, the lifetimes were estimated as the average ones according to the formula (2):

$$t_{avg} = \frac{\int t \cdot I(t) dt}{\int I(t) dt}, \quad (2)$$

where $I(t)$ is dependence of luminescence intensity on time, t – time. The results of calculation are presented in Table 4.

The average luminescence lifetimes of 5D_1 manifold of Eu^{3+} ions decreases with increasing Yb^{3+} ions concentration, while the lifetimes assumed to 5D_0 manifold increases. This suggests that energy transfer from Eu^{3+}

TABLE 4. Average luminescence lifetimes of 5D_0 , 5D_1 of Eu^{3+} and ${}^2F_{5/2}$ of Yb^{3+} ions in $\text{Ba}_4\text{Y}_3\text{F}_{17}:\text{Eu}(0.1 \text{ mol.}\%):\text{Yb}(x \text{ mol.}\%)$ $x = 0, 1.0, 5.0, 10.0$ samples under excitation at 296 nm

Registration wavelengths	617 nm	556 nm	1020 nm	
	(from 5D_0)	(from 5D_1)	(from ${}^2F_{5/2}$)	
Eu content, mol.%	Eu = 0.10	Eu = 0.10	Eu = 0.05	Eu = 0.10
Yb = 0	$3.0 \pm 0.1 \text{ ms}$	$10.3 \pm 0.1 \text{ ms}$	—	—
Yb = 1.0	$2.2 \pm 0.1 \text{ ms}$	$10.2 \pm 0.1 \text{ ms}$	$2.0 \pm 0.1 \text{ ms}$	$2.0 \pm 0.1 \text{ ms}$
Yb = 5.0	$5.6 \pm 0.1 \text{ ms}$	$8.4 \pm 0.1 \text{ ms}$	$0.9 \pm 0.1 \text{ ms}$	$0.8 \pm 0.1 \text{ ms}$
Yb = 10.0	$8.8 \pm 0.1 \text{ ms}$	$7.3 \pm 0.1 \text{ ms}$	$0.7 \pm 0.1 \text{ ms}$	$0.5 \pm 0.1 \text{ ms}$

to Yb^{3+} ions occurs from higher-lying states than the 5D_0 one, which can cause a low quantum yield of ytterbium down-conversion luminescence, since these states are characterized by shorter lifetimes. Therefore, taking into account the absence of the $\text{Eu}^{3+}-\text{Yb}^{3+}$ energy transfer under excitation at 399 nm and 465 nm and despite the fact of existing of luminescence from 5D_3 state of Eu^{3+} , the most probable mechanism is ${}^5H_{5,6}(\text{Eu}^{3+})-{}^2F_{7/2}(\text{Yb}^{3+}) \rightarrow {}^5D_2(\text{Eu}^{3+})-{}^2F_{5/2}(\text{Yb}^{3+})$ energy transfer process.

Finally, using the integrating sphere, the quantum yield of Yb^{3+} luminescence was measured under the 296 nm excitation (Table 5).

TABLE 5. Quantum yields for $\text{Ba}_4\text{Y}_3\text{F}_{17}:\text{Yb}:\text{Eu}$ samples at 296 nm excitation

Eu content mol, %	Yb content, mol, %		
	1.0	5.0	10.0
0.05	$0.4 \pm 0.05 \%$	$0.2 \pm 0.05 \%$	$0.3 \pm 0.05 \%$
0.10	$0.3 \pm 0.05 \%$	$0.4 \pm 0.05 \%$	$0.2 \pm 0.05 \%$

The maximum quantum yields for $\text{Ba}_4\text{Y}_3\text{F}_{17}$ samples were recorded for the Eu/Yb ratios of 0.1/1 and 0.1/10.0 and amounted to 0.4 %. It is obvious that competition of mutually oppositely directed energy transfer processes has determined such a small value of quantum yield of down-conversion luminescence of Yb^{3+} ions in the studied samples.

4. Conclusions

The single-phase solid solutions $\text{Ba}_4\text{Y}_3\text{F}_{17}:\text{Yb}:\text{Eu}$ with fluorite-type structure were synthesized by co-precipitation from aqueous solution technique. The average particle size was approximately 100 nm without agglomeration, which correlated with X-ray coherent scattering domains. The luminescence spectra from all 5D_J manifold of Eu^{3+} ions were observed under irradiation at various wavelengths, whereas the sensitized down-conversion luminescence of Yb^{3+} ions, which was detected for the 296 nm excitation only, was not observed for resonant excitation to 5D_J states of Eu^{3+} . Moreover, the reverse cooperative energy transfer from a pair of Yb^{3+} ions in the excited ${}^2F_{5/2}$ state to 5D_0 state of Eu^{3+} ions was observed. The quantum yield of Yb^{3+} down-conversion luminescence was measured using the integrating sphere. The maximal value was 0.4 % for the Eu/Yb ratios of 0.1/1.0 and 0.1/10.0, which appears because of competition of mutually opposite directed energy transfer processes between Eu^{3+} and Yb^{3+} ions.

Acknowledgements

This work was supported by the Russian Science Foundation, grant 17-73-20352. Authors thank to M. N. Mayakova for valuable help in sample preparation.

References

- [1] Weber E.R. Photovoltaics moving into the terawatt age. *Proc. SPIE, Next Generation Technologies for Solar Energy Conversion VIII*, 2017, **10368**, 1036803.
- [2] Lehr J., Langenhorst M., et al. Energy yield of bifacial textured perovskite/silicon tandem photovoltaic modules. *Solar Energy Materials and Solar Cells*, 2020, **208**, 110367 P. 1–9.
- [3] Im J.-H., Lee C.-R., et al. 6.5 % efficient perovskite quantum-dot-sensitized solar cell. *Nanoscale*, 2011, **3**, P. 4088–4093.
- [4] Han G., Zhang S., et al. Towards high efficiency thin film solar cells. *Prog. Mater. Sci.*, 2017, **87**, P. 246–291.
- [5] Huang X., Han S., Huang W., Liu X., Enhancing solar cell efficiency: the search for luminescent materials as spectral converters. *Chem. Soc. Rev.*, 2013, **42**, P. 173–201.
- [6] Moraitis P., Schropp R.E.I., Sark W.G.J.H.M. Nanoparticles for luminescent solar concentrators – a review. *Opt. Mater.*, 2018, **84**, P. 636–645.
- [7] Green M.A., Bremner S.P. Energy conversion approaches and materials for high efficiency photovoltaics. *Nat. Mater.*, 2017, **16**, P. 23–34.
- [8] Trupke T., Green M.A., Würfel P. Improving solar cell efficiencies by down-conversion of high-energy photons. *J. Appl. Phys.*, 2002, **92**, P. 1668–1674.
- [9] Yu P., Yao Y., et al. Effects of plasmonic metal core-dielectric shell nanoparticles on the broadband light absorption enhancement in thin film solar cells. *Sci. Rep.*, 2017, **7**, P. 7696.
- [10] Fang D., Zhang X., et al. Application of bidirectional (up and down)-conversion luminescence material ($GdBO_3:Yb^{3+}/Tb^{3+}$) in $CdSe_{0.4}S_{0.6}$ quantum dot-sensitized solar cells. *Opt. Mater.*, 2019, **88**, P. 80–90.
- [11] Gu H., Wang J., et al. The core-shell-structured $NaYF_4:Er^{3+}, Yb^{3+}@NaYF_4:Eu^{3+}$ nanocrystals as dual-mode and multifunctional luminescent mechanism for high-performance dye-sensitized solar cells. *Mater. Res. Bull.*, 2018, **108**, P. 219–225.
- [12] Buarque J.M.M., Manzani D., et al. SiO_2-TiO_2 doped with $Er^{3+}/Yb^{3+}/Eu^{3+}$ photoluminescent material: a spectroscopy and structural study about potential application for improvement of the efficiency on solar cells. *Mater. Res. Bull.*, 2018, **107**, P. 295–307.
- [13] Rajesh D., Dousti M.R., Amjad R.J., Camargo A.S.S. Quantum cutting and upconversion investigations in Pr^{3+}/Yb^{3+} co-doped oxyfluorotellurite glasses. *J. Non-Cryst. Solids*, 2016, **450**, P. 149–155.
- [14] Kuznetsov S.V., Nizamutdinov A.S., et al. Synthesis and down-conversion luminescence of $Ba_4Y_3F_{17}:Yb:Pr$ solid solutions for photonics. *Nanosystems: Physics, Chemistry, Mathematics*, 2019, **10**, P. 190–198.
- [15] Li T., Li Y., et al. Novel $Ba(Gd_{1-x}Y_x)_{0.78}F_5: 20 \text{ mol } \% Yb^{3+}, 2 \text{ mol } \% Tm^{3+}$ ($0 < x < 1.0$) solid solution nanocrystals: A facile hydrothermal controlled synthesis, enhanced upconversion luminescent and paramagnetic properties. *J. Alloys Comp.*, 2018, **740**, P. 1204–1214.
- [16] Karbowski M., Cichos J. Does $BaYF_5$ nanocrystals exist? The BaF_2-YF_3 solid solution revisited using photoluminescence spectroscopy. *Journal of Alloys and Compounds*, 2016, **673**, P. 258–264.
- [17] Fedorov P.P., Kuznetsov S.V., et al. Coprecipitation from aqueous solutions to prepare binary fluorides. *Russian J. of Inorg. Chem.*, 2011, **56**, P. 1525–1531.
- [18] Kuznetsov S.V., Proydakova V.Yu., et al. Synthesis and quantum yield investigations of the $Sr_{1-x-y}Pr_xYb_yF_{2+x+y}$ luminophores for photonics. *Nanosystems: Physics, Chemistry, Mathematics*, 2018, **9**, P. 663–668.
- [19] Kuznetsov S.V., Morozov O.A., et al. $Ca_{1-x-y}Yb_xPr_yF_{2+x+y}$ solid solution powders as a promising materials for crystalline silicon solar energetics. *Nanosystems: Physics, Chemistry, Mathematics*, 2018, **9**, P. 259–265.
- [20] Kuznetsov S.V., Nizamutdinov A.S., et al. Synthesis and Luminescence of $Sr_{1-x-y}Yb_xEu_yF_{2+x+y}$. Solid Solutions for Photonics. *Inorganic Materials*, 2019, **55**, P. 1031–1038.
- [21] Yasyrkina D.S., Kuznetsov S.V., et al. Dependence of quantum yield of up-conversion luminescence on the composition of fluorite-type solid solution $NaY_{1-x-y}Yb_xEr_yF_4$. *Nanosystems: Physics, Chemistry, Mathematics*, 2013, **4**, P. 648–656.
- [22] Kuznetsov S.V., Fedorov P.P., et al. Synthesis of $Ba_4R_3F_{17}$ (R stands for Rare-Earth Elements) Powders and Transparent Compacts on Their Base. *Russian Journal of Inorganic Chemistry*, 2010, **55**, P. 484–493.
- [23] Semashko V.V. Problems in searching for new solid-state UV- and VUV active media: the role of photodynamic processes. *Phys. of Solid State*, 2005, **47**, P. 1507–1511.
- [24] Van der Voort D., Dirksen G.J., Blasse G. Luminescence study of $Eu^{3+}-O^{2-}$ associates in fluorides: CaF_2 , $RbCdF_3$, and $RbCaF_3$. *J. Phys. Chem. Solids*, 1992, **53**, P. 219–225.
- [25] Dwivedi Y., Zilio S.C. Infrared cascade and cooperative multicolor upconversion emissions in $Y_8V_2O_{17}:Eu:Yb$ nanophosphors. *Opt. Express*, 2013, **21**, P. 4717–4727.

CeO₂ nanoparticles as free radical regulators in biological systems

M. M. Sozarukova¹, E. V. Proskurnina², A. E. Baranchikov¹, V. K. Ivanov¹

¹Kurnakov Institute of General and Inorganic Chemistry, Russian Academy of Sciences,
Leninsky Prospect, 31, Moscow, 119991, Russia

²Research Centre for Medical Genetics, Moskvorechie St, 1, Moscow, 115522, Russia
s_madinam@bk.ru, proskurnina@gmail.com, a.baranchikov@yandex.ru, van@igic.ras.ru

PACS 68.65.k, 81.20.n, 82.70.Dd, 87.85.Rs

DOI 10.17586/2220-8054-2020-11-3-324-332

Cerium dioxide nanoparticles possess unique physical and chemical properties, among which the enzyme-like activity is of particular interest. In particular, they are able to perform the functions of pro- and antioxidant enzymes, such as superoxide dismutase (SOD), catalase, and peroxidase. Due to the advantages associated with pH and temperature stability and low cost, CeO₂ nanoparticles can be considered as promising mimetics of these enzymes. In this paper, the antioxidant activity of a citrate-stabilized colloidal suspension of CeO₂ nanoparticles has been studied using chemiluminescence in model systems generating superoxide anion radical and hydrogen peroxide. In the lucigenin/xanthine/xanthine oxidase system, generating a superoxide anion radical, CeO₂ nanoparticles exhibit antioxidant properties increasing upon conjugation with SOD. When interacting with hydrogen peroxide, CeO₂ nanoparticles exhibit peroxidase-like activity. In the combined ROS generating system, lucigenin/Co(II)/H₂O₂, CeO₂ nanoparticles demonstrated prooxidant activity.

Keywords: cerium dioxide nanoparticles, superoxide anion radical, hydrogen peroxide, nanozymes, superoxide dismutase, peroxidase, chemiluminescence.

Received: 19 February 2020

1. Introduction

Enzymes are biocatalysts with high substrate specificity which increase the rate of biochemical reactions by several orders of magnitude. The catalytic properties of natural enzymes decrease in the presence of inhibitors, as well as with changes in temperature, pH, etc. One of the main limitations of the widespread use of enzymes is the high cost of their synthesis, isolation and purification [1]. Nanozymes have several advantages over natural enzymes, namely, high specificity and sensitivity, reproducibility of characteristics in a wide temperature and pH range, low cost, the possibility of additional functionalization and biocompatibility [2–5]. In this regard, at present, special attention of researchers is directed to the creation of enzyme mimetics based on nanoparticles – alternative systems that can effectively mimic the catalytic activity of natural enzymes.

The role of free radicals (reactive oxygen species, ROS) in the body is extremely high. They affect the physicochemical properties of biological membranes, their permeability and structure, are involved in cell signalling and maintenance of homeostasis, however, uncontrolled free radical processes can lead to cell damage [6]. Oxidative stress is defined as a pathological condition associated with excessive production of free radicals and their biochemically active intermediates and metabolites, exceeding the protective capabilities of the cell's antioxidant system and leading to destructive consequences for the cell and the organism as a whole [7]. The application of nanoparticles in experimental and clinical conditions is exponentially growing due to a wide range of their functional properties, but at the same time it increases the potentially unpredictable and adverse effects of their impact on the body [8]. Oxidative stress induced by nanoparticles leads to pathophysiological events such as damage to proteins, lipids, DNA, inflammation, cytotoxic effects, inhibition of antioxidant enzymes, activation of the radical-producing function of phagocytes, mitochondrial dysfunction and apoptosis [9].

Nanodisperse cerium dioxide is a promising material that is widely used in modern high-tech industries [10]. In recent years, some unique biochemical enzyme-like properties of cerium dioxide were revealed, which allow it to perform the functions of some natural enzymes such as superoxide dismutase, catalase, peroxidase. Numerous studies on cell cultures and animals have demonstrated the effective radical-scavenging properties of nanocrystalline CeO₂ [11–14]. The ability to act as a nanozyme in combination with relatively low toxicity makes CeO₂ nanoparticles a promising drug for the correction of oxidative stress. In this regard, it seems relevant and necessary to conduct comprehensive studies of CeO₂ nanoparticles as a catalyst/inhibitor of free radical reactions.

One of the most important primary free radicals is the superoxide anion radical. The dismutation of superoxide anion radicals inevitably leads to the formation of hydrogen peroxide molecules that can easily penetrate cell membranes. Recently, more and more attention has been paid to the role of hydrogen peroxide, not only as a cytotoxic component found during phagocytosis, the activity of mitochondria and microsomes, but also to its participation in

the regulation of cellular signalling and transcription factors. Thus, in the present work, we have comprehensively studied the enzyme-like properties of the citrate-stabilized CeO₂ sol with respect to two key participants in the free radical homeostasis – superoxide anion radical and hydrogen peroxide, using the sensitive, informative, and express chemiluminescent method. Moreover, the study involved both standalone biochemical models for generation of ·O₂⁻ and H₂O₂, and a combined ROS-generating system containing their mixture.

2. Materials and methods

2.1. Synthesis and physicochemical study of citrate-stabilized CeO₂ sol

The synthesis of citrate stabilized cerium dioxide sol was carried out according to the procedure based on the thermohydrolysis of the aqueous solution of ammonium cerium(IV) nitrate [15]. Aqueous solution of (NH₄)₂Ce(NO₃)₆ (extra pure grade, Sigma-Aldrich, USA) with a concentration of 100 g/l was kept for 24 h in an oven at 95 °C. The formed precipitate was separated from the mother liquor by centrifugation followed by triple washing with isopropanol. The washed precipitate was redispersed in deionized water, followed by boiling for 1 h with constant stirring until complete removal of isopropanol. The concentration of the CeO₂ sol was determined by the thermogravimetric method. The obtained colloidal solution of CeO₂ was stabilized with ammonium citrate C₆H₁₄O₇N₂ (disubstituted ammonium citrate, extra-pure grade, Sigma-Aldrich, USA) with 1:1 molar ratio.

The citrate-stabilized cerium dioxide sol was analyzed by X-ray diffraction (XRD), transmission electron microscopy (TEM) and dynamic light scattering (DLS). X-ray diffraction analysis of nanocrystalline CeO₂ samples was carried out on a Bruker D8 Advance diffractometer (CuK α radiation, θ - 2θ geometry). The diffraction peaks were identified using the ICDD PDF2 data bank. The average hydrodynamic diameter of CeO₂ nanoparticles was estimated by the DLS method using a Photocor Complex analyzer. The microstructure of the samples was studied by TEM on a Leo 912 AB Omega electron microscope at an accelerating voltage of 100 kV.

2.2. Synthesis of superoxide dismutase conjugated with cerium dioxide nanoparticles

A stock solution of superoxide dismutase (SOD, Sigma-Aldrich, USA, S8160-15KU) with an activity of 2400 U/ml ($c = 25 \mu\text{M}$) was obtained by dissolving a portion of SOD in deionized water. The SOD-CeO₂ conjugate was prepared according to the procedure described by Gil et al. [16]. A SOD working solution with an activity of 100 U/ml ($c = 1 \mu\text{M}$) was mixed with 12 mM citrate-stabilized CeO₂ sol. The resulting mixture was incubated at room temperature in a dark place for 1 and 2.5 hours. To determine the possible effect of citrate ions, a SOD-ammonium citrate mixture with corresponding concentration was prepared the similar way. Individual solutions of SOD, ammonium citrate, and stabilized CeO₂ sol were incubated together with conjugates, under the same conditions.

2.3. Study of SOD-like activity by the chemiluminescent method in the lucigenin/xanthine/xanthine oxidase system

2.3.1. Preparation of solutions. SOD-like activity was determined by chemiluminometry in the xanthine/xanthine oxidase model system in the presence of a chemiluminescent probe, lucigenin, which is selective for the superoxide anion radical. Phosphate buffer solutions (PBS) with a concentration of 100 mM and a pH of 7.4 and 8.6 were prepared by dissolving a weighed portion of KH₂PO₄ (Sigma-Aldrich, USA) in 1.00 L of distilled water, followed by adjusting to the desired pH using granular KOH (Sigma-Aldrich, USA) and/or concentrated HCl solution (Sigma-Aldrich, USA).

Solutions of xanthine (3,7-dihydropurin-2,6-dione, Sigma-Aldrich, USA) and lucigenin (10,10'-dimethyl-9,9'-bicridinium dinitrate, Sigma-Aldrich, USA) with working concentrations of 1 mM were prepared by dissolving weighed portions in the PBS with a pH 8.6 and 7.4, respectively. A xanthine oxidase working solution (Sigma-Aldrich, USA, X1875-25UN) with an activity of 0.11 U/ml was prepared by diluting the initial PBS suspension (pH 7.4). Before CL-measurements, the working solution of the enzyme was kept for 15 min at room temperature. By definition of catalytic activity, one unit of the enzyme in 1 min converts 1.0 μmol of xanthine to uric acid at 25 °C and a pH of 7.5.

2.3.2. Registration of chemiluminescence. Chemiluminescence was recorded on a Lum-100 single-channel chemiluminometer (DISoft, Russia) at 37 °C. Aliquots of xanthine ($c = 25 \mu\text{M}$), lucigenin ($c = 25 \mu\text{M}$) and the analyzed sample were added to a plastic cuvette containing PBS ($c = 100 \text{ mM}$, pH 7.4). The background glow was recorded for 30 – 60 s, then an aliquot of xanthine oxidase ($a = 11 \text{ mU/ml}$) was added. The total volume of the system was 1000 ml. Each experimental point presented in the work was obtained in no less than three parallel experiments ($n = 3$). The original PowerGraph software product was used to conjugate the computer and the instrument.

The light sum was used as an analytical signal – the area under the CL curve for a certain period of time (5 min).

2.4. The study of peroxidase/catalase activity by the chemiluminescent method in the luminol/H₂O₂ system

2.4.1. *Preparation of solutions.* The peroxidase/catalase activity of the analysed samples was studied in the luminol/H₂O₂ system. A solution of luminol (5-amino-1,2,3,4-tetrahydro-1,4-phthalazinedione, 3-aminophthalic acid hydrazide, Sigma-Aldrich, USA) with $c = 1$ mM was prepared by dissolving a sample in PBS (pH 7.4). A working solution of hydrogen peroxide with a concentration of 2.5 M was prepared by diluting 33 % H₂O₂ stock solution (Sigma-Aldrich, USA) with distilled water.

2.4.2. *Registration of chemiluminescence.* Chemiluminescence was recorded on a single-channel Lum-100 chemiluminometer at room temperature. Aliquots of luminol ($c = 50$ μM) and the analysed sample were added to a plastic cuvette containing PBS ($c = 100$ mM, pH 7.4). The background glow was recorded for 30 – 60 s, then an aliquot of H₂O₂ was added ($c = 50$ mM). The total volume of the system was 1000 ml. Each experimental point presented in the work was obtained in no less than three parallel experiments ($n = 3$).

2.5. The study of pro- and antioxidant activity in the lucigenin/Co(II)/H₂O₂ system

2.5.1. *Preparation of solutions.* An analytical model of lucigenin/Co(II)/H₂O₂ was used as a combined ROS generation system (includes a superoxide anion radical, hydrogen peroxide, hydroxyl radical).

Co(II) solutions with a concentration of 20 mM were prepared by dissolving a weighed portion of CoCl₂ · 6H₂O (Sigma-Aldrich, USA) in distilled water. A solution of dithiothreitol ((2*S*, 3*S*)-1,4-bis(sulfanyl)butane-2,3-diol, Sigma-Aldrich, USA) with a concentration of 30 mM was obtained by dissolving a sample in distilled water. A working solution of hydrogen peroxide with a concentration of 0.3 M was prepared by diluting 33 % H₂O₂ stock solution with distilled water.

2.5.2. *Registration of chemiluminescence.* Chemiluminescence was recorded on a 12-channel Lum-1200 chemiluminometer (DISoft, Russia) at room temperature. Aliquots of Co(II) ($c = 0.6$ mM), lucigenin ($c = 0.1$ mM) and the analysed sample were added to a cuvette containing PBS ($c = 100$ mM, pH 8.6). The background glow was recorded for 30 – 60 s, then, without interrupting the recording of the analytical signal, an aliquot of H₂O₂ ($c = 3.0$ mM) was introduced into the system. The total volume of the system was 1000 ml. Each experimental point presented in the work was obtained in no less than three parallel experiments ($n = 3$).

The light sum in 20 min was used as an analytical signal.

3. Results and discussion

An electrostatically stabilized sol of nanocrystalline cerium dioxide was obtained by thermohydrolysis of an aqueous solution of ceric ammonium nitrate. The CeO₂ content in the sol was 23 g/L (0.13 M). According to XRD data, the obtained sol contained single phase cerium dioxide (PDF2 34-0394). The particle size, estimated by the Scherrer ratio, was 3 nm. The average hydrodynamic diameter of the nanoparticles obtained by the DLS method was found to be 10 – 11 nm. Data on the particle size and phase composition of the obtained material were confirmed by the results of TEM and electron diffraction analysis of the CeO₂ sol.

The antioxidant activity of the samples of citrate-stabilized CeO₂ sol, SOD, CeO₂–SOD and ammonium citrate-SOD conjugates at the time of preparation and after incubation for 1 and 2.5 hours at room temperature was evaluated using the chemiluminescent method in the xanthine/xanthine oxidase system in the presence of lucigenin and a selective CL probe for a superoxide anion radical. Fig. 1 shows chemiluminograms for various concentrations of CeO₂ nanoparticles. The addition of a citrate-stabilized cerium dioxide sol to the lucigenin/xanthine/xanthine oxidase system led to a decrease in the stationary level of CL, which indicates the presence of SOD-like activity. Earlier, we estimated the SOD-like activity of 1 mmol/L citrate-stabilized colloidal solution of CeO₂ in units of SOD activity, amounting 2.00 ± 0.03 nmol/L, which is approximately 6 orders of magnitude lower than the activity of the native enzyme.

Similar chemiluminograms are recorded when SOD is introduced into the system (Fig. 2a). The effect of luminescence quenching linearly depends on the concentration of SOD (Fig. 2b):

$$\Delta S, (\times 10^3 \text{ imp}) = S_0 - S = (3.9 \pm 0.6) \times c (\text{SOD, nmol/l}) + (6.8 \pm 1.0), r = 0.992 (P = 0.95, n = 5),$$

where S_0 and S are light sums for the control and experiment, respectively.

Based on the study of the antioxidant properties of individual samples of citrate-stabilized CeO₂ sol and individual SOD, working concentrations were selected (c (CeO₂, ammonium citrate) = 0.12 mM, and (SOD) = 1 U/ml, a (SOD) = 10 nM) and CeO₂-SOD, ammonium citrate-SOD conjugates were prepared. Relative ΔS_{rel} value was calculated from chemiluminograms (Fig. 3), according to the formula:

$$\Delta S_{rel}, \% = \frac{S_0 - S}{S_0} \times 100 \%,$$

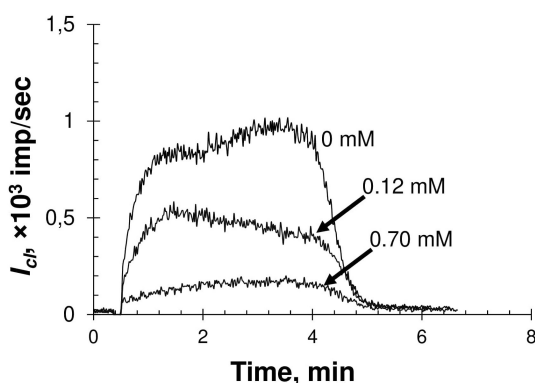


FIG. 1. Chemiluminograms of a citrate-stabilized colloidal solution of CeO₂ (concentrations are shown in the figure) in the lucigenin (25 μM) + xanthine (25 μM) + xanthine oxidase (11 mU/ml) system

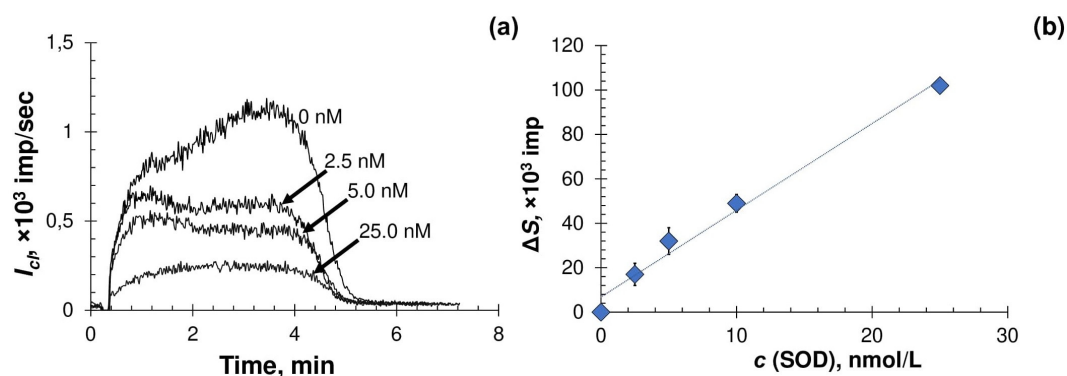


FIG. 2. (a) CL-curves for SOD (concentrations are shown in the figure) in the system containing lucigenin (25 μM) + xanthine (25 μM) + xanthine oxidase (11 mU/ml), (b) the area difference (ΔS_j) under the CL curves, proportional to the number of captured superoxide anion radicals, as a function of the SOD concentration; light sum was calculated in 5 min

where S_0 and S are light sums for the control and experiment, respectively.

According to the data obtained, the CeO₂-SOD conjugate exhibits increased enzyme-like activity which does not depend on the incubation time, more effectively inhibiting superoxide anion radicals in comparison with the citrate-stabilized colloidal CeO₂ solution and individual superoxide dismutase. This result indicates the synergistic effect of CeO₂ nanoparticles and SOD absorbed on their surface, which is in good agreement with published data [16, 17].

Superoxide anion radical (SAR) is one of the primary free radicals formed in living systems. The main sources of SAR in the cell are mitochondria and enzyme systems: xanthine oxidase [18], lipoxygenase [19], cyclooxygenase [20, 21], NADPH oxidase [22]. The SAR serves as a precursor to other active forms of oxygen – hydrogen peroxide, hydroxyl radical, peroxynitrite [23]. For normal functioning a certain level of SAR must be maintained in the cell, however, its uncontrolled formation during pathology can lead to the development of lipid oxidative stress, damage to membranes and cellular apoptosis.

Superoxide dismutase catalyses the disproportionation of superoxide radical anions to molecular oxygen and hydrogen peroxide. The mechanism of SOD action is presented by the following partial reactions (1), (2):



where M is a transition metal cofactor of the active center of the enzyme (Cu, Mn, Fe, and Ni) [1, 24]. The most common type of enzyme in eukaryotic cells is Cu,Zn-SOD, localized in the cytosol [1, 25].

The ability to catalyze the dismutation of superoxide anion radical was one of the first discovered enzyme-like properties of nanocrystalline cerium dioxide [26–29]. The obtained results indicate the important role of the surface state (the presence of Ce(III) in the surface layer) and the size (smaller particles showed greater activity) of CeO₂ nanoparticles. Several methods have been proposed for increasing the SOD-like activity of nanocrystalline CeO₂. Lee

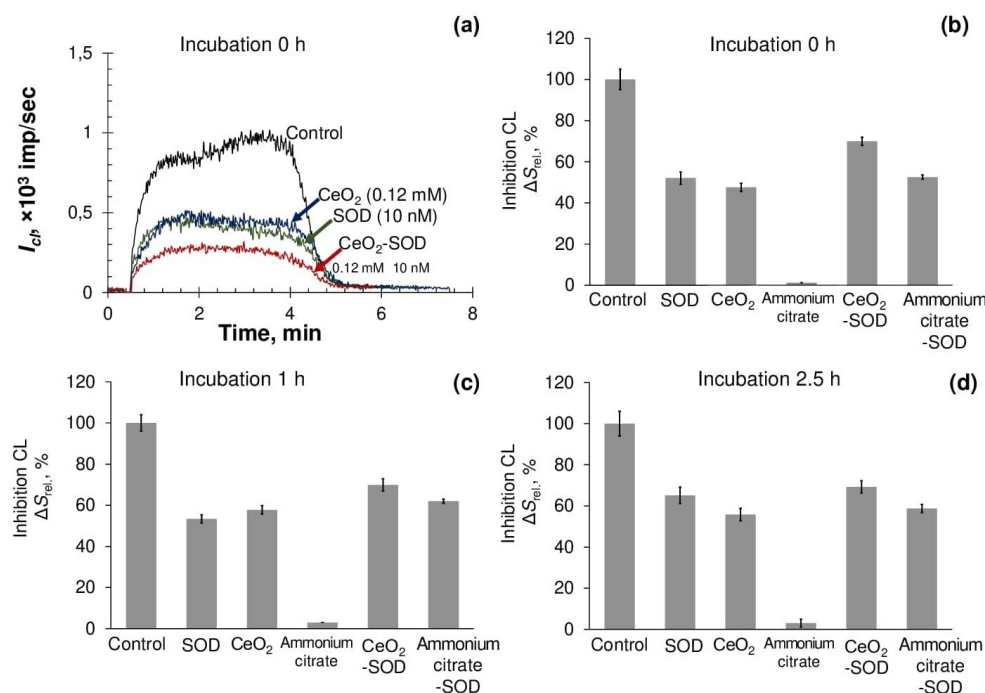


FIG. 3. (a) Chemiluminograms of a citrate-stabilized CeO_2 sol, native SOD, and CeO_2 -SOD conjugate (concentrations are shown in the figure, incubation for 0 h) in the lucigenin system ($25 \mu\text{M}$) + xanthine ($25 \mu\text{M}$) + xanthine oxidase (11 mU/ml), (b), (c), (d) – the degrees of free radical inhibition by native SOD (10 nM), citrate-stabilized CeO_2 sol (0.12 mM), ammonium citrate (0.12 mM), CeO_2 -SOD and ammonium citrate-SOD conjugates calculated on the basis of the recorded CL curves when incubated for 0, 1, and 2.5 hours, respectively. The light sum was calculated in 5 min

et al. [17] showed that the SOD-like activity of cerium dioxide nanoparticles significantly increased after incubation with Cu,Zn-SOD or with an electron-donating molecule $[\text{Ru}(\text{dcbpy})_2(\text{NCS})_2]$. The EPR data showed a 6–12-fold enhanced SOD-mimetic activity upon conjugation of 33 nm nanoparticles of CeO_2 with 20 U/ml Cu,Zn-SOD in PBS [17]. Singh et al. [30] found that the enzyme-like activity of CeO_2 nanoparticles does not change after their modification with bovine serum albumin and polyethylene glycol. In addition, Singh et al. have encapsulated CeO_2 nanoparticles in a polyethylene glycol matrix, after release from which the nanoparticles also retained SOD mimetic activity. These and other studies indicate that organic ligands or biomolecules used to stabilize CeO_2 nanoparticles do not interfere with the manifestation of the antioxidant properties of the latter.

The second key participant in free radical reactions in living systems is hydrogen peroxide. To evaluate the catalase-/peroxidase-like activity of a citrate-stabilized colloidal solution of CeO_2 , the lucigenin/ H_2O_2 and luminol/ H_2O_2 systems were studied (Fig. 4). The lucigenin/ H_2O_2 system is characterized by stationary kinetics of luminescence, which does not change when CeO_2 sol is introduced into the system. Thus, under the chosen conditions, the CeO_2 sol does not exhibit catalase properties. In the luminol/ H_2O_2 system, a dose-dependent increase in the luminescence intensity was observed with an increase in the concentration of the added citrate-stabilized CeO_2 sol, which indicates the manifestation of peroxidase activity by cerium dioxide.

According to existing data, at $\text{pH} > 6.0$ CeO_2 nanoparticles do not demonstrate peroxidase-like properties [31]. However, for stoichiometric cerium dioxide nanoparticles obtained by high-temperature treatment, this type of nanzyme activity was still observed at higher pH values. It was shown that due to peroxidase-like activity, CeO_2 nanoparticles (20 – 30 nm) at pH 7.2 accelerated the interaction of H_2O_2 with luminol, enhancing its luminescence [32]. In this case, cerium perhydroxide, decomposing with the formation of superoxide and hydroxyl radicals in the absence of Ce^{3+} ions, is presumably formed as an intermediate on the surface of the particles.

Peroxidases are glycoproteins that catalyse the oxidation of various organic and inorganic substrates using hydrogen peroxide as an electron acceptor. In biological systems, there are many types of peroxidases, such as glutathione peroxidase, lactoperoxidase, peroxyredoxins, myeloperoxidase, haloperoxidase, etc. [1]. The peroxidase-like activity of nanomaterials is used to detect hydrogen peroxide [5], glucose [33, 34], lead ions [35] and mercury ions [36], DNA methylation [37], as well as for immunoassay applications [38]. The classic work on the peroxidase-like activity of

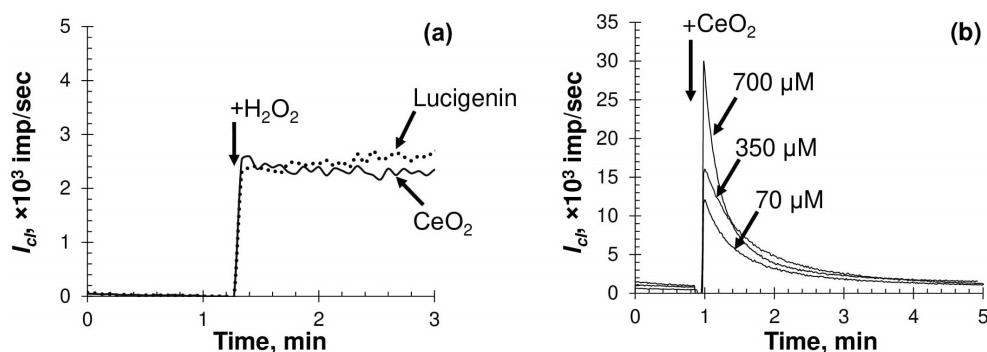
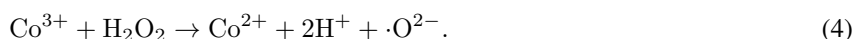


FIG. 4. Chemiluminograms of systems containing (a) lucigenin (0.1 mM) and a citrate-stabilized CeO₂ sol (700 μM) after the addition of H₂O₂ (3.0 mM), (b) luminol (50 μM) + H₂O₂ (50 mM) and a citrate-stabilized CeO₂ sol (concentrations are shown in the figure) after the addition of H₂O₂ (3.0 mM)

CeO₂ is an article by Jiao et al. [31], in which, based on the studied peroxidase activity of the CeO₂ sol, the prospect was substantiated of its application in the glucose test for oxidizing the substrate instead of horseradish peroxidase. Another successful practical application of this type of nanozyme activity is the combined use of CeO₂ nanoparticles and horseradish peroxidase for production of H₂O₂ sensors [9]. In a recent study, Vinothkumar et al. [5] demonstrated the possibility of using CePO₄-CeO₂ composite nanorods, which are peroxidase mimetics, for the detection of glucose and H₂O₂ by the colorimetric method with a high sensitivity.

At the final stage of our investigation, we studied the enzyme-like activity of cerium dioxide in the combined model — Co(II)/H₂O₂ in the presence of lucigenin. The system simultaneously contained hydrogen peroxide, superoxide anion radical and hydroxyl radical [40]:



Hydroxyl radicals have the highest oxidative activity among all other ROS. They can cause DNA damage, oxidative carbonylation of proteins and peroxidation of lipids, which, ultimately, can lead to inflammatory and oncological diseases, as well as aging [41]. In biological systems, there are no specific enzymes to scavenge hydroxyl radicals; yet some researchers suggest that this function is performed by such antioxidants as SOD, catalase, glutathione peroxidase, melatonin, and vitamin E [1]. More recently, there have been reports of the radical-intercepting properties of CeO₂ nanoparticles with respect to hydroxyl radicals [42, 43].

When H₂O₂ was added to the PBS medium (pH 8.6) containing Co(II) and lucigenin, the CL growth kinetics was observed, the intensity of which was proportional to the concentrations of CoCl₂ and H₂O₂ (Fig. 5).

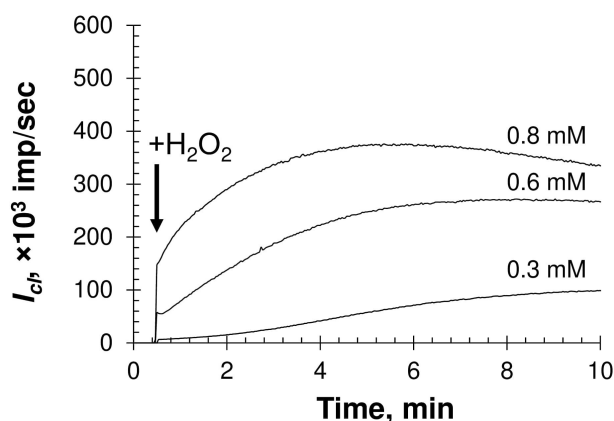


FIG. 5. Chemiluminograms for a system containing lucigenin (0.1 mM), Co(II) (concentrations are shown in the figure) and H₂O₂ (3.0 mM)

In the presence of SOD, luminescence quenching was observed due to the capture of the superoxide anion radical (Fig. 6a). A sulfhydryl compound, dithiothreitol, which also exhibited an inhibitory effect, was used as a selective inhibitor of the hydroxyl radical (Fig. 6b).

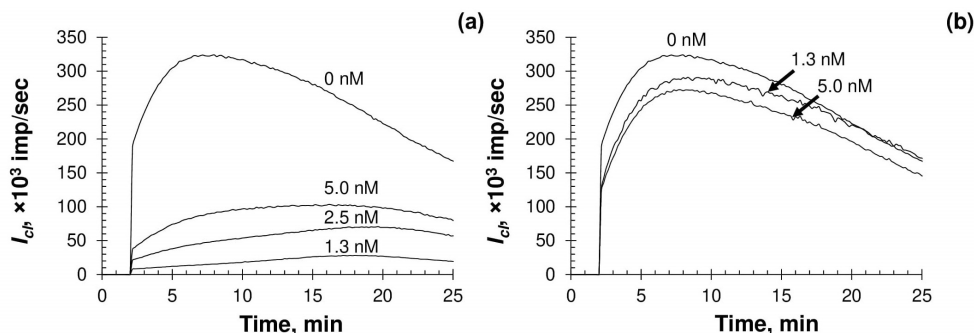


FIG. 6. Chemiluminograms for the system containing lucigenin (0.1 mM) + Co(II) (0.6 mM) + H₂O₂ (3.0 mM) in the presence of (a) SOD and (b) dithiothreitol (concentrations are shown in the figure)

The chemiluminograms obtained by adding a citrate-stabilized CeO₂ sol to the system, as well as the dependence of the light sum on the concentration of the analysed sample in the linear region, are shown in Fig. 7(a, b).

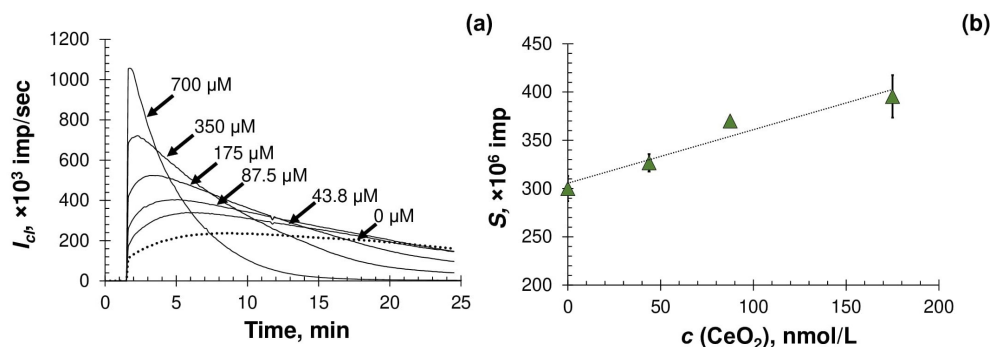


FIG. 7. (a) Chemiluminograms of a citrate-stabilized colloidal solution of CeO₂ (concentrations are shown in the figure) in the system containing lucigenin (0.1 mM) + Co(II) (0.6 mM) + H₂O₂ (3.0 mM), (b) the light sum (S) dependence under the CL curves on the concentration of CeO₂ nanoparticles. The light sum was calculated in 20 min

According to the data obtained, CeO₂ nanoparticles in the lucigenin/Co(II)/H₂O₂ system exhibit prooxidant properties, apparently due to peroxidase activity. With an increase in the concentration of CeO₂ sol introduced into the system, an increase in CL intensity was observed, and saturation occurred at a certain moment.

Thus, in relation to the two main active forms of oxygen – superoxide anion radical and hydrogen peroxide – cerium dioxide exhibits multidirectional activity. Judging by the published data, the pro- and antioxidant properties of CeO₂ nanoparticles are closely related. The determining factors are stoichiometry, redox potential of CeO₂ nanoparticles, pH of the medium, the presence of H₂O₂, etc. [44]. In a recent paper [45], calculations of the difference in redox potentials made it possible to evaluate the protective effect of CeO₂ nanoparticles against H₂O₂, taking into account the pH in the cell and organelles. It is possible to control the pro- and antioxidant properties of cerium dioxide nanoparticles in a wide range of pH values typical to biological media by changing the stoichiometry, design and strategy of synthesis [44, 46, 47]. The maximum prooxidant effect of CeO₂ was observed for the contents of vesicles – lysosomes and endosomes (pH < 6.2) [45]. Prooxidant properties may be useful for the destruction of undesirable exogenous components (toxins, bacteria, viruses), since it is the vesicular absorption mechanism that provides the bulk of the substances into the eukaryotic cell [44]. Analysis of the pH-dependent redox behavior of CeO₂ nanoparticles allows us to conclude that they provide the maximum protective potential against oxidative stress in mitochondria. Currently, evidence has been obtained of the effectiveness of targeted antioxidant therapy of mitochondrial dysfunctions to protect cells under conditions of oxidative stress and aging [48].

4. Conclusion

Oxidative stress underlies many neurodegenerative, cardiovascular, immune diseases, hormonal disorders, and a number of pathological conditions, including inflammation, hypoxia, tumor growth and aging. Numerous studies show that in fact there is not a single disease in which an imbalance of redox homeostasis would not be manifested, in some cases being the cause or primary part of pathogenesis, in others being the consequence. The development of new drugs – regulators of free-radical balance, among which nanodrugs play an important role, is gaining increasing popularity. The prospect of biomedical use of the nanodrugs is due to many unique advantages associated with pharmacokinetics, biodistribution, stable antioxidant activity, etc. [49]. To achieve maximum diagnostic and therapeutic efficacy, the activity of nanozymes can be remotely controlled using external stimuli, including exposure to magnetic field, light, ultrasound, and heat [50].

The increased interest in CeO₂ nanoparticles is due to the unique combination of physicochemical and nanozyme properties that these particles possess. Promising preclinical therapeutic effects require a comprehensive safety analysis of CeO₂ nanoparticles – toxicity and effects on free radical homeostasis. As follows from the study, the pro- and antioxidant properties of cerium dioxide nanoparticles are closely related. The results obtained after assessing relative safety indicate the prospects for the use of CeO₂ nanoparticles as free radical regulators, for example, in redox therapy of cancer.

Acknowledgements

This work was supported by the Russian Science Foundation (project No. 19-13-00416).

References

- [1] Yadav N., Patel V., Singh S. Cerium Oxide-Based Nanozymes in Biology and Medicine. *Springer Proceedings in Physics*, 2018, **236**, P. 193–213.
- [2] Gao L., Zhuang J., et al. Intrinsic peroxidase-like activity of ferromagnetic nanoparticles. *Nat. Nanotechnol.*, 2007, **2** (9), P. 577–583.
- [3] Chen T.M., Tian X.M., et al. Nanodiamonds as pH-switchable oxidation and reduction catalysts with enzyme-like activities for immunoassay and antioxidant applications. *Nanoscale*, 2017, **9** (40), P. 15673–15684.
- [4] Cho S., Shin H.Y., Kim M.I. Nanohybrids consisting of magnetic nanoparticles and gold nanoclusters as effective peroxidase mimics and their application for colorimetric detection of glucose. *Biointerphases*, 2017, **12** (1), P. 01A401–01A407.
- [5] Vinothkumar G., Lalitha A.I., Suresh Babu K. Cerium Phosphate-Cerium Oxide Heterogeneous Composite Nanozymes with Enhanced Peroxidase-Like Biomimetic Activity for Glucose and Hydrogen Peroxide Sensing. *Inorg. Chem.*, 2019, **58** (1), P. 349–358.
- [6] Naito Y., Yoshikawa T. Molecular and cellular mechanisms involved in *Helicobacter pylori*-induced inflammation and oxidative stress. *Free Radic. Biol. Med.*, 2002, **33** (3), P. 323–336.
- [7] Sies H., Cadenas E. Oxidative stress: damage to intact cells and organs. *Philos. Trans. R. Soc. Lond. B Biol. Sci.*, 1985, **311** (1152), P. 617–631.
- [8] Yildirim L., Thanh N.T., et al. Toxicology and clinical potential of nanoparticles. *Nano Today*, 2011, **6** (6), P. 585–607.
- [9] Ganguly R., Singh A.K., et al. *Nanotechnology in Modern Animal Biotechnology*. Elsevier, 2019, 178 p.
- [10] Ivanov V.K., Polezhaeva O.S., Tret'yakov Yu.D. Nanocrystalline ceria: Synthesis, structure-sensitive properties, and promising applications. *Russ. J. Gen. Chem.*, 2010, **80**, P. 604–617.
- [11] Grulke E., Reed K., et al. Nanocerium: factors affecting its pro- and anti-oxidant properties. *Environ. Sci. Nano*, 2014, **1**, P. 429–444.
- [12] Popov A.L., Popova N.R., et al. Cerium oxide nanoparticles stimulate proliferation of primary mouse embryonic fibroblasts in vitro. *Mater. Sci. Eng. C*, 2016, **68**, P. 406–413.
- [13] Zholobak N.M., Shcherbakov A.B., et al. Panthenol-stabilized cerium dioxide nanoparticles for cosmeceutic formulations against ROS-induced and UV-induced damage. *J. Photochem. Photobiol. B*, 2014, **130**, P. 102–108.
- [14] Shcherbakov A.B., Zholobak N.M., Spivak N.Ya., Ivanov V.K. Advances and prospects of using nanocrystalline ceria in cancer theranostics. *Russ. J. Inorg. Chem.*, 2014, **59**, P. 1556–1575.
- [15] Shcherbakov A.B., Teplonogova M.A., et al. Facile method for fabrication of surfactant-free concentrated CeO₂ sols. *Mater. Res. Express*, 2007, **4** (5), P. 4–14.
- [16] Gil D., Rodriguez J., et al. Antioxidant Activity of SOD and Catalase Conjugated with Nanocrystalline Ceria. *Bioengineering*, 2017, **4** (18), P. 1–9.
- [17] Li Y., He X., et al. Acquired superoxide-scavenging ability of ceria nanoparticles. *Angew. Chem. Int. Ed. Engl.*, 2015, **54** (6), P. 1832–1835.
- [18] Kuppasamy P., Zweier J.L. Characterization of free radical generation by xanthine oxidase. Evidence for hydroxyl radical generation. *J. Biol. Chem.*, 1989, **264** (17), P. 9880–9884.
- [19] Phaniendra A., Jestadi D.B., Periyasamy L. Free radicals: properties, sources, targets, and their implication in various diseases. *Indian J. Clin. Biochem.*, 2015, **30** (1), P. 11–26.
- [20] Kontos H.A., Wei E.P. et al. Appearance of superoxide anion radical in cerebral extracellular space during increased prostaglandin synthesis in cats. *Circ. Res.*, 1985, **57** (1), P. 142–151.
- [21] McIntyre M., Bohr D.F., Dominiczak A.F. Endothelial function in hypertension: the role of superoxide anion. *Hypertension*, 1999, **34** (4 Pt 1), P. 539–545.
- [22] Babior B.M., Lambeth J.D., Nauseef W. The neutrophil NADPH oxidase. *Arch. Biochem. Biophys.*, 2002, **397** (2), P. 342–344.
- [23] Kawano T., Kagenishi T., et al. Production and removal of superoxide anion radical by artificial metalloenzymes and redox-active metals. *Commun. Integr. Biol.*, 2015, **8** (6), P. e1000710.
- [24] Lu J.M., Lin P.H., et al. Chemical and molecular mechanisms of antioxidants: experimental approaches and model systems. *J. Cell. Mol. Med.*, 2010, **14** (4), P. 840–860.

- [25] Perry J.J., Shin D.S., et al. The structural biochemistry of the superoxide dismutases. *Biochim. Biophys. Acta*, 2010, **1804** (2), P. 245–262.
- [26] Tarnuzzer R.W., Colon J., et al. Vacancy engineered ceria nanostructures for protection from radiation-induced cellular damage. *Nano Lett.*, 2005, **5** (12), P. 2573–2577.
- [27] Korsvik C., Patil S., et al. Superoxide dismutase mimetic properties exhibited by vacancy engineered ceria nanoparticles. *Chem. Commun. (Camb.)*, 2007, **10**, P. 1056–1058.
- [28] Heckert E.G., Karakoti A.S., et al. The role of cerium redox state in the SOD mimetic activity of nanoceria. *Biomaterials*, 2008, **29** (18), P. 2705–2709.
- [29] Karakoti A.S., Singh S., et al. PEGylated nanoceria as radical scavenger with tunable redox chemistry. *J. Am. Chem. Soc.*, 2009, **131** (40), P. 14144–14145.
- [30] Singh V., Singh S., et al. A facile synthesis of PLGA encapsulated cerium oxide nanoparticles: release kinetics and biological activity. *Nanoscale*, 2012, **4** (8), P. 2597–2605.
- [31] Jiao X., Song H., et al. Well-redispersed ceria nanoparticles: Promising peroxidase mimetics for H₂O₂ and glucose detection. *Analytical Methods*, 2012, **4**, P. 3261–3267.
- [32] Xiaohua L., Zhang Zh., et al. A Chemiluminescence Microarray Based on Catalysis by CeO₂ Nanoparticles and Its Application to Determine the Rate of Removal of Hydrogen Peroxide by Human Erythrocytes. *Appl. Biochem. Biotechnol.*, 2013, **171** (1), P. 63–71.
- [33] Lv C., Di W., et al. Luminescent CePO₄:Tb colloids for H₂O₂ and glucose sensing. *Analyst*, 2014, **139** (18), P. 4547–4555.
- [34] Tanaka S., Kaneti Y.V., et al. Mesoporous Iron Oxide Synthesized Using Poly(styrene-*b*-acrylic acid-*b*-ethylene glycol) Block Copolymer Micelles as Templates for Colorimetric and Electrochemical Detection of Glucose. *ACS Appl. Mater. Interfaces*, 2018, **10** (1), P. 1039–1049.
- [35] Shiralizadeh Dezfuli A., Ganjali M.R., Norouzi P. Facile sonochemical synthesis and morphology control of CePO₄ nanostructures via an oriented attachment mechanism: application as luminescent probe for selective sensing of Pb²⁺ ion in aqueous solution. *Mater. Sci. Eng. C Mater. Biol. Appl.*, 2014, **42**, P. 774–781.
- [36] Han K.N., Choi J.S., Kwon J. Gold nanozyme-based paper chip for colorimetric detection of mercury ions. *Sci. Rep.*, 2017, **7** (1), P. 1–7.
- [37] Bhattacharjee R., Tanaka S., et al. Porous Nanozymes: Peroxidase-Mimetic Activity of Mesoporous Iron Oxide for Colorimetric and Electrochemical Detection of Global DNA Methylation. *J. Mater. Chem. B*, 2018, **6**, P. 4783–4791.
- [38] Maji S.K., Mandal A.K., et al. Cancer Cell Detection and Therapeutics Using Peroxidase-Active Nanohybrid of Gold Nanoparticle-Loaded Mesoporous Silica-Coated Graphene. *ACS Appl. Mater. Interfaces*, 2015, **7**, P. 9807–9816.
- [39] Ansari A.A., Solanki P.R., Malhotra B.D. Hydrogen peroxide sensor based on horseradish peroxidase immobilized nanostructured cerium oxide film. *J. Biotechnol.*, 2009, **142** (2), P. 179–184.
- [40] Zhidkova T.V., Proskurnina E.V., et al. Determination of superoxide dismutase and SOD-mimetic activities by a chemical system: Co²⁺/H₂O₂/lucigenin. *Anal. Bioanal. Chem.*, 2011, **401** (1), P. 381–386.
- [41] Iketani M., Ohsawa I. Molecular Hydrogen as a Neuroprotective Agent. *Curr. Neuropharmacol.*, 2017, **15** (2), P. 324–331.
- [42] Xue Y., Luan Q., et al. Direct Evidence for Hydroxyl Radical Scavenging Activity of Cerium Oxide Nanoparticles. *J. Phys. Chem.*, 2011, **115** (11), P. 4433–4438.
- [43] Schlick S., Danilczuk M., et al. Scavenging of Hydroxyl Radicals by Ceria Nanoparticles: Effect of Particle Size and Concentration. *J. Phys. Chem. C*, 2016, **120** (12), P. 6885–6890.
- [44] Popov A.L., Scherbakov A.B., et al. Cerium dioxide nanoparticles as third-generation enzymes (nanozymes). *Nanosystems: Phys. Chem. Math.*, 2017, **8** (6), P. 760–781.
- [45] Linnane A.W., Kios M., Vitetta L. Healthy aging: regulation of the metabolome by cellular redox modulation and prooxidant signaling systems: the essential roles of superoxide anion and hydrogen peroxide. *Biogerontology*, 2007, **8** (5), P. 445–467.
- [46] Spivak N.Y., Shepel E.A., et al. Ceria Nanoparticles Boost Activity of Aged Murine Oocytes. *Nano Biomedicine and Engineering*, 2012, **4**, P. 188–194.
- [47] Courbiere B., Auffan M., et al. Ultrastructural interactions and genotoxicity assay of cerium dioxide nanoparticles on mouse oocytes. *Int. J. Mol. Sci.*, 2013, **14** (11), P. 21613–21628.
- [48] Smith R.A., Murphy M.P. Mitochondria-targeted antioxidants as therapies. *Discov. Med.*, 2011, **11** (57), P. 106–114.
- [49] Liu Y., Shi J. Antioxidative nanomaterials and biomedical applications. *Nano Today*, 2019, **27**, P. 146–177.
- [50] Jiang D., Ni D., et al. Nanozyme: new horizons for responsive biomedical applications. *Chem. Soc. Rev.*, 2019, **48** (14), P. 3683–3704.

Raman study of glasses in the $\text{NbO}_2\text{F}-\text{BaF}_2-\text{InF}_3-\text{ErF}_3$ and $\text{CdNbOF}_5-\text{BaF}_2-\text{InF}_3$ systems

L. N. Ignatieva¹, N. N. Savchenko¹, Y. V. Marchenko¹, V. A. Mashchenko¹, V. M. Bouznik^{1,2}

¹Institute of Chemistry, Far-Eastern Branch, Russian Academy of Sciences,
159 Stoletiya av., Vladivostok, 690022, Russia

²FSUE All-Russian Scientific Research Institute of Aviation Materials SSC RF,
17 Radio st., Moscow, 105005, Russia

ignatieva@ich.dvo.ru, savchenko@ich.dvo.ru, gor_dvo@mail.ru, mba1111@mail.ru, bouznik@ngs.ru

DOI 10.17586/2220-8054-2020-11-3-333-337

Glasses in the $\text{NbO}_2\text{F}-\text{BaF}_2-\text{InF}_3$ and $\text{CdNbOF}_5-\text{BaF}_2-\text{InF}_3$ systems have been obtained and investigated by means of IR- and Raman spectroscopy. The analysis of the inelastic light scattering spectra was used to identify the contribution of the photoluminescence in the glasses studied. The contribution of the indium photoluminescence into the inelastic light scattering spectrum of the glasses in the $\text{NbO}_2\text{F}-\text{BaF}_2-\text{InF}_3$ and $\text{CdNbOF}_5-\text{BaF}_2-\text{InF}_3$ systems has been established by scattering excitation with a laser at a wavelength of 532 nm.

Keywords: oxyfluoride glasses, structure, inelastic light scattering spectrum, Raman spectrum, photoluminescence.

Received: 6 May 2020

1. Introduction

The authors with great joy dedicate this article for the anniversary of P. P. Fedorov to our friend and colleague and wish him further creative success. Professor P. P. Fedorov is widely known for his outstanding research on the synthesis, structure, and optical properties of fluoride and oxyfluoride glasses, glass ceramics, and crystalline materials, in which he has been engaged for more than half a century.

Glasses based on NbO_2F were synthesized several years ago, but, among the representatives of optically active materials the systems based on niobium oxyfluoride, they still occupy a prominent place [1, 2]. The structure of the glasses based on niobium oxyfluoride was investigated by us both in an earlier study [3] and a later one [4]. The research conducted in this field resulted in the fabrication of glasses in the systems based on MnNbOF_5 . The idea of introducing functional components, such as BiF_3 , InF_3 and fluorides of rare earth elements to various type of glasses, was implemented in [4–7]. A series of the objects fabricated according to this concept exhibited rather interesting transport and crystallization properties. In particular, the study of the crystallization process in these systems revealed the possibility of obtaining transparent glass-ceramic nanocomposites. In the study of $\text{NbO}_2\text{F}-\text{BaF}_2-\text{InF}_3-\text{ErF}_3$ glass system, the contribution of erbium photoluminescence to the spectra of inelastic light scattering was recorded [4]. The researchers repeatedly [8, 9] turned to the glasses that contain CdF_2 , considering it as a functional component promising for the formation of glass objects. Taking into account the demonstrated in [5] specific features of the glasses crystallization in the $\text{MnNbOF}_5-\text{BaF}_2-\text{InF}_3$ system, it was interesting to investigate the option of synthesizing similar systems with cadmium difluoride. The system of this type ($\text{CdNbOF}_5-\text{BaF}_2-\text{InF}_3$) was synthesized in [10]. During the course of its study [11], the possibility of fabricating transparent glass-crystalline composites containing crystalline phases of CdF_2 and $\text{Ba}_3\text{In}_2\text{F}_{12}$ was established via thermal treatment of glasses.

One of the important features of oxyfluoride glasses consists in the possibility of their doping by rare earth elements [12, 13]. Such glasses, including the glasses in the aforementioned systems [14, 15], often have luminescent properties, which allows them to be considered as candidates for the production of infrared fiber lasers and advanced glass ceramics. Recently, photoluminescence properties have been discovered in glasses containing elements other than only rare earth elements (REEs). Photoluminescence of Bi in glasses based on zirconium tetrafluoride was detected in [16, 17]. Herewith, in [15, 17], a non-trivial approach proposed in [4, 6, 14] for detecting photoluminescence was used. The essence of the approach is to analyze inelastic light scattering spectra in which the contributions of Raman scattering and photoluminescence are separated by using lasers with different wavelengths to excite scattering. This approach allows one to obtain the results which cannot always be achieved using traditional analyses of luminescence spectra.

When studying glasses in the $\text{NbO}_2\text{F}-\text{BaF}_2-\text{InF}_3$ system [4], which does not contain REEs, the contribution of photoluminescence, presumably attributed to indium photoluminescence, was recorded in the inelastic light scattering spectra. In the present study, the glasses in the $\text{NbO}_2\text{F}-\text{BaF}_2-\text{InF}_3$ system we studied more thoroughly and the above approach for detecting photoluminescence was applied to another system containing indium trifluoride. These are newly obtained glasses in the $\text{CdNbOF}_5-\text{BaF}_2-\text{InF}_3$ system [11].

2. Material and methods

The synthesis methodology of fabrication of the glasses in the $\text{NbO}_2\text{F}-\text{BaF}_2-\text{InF}_3-\text{ErF}_3$ and $\text{CdNbOF}_5-\text{BaF}_2-\text{InF}_3$ systems was detailed in our works [4, 11]. Glasses were transparent and resistant to aerobic conditions.

The absence or presence of crystalline phases in the samples was determined using a Bruker D8 ADVANCE diffractometer (CuK_α radiation).

Measurements of the Raman light scattering spectra were performed using a WiTec alpha500 confocal Raman microscope (laser wavelength of $\lambda_0 = 532$ nm, signal build-up time 1, averaging over 100 spectra) and a BRUKER RFS/100 Raman spectrometer (Nd:YAG laser, laser wavelength of $\lambda_0 = 1064$ nm).

IR absorption spectra were recorded on an IFS VERTEX 70 spectrometer (region of $4000 - 350$ cm^{-1} , wave number accuracy of 0.5 cm^{-1}). The studied samples were ground to a finely dispersed state in an agate mortar and pressed into tablets with KBr or, in the form of a suspension in liquid paraffin, were applied onto KBr substrates.

The luminescence measuring device was assembled on the basis of the Solar TII MS3504 monochromator, optical lenses and detectors were selected for different ranges. To amplify weak signals, we used a lock-in amplifier (Lock-in) SR-810 (Stanford research) together with an optical modulator. The measurements were carried out according to the method: monochromatic radiation (from the laser) was applied to the sample, the reflected signal was fed into the monochromator.

3. Results and discussion

The structures of oxyfluoroniobate glasses including the discussed in this paper systems were earlier investigated in [5, 11, 14]. The typical structural units in NbO_2F -based glasses are the NbO_3F_3 and NbO_2F_4 polyhedra, connected by oxygen bridges in the glass network. This is indicated by the presence in IR spectra of bands in the ranges of $900 - 800$, $700 - 800$, and $550 - 420$ cm^{-1} , which were assigned to the vibrations of bonds of $\text{Nb}=\text{O}$, $-\text{Nb}-\text{O}-\text{Nb}-$ and $\text{Nb}-\text{F}$, respectively. Glasses in the $\text{MnNbOF}_5-\text{BaF}_2-\text{InF}_3-\text{ErF}_3$, and $\text{CdNbOF}_5-\text{BaF}_2-\text{InF}_3$ systems belong to the structural type of $\text{NbO}_2\text{F}-\text{BaF}_2$; for this reason, their IR spectra practically do not differ from each other, regardless of which of the components (MnNbOF_5 , CdNbOF_5 or only NbO_2F) forms the glass (Fig. 1).

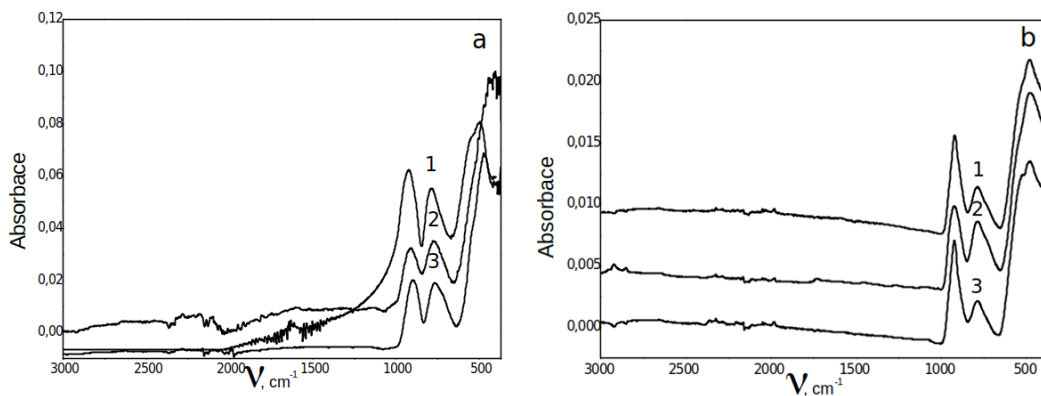


FIG. 1. IR spectra of the glasses in the systems of $\text{MnNbOF}_5-\text{BaF}_2-\text{InF}_3-\text{ErF}_3$ and $\text{CdNbOF}_5-\text{BaF}_2-\text{InF}_3$: (a) [11]: 1 – $39\text{CdNbOF}_5-60\text{BaF}_2-1\text{ErF}_3$; 2 – $30\text{CdNbOF}_5-40\text{BaF}_2-30\text{InF}_3$; 3 – $40\text{CdNbOF}_5-60\text{BaF}_2$; (b) [5]: 1 – $30\text{MnNbOF}_5-50\text{BaF}_2-20\text{InF}_3$; 2 – $39\text{MnNbOF}_5-40\text{BaF}_2-20\text{InF}_3-1\text{ErF}_3$; 3 – $38\text{MnNbOF}_5-40\text{BaF}_2-20\text{InF}_3-2\text{ErF}_3$

The IR-spectra of the glasses in the system of $\text{MnNbOF}_5-\text{BaF}_2-\text{InF}_3-\text{ErF}_3$ doped by rare earth elements do not differ from those of the glasses not containing of ErF_3 due the absence of substantial changes in the structure of glasses. This result is quite expected considering the amount of REE trifluoride in the glasses. The same situation was observed in the IR spectra of glasses in the $\text{NbO}_2\text{F}-\text{BaF}_2-\text{InF}_3-\text{ErF}_3$ system studied in [4].

A completely different situation was observed in the Raman spectra of oxyfluoroniobate glasses. For example, the Raman spectrum of the glass of $55\text{NbO}_2\text{F}-45\text{BaF}_2$ [4] is represented by two intensive bands at 920 and 410 cm^{-1} , which correspond to stretching vibrations of the $\text{Nb}=\text{O}$ and $\text{Nb}-\text{F}$ bonds, respectively.

As soon as the erbium trifluoride, even 0.5 mol %, is introduced into the system, the Raman spectrum was radically altered. The changes were so great that even the most intensive band at 920 cm^{-1} was not observable on the background of two intensive bands, which appeared at 656 and 420 cm^{-1} . The investigations performed in [4] allow one to conclude that the changes observed in the spectra were related to the contribution of erbium photoluminescence

into the inelastic light scattering spectrum, and this contribution was so significant that it was impossible to observe even the most intensive Raman bands on its background. Note that the conclusion made was confirmed by direct measurements of photoluminescence. The same pattern was observed in the Raman spectra of the glasses in the $\text{MnNbOF}_5-\text{BaF}_2-\text{InF}_3-\text{ErF}_3$ system [5].

When indium trifluoride is introduced to the oxyfluoroniobate system, InF_6 polyhedra are formed in the glass networks [17]. Since $\text{NbO}_2\text{F}_4^{3-}$ and InF_6^{3-} ions have the same charge, InF_6 polyhedra are situated between oxyfluoroniobate ions, thus forming mixed glass networks or their own layers or regions in the case of high content of indium trifluoride in the glass. However, since there are no radical changes in the structure of glass, noticeable changes in the IR spectra are also absent. All the bands corresponding to oxyfluoroniobate polyhedra remain. The bands corresponding to the In-F vibrations appear in the spectra, but these bands are located in the range of $500 - 400 \text{ cm}^{-1}$ and are not always recognized as individual bands: they mask themselves under the band characterizing the Nb-F vibrations, although this leads to its broadening and shifting to the low-frequency region of the spectrum.

In the Raman spectrum of the $55\text{NbO}_2\text{F}-45\text{BaF}_2$ glass, the most intensive band at 906 cm^{-1} characterizes the vibrations of $\nu(\text{Nb}=\text{O})$, below are the bands characterizing the vibrations of Nb-F, which are also clearly visible (Fig. 2).

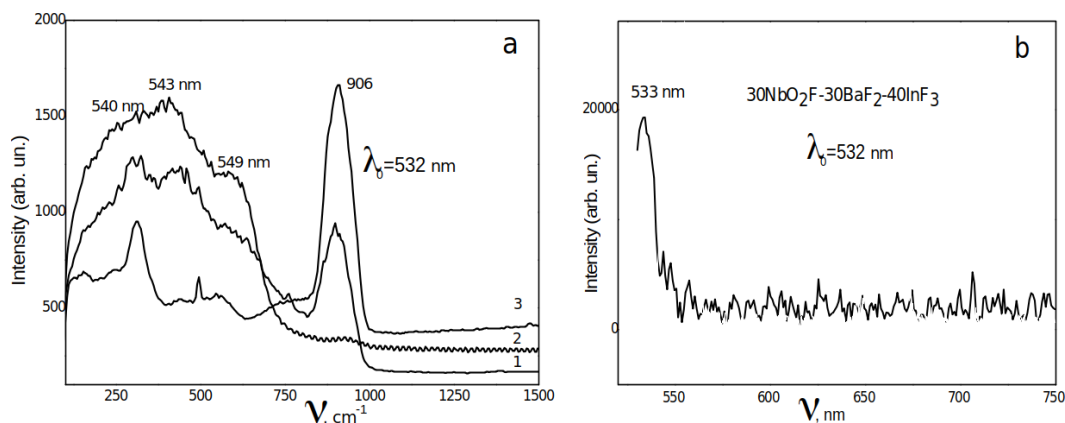


FIG. 2. Inelastic light scattering spectra of glasses (a): 1 – $55\text{NbO}_2\text{F}-45\text{BaF}_2$; 2 – $40\text{NbO}_2\text{F}-50\text{BaF}_2-10\text{InF}_3$; 3 – $30\text{NbO}_2\text{F}-30\text{BaF}_2-40\text{InF}_3$, and spectrum of luminescence (b) of $30\text{NbO}_2\text{F}-30\text{BaF}_2-40\text{InF}_3$ glass

However, as soon as indium trifluoride is introduced into the system, the spectrum changes dramatically (Fig. 2a). In the spectrum of the $40\text{NbO}_2\text{F}-50\text{BaF}_2-10\text{InF}_3$ glass, we still see a band characterizing the vibrations $\nu(\text{Nb}=\text{O})$, but in the spectrum of glass with 40 mol. % indium trifluoride content, even that band is not identified against the background of wide intense bands in the region of $600 - 300 \text{ cm}^{-1}$. We believe that the changes in the spectra are also related to the contribution of photoluminescence in the inelastic light scattering spectrum. A confirmation of this is that in the spectrum obtained using a laser with a different wavelength (1064 nm), all bands are observed that characterize the vibrations of oxyfluoroniobate and fluorindate polyhedra. This convincing evidence confirms the presence of an intense band at 533 nm in the spectrum of direct measurement of luminescence in $30\text{NbO}_2\text{F}-30\text{BaF}_2-40\text{InF}_3$ glass. These two facts suggest that in the inelastic scattering spectra of the glasses in the $\text{NbO}_2\text{F}-\text{BaF}_2-\text{InF}_3$ system, when using a laser with a wavelength of 532 nm, we observe the contribution of photoluminescence corresponding to emission levels in 500 nm region. The intense bands attributed to photoluminescence observed in the region of $500 - 300 \text{ cm}^{-1}$ are amplified with increasing indium trifluoride content in the system. Based on this, is logical to assume that this contribution is due to the presence of indium trifluoride in the glass composition.

Recently the glasses in the $\text{CdNbOF}_5-\text{BaF}_2-\text{InF}_3$ system were fabricated and investigated [10, 11]. As was noted above, analysis of the IR absorption spectra of the glasses in the $\text{CdNbOF}_5-\text{BaF}_2-\text{InF}_3$ system demonstrated the similarity to the IR-spectra of the earlier investigated oxyfluoroniobates in the systems of $\text{MnNbOF}_5-\text{BaF}_2-\text{BiF}_3$, $\text{MnNbOF}_5-\text{BaF}_2-\text{InF}_3$, and $\text{NbO}_2\text{F}-\text{BaF}_2-\text{InF}_3$, which indicates the structural similarity of glass networks of all these oxyfluoroniobate systems. In all cases, including the $\text{CdNbOF}_5-\text{BaF}_2-\text{InF}_3$ system, the IR-spectra demonstrated well-observed bands in the ranges of $920 - 960$, 800 , and $500 - 400 \text{ cm}^{-1}$ [11]. According to the assignments, in the case of the $\text{CdNbOF}_5-\text{BaF}_2-\text{InF}_3$ system, these bands also characterize the vibrations of Nb=O, -Nb-O-Nb-, Nb-F, and In-F bonds, respectively. The structural similarities of the $\text{CdNbOF}_5-\text{BaF}_2-\text{InF}_3$, $\text{MnNbOF}_5-\text{BaF}_2-\text{InF}_3$, and $\text{NbOF}_5-\text{BaF}_2-\text{InF}_3$ glasses suggest there should be similarities in not only their IR-spectra, but of the Raman spectra

as well. This was indeed observed in the case of the spectrum of the glass of $40\text{CdNbOF}_5\text{-}60\text{BaF}_2$ (Fig. 3). The most intensive band at 912 cm^{-1} characterizes the $\text{Nb}=\text{O}$ vibrations, at 773 cm^{-1} – those of $-\text{Nb}-\text{O}-\text{Nb}-$, and at 559 cm^{-1} – those of $\text{Nb}-\text{F}$.

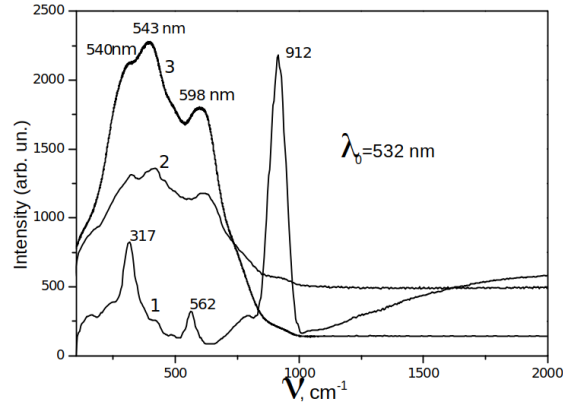


FIG. 3. Inelastic light scattering spectra in the system of $\text{CdNbOF}_5\text{-BaF}_2\text{-InF}_3$: 1 – $40\text{CdNbOF}_5\text{-}60\text{BaF}_2$; 2 – $30\text{CdNbOF}_5\text{-}40\text{BaF}_2\text{-}30\text{InF}_3$; 3 – $20\text{CdNbOF}_5\text{-}40\text{BaF}_2\text{-}40\text{InF}_3$

However, the Raman spectra of the $30\text{CdNbOF}_5\text{-}40\text{BaF}_2\text{-}30\text{InF}_3$ and $20\text{CdNbOF}_5\text{-}40\text{BaF}_2\text{-}40\text{InF}_3$ glasses displayed a different pattern (Fig. 3). The Raman spectrum was not observed on the background of two intensive bands at 598 and 397 cm^{-1} . A similar pattern was observed in the spectrum of the glass of $30\text{NbO}_2\text{F-}30\text{BaF}_2\text{-}40\text{InF}_3$ (Fig. 2). The appearance of these bands was explained by the appearance of the contribution of photoluminescence in the spectrum of inelastic light scattering, wherein, it was shown, this photoluminescence is caused by the presence of indium ions in the glass. Apparently, the same phenomenon takes place in the spectrum of glasses in the $\text{CdNbOF}_5\text{-BaF}_2\text{-InF}_3$ system.

The same of $\text{NbO}_2\text{F-BaF}_2\text{-InF}_3$ system this suggestion is corroborated by two facts. All the bands corresponding to the Raman spectra of the glasses containing or not containing indium trifluoride are clearly observed in the Raman spectra of the investigated glasses at scattering excitation by the laser with the wavelength of 1064 nm (Fig. 4). The intensities of the bands attributed to photoluminescence (the wide bands in region of $600 - 300\text{ cm}^{-1}$) grow with increasing indium trifluoride content in the system (Fig. 3). Therefore, we can conclude that for the scattering excitation by the laser with the wavelength of 532 nm , we observed a contribution of indium photoluminescence in the inelastic scattering spectra of glasses in the $\text{CdNbOF}_5\text{-BaF}_2\text{-InF}_3$ system. The revealed photoluminescence corresponds to the emission levels of 549 , 543 and 539 nm . The indium photoluminescence in the glasses is not well-known fact; however, there are some examples of photoluminescence properties in the compounds containing indium [18].

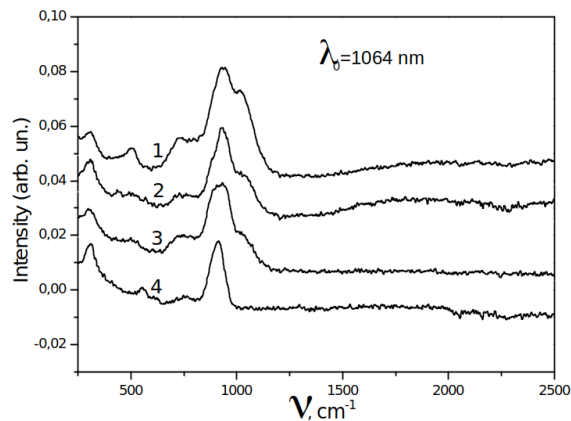


FIG. 4. Inelastic light scattering spectra in the system of $\text{CdNbOF}_5\text{-BaF}_2\text{-InF}_3$: 1 – $20\text{CdNbOF}_5\text{-}40\text{BaF}_2\text{-}40\text{InF}_3$; 2 – $30\text{CdNbOF}_5\text{-}40\text{BaF}_2\text{-}30\text{InF}_3$; 3 – $40\text{CdNbOF}_5\text{-}30\text{BaF}_2\text{-}30\text{InF}_3$; 4 – $40\text{CdNbOF}_5\text{-}60\text{BaF}_2$

4. Conclusion

The inelastic light scattering spectra of glasses in the $\text{NbO}_2\text{F}-\text{BaF}_2-\text{InF}_3$ and $\text{CdNbOF}_5-\text{BaF}_2-\text{InF}_3$ systems are studied. In the analysis of the spectra, the contributions of Raman scattering and photoluminescence were separated by using lasers of different wavelengths to excite scattering.

The contribution of indium photoluminescence to the inelastic light scattering spectrum of glasses in the $\text{NbO}_2\text{F}-\text{BaF}_2-\text{InF}_3$ system was established when scattering was excited by a laser with a wavelength of 532 nm. This contribution corresponds to emission levels of 540, 543, 549 nm.

With scattering excitation by the 532 nm laser, we observed a contribution of indium photoluminescence in the inelastic scattering spectra of glasses in the $\text{CdNbOF}_5-\text{BaF}_2-\text{InF}_3$ system. The revealed photoluminescence corresponds to the emission levels of 540, 543 and 549 nm.

Acknowledgements

The present study was performed with a support of the Russian Foundation for Basic Research (project No. 18-03-00034)

References

- [1] Poulain Mi., Poulain Ma. Oxyfluoride glasses. *Mater. Sci. Forum*, 1991, **67–68**, P. 129–136.
- [2] Polishchuk S.A., Ignat'eva L.N., Marchenko Yu.V., Bouznic V.M. Oxyfluoride glasses (A review), *Glass Phys. Chem.*, 2011, **37**, P. 1–20.
- [3] Ignatieva L.N., Antokhina T.F., et al. A spectroscopy study of the structure of fluoroniobate glass. *Glass Phys. Chem.*, 1998 **24**, P. 97–100.
- [4] Ignatieva L.N., Savchenko N.N., Marchenko Yu.V. Glasses in the $\text{NbO}_2\text{F}-\text{BaF}_2-\text{InF}_3-\text{ErF}_3$ system. *J. Fluorine Chem.*, 2018, **213**, P. 37–41.
- [5] Ignatieva L.N., Savchenko N.N., et al. Structure and crystallization of glasses in the $\text{MnNbOF}_5-\text{BaF}_2-\text{InF}_3$ system. *Russ. J. Inorg. Chem.*, 2018, **63**, P. 1389–1394.
- [6] Ignatieva L.N., Surovtsev N.V., et al. Glasses in the system of $\text{MnNbOF}_5-\text{BaF}_2-\text{BiF}_3-\text{ErF}_3$. *J. Non-Cryst. Solids*, 2011, **357**, P. 3807–3812.
- [7] Fedorov P.P., Luginina A.A., Popov A.I. Transparent oxyfluoride glass ceramics. *J. Fluorine Chem.*, 2015, **172**, P. 22–50.
- [8] Aggarwal I.D., Lu G. *Fluoride glass fiber optics*, New York, 1991.
- [9] Doweidar H., El-Egili K., Ramadan R., Khalil E. Structural studies and properties of $\text{CdF}_2-\text{B}_2\text{O}_3$ glasses. *J. Non-Cryst. Solids*, 2018, **481**, P. 494–502.
- [10] Savchenko N.N., Ignatieva L.N., Marchenko Yu.V. Synthesis and study of glasses on the base of CdNbOF_5 , Abs. *13-th Int Conf. on Solid State Chem. Pardubice, Czech Republic*, 2018, 172.
- [11] Ignatieva L.N., Savchenko N.N., Marchenko Yu.V., Sarin S.A. Synthesis, structure and crystallization of glasses in the $\text{CdNbOF}_5-\text{BaF}_2-\text{InF}_3$ system. *Ceram. Int.*, 2019, **45**, P. 17737–17741.
- [12] Ignatieva L.N., Maslennikova I.G., et al. The role of the REE ions in the glass systems $\text{TeO}_2-\text{PbO}-\text{P}_2\text{O}_5-\text{PbF}_2:\text{MF}_3$ (M=Er, Nd). *Appl. Phys. A*, 2018, **124**, 640.
- [13] Barbosa L.C., Filho C.O., Chilloce E.F. Tellurite glasses for optical amplifiers. *Springer Series in Materials Science*, 2017, **254**, P. 131–153.
- [14] Ignatieva L.N., Surovtsev N.V., et al. Glasses in the system of $\text{MnNbOF}_5-\text{BaF}_2-\text{BiF}_3-\text{ErF}_3$. *J. Non-Cryst. Solids*, 2011, **357**, P. 3807–3812.
- [15] Ignatieva L.N., Savchenko N.N., et al. Glasses in the systems $\text{TeO}_2-\text{PbO}-\text{P}_2\text{O}_5-\text{PbF}_2:\text{EuF}_3$: peculiarities of structure, crystallization and luminescence. *J. Non-Crystalline Solids*, 2016, **450**, P. 103–108.
- [16] Romanov A.N., Haula E.V., et al. Near-IR luminescence from subvalent bismuth species in fluoride glass. *Opt. Mater.*, 2011, **34**, P. 155–158.
- [17] Ignatieva L.N., Surovtsev N.V., et al. Glasses in the system $\text{ZrF}_4-\text{BaF}_2-\text{BiF}_3$: Thermal and spectroscopic properties. *J. Non-Cryst. Solids*, 2015, **426**, P. 7–12.
- [18] Midryi A.V., Ivanyukovich A.V., et al. Optical properties of indium nitride powder and films. *J. Appl. Spectrosc.*, 2006, **73**, P. 95–98.

Formation of Bi_2WO_6 nanocrystals under conditions of hydrothermal treatment

A. S. Svinolupova^{1,2}, M. S. Lomakin³, S. A. Kirillova², O. V. Almjashaeva³

¹St. Petersburg State Institute of Technology, Moskovsky Pr., 26, St. Petersburg, 190013, Russia

²St. Petersburg Electrotechnical University “LETI”, Professor Popov St. 5, St. Petersburg, 197376, Russia

³Ioffe Institute, Politekhnicheskaya St. 26, St. Petersburg, 194021, Russia

assvinolupova@etu.ru, almjasheva@mail.ru

PACS 81.07.Wx, 81.07.-b

DOI 10.17586/2220-8054-2020-11-3-338-344

Nanocrystalline Bi_2WO_6 was synthesized by means of hydrothermal treatment. It was shown that the formation rate of bismuth tungstate nanocrystals was determined by the presence of clusters formed at the stage of precipitation and having the same structure as that of Bi_2WO_6 , and the morphology of particles formed during hydrothermal treatment depended on the hydrothermal medium's pH.

Keywords: nanoparticles, nanocrystals, hydrothermal synthesis, bismuth tungstate.

Received: 3 June 2020

1. Introduction

Currently, materials based on perovskite-like oxides are of great interest, since they are characterized by a wide spectrum of functional properties, which make them promising products with respect to various technical fields [1–5]. Bismuth tungstate, a compound with a laminated perovskite-like structure of the Aurivillius phase type $(\text{Bi}_2\text{O}_2)^{2+}(\text{A}_{n-1}\text{B}_n\text{O}_{3n+1})^{2-}(\text{Bi}_2\text{WO}_6)$ that has a wide spectrum of important functional characteristics is one of the most in-demand materials [6–14].

To obtain Bi_2WO_6 , different methods may be applied, including the solid-phase synthesis [15], solution burning [16–18], microwave heating [19], sol-gel technique [20], solvothermal reaction [21, 22], electro spinning [23, 24], hydrothermal synthesis [25–30], etc. The most common methods include soft chemistry processes [7–9, 16–21, 25–30], among which a hydrothermal treatment method should be emphasized [7–9, 25–30]. The hydrothermal or solvothermal synthesis popularity is due to the possibility of obtaining bismuth tungstate in one step.

It should be noted that varying the synthesis procedures usually leads to variation in the structure, particle size, particle size distribution, morphology, which, in turn, significantly affects the synthesized compound's functional characteristics [6–30].

Thus, it is important to understand mechanisms of formation of the compounds depending on the synthesis conditions for the synthesis of materials with specified properties. Therefore, the objective of this study is to examine the effect of hydrothermal treatment conditions on the formation process and morphology of nanostructured Bi_2WO_6 .

2. Experimental

Aqueous solutions of bismuth (III) nitrate $(\text{Bi}(\text{NO}_3)_3 \cdot 5\text{H}_2\text{O})$, AR grade, GOST 4110-75) and sodium tungstate $(\text{Na}_2\text{WO}_4 \cdot 2\text{H}_2\text{O})$, AR grade, GOST 18289-78) were used as the starting materials for bismuth tungstate synthesis.

The separately prepared bismuth nitrate solution in nitric acid – acidified distilled water and sodium tungstate aqueous solution were mixed in the stoichiometric ratio and stirred using a mechanical agitator for 30 minutes (BWO_start). Then, a concentrated (12 M) aqueous solution of ammonium hydroxide (NH_4OH) , CP, GOST 3760-79) was added, to achieve a specified pH value. The pH values varied in the range from 2 to 13.

The hydrothermal treatment was performed in a steel autoclave with a teflon liner. The hydrothermal treatment temperature was 120, 150, 180 °C, the pressure was 70 MPa, and the isothermal time was 0.5 – 20 h. The obtained sediment was separated by decantation, flushed with distilled water and dried to a constant weight at 80 °C.

To study the effect of the starting components' pre-history on the formation process of bismuth tungstate under hydrothermal conditions, four variants of an initial suspension have been used as the starting material, and the suspension was obtained by mixing the aqueous solutions of sodium tungstate and bismuth nitrate, with the addition of ammonium hydroxide solution until pH = 10 (BWO_init):

- (1) the initial suspension was subjected to hydrothermal treatment without flushing or any additional procedures ($T = 180$ °C, $P = 70$ MPa, $\tau = 2$ h) – sample BWO_init.HT;

- (2) the initial suspension was filtered (without flushing) and dried at 80 °C (sample – BWO_init_dry), then the powder was subjected to hydrothermal treatment ($T = 180$ °C, $P = 70$ MPa, $\tau = 2$ h) – sample BWO_init_dry_HT;
- (3) the initial suspension was flushed with distilled water to remove impurity ions, until pH = 7 and the absence of NO_3^- and subjected to hydrothermal treatment ($T = 180$ °C, $P = 70$ MPa, $\tau = 2$ h) – sample BWO_clean_HT;
- (4) the initial suspension was flushed with distilled water to remove impurity ions, until pH = 7 and the absence of NO_3^- , dried at 80 °C (sample BWO_clean_dry) and subjected to hydrothermal treatment ($T = 180$ °C, $P = 70$ MPa, $\tau = 2$ h) – sample BWO_clean_dry_HT.

The elemental composition was determined by X-ray fluorescence analysis (XRF) (using Spectrascan Max GF2E) and by energy-dispersive X-ray spectroscopy (EDX) with the use of a scanning electron microscope (Vega3 Tescan and FEI Quanta-200) with EDAX energy-dispersive analyzer.

The samples' phase composition was analyzed by means of X-ray powder diffraction, using RigakuSmartLab 3 X-ray diffractometer (CoK_α -radiation). The peaks in the diffractogram were identified using PDWin 4.0 software package and Crystallographica Search-Match package. The mean crystallite size was assessed by way of X-ray diffraction line profile analysis, using the Scherrer formula and a software package (SmartLabStudio III).

The obtained materials' morphology was studied by means of scanning electron microscopy (Tescan Vega3 microscope).

The IR-spectroscopy was carried out using Shimadzu IRTracer-100 spectrometer equipped with LabSolutions IR software.

3. Results and discussion

The ratio of elements in all of the non-flushed samples corresponded to the vicinity of bismuth tungstate singular point (Table 1), within the predetermined error tolerance.

TABLE 1. The results of elemental analysis of the studied materials

Sample	Molar ratio Bi/W	
	XRF	EDX
BWO_init_HT	2.2	1.9
BWO_init_dry	2.2	–
BWO_init_dry_HT	2.2	–
BWO_clean_HT	2.6	–
BWO_clean_dry	2.8	–
BWO_clean_dry_HT	2.8	–

As follows from Table 1, when the suspension is flushed, a change in the Bi/W ratio, i. e. an increase in bismuth content occurs. This may be due to the fact that at pH = 10 some portion of tungsten passes into solution as a result of the interaction with excessive NH_4OH and is removed from the system during decantation.

It should also be noted that, within the methods sensitivity, the samples following hydrothermal treatment contained no impurity elements (Na), the presence of which may be associated with the starting reagents' chemical composition.

The results of X-ray analysis of the samples following hydrothermal treatment are presented in Fig. 1(a,b). According to X-ray diffraction data, when a suspension with no additional treatment (Fig. 1(b), BWO_init_HT) is used as the starting material for hydrothermal synthesis, X-ray peaks corresponding only to Bi_2WO_6 are observed (ICSD code 73-1126). The size of Bi_2WO_6 crystallites is approximately 30 nm. If the suspension is first flushed with distilled water until neutral pH, then, following hydrothermal treatment, the X-ray diffractogram will show peaks indicating the predominant formation of bismuth oxide ($\delta\text{-Bi}_2\text{O}_3$), with an insignificant amount of Bi_2WO_6 (Fig. 1(b) BWO_clean_HT). In this case, the tungsten-containing component appears to be washed out of the immediate surrounding of $\text{Bi}(\text{OH})_3$, which contributes to $\delta\text{-Bi}_2\text{O}_3$ formation during hydrothermal treatment of the composition.

After the initial suspension drying at 80 °C, an X-ray amorphous powder was formed (Fig. 1(a), BWO_init_dry), the hydrothermal treatment of which at 180 °C for 2 hours did not lead to any noticeable changes in the phase state

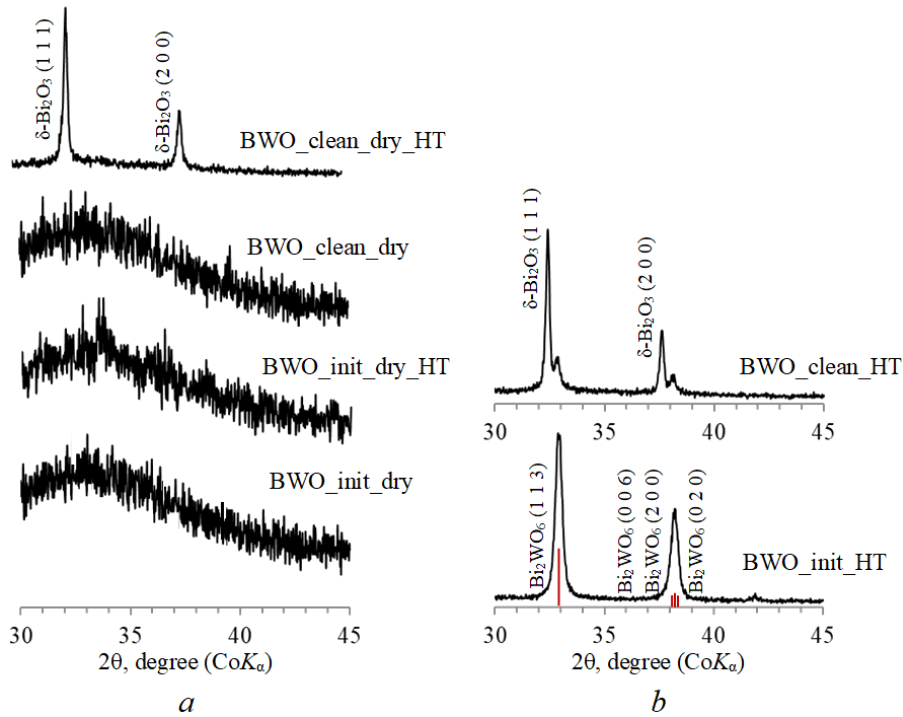


FIG. 1. X-ray diffractograms of the samples with various pre-histories of the initial suspension: a – the suspensions were dried; b – the suspensions were not dried

(Fig. 1(a), BWO_init_dry_HT). Drying of the flushed suspension (sample BWO_clean_dry) led to formation of X-ray amorphous powder (Fig. 1(a), BWO_clean_dry), as well as in the case with no flushing procedure. However, following hydrothermal treatment, a crystalline phase was formed, which was solely presented by δ - Bi_2O_3 (Fig. 1(a), BWO_clean_dry_HT). It should be noted that the size of δ - Bi_2O_3 crystallites was about 70 nm for all samples, which is significantly greater than that of Bi_2WO_6 crystallites formed as a result of hydrothermal treatment (Fig. 1(b), BWO_init_HT).

Note that for the synthesis of ZrO_2 [31], CoFe_2O_4 [32], BiFeO_3 [33, 34] nanoparticles, there was a substantial difference in the samples' phase state following hydrothermal treatment of precipitated hydroxides – without their preliminary drying and after drying. Such differences seem to be associated with a change in the initial amorphous deposit composition and structure as a result of its thermal processing.

Since the suspension flushing and drying appeared to result in a change in the hydrothermal medium pH value from 10 to 7, the effect of pH on the crystallization process was studied. A suspension obtained with no flushing and drying (BWO.start) was used as the starting material. The medium acidity was 2, 8, 10, 13. The hydrothermal treatment temperature was 180 °C, the pressure was 70 MPa, and the duration was 2 h.

The results of elemental analysis are presented in Table 2. The results of X-ray diffraction analysis and morphological analysis of the obtained materials are presented in Fig. 2.

TABLE 2. The results of the studied materials' elemental analysis, following hydrothermal treatment at 180 °C for 20 h

pH	Molar ratio Bi/W	
	XRF	EDX
2	2.1	2.0
8	2.2	1.9
13	2.1	1.9

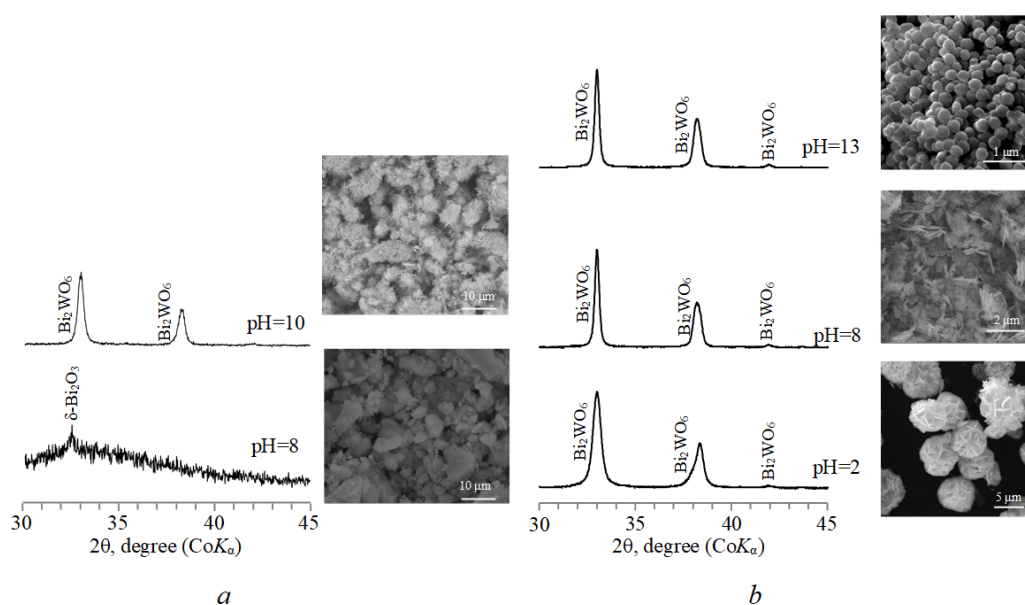


FIG. 2. X-ray diffractograms and microphotographs of the samples at various pH values of the hydrothermal medium. Hydrothermal treatment conditions: temperature of 180 °C, pressure of 70 MPa, isothermal time of 2 h (a) and 20 h (b)

Hydrothermal treatment of the sample BWO_start at the medium pH = 8 and the isothermal time of 2 h did not lead to bulk crystallization: only insignificant intensity reflection corresponding to crystalline $\delta\text{-Bi}_2\text{O}_3$ was observed in the X-ray diffractogram (Fig. 2(a)). Additionally, the sample was mostly presented by large, rather dense agglomerates (Fig. 2(a)), which is characteristic of materials in the X-ray amorphous state. An increase in the hydrothermal medium pH resulted in active crystallization process (Fig. 2(a)); peaks corresponding to crystalline Bi_2WO_6 with a crystallite size of about 25 nm were observed in the X-ray diffractogram. According to scanning electron microscopy data, the sample is represented by the agglomerates of particles of non-isometric shape, with a thickness of significantly less than 1 μm and a length of several μm .

When the hydrothermal treatment duration is increased to 20 h, crystalline bismuth tungstate formation is observed (Fig. 2(b)), irrespective of the medium pH value; and an increase in the pH values results in the narrowing of X-ray diffraction lines, which reflects an increase in the formed crystallites' size: from 23 nm at pH = 2 to 50 nm at pH = 13. It should be noted that the change in pH is accompanied by a significant change in the formed particles' morphology (Fig. 2(b)). In acidic conditions (pH = 2), flower-like agglomerates consisting of plates, with a size of 5 – 7 μm and a thickness of several hundred nanometers are formed. The sample obtained in mildly alkaline conditions is represented by unstructured plates with a thickness of 100 – 500 nm. The hydrothermal treatment of BWO_init in strongly alkaline conditions (pH = 13) results in the formation of spherical particles with a diameter from 200 to 700 nm (Fig. 2(b)).

Thus, basing on the presented data, it can be concluded that bismuth oxide ($\delta\text{-Bi}_2\text{O}_3$) is first crystallized, and then bismuth tungstate is formed during the hydrothermal treatment. In alkaline conditions, the formation rate of Bi_2WO_6 is significantly higher due to tungsten passing into solution, which contributes to the mass transfer process. The effect of pH may also be responsible for processes observed when varying the initial suspension pre-history. If a suspension subjected to no additional treatment is used, then the hydrothermal medium pH is equal to 10, and the formation rate of Bi_2WO_6 is so high that no intermediate product ($\delta\text{-Bi}_2\text{O}_3$) can be observed (Fig. 1, BWO_init). All other samples are subjected to a drying procedure, and the stock solution is decanted, which appears to result in lower pH values and thus a lower formation rate of both the intermediate product, and the end product, i.e. bismuth tungstate. The initial suspension flushing not only leads to a lower pH value, it may also lead to tungsten “washing out” of the system and to a deviation from the components' stoichiometric ratio (Table 1), which results in a lower formation rate of Bi_2WO_6 . Moreover, spatial separation of the system components is likely to occur during the suspension flushing and subsequent drying, which hinders the formation of Bi_2WO_6 under these conditions.

As a result of comparing the IR-spectra of pure bismuth- and tungsten-containing components of the system $\text{Bi}_2\text{O}_3\text{-WO}_3\text{-H}_2\text{O}$ (Fig. 3, curves 1 and 2) and the spectrum of the initial composition obtained by co-precipitation, i.e. of the sample BWO_init_dry (Fig. 3, curve 3), it can be concluded that clusters with a short-range order similar to the end product structure are formed during precipitation in the system. This is evidenced by, e. g., spectral

lines $\sim 780\text{ cm}^{-1}$ observed in the IR-spectra of the co-precipitated mixture but not present in the spectra of individual components of the system, and spectral lines $\sim 730\text{ cm}^{-1}$ corresponding to W–O bonds within Bi_2WO_6 [35–37]. It seems to be the number of such clusters in the co-precipitated sample that determines the activity of formation of either Bi_2WO_6 , or $\delta\text{-Bi}_2\text{O}_3$.

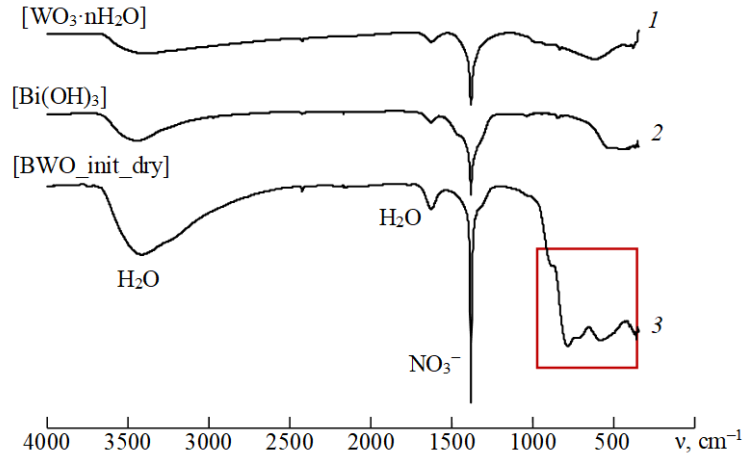


FIG. 3. IR-spectra of the samples obtained by precipitation

An initial suspension (BWO_init) was used as the starting material, and the hydrothermal medium pH 10 was maintained for studying the formation rate of Bi_2WO_6 at various temperatures of hydrothermal treatment. The elemental composition of the obtained samples is presented in Table 3.

TABLE 3. The results of elemental analysis of the test materials

$T, ^\circ\text{C}$	τ, hours	Molar ratio Bi/W	
		XRF	EDX
120	1	2.19	–
	2	2.18	–
	4	2.21	–
150	1	–	2.23
	2	–	2.05
	4	–	2.11
180	0.5	–	1.85
	1	–	2.23
	1.5	–	1.97
	2	–	2.04

As indicated by the data presented in Fig. 4, the formation rate of bismuth tungstate to a significant degree depends on the hydrothermal treatment temperature. At the hydrothermal treatment temperature of $120\text{ }^\circ\text{C}$, almost trace quantity of bismuth tungstate is observed after 4 hours (Fig. 4(a)). If the temperature is increased to $150\text{ }^\circ\text{C}$, Bi_2WO_4 will be completely formed within the same period, and an additional increase by $30\text{ }^\circ\text{C}$ will result in the completion of bismuth tungstate crystallization in 2 hours (Fig. 4(a)). The formed bismuth tungstate crystallite size is about 30 nm, and it does not change as the hydrothermal treatment duration is increased (Fig. 4(b)).

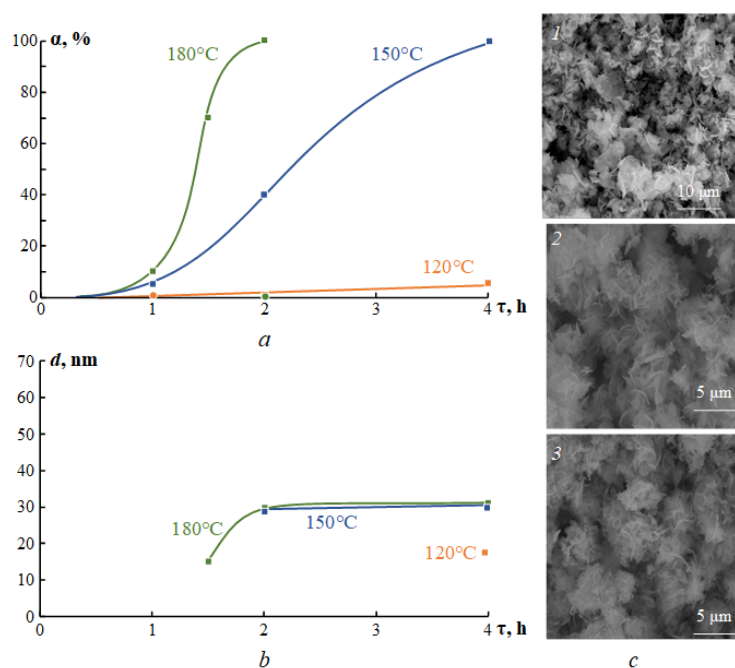


FIG. 4. Crystallization degree (a), crystallite size (b) and morphology (c) as a function of hydrothermal treatment temperature and duration: 1c – $T = 150$ °C, $\tau = 4$ h; 2c – $T = 180$ °C, $\tau = 1.5$ h; 3c – $T = 180$ °C, $\tau = 2$ h

As it follows from scanning electron microscopy data (Fig. 4(c)), changes in the hydrothermal treatment temperature and duration produce almost no effect on the formed particles' morphology. In all cases, particles of a non-isometric (plate-like) shape with a thickness of 100 – 500 nm and a plate width of up to 5 μm are formed. According to the results of X-ray diffraction line broadening analysis, the plates observed in Fig. 4(c) consist of crystallites with a size of about 30 nm. And both the particle size (Fig. 4(c)) and the crystallite size (Fig. 4(b)) remain almost unaffected by an increase in the hydrothermal treatment temperature and duration.

4. Conclusion

Thus, the presented data allows us to conclude that clusters with a Bi_2WO_6 -like structure are formed at the stage of precipitation, and the presence of such clusters to a significant degree determines the formation rate of bismuth tungstate nanocrystals. It should also be noted that the morphology of the particles formed during hydrothermal treatment depends on the hydrothermal medium's pH.

Acknowledgements

The authors express their gratitude to V. V. Gusarov for the attention he paid to the work.

X-ray diffraction and SEM was performed using the equipment of the Engineering Center Saint Petersburg State Institute of Technology.

This study was financially supported by the Russian Science Foundation (project no. 16-13-10252).

References

- [1] Pattanayak S., Choudhary R.N.P. Synthesis, electrical and magnetic characteristics of Nd-modified BiFeO_3 . *Ceramics International*, 2015, **41** (8), P. 9403–9410.
- [2] Popkov V.I., Almjasheva O.V., et al. Magnetic properties of YFeO_3 nanocrystals obtained by different soft-chemical methods. *Journal of Materials Science: Materials in Electronics*, 2017, **28** (10), P. 7163–7170.
- [3] Kaur P., Singh K. Review of perovskite-structure-related cathode materials for solid oxide fuel cells. *Ceramics International*, 2020, **46** (51), P. 5521–5535.
- [4] Martinson K.D., Ivanov V.A., et al. Facile combustion synthesis of TbFeO_3 nanocrystals with hexagonal and orthorhombic structure. *Nanosyst.: Phys. Chem. Math.*, 2019, **10** (6), P. 694–700.
- [5] Lomanova N.A., Tomkovich M.V., et al. Magnetic Properties of $\text{Bi}_{1-x}\text{Ca}_x\text{FeO}_{3-\delta}$ Nanocrystals. *Physics of the Solid State*, 2019, **61**, P. 2535–2541.

- [6] Lin X., Liu Z., et al. Controllable synthesis and photocatalytic activity of spherical, flower-like and nanofibrous bismuth tungstates. *Mater. Sci. Eng. B*, 2014, **188**, P. 35–42.
- [7] Liu Y., Ding Z., et al. Hydrothermal synthesis of hierarchical flower-like Bi_2WO_6 microspheres with enhanced visible-light photoactivity. *Mater. Lett.*, 2015, **157**, P. 158–162.
- [8] Phuruangrat A., Maneechote A., et al. Effect of pH on visible-light-driven Bi_2WO_6 nanostructured catalyst synthesized by hydrothermal method. *Superlattice. Microst.*, 2015, **78**, P. 106–115.
- [9] Ge M., Liu L. Sunlight-induced photocatalytic performance of Bi_2WO_6 hierarchical microspheres synthesized via a relatively green hydrothermal route. *Mater. Sci. Semicond. Process.*, 2014, **25**, P. 258–263.
- [10] Er X., Zhang Y., et al. Atomic structure of domain and defect in layered-perovskite Bi_2WO_6 thin films. *Mater. Charact.*, 2019, **154**, P. 395–399.
- [11] Utkin V.I., Roginskaya Y.E., et al. Dielectric properties, electrical conductivity, and relaxation phenomena in ferroelectric Bi_2WO_6 . *Phys. Status Solidi A – Appl. Mater. Sci.*, 1980, **59** (1), P. 75–82.
- [12] Kudo A., Hijii S. H_2 or O_2 evolution from aqueous solutions on layered oxide photocatalysts consisting of Bi^{3+} with $6s^2$ configuration and dtransition metal ions. *Chem. Lett.*, 1990, **28** (10), P. 1103–1104.
- [13] Zhang Q., Jiang Z., Wang M., Ge X. Gamma ray radiation effect on Bi_2WO_6 photocatalyst. *Chin. J. Chem. Phys.*, 2018, **31** (5) P. 701–706.
- [14] Wang D., Zhen Y., et al. Synthesis of mesoporous Bi_2WO_6 architectures and their gas sensitivity to ethanol. *J. Mater. Chem. C1*, 2013, **26**, P. 4153–4162.
- [15] Finlayson A.P., Ward E., Tsaneva V.N., Glowacki B.A. Bi_2O_3 – WO_3 compounds for photocatalytic applications by solid state and viscous processing. *Journal of Power Sources*, 2005, **145** (2), P. 667–674.
- [16] Zhang Z.J., Wang W.Z., et al. Low-temperature combustion synthesis of Bi_2WO_6 nanoparticles as a visible-light-driven photocatalyst. *J. Hazard. Mater.*, 2010, **177**, P. 1013–1018.
- [17] Zawawi S.M.M., Yahya R., et al. Structural and optical characterization of metal tungstates (MWO_4 ; M = Ni, Ba, Bi) synthesized by a sucrose-templated method. *Chem. Cent. J.*, 2013, **7** (1), P. 80–90.
- [18] Yu S.-H., Liu B., et al. General synthesis of single-crystal tungstate nanorods/nanowires: a facile low-temperature solution approach. *Advanced Functional Materials*, 2003, **13**, P. 639–647.
- [19] Phu N.D., Hoang L.H., et al. Study of photocatalytic activities of Bi_2WO_6 nanoparticles synthesized by fast microwave-assisted method. *J. Alloys. Compd.*, 2015, **647**, P. 123–128.
- [20] Zhang G.K., Lu F., et al. Synthesis of nanometer Bi_2WO_6 synthesized by sol-gel method and its visible-light photocatalytic activity for degradation of 4BS. *J. Phys. Chem. Solids*, 2010, **71**, P. 579–582.
- [21] Zhu J., Wang J.G., et al. Solvothermal synthesis of highly active Bi_2WO_6 visible photocatalyst. *Res. Chem. Intermed.*, 2009, **35**, P. 799–806.
- [22] Xu C.X., Wei X., et al. Solvothermal preparation of Bi_2WO_6 nanocrystals with improved visible light photocatalytic activity. *Mater. Lett.*, 2009, **63**, P. 2194–2197.
- [23] Shang M., Wang W., et al. A practical visible-light-driven Bi_2WO_6 nanofibrous mat prepared by electrospinning. *J. Mater. Chem.*, 2009, **19** (34), P. 6213–6218.
- [24] Zhao G., Liu S.W., et al. Fabrication of electrospun Bi_2WO_6 microbelts with enhanced visible photocatalytic degradation activity. *J. Alloys Compd.*, 2013, **578**, P. 12–16.
- [25] Xu F., Xu C., et al. The synthesis of $\text{Bi}_2\text{S}_3/2\text{D}$ – Bi_2WO_6 composite materials with enhanced photocatalytic activities. *J. Alloys Compd.*, 2019, **780**, P. 634–642.
- [26] Liu Y., Tang H., et al. Self-assembled three-dimensional hierarchical Bi_2WO_6 microspheres by sol-gel-hydrothermal route. *Ceram. Int.*, 2014, **40**, P. 6203–6209.
- [27] Amano F., Nogami K., Abe R., Ohtani B. Preparation and characterization of bismuth tungstate polycrystalline flake-ball particles for photocatalytic reactions. *J. Phys. Chem. C*, 2008, **112**, P. 391–401.
- [28] Lomakin M.S., Proskurina O.V., Gusarov V.V. Influence of hydrothermal synthesis conditions on the composition of the pyrochlore phase in the Bi_2O_3 – Fe_2O_3 – WO_3 system. *Nanosyst.: Phys. Chem. Math.*, 2020, **11** (2), P. 246–251.
- [29] Zhang Z., Lin Y., Liu F. Preparation, crystallization and properties of Bi_2WO_6 nanoparticles. *Colloids and Surfaces A*, 2020, **5905**, 124493.
- [30] Tahmasebi N., Maleki Z., Farahnak P. Enhanced photocatalytic activities of $\text{Bi}_2\text{WO}_6/\text{BiOCl}$ composite synthesized by one-step hydrothermal method with the assistance of HCl. *Mater. Sci. Semicond. Process.*, 2019, **89**, P. 32–40.
- [31] Sharikov F.Yu., Almjasheva O.V., Gusarov V.V. Thermal analysis of formation of ZrO_2 nanoparticles under hydrothermal conditions. *Russ. J. Inorg. Chem.*, 2006, **51** (10), P. 1538–1542.
- [32] Kuznetsova V.A., Almjasheva O.V., Gusarov V.V. Influence of microwave and ultrasonic treatment on the formation of CoFe_2O_4 under hydrothermal conditions. *Glass Physics and Chemistry*, 2009, **35** (2), P. 205–209.
- [33] Proskurina O.V., Abiev R.S., et al. Formation of nanocrystalline BiFeO_3 during heat treatment of hydroxides co-precipitated in an impinging-jets microreactor. *Chemical Engineering and Processing – Process Intensification*, 2019, **143**, 107598.
- [34] Proskurina O.V., Nogovitsin I.V., et al. Formation of BiFeO_3 Nanoparticles Using Impinging Jets Microreactor. *Russ. J. Gen. Chem.*, 2018, **88** (10), P. 2139–2143.
- [35] Xia J.X., Di J., et al. Facile fabrication of the visible-light-driven $\text{Bi}_2\text{WO}_6/\text{BiOBr}$ composite with enhanced photocatalytic activity. *RSC Advances*, 2014, **4**, P. 82–90.
- [36] Qamar M., Elsayed R.B., et al. Highly efficient and selective oxidation of aromatic alcohols photocatalyzed by nanoporous hierarchical Pt/ Bi_2WO_6 in organic solvent-free environment. *ACS Applied Materials & Interfaces*, 2015, **7** (2), P. 1257–1269.
- [37] Liu L., Qi Y., et al. Dramatic activity of a $\text{Bi}_2\text{WO}_6@g\text{-C}_3\text{N}_4$ photocatalyst with a core@shell structure. *RSC Advances*, 2015, **5** (120), P. 99339–99346.

3D computer models of the T-x-y diagrams, forming the LiF–NaF–CaF₂–LaF₃ T-x-y-z diagram

V. P. Vorob'eva, A. E. Zelenaya, V. I. Lutsyk, M. V. Lamueva

Institute of Physical Materials Science SB RAS, 6, Sakhyanova str., Ulan-Ude, 670047, Russia

vvorobjeva@mail.ru

PACS 81.30.Dz

DOI 10.17586/2220-8054-2020-11-3-345-354

Giving professor P.P. Fedorov his due as the leading specialist in fluoride systems and using his theoretical investigations on the topology and geometry of phase diagrams of binary and ternary fluoride systems, as well as experimental results, obtained by colleagues under his leadership, the total geometric description of the systems, forming the LiF–NaF–CaF₂–LaF₃ system, which has considerable promise for the development of fourth generation fuels for nuclear reactors, has been received. For this purpose, three-dimensional computer models of all four ternary systems have been constructed and the T-x-y-z diagram of this fluoride system has been predicted.

Keywords: phase diagram, computer model, four-dimensional visualization, lithium fluoride, sodium fluoride, calcium fluoride, lanthanum fluoride.

Received: 3 June 2020

1. Introduction

The compositions obtained from the LiF–NaF–CaF₂–LaF₃ system, as well as many other fluoride systems, are investigated in connection with the development of fourth generation nuclear reactors [1]. In this case, LaF₃ serves as a proxy-compound for PuF₃, since the direct use of PuF₃ would cause enormous experimental difficulties. For the successful design of multicomponent materials, it is very convenient to use spatial (3D – three-dimensional, 4D – four-dimensional) computer models of T-x-y and T-x-y-z diagrams, correspondingly [2, 3]. On the one hand, they generalize the known experimental data and provide opportunities for model adjustment as new knowledge about the system becomes available. On the other hand, the information, accumulated in the 3D model, allows one to understand and to follow the crystallization history of a particular 3-component melt (alloy, ceramic, salts composition).

A huge long-term work on the study of fluoride systems was carried out by professor P.P. Fedorov and colleagues [4–22]. It included a comprehensive experimental study of binary and ternary halide systems, and a theoretical analysis of the topological and geometric features of the obtained phase diagrams. For instance, saddle points on the liquidus surfaces, associated with the congruent nature of melting, were experimentally discovered [20, 21] in the systems BaF₂–SrF₂–LaF₃ [10], PbF₂–CdF₂–RF₃ (R=Er, Lu) [18], CaF₂–SrF₂–RF₃ (R=La, Nd, Yb) [19]. It was shown that the conjugate surfaces of the liquidus and solidus can have a singular point of the saddle type [22], and the saddle point on the surface of the diagram appears if the liquidus of two boundary binary systems has a minimum and the third one has a maximum or vice versa.

The surfaces of the phase diagrams formed by the fluorides of lithium, sodium, calcium, and lanthanum are not so complicated; they haven't the saddle or extrema points. But the geometric structure of these diagrams becomes more complicated by the formation of the binary NaLaF₄ compound and polymorphism of CaF₂ [23]. 3D models are constructed on the basis of data on binary systems, projections of liquidus surfaces with isothermal lines, drawn on them.

2. Binary and ternary systems, forming the LiF–NaF–CaF₂–LaF₃ T-x-y-z diagram

Before designing a computer 3D (and 4D too) model, it is necessary to discuss the boundary systems [23], as well as to make a formal indication of the quaternary system under consideration, that is, to indicate the LiF–NaF–CaF₂–LaF₃ system as A-B-C-D, and to give the necessary indication of all phase transformations. For example, two polymorphic modifications of CaF₂ are involved in the formation of the LiF–NaF–CaF₂–LaF₃ (A-B-C-D) diagram and they received the appropriate indicators: C and C1.

The systems LiF–NaF (A-B) and LiF–LaF₃ (A-D) are eutectic ones, LiF–CaF₂ (A-C) and NaF–CaF₂ (B-C) are also of eutectic type, but they include a polymorphic transition in the form of the metatectic reaction ($C \rightarrow C1 + L$), due to the allotropy of calcium fluoride (CaF₂).

The incongruently melting NaLaF₄ (R) compound is formed in the NaF–LaF₃ (B-D) system and two reactions – peritectic p_{DR} : $L + D \rightarrow R$ and eutectic e_{BR} : $L \rightarrow B + R$ – take a place.

The eutectic $\text{CaF}_2\text{-LaF}_3$ (C-D) system is characterized by the eutectoid reaction $\text{C} \rightarrow \text{C1} + \text{D}$ because of the polymorphism of calcium fluoride.

The ternary eutectic system LiF-NaF-CaF_2 (A-B-C) with a single invariant reaction $\text{E}_1: \text{L} \rightarrow \text{A} + \text{B} + \text{C1}$ is complicated by the univariant polymorphic $\text{C} \rightarrow \text{C1} + \text{L}$ transition between two CaF_2 modifications (Fig. 1a).

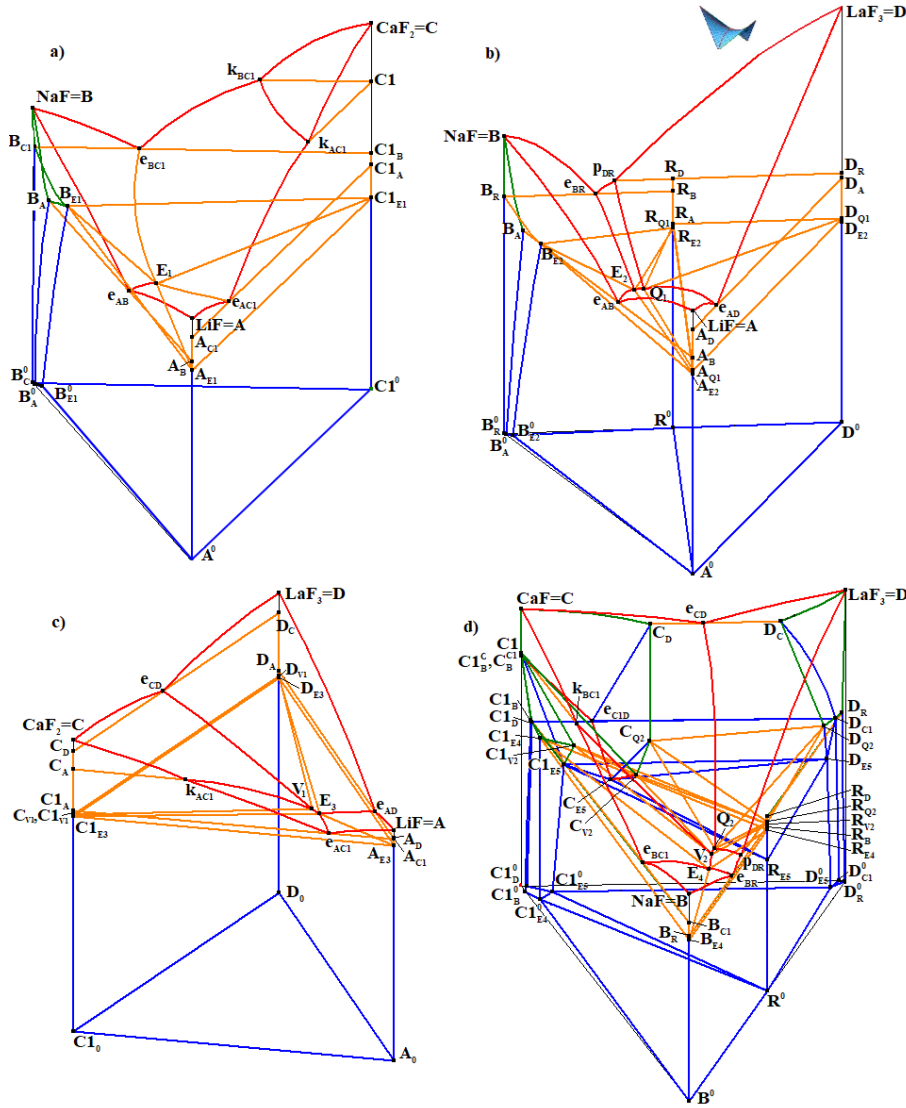


FIG. 1. 3D computer models of T-x-y diagrams LiF-NaF-CaF_2 (A-B-C) (a), LiF-NaF-LaF_3 (A-B-D) (b), $\text{LiF-CaF}_2\text{-LaF}_3$ (A-C-D) (c) – simplified model, $\text{NaF-CaF}_2\text{-LaF}_3$ (B-C-D) (d)

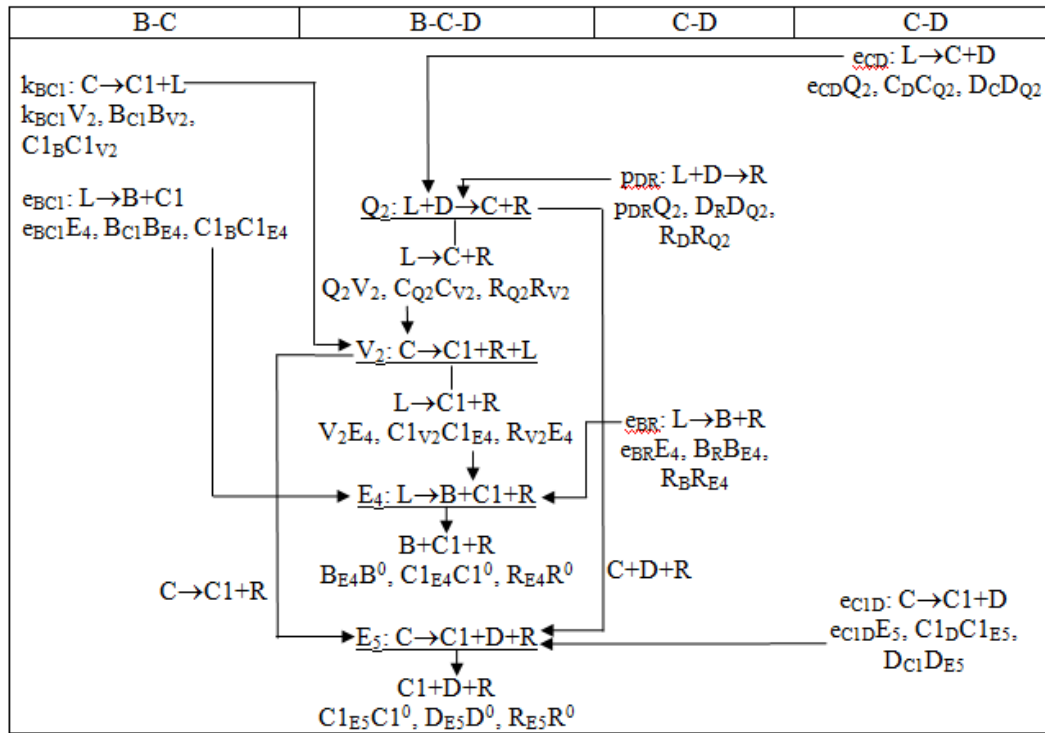
The system LiF-NaF-LaF_3 (A-B-D) with the NaLaF_4 (R) binary incongruently melting compound is characterized by quasi-peritectic $\text{Q}_1: \text{L} + \text{D} \rightarrow \text{A} + \text{R}$ and eutectic $\text{E}_2: \text{L} \rightarrow \text{A} + \text{B} + \text{R}$ invariant reactions (Fig. 1b).

There are two invariant transformations in the $\text{LiF-CaF}_2\text{-LaF}_3$ (A-C-D) system (Fig. 1c). One of them is the eutectic reaction $\text{E}_3: \text{L} \rightarrow \text{A} + \text{D} + \text{C1}$. The second one in [23] is called a quasi-peritectic reaction and is written as $\text{L} + \text{C} \rightarrow \text{C1} + \text{D}$. However, it is not. Since the $\text{C} \rightarrow \text{C1} + \text{L}$ polymorphic transition in the A-C binary system is associated with this reaction, the $\text{V}_1: \text{C} \rightarrow \text{C1} + \text{D} + \text{L}$ polymorphic transition also takes a place in the ternary system, formed by it, with the passive role of the L and LaF_3 (D). More details on ternary systems with allotropy of components, including a similar case, are described in the paper [24].

A similar polymorphic transition $\text{V}_2: \text{C} \rightarrow \text{C1} + \text{R} + \text{L}$ takes a place in the $\text{NaF-CaF}_2\text{-LaF}_3$ (B-C-D) system. This reaction is intermediate between two other invariant reactions, quasi-peritectic $\text{Q}_2: \text{L} + \text{D} \rightarrow \text{C} + \text{R}$ and eutectic $\text{E}_4: \text{L} \rightarrow \text{B} + \text{R} + \text{C1}$ (Fig. 1d). The logic of phase reactions leads to the fact that it should expect another invariant reaction – the eutectoid one $\text{E}_5: \text{C} \rightarrow \text{C1} + \text{D} + \text{R}$. The scheme of uni- and invariant states of this system (Table 1), as

well as three other geometrically simpler systems (Fig. 1a-c), gives a possibility to describe all surfaces (Table 2) and all phase regions (Table 3) of the NaF-CaF₂-LaF₃ (B-C-D) T-x-y diagram.

TABLE 1. The scheme of uni- and invariant states of the NaF-CaF₂-LaF₃ (B-C-D) T-x-y diagram with the NaLaF₄ (R) incongruently melting compound and CaF₂ allotropy (Fig. 1d), $D > C > e_{CD} > k_{BC1} > B > e_{BC1} > p_{DR} > Q_2 > V_2 > e_{BR} > e_{C1D} > E_4 > E_5$



Three-dimensional (3D) computer models allow to get any isothermal section (Fig. 2a) or isopleth (Fig. 2b).

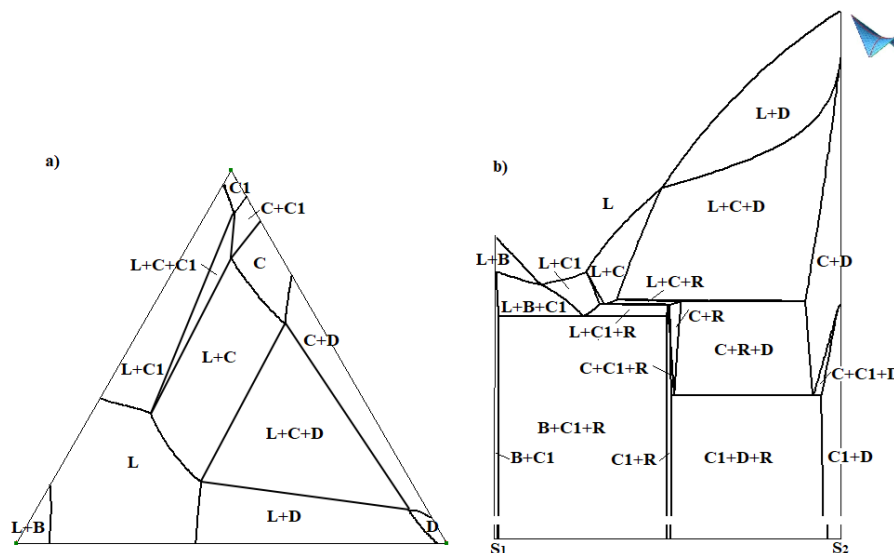


FIG. 2. Isothermal section at 1200 K (a) and isopleth $S_1(0.8, 0.2, 0)-S_2(0, 0.2, 0.8)$ (b) of the NaF-CaF₂-LaF₃ (B-C-D) T-x-y diagram 3D model

To visualize the results of calculations of mass balances of coexisting phases, mass balance diagrams (DMB) are used [25]. Such DMB, called vertical (VDMB) one (Fig. 3a), is able to show not only the phase ratios for a given mass

TABLE 2. Surfaces of the NaF–CaF₂–LaF₃ (B–C–D) T–x–y diagram with the NaLaF₄ (R) incongruently melting compound (Fig. 1d)

No	Designation	Points of contour	No	Designation	Points of contour
liquidus – solidus					
1	q _B	B _e BC ₁ E ₄ e _{BR}	6	s _B	BB _{C1} B _{E4} B _R
2	q _C	Ck _{BC1} V ₂ Q ₂ e _{CD}	7	s _C	CC ^{C1} _B CV ₂ CQ ₂ C _D
3	q _{C1}	k _{BC1} V ₂ E ₄ e _{BC1}	8	s _{C1}	C1 ^C _B C1V ₂ C1E ₄ C1 _B
4	q _D	Dp _{DR} Q ₂ e _{CD}	9	s _D	DD _R DQ ₂ D _C
5	q _R	p _{DR} e _{BR} E ₄ V ₂ Q ₂	10	s _R	R _D R _B R _{E4} R _{V2} R _{Q2}
transus					
11	t ^q	C1C ^{C1} _B e _{C1D} C _{E5} C _{V2}	12	t ^s	C1C1 ^C _B C1 _D C1 _{E5} C1 _{V2}
solvus					
13	v _{BC1}	B _{C1} B _{E4} B ⁰ _{E4} B ⁰ _{C1}	20	v _{C1B}	C1 _B C1 _{E4} C1 ⁰ _{E4} C1 ⁰ _B
14	v _{BR}	B _R B _{E4} B ⁰ _{E4} B ⁰ _R	21	v _{RB}	R _B R _{E4} R ⁰ _{E4} R ⁰ _B
15	v _{CD}	C _D e _{C1D} C _{E5} C _{Q2}	22	v _{DC}	D _C D _{C1} D _{E5} D _{Q2}
16	v _{CR}	C _{Q2} C _{V2} C _{E5}	23	v _{RC}	R _{Q2} R _{V2} R _{E5}
17	v _{C1R}	C1V ₂ C1E ₄ C1 ⁰ _{E4} C1 ⁰ _{E5} C1 _{E5}	24	v _{RC1}	R _{V2} R _{E4} R ⁰ _{E4} R ⁰ _{E5} R _{E5}
18	v _{DR}	D _R D _{Q2} D _{E5} D ⁰ _{E5} D ⁰ _R	25	v _{RD}	R _D R _{Q2} R _{E5} R ⁰ _{E5} R ⁰ _D
19	v _{C1D}	C1 _D C1 _{E5} C1 ⁰ _{E5} C1 ⁰ _D	26	v _{D1}	D _{C1} D _{E5} D ⁰ _{E5} D ⁰ _{C1}
ruled surfaces					
27	q ^r _{BC1}	e _{BC1} E ₄ -B _{C1} B _{E4}	45	q ^r _{BR}	e _{BR} E ₄ -B _R B _{E4}
28	q ^r _{C1B}	e _{BC1} E ₄ -C1 _B C1 _{E4}	46	q ^r _{RB}	e _{BR} E ₄ -R _B R _{E4}
29	s ^r _{BC1}	B _{C1} B _{E4} -C1 _B C1 _{E4}	47	s ^r _{BR}	B _R B _{E4} -R _B R _{E4}
30	q ^r _{CD}	e _{CD} Q ₂ -C _D C _{Q2}	48	q ^r _{CR}	Q ₂ V ₂ -C _{Q2} C _{V2}
31	q ^r _{DC}	e _{CD} Q ₂ -D _C D _{Q2}	49	q ^r _{RC}	Q ₂ V ₂ -R _{Q2} R _{V2}
32	s ^r _{CD}	C _D C _{Q2} -D _C D _{Q2}	50	s ^r _{CR}	C _{Q2} C _{V2} -R _{Q2} R _{V2}
33	q ^r _{C1R}	V ₂ E ₄ -C1 _{V2} C1 _{E4}	51	q ^r _{DR}	p _{DR} Q ₂ -D _R D _{Q2}
34	q ^r _{RC1}	V ₂ E ₄ -R _{V2} R _{E4}	52	q ^r _{RD}	p _{DR} Q ₂ -R _D R _{Q2}
35	s ^r _{C1R}	C1 _{V2} C1 _{E4} -R _{V2} R _{E4}	53	s ^r _{DR}	D _R D _{Q2} -R _D R _{Q2}
36	q ^r _{CC1}	k _{BC1} V ₂ -C ^{C1} _B C _{V2}	54	q ^{rC} _{C1D}	e _{C1D} C _{E5} -C1 _D C1 _{E5}
37	q ^r _{C1C}	k _{BC1} V ₂ -C1 ^C _B C1 _{V2}	55	q ^{rC} _{DC1}	e _{C1D} C _{E5} -D _{C1} D _{E5}
38	s ^r _{CC1}	C ^{C1} _B CV ₂ -C1 ^C _B C1 _{V2}	56	s ^{rC} _{C1D}	C1 _D C1 _{E5} -D _{C1} D _{E5}
39	q ^{rC} _{C1R}	C _{V2} C _{E5} -C1 _{V2} C1 _{E5}	57	v ^r _{CD(Q2)}	C _{Q2} C _{E5} -D _{Q2} D _{E5}
40	q ^{rC} _{RC1}	C _{V2} C _{E5} -R _{V2} R _{E5}	58	v ^r _{CR(Q2)}	C _{Q2} C _{E5} -R _{Q2} R _{E5}
41	s ^{rC} _{C1R}	C1 _{V2} C1 _{E5} -R _{V2} R _{E5}	59	v ^r _{DR(Q2)}	D _{Q2} D _{E5} -R _{Q2} R _{E5}
42	v ^r _{BC1(E4)}	B _{E4} B ⁰ _{E4} -C1 _{E4} C1 ⁰ _{E4}	60	v ^r _{C1D(E5)}	C _{E5} C ⁰ _{E5} -D _{E5} D ⁰ _{E5}
43	v ^r _{BR(E4)}	B _{E4} B ⁰ _{E4} -R _{E4} R ⁰ _{E4}	61	v ^r _{C1R(E5)}	C1 _{E5} C1 ⁰ _{E5} -R _{E5} R ⁰ _{E5}
44	v ^r _{C1R(E4)}	C1 _{E4} C1 ⁰ _{E4} -R _{E4} R ⁰ _{E4}	62	v ^r _{DR(E5)}	D _{E5} D ⁰ _{E5} -R _{E5} R ⁰ _{E5}
horizontal planes					
63	h ^{Q2} _{CDR}	C _{Q2} D _{Q2} R _{Q2}	71	h ^{V2} _{CC1R}	C _{V2} C1 _{V2} R _{V2}
64	h _{CDQ2}	C _{Q2} D _{Q2} Q ₂	72	h _{CC1V2}	C _{V2} C1 _{V2} V ₂
65	h _{CRQ2}	C _{Q2} R _{Q2} Q ₂	73	h _{CRV2}	C _{V2} R _{V2} V ₂
66	h _{DRQ2}	D _{Q2} R _{Q2} Q ₂	74	h _{C1RV2}	C1 _{V2} R _{V2} V ₂
67	h ^{E4} _{BC1R}	B _{E4} C1 _{E4} R _{E4}	75	h ^{E5} _{CC1D}	C _{E5} C1 _{E5} D _{E5}
68	h _{BC1E4}	B _{E4} C1 _{E4} E ₄	76	h ^{E5} _{CC1R}	C _{E5} C1 _{E5} R _{E5}
69	h _{BRE4}	C _{E4} R _{E4} E ₄	77	h ^{E5} _{CDR}	C _{E5} D _{E5} R _{E5}
70	h _{C1RE4}	C1 _{E4} R _{E4} E ₄	78	h ^{E5} _{C1DR}	C1 _{E5} D _{E5} R _{E5}

TABLE 3. Phase regions of the NaF–CaF₂–LaF₃ (B-C-D) T-x-y diagram with the NaLaF₄ (R) incongruently melting compound (Fig. 1d)

No	Phase region	Border hypersurfaces	Adjacent phase regions
1	L+B	$q_B, s_B, q_{BC1}^r, q_{BR}^r$	L, B, L+B+C1, L+B+R
2	L+C	$q_C, s_C, q_{CD}^r, q_{CR}^r, q_{CC1}^r$	L, C, L+C+D, L+C+R, L+C+C1
3	L+C1	$q_{C1}, s_{C1}, q_{C1B}^r, q_{C1C}^r, q_{C1R}^r$	L, C1, L+B+C1, L+C+C1, L+C1+R
4	L+D	$q_D, s_D, q_{DC}^r, q_{DR}^r$	L, D, L+C+D, L+D+R
5	L+R	$q_R, s_R, q_{RB}^r, q_{RC}^r, q_{RC1}^r, q_{RD}^r$	L, R, L+B+R, L+C+R, L+C1+R, L+D+R
6	L+B+C1	$q_{BC1}^r, q_{C1B}^r, s_{BC1}^r, h_{BC1E4}$	L+B, L+C1, B+C1, L+B+C1+R
7	L+B+R	$q_{BR}^r, q_{RB}^r, s_{BR}^r, h_{BRE4}$	L+B, L+R, B+R, L+B+C1+R
8	L+C+D	$q_{CD}^r, q_{DC}^r, s_{CD}^r, h_{CDQ2}$	L+C, L+D, C+D, L+C+D+R
9	L+C+R	$q_{CR}^r, q_{RC}^r, s_{CR}^r, h_{CRQ2}, h_{CRV2}$	L+C, L+R, C+R, L+C+D+R, L+C+C1+R
10	L+C1+R	$q_{C1R}^r, q_{RC1}^r, s_{C1R}^r, h_{C1RV2}, h_{C1RE4}$	L+C1, L+R, C1+R, L+C+C1+R, L+B+C1+R
11	L+D+R	$q_{DR}^r, q_{RD}^r, s_{DR}^r, h_{DRQ2}$	L+D, L+R, D+R, L+C+D+R
12	L+C+C1	$q_{CC1}^r, q_{C1C}^r, s_{CC1}^r, h_{CC1V2}$	L+C, L+C1, C+C1, L+C+C1+R
13	B	s_B, v_{BC1}, v_{BR}	L+B, B+C1, B+R
14	C	s_C, v_{CD}, v_{CR}, t^q	L+C, C+D, C+R, C+C1
15	C1	$t^s, s_{C1}, v_{C1B}, v_{C1D}, v_{C1R}$	C+C1, L+C1, B+C1, C1+D, C1+R
16	D	$s_D, v_{DC}, v_{DR}, v_{DC1}$	L+D, C+D, D+R, C1+D
17	R	$s_R, v_{RB}, v_{RC}, v_{RC1}, v_{RD}$	L+R, B+R, C+R, C1+R, D+R
18	B+C1	$v_{BC1}, v_{C1B}, s_{BC1}^r, v_{BC1(E4)}^r$	B, C1, L+B+C1, B+C1+R
19	B+R	$v_{BR}, v_{RB}, s_{BR}^r, v_{BR(E4)}^r$	B, R, L+B+R, B+C1+R
20	C+R	$v_{CR}, v_{RC}, s_{CR}^r, v_{CR(Q2)}^r, s_{C1R}^{rC}$	C, R, L+C+R, C+D+R, C+C1+R
21	C+D	$v_{CD}, v_{DC}, s_{CD}^r, v_{CD(Q2)}^r, s_{C1D}^{rC}$	C, D, L+C+D, C+D+R, C+C1+D
22	C1+R	$v_{C1R}, v_{RC1}, s_{C1R}^r, v_{C1R(E4)}^r, q_{C1R}^{rC}, v_{C1R(E5)}^r$	C1, R, L+C1+R, B+C1+R, C+C1+R, C1+D+R
23	C1+D	$v_{C1D}, v_{DC1}, q_{C1D}^{rC}, v_{C1D(E5)}^r$	C1, D, C+C1+D, C1+D+R
24	D+R	$v_{DR}, v_{RD}, s_{DR}^r, v_{DR(Q2)}^r, v_{DR(E5)}^r$	D, R, L+D+R, C+D+R, C1+D+R
25	B+C1+R	$v_{BC1(E4)}^r, v_{BR(E4)}^r, v_{C1R(E4)}^r, h_{BC1R}^{E4}$	B+C1, B+R, C1+R, L+B+C1+R
26	C+C1+D	$q_{C1D}^{rC}, q_{DC1}^{rC}, s_{C1D}^{rC}, h_{CC1D}^{E5}$	C+C1, C+D, C1+D, C+C1+D+R
27	C+C1+R	$q_{C1R}^{rC}, q_{RC1}^{rC}, s_{C1R}^{rC}, h_{CC1R}^{V2}, h_{CC1R}^{E5}$	C+C1, C+R, C1+R, L+C+C1+R, C+C1+D+R
28	C+D+R	$v_{CD(Q2)}^r, v_{CR(Q2)}^r, v_{DR(Q2)}^r, h_{CDR}^{Q2}, h_{CDR}^{E5}$	C+D, C+R, D+R, L+C+D+R, C+C1+D+R
29	C1+D+R	$v_{C1D}^r, v_{C1R}^r, v_{DR}^r, h_{C1DR}^{E5}$	C1+D, C1+R, D+R, C+C1+D+R

center G at a fixed temperature, but also to observe the crystallization of liquid over the entire temperature range. The crystallization pathways (Fig. 3b) were considered earlier in ternary oxide and salt systems [26].

Projection of all surfaces of the T-x-y diagram onto the temperature-free x-y triangle divides it into a concentration fields. Each field differs from the others in the sequence of phase reactions and, accordingly, in the unique crystallization history (Fig. 3a). E.g., mass center *G* (0.368, 0.416, 0.216) (Fig. 3b), cuts 4 phase regions: L + C, L + C + C1, L + C1 + R, B + C1 + R. It's understandable from the VDMB (Fig. 3a), that a vertical line in point *G* cuts liquidus surface q_C and appears in the 2-phase region L + C, where a reaction of primary crystallization $L \rightarrow C^1$ proceeds. Then it cuts the ruled surface q_{CC1}^r , passing the 3-phase region L + C + C1, with the peritectic reaction $L + C \rightarrow C1^{P(C)}$, with a decrease in phases C and L share, simultaneously with the C1 phase share increasing. There is the polymorphic transition $V_2: C \rightarrow C1^{V2} + R^{V2} + L^{V2}$ at 1016 K. As a result of this reaction, the crystals C is fully expended. After the postperitectic secondary reaction $L + C1 \rightarrow R^{pp(C1)}$ occurs in the three-phase region L + R + C1 and the resulting by the invariant eutectic reaction $E_4: L \rightarrow B^{E4} + R^{E4} + C1^{E4}$ on the horizontal plane. There is the

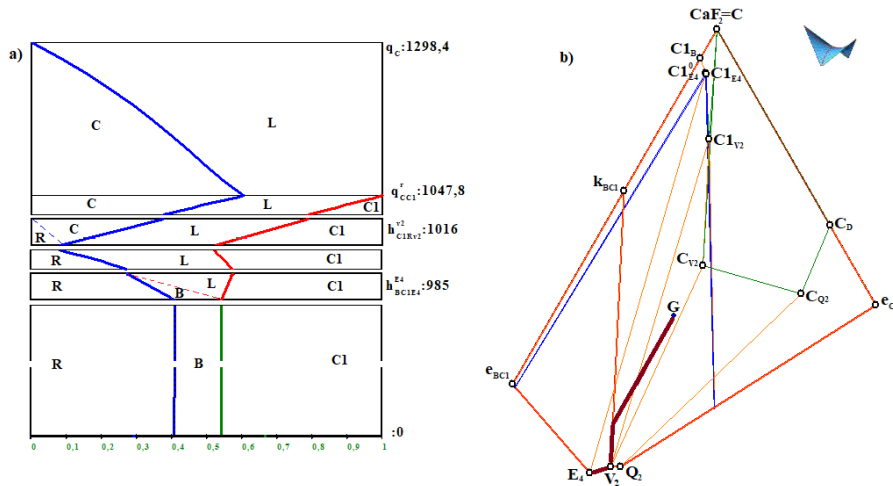


FIG. 3. Vertical mass balance diagram for the mass center G (0.368, 0.416, 0.216) (a), fragment of the x-y projection of the NaF–CaF₂–LaF₃ (B-C-D) T-x-y diagram with the crystallization path for G

sub-solidus 3-phase region $B + C1 + R$ below this plane. So, the mass center G can be characterized by the next set of the microstructural elements: $C1^{P(C)}$, $C1^{V2}$, R^{V2} , $R^{pp(C1)}$, B^{E4} , R^{E4} , $C1^{E4}$.

Presented at the VDMB crystallization stages are confirmed by the calculation of crystallization paths for the given composition (Fig. 3b).

Another option for DMB is the horizontal mass balance diagram (HDMB) (Fig. 4a). It is added to the isopleth and shows the ratios of coexisting phases for all compositions in this section at a fixed temperature (Fig. 4b). The electrical conductivity curve during melt crystallization (Fig. 4c) is performed too.

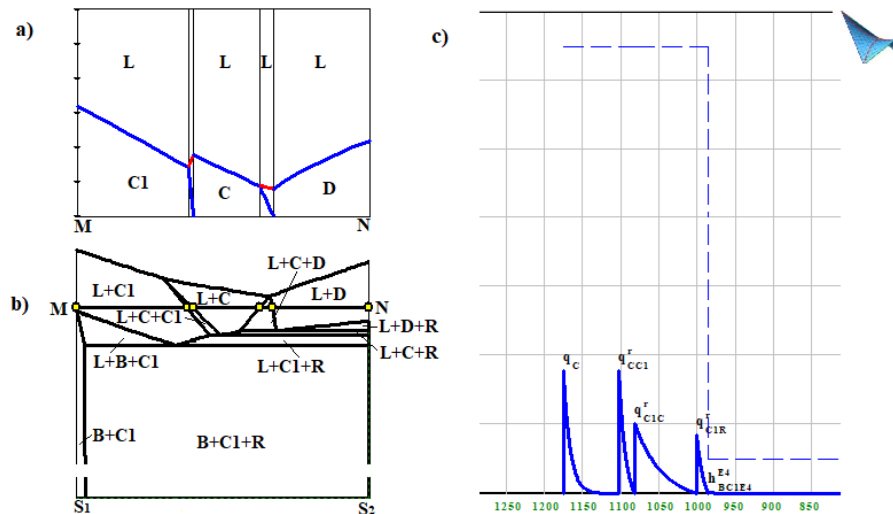


FIG. 4. Horizontal mass balance diagram at $T = 1100$ K (a) for the $S_1(0.5, 0.5, 0)$ – $S_2(0.5, 0, 0.5)$ isopleth (b), imitation of the DTA-spectra and the electrical conductivity leap for $G(0.368,0.416,0.216)$ (c) in the NaF–CaF₂–LaF₃ (B-C-D) T-x-y diagram

Thus, a 3D computer model provides an excellent opportunity to obtain a complete and comprehensive view of the T-x-y diagram, either its geometric structure or the options for its melts crystallization. In addition, 3D models are very useful as for their structures understanding and for the 4D model designing of the four-component system T-x-y-z diagram, formed by them.

3. Prediction and prototype design of the LiF–NaF–CaF₂–LaF₃ T-x-y-z diagram 4D computer model

Construction of the 3D computer model of the T-x-y diagram begins with the 3D scheme of uni- and invariant states [24,25]. This is a 3D variant of well-known scheme of phase reactions (planar Sheil scheme [27]), supplemented

- 12 two-phase regions I + J without liquid (A + B, A + C1, A + D, A + R, B + C1, B + R, C + D, C + R, C + C1, C1 + D, C1 + R, D + R) and 12 three-phase regions with liquid L + I + J;
- 10 three-phase regions I + J + K without liquid (A + B + C1, A + B + R, A + C1 + D, A + C1 + R, A + D + R, B + C1 + R, C + C1 + D, C + C1 + R, C + D + R, C1 + D + R) and 10 four-phase regions with liquid L + I + J + K;
- 3 four-phase regions without liquid A + B + C1 + R, A + C1 + D + R, C + C1 + D + R, and 3 five-phase regions degenerated into planar hyperplanes L + A + B + C1 + R, L + A + C1 + D + R, L + C + C1 + D + R.

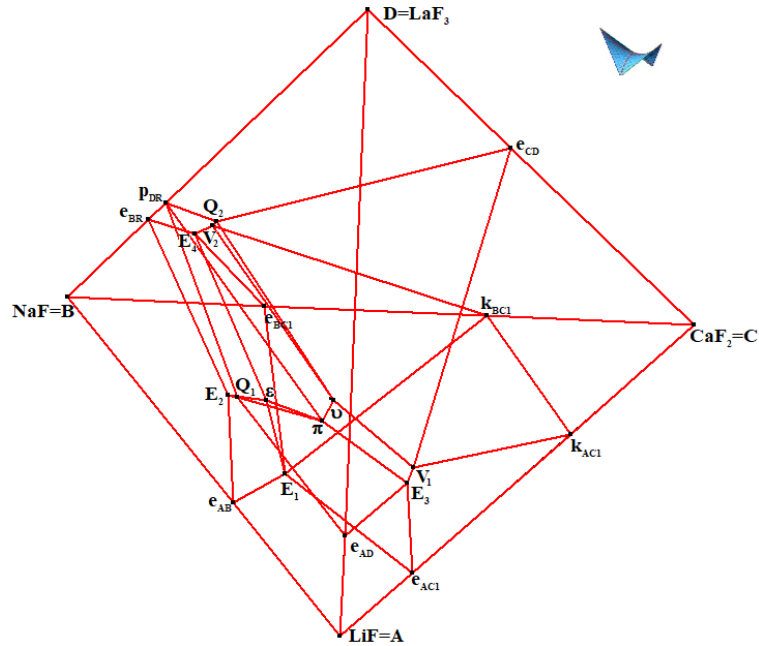


FIG. 5. Liquidus prototype 4D model: x-y-z projection of the LiF–NaF–CaF₂–LaF₃ (A-B-C-D) T-x-y-z diagram

Of course, the final confirmation (or clarification) of the prediction may be given by the experiment only.

To construct the spatial computer models of phase diagrams, it is convenient to use a special reference database for the main topological types of T-x-y and T-x-y-z diagrams. It includes the results of the phase diagrams analysis and classification for the three- and four-component systems of the main topological types [28]. This electronic guide contains 3D computer models of T-x-y diagrams: with uni- and invariant transformations, given by one, two or three binary eutectics and peritectics; with binary and ternary compounds, melting congruently or incongruently, with endothermic and exothermic phases; with the allotropy of one, two or three components, manifested in different temperature intervals; with uni- and invariant monotectic and syntectic transformations, when initial melt is decomposed into two liquids within the primary crystallization regions; with 1–3 binary monotectics or in the absence of the liquid immiscibility in binary systems; and 4D models of T-x-y-z diagrams for the six types of systems, with eutectic (peritectic) solubility gap in 1–6 border binary systems, as well as the diagrams with a binary compound, melting congruently or incongruently.

Each spatial computer model is a prototype of a phase diagram, which is able to become a perfect model of a real system after the experimental or calculated parameters (concentrations and temperatures of binary and ternary points, curvature characteristics of surfaces, according to isothermal sections and isopleths) input.

4. Conclusion

1) 3D computer models of T-x-y diagrams forming the LiF–NaF–CaF₂–LaF₃ T-x-y-z diagram have been constructed. The quality of models was confirmed by comparing of the model sections with experimental ones [23]. The ability of models to describe the history of crystallization of any melt of an arbitrary concentration or any melt belonging to a given isopleth at a given temperature, to draw crystallization paths and to simulate DTA spectra was demonstrated.

2) The T-x-y-z diagram, based on the T-x-y diagrams 3D models, has been predicted and the 4D model of its prototype has been constructed. It includes three invariant transformations: the polymorphic transition between two modifications of calcium fluoride in the passive presence of liquid, LaF₃ and the NaLaF₄ compound, the quasi-peritectic and eutectic reactions. In general, the T-x-y-z diagram may consist of 169 hypersurfaces and 66 phase regions.

3) When designing spatial computer models of phase diagrams of ternary, quaternary, and more complex systems, more attention should be paid to updating the data on their edges, including information about the initial components and compounds. In the 4D model of the LiF–NaF–CaF₂–LaF₃ diagram, considered in this paper and forming it 3D models of ternary systems, it is necessary in the future to take into account the decomposition of the binary compound NaLaF₄ in the sub-solidus at 330 °C [15], which is not mentioned in [23], where a binary system has been limited from below by the temperature of 600 K.

This 4D model is based on data from [23] with CaF₂ allotropy. However, this property of calcium fluoride is not taken into account in [29–31]. It is possible that the authors of these papers were not interested, for practical reasons, in such high temperatures (1420 K) and they did not take into account the high-temperature modification of calcium fluoride, which is stable at atmospheric pressure [32].

Nanostructured compounds (similar to Cu₂ZnSnSe₄, Ag₂ZnSnSe₄, Cu₂ZnSn_{1-x}In_xSe₄ [33–36]) should be characterized within the quaternary, quinary and more complex systems. However, research and development of multi-component materials were carried out mainly by experiments, which is quite time-consuming and needs considerable effort. In addition to the CALPHAD technique, the new ideas to develop an integrated calculation, synthesis and characterization approach, aiming to accelerate the research efficiency, are offered [37]. Multidimensional computer model of phase diagram became an important tool to investigate the multicomponent systems. It permits to receive an adequate evaluation for the thermodynamic calculation and for the interpretation of experimental data. Computer design of materials gives a possibility to detect such nuances of micro- and nanostructure formation as 3-phase transformation type change and competition of crystals with different dispersity [38, 39].

Acknowledgements

This work was been performed under the program of fundamental research SB RAS (project 0336-2019-0008) and it was partially supported by the RFBR projects 19-38-90035, 20-21-00056.

References

- [1] Beneš O., Konings R.J.M. Molten Salt Reactor Fuel and Coolant. *Comprehensive Nuclear Materials*, 2012, **3**, P. 359–389.
- [2] Lutsyk V.I., Vorob'eva V.P., Zelenaya A.E. 3D Computer Model of the Ni–Cu–NiS–Cu₂S Subsystem T-x-y Diagram above 575 °C. *Russ. J. Phys. Chem.*, 2019, **93** (13), P. 2593–2599.
- [3] Lutsyk V.I., Vorob'eva V.P. 3D Computer Models of the T-x-y Diagrams, Forming the Fe–Ni–Co–FeS–NiS–CoS Subsystem. *Russ. J. Phys. Chem.*, 2017, **91** (13), P. 2593–2599.
- [4] Lukiyanchuk G., Fedorov P.P. The BaF₂–SnF₄ System. *Russ. J. Inorgan. Chem.*, 1996, **41** (5), P. 826–827.
- [5] Fedorov P.P., Buchinskaya I.I., et al. Phase Diagrams of the NaF–RF₃ (R = Tb, Dy, Er) Systems. *Russ. J. Inorgan. Chem.*, 1996, **41** (10), P. 1715–1719.
- [6] Fedorov P.P., Buchinskaya I.I., et al. Phase Diagrams of the NaF–RF₃ (R = Tm, Yb, Lu) Systems. *Russ. J. Inorgan. Chem.*, 1996, **41** (11), P. 1920–1924.
- [7] Ratnikova I.D., Korenev Y.M., et al. Phase Diagrams of the Systems BaF₂–RF₄ (R=Zr, Hf). *Russ. J. Inorgan. Chem.*, 1997, **42** (2), P. 302–307.
- [8] Stasyuk V.A., Buchinskaya I.I., et al. Phase Diagram of the CaF₂–SrF₂–NdF₃ System. *Russ. J. Inorgan. Chem.*, 1998, **43** (5), P. 844–848.
- [9] Buchinskaya I.I., Fedorov P.P. Interaction of Lead Fluoride with Strontium and Calcium Fluorides. *Russ. J. Inorgan. Chem.*, 1998, **43** (7), P. 1106–1110.
- [10] Fedorov P.P., Ivanovskaya N.A., et al. Phase Equilibria in the SrF₂–BaF₂–LaF₃ System. *Doklady Physical Chemistry*, 1999, **366** (4–6), P. 168–170.
- [11] Zakalyukin R.M., Glazunova T.Yu., et al. Phase Equilibria in the Pb₃Al₂F₁₂–Ba₃In₂F₁₂ Section of the PbF₂–BaF₂–AlF₃–InF₃ Quaternary System. *Russ. J. Inorgan. Chem.*, 1999, **44** (10), P. 1645–1648.
- [12] Fedorov P.P. Systems of Alkali and Rare-Earth Metal Fluorides. *Russ. J. Inorgan. Chem.*, 1999, **4** (11), P. 1703–1727.
- [13] Korenev Yu.M., Antipov P.I., et al. Phase Diagrams for the RF₃–HfF₄ Systems (R is a rare-earth elements). *Russ. J. Inorgan. Chem.*, 2000, **45** (2), P. 164–169.
- [14] Filatova N.G., Fedorov P.P. RbF–PrF₃ System. *Russ. J. Inorgan. Chem.*, 2000, **45** (5), P. 785–788.
- [15] Fedorov P.P., Buchinskaya I.I., et al. Phase Diagrams of the NaF–RF₃ (R = La, Ce, Pr, Nd, Sm) Systems. *Russ. J. Inorgan. Chem.*, 2000, **45** (6), P. 949–952.
- [16] Fedorov P.P., Buchinskaya I.I., et al. CaF₂–BaF₂ Phase Diagram. *Doklady Physical Chemistry*, 2005, **401** (2), P. 53–55.
- [17] Fedorov P.P., Rappo A.V. NaF–CaF₂–YbF₃ Phase Diagram. *Russ. J. Inorgan. Chem.*, 2008, **53** (7), P. 1126–1129.
- [18] Fedorov P.P., Buchinskaya I.I., et al. Saddle Points on the Liquidus Surfaces of Solid Solutions in the PbF₂–CdF₂–RF₃ Systems. *Russ. J. Inorgan. Chem.*, 1996, **41** (3), P. 445–449.
- [19] Stasjuk V.A., Buchinskaya I.I., et al. Liquidus and Solidus of Fluorite Solid Solutions in the CaF₂–SrF₂–LaF₃ System. *Russ. J. Inorgan. Chem.*, 1998, **43** (8), P. 1266–1269.
- [20] Fedorov P.P., Sobolev B.P. Conditions for the Formation of Maxima on the Fusion Curves of Solid Solutions in Salt Systems. *Russ. J. Inorgan. Chem.*, 1979, **24** (4), P. 574–575.

- [21] Fedorov P.P. Geometric Thermodynamic Description of the Congruent-Melting Points of Solid Solutions in Binary and Ternary Systems. *Russian J. Inorgan. Chem.*, 2007, **52** (1), P. 116–120.
- [22] Fedorov P.P. Thermodynamic-Topological Analysis of Melt Solidification in the Vicinity of Singular Points in Phase Diagrams. *Russ. J. Inorgan. Chem.*, 2005, **50** (12), P. 1933–1941.
- [23] Beilmann M., Beneš O., Konings R.J.M., Fanghnel Th. Thermodynamic Investigation of the (LiF+NaF+CaF₂+LaF₃) System. *J. Chem. Thermodynamics*, 2011, **43**, P. 1515–1524.
- [24] Lutsyk V.I., Vorobeva V.P., Computer Models of Eutectic Type T-x-y Diagrams with Allotropy. Two Inner Liquidus Fields of Two Low-Temperature Modifications of the Same Component. *J. Therm. Anal. Calorim.*, 2010, **101** (1), P. 25–31.
- [25] Lutsyk V.I., Vorobeva V.P. 3D Model of the T-x-y Diagram of the Bi–In–Sn System for Designing Microstructure of Alloys. *Rus. J. Inorgan. Chem.*, 2016, **61** (2), P. 188–207.
- [26] Lutsyk V.I., Zelenaya A.E., Nasrulin E.R., Bimbaev E.S. System NaCl–CaCl₂–MgCl₂ system: elaboration of spatial computer model of T-diagram. *Journal Melts*, 2016, **3**, P. 206–215. (In Russian)
- [27] Miura S. Geometrical Approach to Reaction Schemes of Multicomponent Phase Diagrams. *J. Phase Equilibria and Diffusion*, 2006, **27** (1), P. 34–46.
- [28] Lutsyk V.I., Vorob'eva V.P., Zelenaya A.E., Reference Book on the Oxide Systems Space Diagrams as a Tool for Data Mining. *Solid State Phenomena*, 2015, **230**, P. 51–54.
- [29] Sobolev B.P., Fedorov P.P. Phase Diagrams of the CaF₂–(Y, Ln)F₃ Systems. I. Experimental. *J. Less-Common Metals*, 1978, **60**, P. 33–46.
- [30] Švantner M., Mariani E., et al. Solid Solution with Fluorite Structure in the CaF₂–LaF₃ System. *Crystal Research and Technology*, 1979, **14** (3), P. 365–369.
- [31] Fedorov P.P., Mayakova M.N., et al. Phase Diagram of the NaF–CaF₂ System and the Electrical Conductivity of a CaF₂-Based Solid Solution. *Rus. J. Inorg. Chem.*, 2016, **61** (11), P. 1472–1478.
- [32] Cazorla C., Errandonea D. Superionicity and Polymorphism in Calcium Fluoride at High Pressure. *Physical Review Letters*, 2014, **113**, 235902.
- [33] Sharma YC. Synthesis and characterisation of CZTSe bulk materials for thermoelectric applications. *Nanosystems: Physics, Chemistry, Mathematics*, 2020, **11** (2), P. 195–204.
- [34] Dong Y., Wang H., Nolas G.S. Synthesis and thermoelectric properties of Cu excess Cu₂ZnSnSe₄. *Phys. Status Solidi RRL*, 2014, **8**, P. 61–64.
- [35] Raju C., Falmbigl M., et al. Thermoelectric properties of chalcogenide based Cu_{2+x}ZnSn_{1-x}Se₄. *AIP Advanced.*, 2013, **3**, 032106.
- [36] Shi X.Y., Huang F.Q., Liu M.L., Chen L.D. Thermoelectric properties of tetrahedrally bonded wide-gap stannite compounds Cu₂ZnSn_{1-x}In_xSe₄. *Appl. Phys. Lett.*, 2009, **94**, 122103.
- [37] Chang K., Meng F., et al. Theory-guided bottom-up design of the FeCrAl alloys as accident tolerant fuel cladding materials. *Journal of Nuclear Materials*, 2019, **516**, P. 63–72.
- [38] Lutsyk V.I. T-x-y diagrams of lead-free soldering systems with thermodynamic contours of minimal surfaces. *Nanomaterials: Applications and Properties*, 2011, **2** (1), P. 11–19.
- [39] Lutsyk V.I., Vorobeva V.P., Zelenaya A.E. 3D Computer Models of the Ag–Sb–Sn and MgO–Al₂O₃–SiO₂ T-x-y Diagrams. *Acta Physica Polonica*, 2018, **133** (4), P. 763–766.

Hydrothermal synthesis of CeO₂ nanostructures and their electrochemical properties

A. N. Bugrov^{1,2}, V. K. Vorobiov¹, M. P. Sokolova¹, G. P. Kopitsa^{3,4}, S. A. Bolshakov², M. A. Smirnov¹

¹Institute of Macromolecular Compounds RAS, Bolshoy pr. 31, 199004 St. Petersburg, Russia

²St. Petersburg Electrotechnical University "LETI", ul. Professora Popova 5, 197376 St. Petersburg, Russia

³Grebenshchikov Institute of Silicate Chemistry RAS, Makarova emb. 2., letter B, 199034 St Petersburg, Russia

⁴St. Petersburg Nuclear Physics Institute, NRC KI, Orlova roscha mcr. 1, 188300 Gatchina, Leningrad region, Russia

alexander.n.bugrov@gmail.com, vrbvrbvrb@mail.ru, pmarip@mail.ru, kopitsa@mail.pnpi.spb.ru,

sergey_bolshakov01@mail.ru, smirnov_michael@mail.ru

PACS 78.67.Bf; 82.47.Uv

DOI 10.17586/2220-8054-2020-11-3-355-364

Functional nanomaterials based on transition metal oxides are often used for the manufacture of supercapacitors and batteries, due to their special redox properties. The nanosized transition metal oxides used as the electrode material in some cases exhibit abnormally high values of capacitance and energy density. In this regard, it is important to understand what structural features of the nanomaterial determine the electrochemical characteristics of an electronic device. For this purpose, ceria nanorods and nanocubes were specifically synthesized under hydrothermal conditions at elevated pressure (15 MPa), different alkali contents, and two temperature regimes (100 and 180 °C). The obtained CeO₂ nanostructures were characterized using the methods of X-ray diffraction, transmission electron microscopy, and low-temperature nitrogen adsorption. The electrochemical properties of ceria nanostructures were investigated in 1 M Na₂SO₄ water electrolyte. The influence of the structural and surface characteristics of the synthesized nanorods and nanocubes on their charge storage ability is discussed. It was shown that CeO₂ in the form of nanocubes demonstrate higher specific capacitance in comparison with nanorods, which makes them more attractive for application in supercapacitors with neutral electrolytes.

Keywords: cerium dioxide, hydrothermal method, nanorods, nanocubes, fluorite structure, specific surface area, cyclic voltammetry, specific capacitance.

Received: 12 December 2019

Revised: 9 January 2020

1. Introduction

Inorganic oxides and composites based on them with electroconducting polymers or carbon nanomaterials attract increased attention as prospective materials for electrochemical energy storage devices due to their capability to store charge via reversible redox reactions. In a number of recent works, the electrochemical properties of supercapacitor electrode materials containing MnO₂ [1], WO₃ [2], Fe₃O₄ [3], Mn₃O₄ [4], RuO₂ [5], MoO₃ [6] or Fe₂O₃ [7] were reported. Ceria (CeO₂) is also one of the widely investigated prospective candidate [8]. In ceria structure, each Ce⁴⁺ cation is coordinated by eight neighboring oxygen anions, which occupy octahedral interstitials surrounded by four cerium atoms [9]. Fluorite-structured CeO₂, as a rule, contains internal Schottky and Frenkel defects caused by thermal motion in crystals and equilibrium reactions with gaseous oxygen in the environment [10]. At low oxygen partial pressure and elevated temperatures, Ce⁴⁺ can spontaneously reduce to the trivalent state, creating both oxygen vacancies and quasi-free localized electrons in the ceria crystal lattice [11, 12]. Oxygen non-stoichiometry of CeO₂ substantially determines its electrochemical [13], but does not have any complex mechanism that causes phase transformation and structural symmetry changes like in zirconia [14, 15]. The low redox potential of transition between Ce⁴⁺ and Ce³⁺, along with the high mobility of oxygen in the crystalline structure of CeO₂, leads to the manifestation of mixed ion-electron conductivity. The ability to accumulate and release oxygen as a result of reversible redox transitions of Ce⁴⁺/Ce³⁺ valence states causes CeO₂ to be used as a promoter in three-component catalysts for removing toxic exhaust gases [16], as a regulator of the thermal properties of polymers [17], a solid oxide fuel cell [18], an antioxidant [19] and anode material in lithium-ion batteries [20].

It is known that the concentration of oxygen defects increases with decreasing particle size of ceria, as well as with the transition from zero- to the one-dimensional nanostructures [21, 22]. An increase in the number of point defects is observed in a series of nanoscale rods ζ cubes ζ octahedra [22]. Usually, three planes (100), (110) and (111) go out onto the surface of ceria nanostructures. The formation energy of oxygen vacancies in the {111} facets is higher than in the {110} and {100} ones [23]. The growth directions of CeO₂ crystals and the type of planes forming their surfaces can be controlled by varying the synthesis conditions [24, 25]. In the case of nanosized octahedra, eight (111) and six (100) planes go outside, while CeO₂ cubes are usually surrounded by six {100} facets. The situation is much more complicated for nanorods since they can grow both 1) along the [110] direction with the exposure of the {100} and {110} facets, and 2) along [211], [111], [102] and [100] directions, which open the {111} and

{110} facets to the surface [26]. Moreover, the specific surface area of one-dimensional structures is usually higher than that of cubes and octahedra. According to published data, the defectiveness and the ratio of the surface area to volume for CeO₂ nanostructures are decisive not only in terms of catalytic [27] and biological properties [28–30], but also in electrochemical characteristics. The higher specific electrochemical capacitance for nanorods (162.47 F g⁻¹) compared to nanoscale octahedra and cubes in alkali electrolyte (3 M KOH) was reported [31]. This result was attributed simultaneously to the high surface area of nanorods and to the predominant effect of {110} and {100} facets. For the case of ceria electrochemical properties in eco-friendly neutral electrolyte it was demonstrated that increasing of amount of surface defects leads to an increase in electrochemical capacitance [32]. At the same time, the electrochemical performance in neutral electrolyte can also be influenced by crystalline facets exhibited on the surface of ceria nanoparticles and this point was not discussed yet.

Therefore, the aim of this study was to investigate the electrochemical performance of CeO₂ nanoparticles in a neutral electrolyte and to compare the electrochemical charge storage ability of ceria nanorods, the contact surface of which is represented by {110} / {111} facets with nanocubes surrounded exclusively by {100} ones. To this end, ceria nanostructures of the above morphology were obtained under hydrothermal conditions. The structure of nanoparticles and their electrochemical charge storage ability in 1 M Na₂SO₄ electrolyte were studied.

2. Experimental

2.1. Synthesis of ceria nanostructures

To obtain ceria nanostructures in the form of rods and cubes Ce(NO₃)₃·6H₂O (chemically pure, CAS 10294-41-4, Vekton, Russia) and sodium hydroxide (analytically pure, GOST 4328-77, Vekton, Russia) as a precipitant were used. A highly concentrated alkali solution (9 M for rods and 6 M for cubes) was added dropwise to a previously prepared 0.5 M solution of cerium(III) nitrate. Initially, a brown suspension formed, which after 30 minutes stirring at room temperature changed color to light yellow. The resulting suspension was transferred to an autoclave and treated under hydrothermal conditions for 24 hours at a pressure of 15 MPa and a temperature of 100 °C to obtain one-dimensional nanostructures or 180 °C in the case of crystallization of nanoscale cubes. After hydrothermal treatment, the obtained white precipitates of CeO₂ nanoparticles were repeatedly washed with distilled water and ethanol, followed by drying at 60 °C in air for a day.

2.2. Instruments and characterization

The size, shape and structure of the ceria nano-objects obtained in this study were determined using a JEM-2100F (Jeol Ltd., Japan) transmission electron microscope at an accelerating voltage of 200 kV. Aqueous dispersions of CeO₂ nanopowders were deposited on copper grids coated with graphene to obtain bright-field images and electron microdiffraction patterns.

X-ray diffraction (XRD) patterns of CeO₂ nanostructures were obtained using a SmartLab 3 (Rigaku Corporation, Tokyo, Japan) diffractometer with CuK_α radiation. The scanning was conducted in the range of 2θ angles from 20 to 80°. To take into account the instrumental broadening, the Caglioti parameters established by fitting the complete profile of the diffraction pattern of the external LaB₆ standard in the MAUD program were used. The unit cell parameters of CeO₂ nanostructures were determined in the same software package using a crystallographic information file of ceria [33] from the COD database according to the procedure described in [34]. The average size of the coherent scattering regions for both nanoscale rods and cubes was calculated using the Scherrer equation.

The values of *S*_{BET} of the powders of CeO₂ nanorods and nanocubes were measured by low-temperature nitrogen adsorption using a Nova 4200V analyzer (QuantaChrome, USA). Before measurements, the samples were degassed at 150 °C in vacuo for 16 hours. *S*_{BET} of the samples was calculated using the Brunauer–Emmett–Teller model by 7 points in the range of partial nitrogen pressures *P*/*P*₀ = 0.07 – 0.25. The pore size distribution was estimated on the basis of nitrogen desorption isotherms by the Barrett–Joyner–Halenda (BJH) method.

Fourier transform infrared (FTIR) spectroscopy study was performed on the IRAffinity-1S spectrometer (Shimadzu, Japan) in the range 350 – 4000 cm⁻¹. Spectra for CeO₂ nanopowders were measured in the transmission mode using KBr pellets.

The electrochemical properties of the synthesized nano-objects were tested in standard 3-electrode cells. The working electrodes were prepared by dispersion of ceria in the N,N-dimethylformamide (anhydrous, 99.8 %, CAS 68-12-2, Sigma-Aldrich) containing carbon black and poly(1,1-difluoroethylene) (PVDF; average *M*_w = 1.9 × 10⁵, Kynar-720®, Atofina Chemicals Inc., USA). The glass carbon electrode with working area 1.3 cm² was covered with 0.3 ml of prepared dispersion and dried at 60 °C. As a result, the electrodes containing 1.5 mg of ceria nanoparticles, 0.2 mg of carbon black and 0.2 mg of PVDF as a binder were prepared. The Ag/AgCl electrode as a reference and

Pt foil as a counter electrode were used. 1 M Na₂SO₄ was used as an electrolyte. Experiments were conducted with P-40X potentiostat-galvanostat (“Elins”, Moscow, Russia).

3. Results and discussion

Alkali concentration and hydrothermal treatment temperature were key factors in the formation of CeO₂ structures in the form of nanocubes and nanorods. CeO₂ nanosized rods with an average diameter of 10 nm and a length of 100 nm are formed according to transmission electron microscopy (TEM) in the case of using a 9 M NaOH solution as a hydrothermal medium at 100 °C and a pressure of 15 MPa after 24 hours (Fig. 1a, row 1). Weaker alkaline solutions reduce the anisotropy of ceria nanostructures, which crystallize under hydrothermal conditions, and increasing the temperature to 180 °C intensifies the dissolution/recrystallization processes and oxidation of the Ce(OH)₃ clusters to CeO₂ [25, 35]. The above processes contribute to the formation of nanoscale cubes, rather than nanorods (Fig. 1b, row 2). The CeO₂ nanocubes synthesized in a 6 M NaOH solution at an elevated temperature from cerium (III) hydroxide exhibit a wide particle size distribution ranging from 10 to 54 nm. The average nanocube size was 38 nm, in accordance with the statistics collected on the base of 15 TEM micrographs. The rings in the microdiffraction patterns of both nanorods and nanocubes corresponding to the diffraction planes (111), (200), (220), (311), (222), (400), (331), (420) confirm their cubic crystalline lattice (Fig. 1b).

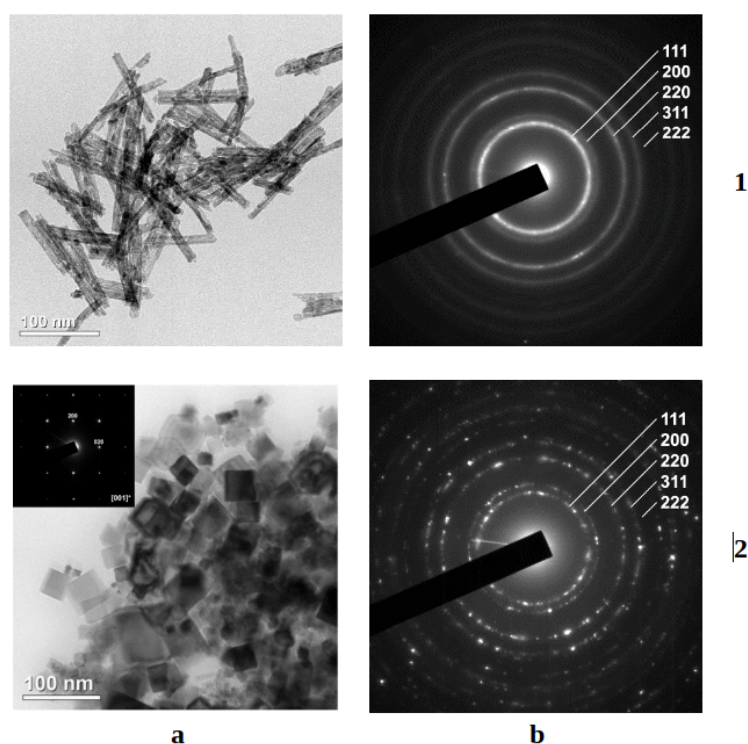


FIG. 1. TEM micrographs (a) and electron microdiffraction patterns (b) of CeO₂ nanorods (1) and nanocubes (2) obtained under hydrothermal conditions with varying pH and synthesis temperature

The surface structure of CeO₂ nanoparticles was investigated with high-resolution transmission electron microscopy (HRTEM), images for nanocubes and nanorods are given in Fig. 2a and Fig. 2b,c, respectively. The obtained results confirm that nanocubes exhibit {100} facets on the surface, while {110} and {111} facets are characteristic for nanorods. On the base of this data the 3D models of CeO₂ crystallites with the relevant top surfaces (Fig. 2b, e, h) and the projections of atoms positions on the plane which is perpendicular to the surface (Fig. 2c, f, i) were built. These projections clearly demonstrate the distance between the surface and neighboring Ce⁴⁺ ions for the different types of crystalline facets. The maximal distance is observed for {100} facet (0.14 nm), while for {111} facet this value is 0.08 nm. In the case of {110} facet, Ce⁴⁺ ions appear on the surface. These data allow one to propose that adsorption of sodium ions from electrolyte on {100} facet is favorable in comparison with {110} and {111} facets due to lower electrostatic repulsion between Ce⁴⁺ and Na⁺ ions. As a result, the highest electrical capacitance can be expected for the {100} surface, which is in agreement with results of electrochemical measurements presented below.

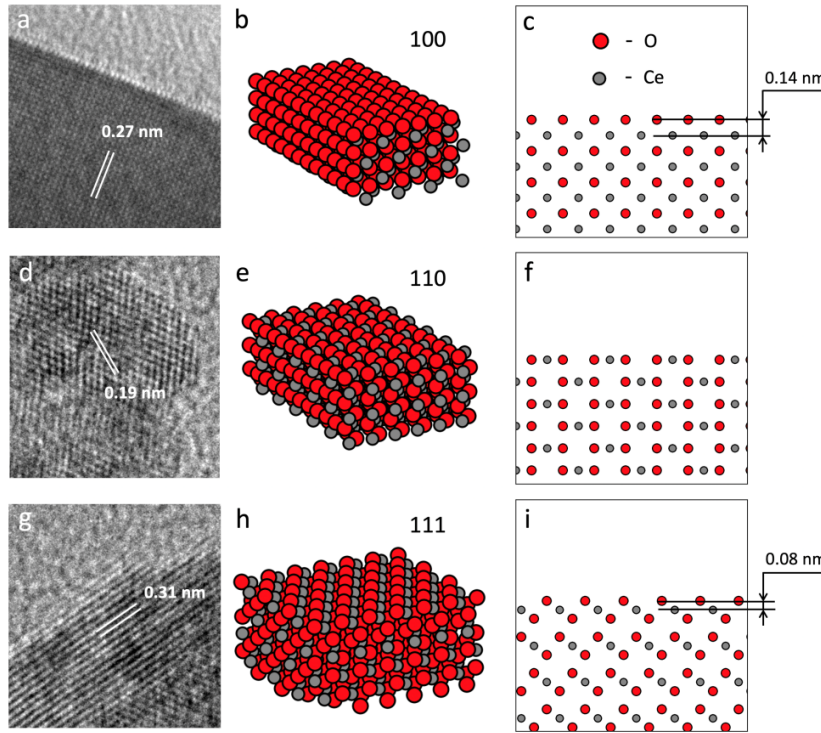


FIG. 2. HRTEM images for surfaces of the CeO_2 nanostructures (a, d, g), 3D model perspectives (b, e, h) and projections on the plane perpendicular to the surface (c, f, i) for nanocubes (a – c) and nanorods (d – i)

The XRD patterns of the synthesized CeO_2 nanostructures are shown in Fig. 3. The XRD analysis performed using the PD-Win 4.0 software package revealed the complete correspondence of nanoscale rods and cubes to the fluorite structure with the $\text{Fm}\bar{3}\text{m}$ space group (Card No. 43-1002 according to the ASTM database [36]). The average size of the coherent scattering regions for CeO_2 nanorods, calculated using the Scherrer equation for broadening of the XRD peaks, was 9 ± 1 nm (Fig. 3a). The crystallite size for cubic nanoparticles was larger, approximately 40 nm (Fig. 3b). Compared to CeO_2 nanocubes, the unit cell parameters calculated for nanorods were higher due to a greater number of structural defects, the evolution of distortions and stresses in crystallites [37] (Table 1).

TABLE 1. X-ray diffraction data for prepared ceria nanostructures

Morphology	Unit cell parameters			Average crystallite size, nm	Microstrain
	Lengths, Å	Angles, °	V, Å ³		
Nanorods	$a = b = c = 5.427$	$\alpha = \beta = \gamma = 90$	159.8	9 ± 1	$2.73 \cdot 10^{-3}$
Nanocubes	$a = b = c = 5.414$	$\alpha = \beta = \gamma = 90$	158.7	40 ± 3	$2.86 \cdot 10^{-8}$

According to the data of low-temperature nitrogen adsorption, the porosity and S_{BET} of ceria nanopowders substantially depend on the morphology of structures formed during hydrothermal treatment, their imperfection, and size. Fig. 4 shows the complete adsorption-desorption isotherms for CeO_2 powders of nanorods and nanocubes. Both measured isotherms are characterized by a rather narrow capillary-condensation hysteresis and are of type IV according to the IUPAC classification. This type corresponds to adsorption on mesoporous materials. The hysteresis loop can be classified as type H3, which is characteristic of materials with slit-like pores. Estimates of the S_{BET} are presented in Table 2 and indicate a significant decrease in its value from 108.2 to 18.5 m^2/g during the transition from CeO_2 nanorods to nanocubes. This fact is in good agreement with the XRD data and electron microscopy, according to which the crystallite size decreases and the fraction of oxygen vacancies in them increases, contributing to the formation of a more developed surface (Fig. 1, Table 1).

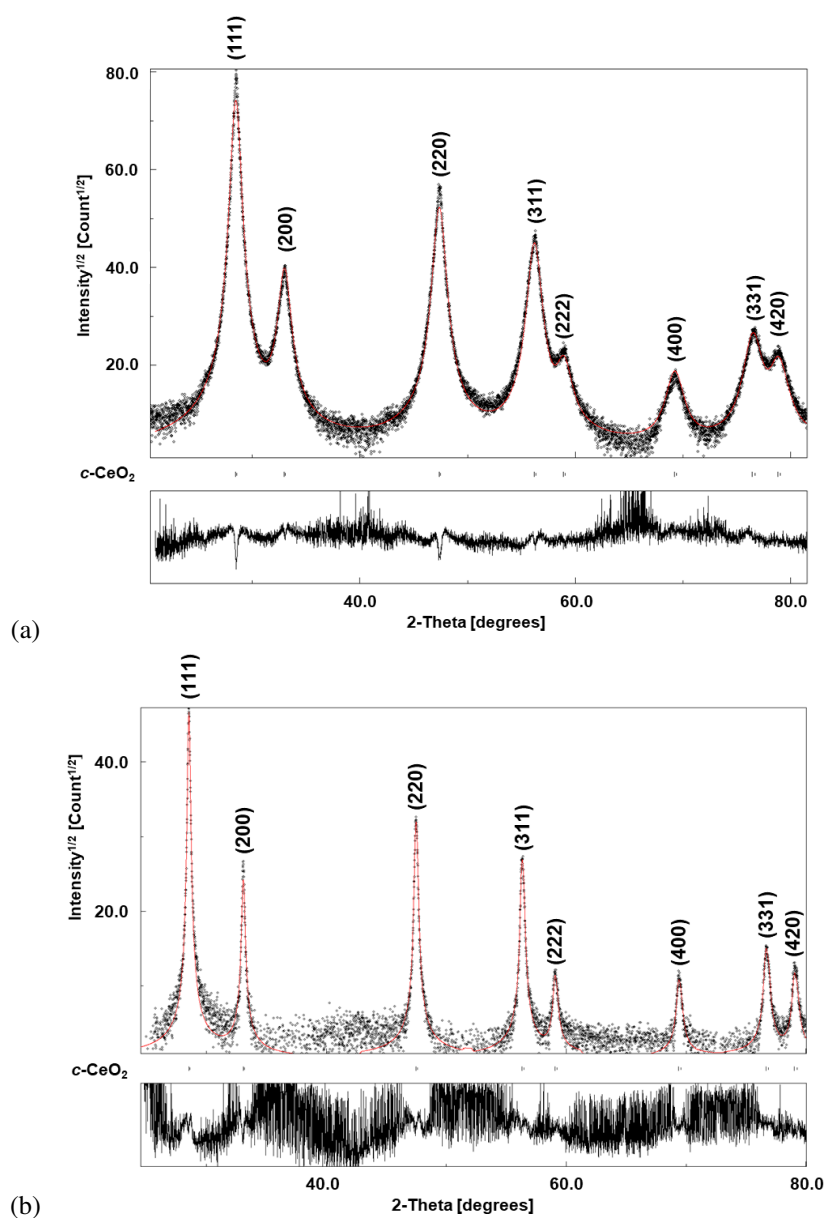


FIG. 3. XRD patterns of CeO₂ nanorods (a) and nanocubes (b) obtained under hydrothermal conditions with varying pH and temperature of the synthesis

TABLE 2. The structural parameters determined by the method of low-temperature nitrogen adsorption for prepared CeO₂ nanoparticles

Morphology	S_{BET} , m ² /g	D_1 , nm	D_2 , nm	V_{pores}^* , cm ³ /g
Nanorods	108.2 ± 2.2	2.4	13.2	0.43
Nanocubes	18.5 ± 2.8	1.9	36.4	0.22

* The specific pore volume is determined by the maximum filling ($P/P_0 = 0.99$).

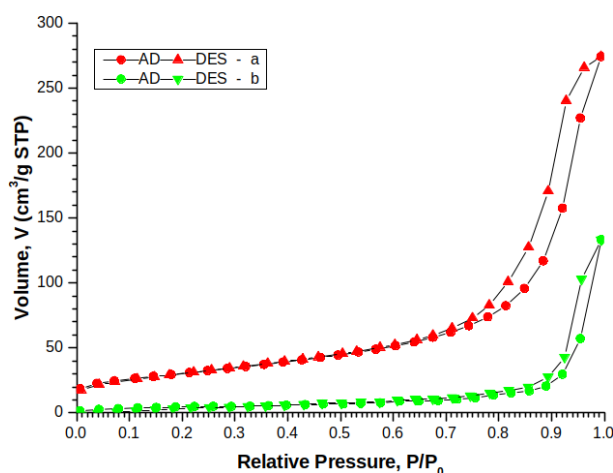


FIG. 4. Adsorption (AD)-desorption (DES) isotherms for CeO_2 nanorods (a) and nanocubes (b) obtained under hydrothermal conditions with varying pH and temperature of the synthesis

The pore size distributions calculated from the desorption branch of isotherm by the BJH algorithm for nanorod and nanocube powders are shown in Fig. 5. Both types of synthesized CeO_2 nanostructures are characterized by a bimodal pore size distribution. Micropores are formed as a result of the splicing of nanocrystallites by the mechanism of oriented attachment, and mesopores are the result of their subsequent aggregation [38]. The position of the second maximum (D_2) for nanocubes is substantially (about 3 times) shifted toward larger pore sizes in comparison with nanorods (Table 2). The specific pore volume for nanostructures with a minimum axial ratio, on the contrary, decreases from 0.43 to $0.22 \text{ cm}^3/\text{g}$ due to dense crystallite compaction.

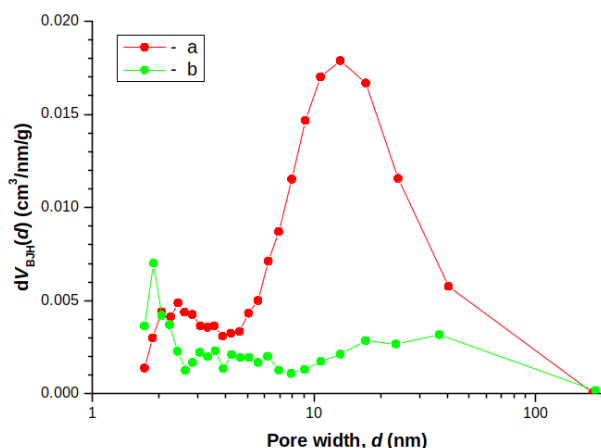


FIG. 5. Pore size distributions for CeO_2 nanorods (a) and nanocubes (b), calculated by the BJH algorithm

FTIR analysis was carried out to take into account possible effect of the surface hydroxylation degree of CeO_2 nanostructures formed under different conditions of hydrothermal synthesis on the electrochemical properties of electrodes. It is known that surface hydroxyl groups can influence the electrochemical performance of inorganic electrodes. For example, significant increase of specific capacitance of MoO_3 nanowires was observed after its hydrogenation [39]. The authors mention that along with increasing of electrical conductivity, the increasing of density of surface hydroxyl groups can be the factor that increases the specific capacitance.

However, the mechanism of influence for surface hydroxylation on the capacitance properties of metal oxides is not clear. It can be proposed that if hydrogen is involved in electrochemical process, surface hydroxylation can promote the reaction. This was demonstrated for electrochemical reduction of CO_2 on the surface of tin oxide [40]. The increasing of electrical current during CV cycling for WO_3 in acidic electrolyte was also observed [41].

The FTIR spectra of CeO_2 nanostructures obtained in this work are given in Fig. 6. The following bands corresponding to surface OH groups can be found within the $3800 - 3000 \text{ cm}^{-1}$ region of FTIR spectra in the case of CeO_2 synthesized under hydrothermal conditions at high pH: isolated (3700 cm^{-1}), bridging (3641 cm^{-1}), multiple bonded

(3550 – 3500 cm⁻¹) and hydrogen bridging hydroxyls (wide band around 3400 cm⁻¹) [42,43]. It is seen in Fig. 6a and 6b, that in our case these bands overlap forming one wide peak 3700 – 3000 cm⁻¹ centered near 3447 cm⁻¹ for both prepared samples. The relative number of surface hydroxyls can be estimated from the maximum of intensity of the band centered at 3447 cm⁻¹ (I_{3447}) after normalization of the spectra according to the intensity of Ce–O stretching vibration peak (around 430 cm⁻¹). The found values of I_{3447} were 0.080 and 0.414 for nanocubes and nanorods, respectively (ratio nanorods:nanocubes = 5.2). Taking into account the ratio between the specific surface of nanorods and nanocubes (5.8), the slightly higher surface density of hydroxyl groups for nanocubes in comparison to nanorods can be proposed. However, the difference is rather small (about 12 %) thus, it can be assumed that for our experiment the type of exhibited crystallographic plane will be the main parameter that leads to the difference in the electrochemical performance between nanorods and nanocubes.

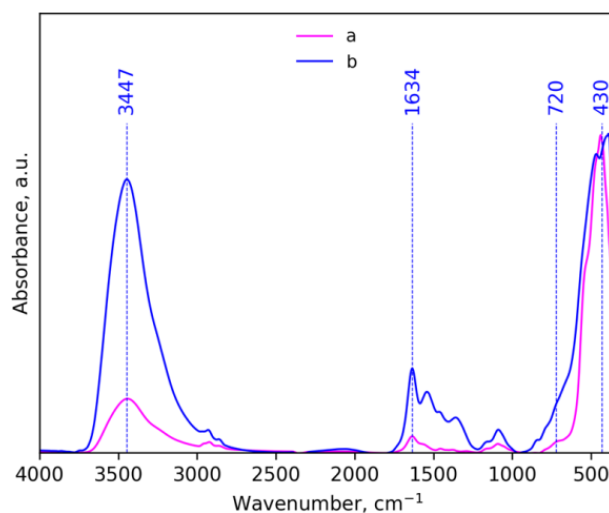


FIG. 6. FTIR spectra of CeO₂ nanocubes (a) and nanorods (b), normalized to a band of 430 cm⁻¹

The absorption bands for the 1250 – 850 cm⁻¹ region in the FTIR spectra of CeO₂ nanocubes and nanorods can be attributed to the deformation vibrations of formates or carbonates formed due to the interaction of the surface of ceria nanostructures with atmospheric CO₂. Signals in the 2800 – 2900 cm⁻¹ range correspond to stretching vibrations of C–H groups, and the bands at 1634 and 720 cm⁻¹ are deformation vibrations of O–H and stretching vibrations of Ce–O–Ce groups, respectively.

The capacitance properties of CeO₂ nanostructures were investigated with cyclic voltammetry (CV) and galvanic charge-discharge (GCD) measurements. The CV curves of ceria nanostructures with different morphology were measured at a scan rate of 10 mV/s in the potential range –0.2 – +0.5 V vs Ag/AgCl reference electrode. The results shown in Fig. 7a demonstrate that ceria in the form of cubes has significantly higher area covered with CV curve in comparison with CeO₂ nanorods. This means higher capacitance of electrode material containing CeO₂ nanocubes, which agrees with GCD curves given in Fig. 7b. GCD curves demonstrate slightly disturbed triangular shape, which is characteristic for capacitive behavior of the material. Non-ideal triangular shape in the connection with waves on CV curves gives evidence that pseudocapacitance mechanism of charge storage also takes place. The specific capacitance (C_{GCD}) of electrodes was calculated from GCD experiments as:

$$C_{GCD} = \frac{It}{A(U_2 - U_1)},$$

where I – applied current, t – discharge time, A – electrode area, U_2 and U_1 are the upper and the lower limits of the voltage range.

Values of C_{GCD} for CeO₂ in the form of nanocubes and nanorods found using this equation are 5.7 and 0.59 mF/cm², respectively. Since the specific surface for nanorods is significantly higher than that of nanocubes, it can be suggested that the difference in capacitance is connected with crystalline structure of the surface of nanoparticles. As it was mentioned earlier, depending on the conditions of hydrothermal synthesis, various directions of crystal growth and exposing of CeO₂ planes can be realized. In addition, the possibility of the transformation of the {110} and {100} exposed facets into {111} for nanorods obtained under hydrothermal conditions during their subsequent heat treatment was reported [44,45]. In our case, growth of one-dimensional ceria structures through the [211] direction with exposed {111} and {110} facets takes place. As a result of a careful analysis of the changes in the morphology

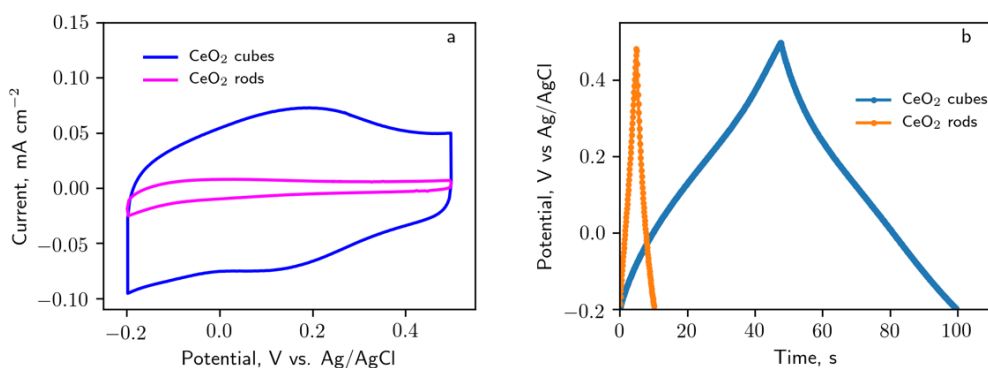
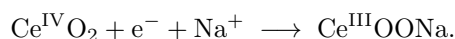


FIG. 7. Cyclic voltammetry curves measured at 10 mV/s (a) and galvanostatic charge-discharge curves measured at 0.08 mA/cm²(b)

of CeO₂ nanorods at different stages of hydrothermal synthesis, prior authors [28] found that one-dimensional structures with orientation along the [211] direction are formed by the so-called “oriented attachment” mechanism. The driving force for this spontaneously oriented attachment is a decrease in the total surface energy due to the union of the planes by means of which the crystals are joined. The attachment can take place either along the [211] direction with exposed {111} facets or along the [110] direction with {200} facets exposure [46]. The former would be more favorable because the CeO₂ {111} surface is the most stable one. The formation of nanorods along the [211] direction via oriented attachment followed by Ostwald ripening under the conditions of hydrothermal synthesis applied in this work was observed in contrast to [25]. This fact is supported with the significantly lower electrochemical activity of nanorods in the electrochemical experiment. The mechanism, proposed for the charge storage process in ceria, takes into account the adsorption of cation from electrolyte on the surface of crystal [31]. At the next stage, the reduction of cerium (IV) to cerium (III) can occur, leading to the realization of pseudocapacitance in the electrode [47]. These two stages can be summarized as follows:



As it was demonstrated earlier, among the most common surface planes of ceria, exactly (100) is characterized with the highest projection of distance between cerium and oxygen atoms on the axis perpendicular to the surface of the nanocrystal. Thus, the possibility of most negative surface potential can be proposed for (100) plane in comparison with others. This can lead to the enhancement of Na⁺ adsorption on the surface presented with this plane.

For further investigation of capacitance properties of CeO₂ nanocubes, the contributions of two different mechanisms of charge storage: i.e., capacitance of “outer” active surface and capacitance connected with the ion insertion process (capacitance of the “inner” active surface) were estimated according to the method developed by Trasatti [48]. This method is based on the analysis of variation of electrode capacitance on the scan rate during CV experiments. The corresponding CV measurements in the range of scan rates from 1 up to 20 mV/s are given in Fig. 8a. The capacitance values, calculated from given results, are plotted versus the square root of the reciprocal scan rate (Fig. 8b) and the reciprocal capacitance – versus the square root of the scan rate (Fig. 8c). Linear extrapolation of both plots to $x = 0$ gives the values of the “outer” surface and total theoretical (C_{total}) capacitances of the material, respectively. The “outer” surface capacitance, which is scan-rate independent can be considered as the double-layer-like capacitance (C_{dl}). The value of C_{total} includes both the “inner” and “outer” surface capacitances. The “scan-rate dependent” capacitance of “inner” surface can be considered as a pseudocapacitance-like (C_{p}) one, which, in our case, can be connected with an oxidation/reduction transition between Ce⁴⁺ and Ce³⁺ accompanied with insertion/release of sodium ions. The value of C_{p} can be calculated as $C_{\text{p}} = C_{\text{total}} - C_{\text{dl}}$.

As it is seen from Fig. 8b and c, the values of C_{dl} and C_{total} for CeO₂ nanocubes are 4.7 and 7.7 mF cm⁻², respectively. The value of capacitance, obtained from GCD measurements (5.7 mF/cm²) is between C_{dl} and C_{total} , which is the reasonable result. This allows to propose that 61 % of CeO₂ capacitance is connected with charge-discharge of electrochemical double layer, while only 39 % is provided by pseudocapacitance-like mechanism. It worth mentioning that, both mechanisms of charge storage are closely connected with the adsorption of cations from solution onto the surface of nanoparticles. Thus, the structural characteristics of ceria’s surface are of prime importance for its capacitance properties.

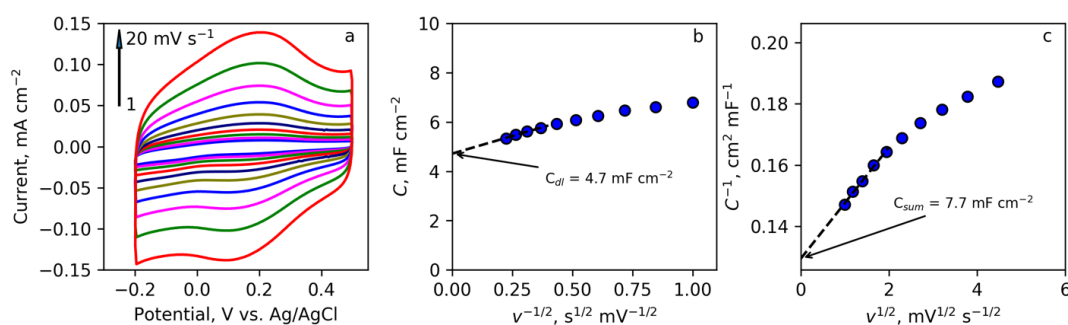


FIG. 8. Cyclic voltammetry curves for CeO₂ nanocubes at different scan rates (a), capacitance dependence on the square root of the reciprocal scan rate (b), and the reciprocal capacitance dependence on the square root of scan rate (c)

4. Conclusions

It was revealed using XRD, TEM, HRTEM that ceria nanorods are formed from the CeO₂ nucleating centers along the [211] direction with inactive {111} facets exposure by the attachment mechanism followed by Oswald ripening during hydrothermal synthesis at 100 °C. An increase in the synthesis temperature leads to the formation of CeO₂ nanocubes, with surface represented exclusively by {100} facets. It was demonstrated that despite the lower specific surface area, the capacitance of the CeO₂ nanocubes is 10 times higher than one for nanorods. It was suggested that this result is connected with the possibility of more favorable adsorption of cations onto {100} facets in comparison with those of {110} and {111}. Investigation of mechanism of charge storage using Trasatti method allows to assume that 61 % of total capacitance of CeO₂ nanocubes is realized via charging of double-layer, while 39 % can be attributed to the pseudocapacitance-like processes. The obtained results can be significant for further elaboration of polymer-inorganic composites based on CeO₂ for application in electrochemical devices and electrodes.

Acknowledgements

The reported study was funded by Russian Foundation for Basic Research (Grant 18-03-01167 a). TEM studies were carried out in the Federal Joint Research Center “Material science and characterization in advanced technology”. XRD measurements were performed using Engineering Center equipment of the St. Petersburg State Technological Institute (Technical University).

References

- [1] Ivanova A.G., Karasev L.V., et al. Development and research of electroactive pseudocapacitor electrode pastes based on MnO₂. *Glass Physics and Chemistry*, 2020, **46** (1), P. 96–101.
- [2] Zhuzhelskii D.V., Tolstopjatova E.G., et al. Electrochemical properties of PEDOT/WO₃ composite films for high performance supercapacitor application. *Electrochimica Acta*, 2019, **299**, P. 182–190.
- [3] Nawwar M., Poon R., et al. High areal capacitance of Fe₃O₄-decorated carbon nanotubes for supercapacitor electrodes. *Carbon Energy*, 2019, **1**, P. 124–133.
- [4] Ata M.S., Milne J., Zhitomirsky I. Fabrication of Mn₃O₄-carbon nanotube composites with high areal capacitance using cationic and anionic dispersants. *Journal of Colloid and Interface Science*, 2018, **512**, P. 758–766.
- [5] Asim S., Javed M.S., et al. RuO₂ nanorods decorated CNTs grown carbon cloth as a free standing electrode for supercapacitor and lithium ion batteries. *Electrochimica Acta*, 2019, **326**, P. 135009.
- [6] Ahmed S., Etmán A.S., Wang Z., et al. Flexible freestanding MoO_{3-x}-carbon nanotubes-nanocellulose paper electrodes for charge-storage applications. *ChemSusChem*, 2019, **12**, P. 5157–5163.
- [7] Yang Z., Tang L., et al. Hierarchical nanostructured α -Fe₂O₃/polyaniline anodes for high performance supercapacitors. *Electrochimica Acta*, 2018, **269** (10), P. 21–29.
- [8] Khan A.J., Hanif M., et al. Energy storage properties of hydrothermally processed nanostructured porous CeO₂ nanoparticles. *Journal of Electroanalytical Chemistry*, 2020, **865**, P. 114158.
- [9] He L., Su Y., Jiang L., Shi S. Recent advances of cerium oxide nanoparticles in synthesis, luminescence and biomedical studies: A review. *Journal of Rare Earths*, 2015, **33** (8), P. 791–799.
- [10] Younis A., Chu D., Li S. Cerium oxide nanostructures and their applications. *Functionalized Nanomaterials*, 2016, **3**, P. 53–68.
- [11] Ivanov V.K., Baranchikov A.E., et al. Oxygen nonstoichiometry of nanocrystalline ceria. *Russian Journal of Inorganic Chemistry*, 2010, **55** (3), P. 325–327.
- [12] Kabir A., Zhang H., Esposito V. Mass diffusion phenomena in cerium oxide. In S. Scirè, & L. Palmisano (Eds.), *Cerium Oxide (CeO₂): Synthesis, Properties and Applications*, 2019, **5**, P. 169–210.
- [13] Mogensen M., Sammes N.M., Tompsett G.A. Physical, chemical and electrochemical properties of pure and doped ceria. *Solid State Ionics*, 2000, **129** (1–4), P. 63–94.

- [14] Bugrov A.N., Almjasheva O.V. Effect of hydrothermal synthesis conditions on the morphology of ZrO₂ nanoparticles. *Nanosystems: Physics, Chemistry, Mathematics*, 2013, **4** (6), P. 810–815.
- [15] Bugrov A.N., Smyslov R.Yu., Zavialova A.Yu., Kopitsa G.P. The influence of chemical prehistory on the structure, photoluminescent properties, surface and biological characteristics of Zr_{0.98}Eu_{0.02}O_{1.99} nanophosphors. *Nanosystems: Physics, Chemistry, Mathematics*, 2019, **10** (2), P. 164–175.
- [16] Trovarelli A. Catalytic properties of ceria and CeO₂-containing materials. *Catalysis Reviews – Science and Engineering*, 1996, **38** (4), P. 439–520.
- [17] Nikolaeva A.L., Gofman I.V., et al. Interplay of polymer matrix and nanosized Redox dopant with regard to thermo-oxidative and pyrolytic stability: CeO₂ nanoparticles in a milieu of aromatic polyimides. *Materials Today Communications*, 2020, **22**, P. 100803.
- [18] Omar S., Wachsman E.D., Nino J.C. Higher ionic conductive ceria-based electrolytes for solid oxide fuel cells. *Applied Physics Letters*, 2007, **91** (14), P. 144106.
- [19] Dhall A., Self W. Cerium oxide nanoparticles: A brief review of their synthesis methods and biomedical applications. *Antioxidants*, 2018, **7** (97), 13 p.
- [20] Zhou F., Zhao X., Xu H., Yuan C. CeO₂ spherical crystallites: Synthesis, formation mechanism, size control, and electrochemical property study. *Journal of Physical Chemistry C*, 2007, **111** (4), P. 1651–1657.
- [21] Deshpande S., Patil S., Kuchibhatla S.V., Seal S. Size dependency variation in lattice parameter and valency states in nanocrystalline cerium oxide. *Applied Physics Letters*, 2005, **87** (13), P. 133113.
- [22] Wu Z., Li M., et al. Probing defect sites on CeO₂ nanocrystals with well-defined surface planes by Raman spectroscopy and O₂ adsorption. *Langmuir*, 2010, **26** (21), P. 16595–16606.
- [23] Li C., Sun Y., et al. Shape-controlled CeO₂ nanoparticles: Stability and activity in the catalyzed HCl oxidation reaction. *ACS Catalysis*, 2017, **7** (10), P. 6453–6463.
- [24] Tang W.-X., Gao P.-X. Nanostructured CeO₂: preparation, characterization, and application in energy and environmental catalysis. *MRS Communications*, 2016, **6** (4), P. 311–329.
- [25] Mai H.-X., Sun L.-D., et al. Shape-selective synthesis and oxygen storage behavior of ceria nanopolyhedra, nanorods, and nanocubes. *Journal of Physical Chemistry B*, 2005, **109**, P. 24380–24385.
- [26] Trovarelli A., Llorca J. Ceria catalysts at nanoscale: How do crystal shapes shape catalysis? *ACS Catalysis*, 2017, **7**, P. 4716–4735.
- [27] Zhang D., Du X., Shi L., Gao R. Shape-controlled synthesis and catalytic application of ceria nanomaterials. *Dalton Transactions*, 2012, **41** (48), P. 14455–14475.
- [28] Ji Z., Wang X., et al. Designed synthesis of CeO₂ nanorods and nanowires for studying toxicological effects of high aspect ratio nanomaterials. *ACS Nano*, 2012, **6** (6), P. 5366–5380.
- [29] Popov A.L., Ermakov A.M., et al. Biosafety and effect of nanoparticles of CeO₂ on metabolic and proliferative activity of human mesenchymal stem cells in vitro. *Nanomechanics Science and Technology: An International Journal*, 2016, **7** (2), P. 165–175.
- [30] Shcherbakov A.B., Zholobak N.M., Spivak N.Ya., Ivanov V.K. Advances and prospects of using nanocrystalline ceria in cancer theranostics. *Russian Journal of Inorganic Chemistry*, 2014, **59** (13), P. 1556–1575.
- [31] Jeyaranjan A., et al. Morphology and crystal planes effects on supercapacitance of CeO₂ nanostructures: Electrochemical and molecular dynamics studies. *Particles and Particle Systems Characterization*, 2018, **35** (10), P. 1800176.
- [32] Kumar M., Bhatt V., et al. Role of Ce³⁺ valence state and surface oxygen vacancies on enhanced electrochemical performance of single step solvothermally synthesized CeO₂ nanoparticles. *Electrochimica Acta*, 2018, **284**, P. 709–720.
- [33] Ranjith K.S., Saravanan P., et al. Enhanced room-temperature ferromagnetism on co-doped CeO₂ nanoparticles: Mechanism and electronic and optical properties. *Journal of Physical Chemistry C*, 2014, **118** (46), P. 27039–27047.
- [34] Lutterotti L., Pilliere H., et al. Full-profile search–match by the Rietveld method. *Journal of Applied Crystallography*, 2019, **52**, P. 587–598.
- [35] Plakhova T.V., Romanchuk A.Yu., et al. Solubility of nanocrystalline cerium dioxide: Experimental data and thermodynamic modeling. *The Journal of Physical Chemistry C*, 2016, **120** (39), P. 22615–22626.
- [36] Grier D., McCarthy G. ICDD Grant-in-Aid, North Dakota State University, Fargo, North Dakota, USA, 1991.
- [37] Yan L., Yu R., Chen J., Xing X. Template-free hydrothermal synthesis of CeO₂ nano-octahedrons and nanorods: Investigation of the morphology evolution. *Crystal Growth & Design*, 2008, **8** (5), P. 1474–1477.
- [38] Ivanov V.K., Polezhaeva O.S., et al. Specifics of high-temperature coarsening of ceria nanoparticles. *Russian Journal of Inorganic Chemistry*, 2009, **54** (11), P. 1689–1696.
- [39] Shakir I., Shahid M., Rana A.U., Warsi F.M. In situ hydrogenation of molybdenum oxide nanowires for enhanced supercapacitors. *RSC advances*, 2014, **4** (17), P. 8741–8745.
- [40] Cui C., Han J., et al. Promotional effect of surface hydroxyls on electrochemical reduction of CO₂ over SnO_x/Sn electrode. *Journal of catalysis*, 2016, **343**, P. 257–265.
- [41] Yoshiike N., Kondo S. Electrochemical properties of WO₃x(H₂O): I. The influences of water adsorption and hydroxylation. *Journal of The Electrochemical Society*, 1983, **130** (11), P. 2283–2287.
- [42] Agarwal S., Lefferts L., Mojet B.L. Ceria nanocatalysts: Shape dependent reactivity and formation of OH. *ChemCatChem*, 2013, **5** (2), P. 479–489.
- [43] Lypez J.M., Gilbank A.L., et al. The prevalence of surface oxygen vacancies over the mobility of bulk oxygen in nanostructured ceria for the total toluene oxidation. *Applied Catalysis B: Environmental*, 2015, **174–175**, P. 403–412.
- [44] Ta N., Liu J., et al. Stabilized gold nanoparticles on ceria nanorods by strong interfacial anchoring. *Journal of the American Chemical Society*, 2012, **134** (51), P. 20585–20588.
- [45] Wang S., Zhao L., et al. Morphology control of ceria nanocrystals for catalytic conversion of CO₂ with methanol. *Nanoscale*, 2013, **5**, P. 5582–5588.
- [46] Ivanov V.K., Polezhaeva O.S., Tret'yakov Yu.D. Nanocrystalline ceria: Synthesis, structure-sensitive properties, and promising applications. *Russian Journal of General Chemistry*, 2010, **80** (3), P. 604–617.
- [47] Maheswari N., Muralidharan G. Supercapacitor behaviour of cerium oxide nanoparticles in neutral aqueous electrolytes. *Energy Fuels*, 2015, **29**(12), P. 8246–8253.
- [48] Ardizzone S., Fregonara G., Trasatti S. “Inner” and “outer” active surface of RuO₂ electrodes. *Electrochimica Acta*, 1990, **35** (1), P. 263–267.



NANOSYSTEMS:

PHYSICS, CHEMISTRY, MATHEMATICS

INFORMATION FOR AUTHORS

The journal publishes research articles and reviews, and also short scientific papers (letters) which are unpublished and have not been accepted for publication in other magazines. Articles should be submitted in English. All articles are reviewed, then if necessary come back to the author to completion.

The journal is indexed in Web of Science Core Collection (Emerging Sources Citation Index), Chemical Abstract Service of the American Chemical Society, Zentralblatt MATH and in Russian Scientific Citation Index.

Author should submit the following materials:

1. Article file in English, containing article title, the initials and the surname of the authors, Institute (University), postal address, the electronic address, the summary, keywords, MSC or PACS index, article text, the list of references.
2. Files with illustrations, files with tables.
3. The covering letter in English containing the article information (article name, MSC or PACS index, keywords, the summary, the literature) and about all authors (the surname, names, the full name of places of work, the mailing address with the postal code, contact phone number with a city code, the electronic address).
4. The expert judgement on possibility of publication of the article in open press (for authors from Russia).

Authors can submit a paper and the corresponding files to the following addresses: nanojournal.ifmo@gmail.com, popov1955@gmail.com.

Text requirements

Articles should be prepared with using of text editors MS Word or LaTeX (preferable). It is necessary to submit source file (LaTeX) and a pdf copy. In the name of files the English alphabet is used. The recommended size of short communications (letters) is 4-6 pages, research articles– 6-15 pages, reviews – 30 pages.

Recommendations for text in MS Word:

Formulas should be written using Math Type. Figures and tables with captions should be inserted in the text. Additionally, authors present separate files for all figures and Word files of tables.

Recommendations for text in LaTeX:

Please, use standard LaTeX without macros and additional style files. The list of references should be included in the main LaTeX file. Source LaTeX file of the paper with the corresponding pdf file and files of figures should be submitted.

References in the article text are given in square brackets. The list of references should be prepared in accordance with the following samples:

- [1] Surname N. *Book Title*. Nauka Publishing House, Saint Petersburg, 2000, 281 pp.
- [2] Surname N., Surname N. Paper title. *Journal Name*, 2010, **1** (5), P. 17-23.
- [3] Surname N., Surname N. Lecture title. In: Abstracts/Proceedings of the Conference, Place and Date, 2000, P. 17-23.
- [4] Surname N., Surname N. Paper title, 2000, URL: <http://books.ifmo.ru/ntv>.
- [5] Surname N., Surname N. Patent Name. Patent No. 11111, 2010, Bul. No. 33, 5 pp.
- [6] Surname N., Surname N. Thesis Title. Thesis for full doctor degree in math. and physics, Saint Petersburg, 2000, 105 pp.

Requirements to illustrations

Illustrations should be submitted as separate black-and-white files. Formats of files – jpeg, eps, tiff.



NANOSYSTEMS:

PHYSICS, CHEMISTRY, MATHEMATICS

Журнал зарегистрирован

Федеральной службой по надзору в сфере связи, информационных технологий и массовых коммуникаций

(свидетельство ПИ № ФС 77 - 49048 от 22.03.2012 г.)

ISSN 2220-8054

Учредитель: федеральное государственное автономное образовательное учреждение высшего образования

«Санкт-Петербургский национальный исследовательский университет информационных технологий, механики и оптики»

Издатель: федеральное государственное автономное образовательное учреждение высшего образования

«Санкт-Петербургский национальный исследовательский университет информационных технологий, механики и оптики»

Отпечатано в Учреждении «Университетские телекоммуникации»

Адрес: 197101, Санкт-Петербург, Кронверкский пр., 49

Подписка на журнал НФХМ

На второе полугодие 2020 года подписка осуществляется через

ОАО Агентство «Роспечать»

Подписной индекс 57385 в каталоге «Издания органов научно-технической информации»